The Layers of Meteoric Nickel and Aluminium in the Earth's Upper Atmosphere

Shane Marcus Daly

Submitted in accordance with the requirements for the degree of Doctor of Philosophy

The University of Leeds

School of Chemistry

May 2020

The candidate confirms that the work submitted is his own, except where work which has formed part of jointly authored publications has been included. The contribution of the candidate and the other authors to this work has been explicitly indicated below. The candidate confirms that appropriate credit has been given within the thesis where reference has been made to the work of others.

Please see the contributions section for full details of the contributions of the candidate and other authors.

Acknowledgements

First and foremost, I would like to thank my primary supervisor Prof John Plane, for giving me the opportunity in April 2016 to undertake such an interesting and challenging PhD about a part of the atmosphere I knew little about initially. The research environment created within the Plane group has been excellent and encompasses a wide understanding of different backgrounds which has always been useful during my study. John also has great taste in whiskey which for me as an Irishman is very important to have. I would also like to thank my second supervisor Dr Wuhu Feng, for all the help he provided with modelling work and patience while dealing with my initial incompetence; and my third supervisor Prof. Martyn Chipperfield, for his advice and always offering a welcome outlet during his weekly meetings. I would also like to thank NERC for funding the project and supporting me with the opportunity to talk about my research around the world. A further thanks to the NERC DTP administration for their support, including Nigel.

Thanks are extended to all researchers who I have worked with and helped me at Leeds during my PhD: Sandy, Tom, David, Tasha, Kevin, Tom, JD, Wuhu, JC, Chris, James, Nat, the NERC Cohort I was part of and to everyone else I have not named here. A noted thanks to the D&D group (Aidan, Anthony, Jamie, Phil, Anthony) for keeping me sane throughout the PhD.

An extended thanks goes to my bachelor and master's degree supervisor, Prof. John Sodeau, for putting me back on track in 2016 with a great project that ultimately lead to my study in Leeds.

Many thanks to Michael at IAP for his assistance and knowledge during the two visits to the IAP in 2017 along with the rest of the department (Josef,

Franz, Marwa etc) for their immense hospitality. Many thanks to David and Tom also for helping me throughout the flow tube experiments as well as JC for taking me under his wing during the initial period of the PhD.

Finally, a special thanks go out to my family, particularly my Parents for keeping me focused and supported throughout my life, as well as extended family members that have offered guidance to me and close friends at home and abroad.

Contributions

My own contributions and those of other researchers, fully and explicitly indicated in the thesis and associated publications, have been:

In developing experimental methods (Chapter 2):

- Modification and maintenance of the Laser Ablation-Fast flow tube/Time-of-Flight Mass Spectrometer system for use in experiments in Chapter 3 (developed by Dr. Juan Carlos Gómez Martín).
- Modification and maintenance of the Ion Fast flow tube/Quadrupole Mass Spectrometry system for use in experiments in Chapter 3 and 4 (assisted initially by Dr. David Bones and Dr. Thomas Mangan).
- Development of the flow tube calibration cell for use in lidar observations in Chapter 6.
- The metal resonance and Rayleigh-Mie-Raman lidar systems were developed at the Leibniz Institute of Atmospheric Physics, Kühlungsborn, Germany. Dr. Michael Gerding assisted me in the setup for each instrument for the observations (Chapter 5 & 6).
- Development of the Whole Atmospheric Community Climate Model for mesospheric metals was done by Dr. Wuhu Feng. I was later deployed to maintain the updates for WACCM in relation to Ni and to analyse the output from those model runs (see Chapter 5).

In an investigation of the absorption cross sections and kinetics of AlO (Chapter 3, Section 3.1) and associated publication:

"*Gómez Martín, J. C., Daly, S. M., Plane, J. M. C., (2017), Absorption cross sections and kinetics of formation of AlO at 298 K., Chemical Physics Letters., 675, 56-62."*

- I assisted Dr. Juan Carlos Gómez Martín for the majority of all the kinetic experiments in this Chapter and jointly analysed the data output.
- The theoretical calculations were performed by Prof. John Plane while the theoretical simulations using PGOPHER were performed by Dr. James Brooke.

In an investigation of the kinetics of Al^+ (Chapter 3, Section 3.2) and associated publication:

"*Daly, S. M., Bones, D. L., Plane, J. M. C., (2019), A study of the reactions of Al^+ ions with O_3, N_2, O_2, CO_2 and H_2O: influence on Al^+ chemistry in planetary ionospheres., Physical Chemistry Chemical Physics., 21, 14080-14089."*

- I performed the majority of the laboratory experiments for the kinetics of Al^+ and AlO^+ while assisting Dr. David Bones with the measurement of $Al^+ + O_3$.
- The data analysis was done by me while David operated the kinetic model used to measure Al^+ and $AlO^+ + O_3$.

In an investigation of the kinetics of Ni^+ and NiO^+ (Chapter 4) and associated publication:

"*Bones, D. L., Daly, S. M., Mangan, T. P., Plane, J. M. C., (2020), A study of the reactions of Ni^+ and NiO^+ ions relevant to planetary upper atmospheres., Physical Chemistry Chemical Physics., 22, 8940-8951."*

- I performed all laboratory flow tube experiments for Ni^+ and NiO^+
- The data analysis was jointly done by me, Dr. David Bones and Dr. Thomas Mangan with the kinetic model developed by David.

In an investigation of the mesospheric Ni layer using lidar (Chapter 5, Section 5.1) and associated publication:

"*Gerding, M., Daly, S. M., Plane, J. M. C., (2019), Lidar Soundings of the Mesospheric Nickel Layer Using Ni(^{3}F) and Ni(^{3}D) Transitions., Geophysical Research Letters., 46, 408-415."*

- I assisted Dr. Michael Gerding in Kühlungsborn in setting up the lidar system for Ni observations and took part in the initial observations for Ni. Michael performed the observations from January – March 2018 since I had to return to Leeds, but we recommended applying the Ni(^{3}D) transition for observations. The data output was jointly analysed by me and Michael. I further investigated the relative transitions of Ni using the NIST spectroscopic database.

In an investigation of the Ni in the upper atmosphere by model simulations, neutral kinetics of NiO and NiO_2 (Chapter 5, Section 5.2 and Chapter 3, Section 3.3) and the associated publication:

"*Daly, S. M., Feng, W., Gerding, M., Mangan, T. P., Plane, J. M. C., (2020), The Meteoric Ni Layer in the Upper Atmosphere., Journal of Geophysical Research – in press."*

- I performed all the laboratory flow tube kinetics for NiO with CO and O along with NiO_2 and O.
- The model, WACCM-Ni, was initially set up by Dr. Wuhu Feng, with a number of model runs operated by him. I updated the model with Ni chemistry every time a new measurement was made in the laboratory. I also analysed the WACCM output and did the comparisons with Ni and Fe observations for the paper.
- Theoretical calculations for the paper were performed by Prof. John Plane.

In investigation of Al in the upper atmosphere (Chapter 6):

- I performed the majority of lidar observations at Kühlungsborn, Germany, with the assistance of Dr. Michael Gerding while the initial observations in 2016 performed by Michael.
- I analysed the lidar and rocket data respectively, where the upper limit for AlO was determined from the lidar observations and Al^+ was compared with Fe^+ in the rocket data.
- Theoretical calculations for the paper were performed by Prof. John Plane.

Throughout the studies detailed here I was supervised, managed, and directed by Prof John Plane, Dr. Wuhu Feng and Prof Martyn Chipperfield.

Abstract

The major source of metals in the upper atmosphere is the ablation of the roughly 28 tonnes of interplanetary dust that enters each day from space. This gives rise to the layers of metal atoms and ions that occur globally in the upper mesosphere/lower thermosphere (MLT) region between about 70 and 110 km. Metal species in the upper atmosphere offer a unique way of observing this region and of testing the accuracy of climate models in this domain. The overarching objective of this project will be to explore the MLT chemistry of two elements - Ni and Al. Specific objectives of the thesis will include conducting a laboratory study of the reaction kinetics of Ni and Al species, both neutral and ionized, that are relevant to understanding and modelling the contrasting chemistry of these elements in the MLT; extend lidar observations of the recently discovered Ni layer, which appears to be significantly broader than the well-known Na and Fe layers, with a Ni density that is roughly an order of magnitude higher than expected; attempt the first lidar observations of the AlO layer in the upper atmosphere where if successful, would be the first time that a molecular metallic species had been observed in the atmosphere; and develop the first global models of Ni by inserting the chemistry and MIF of Ni into a whole atmosphere chemistry-climate model. Validate the resulting model simulations against lidar and rocket-borne mass spectrometric data of metallic ions.

Table of Contents

List of Tables

List of Figures

List of Abbreviations

ARAS	Atomic Resonance Absorption Spectrometry
AST	ASTeroid belt
BUV	Nimbus-4 Backscatter UltraViolet
CABMOD	Chemical ABlation MODel
CESM	Community Earth System Model
FWHM	Full Width at Half Maximum
FTCC	Flow-Tube Calibration Cell
GLO	Arizona Airglow Instrument
GOMOS	Global Ozone Measurement by Occulation of Stars
HTC	Halley-Type Comet
HTFFR	High Temperature Fast Flow Reactor
IAP	Leibniz Institute of Atmospheric Physics
IDP	Interplanetary Dust Particle
IFFT	Ion-Fast Flow Tube
JFC	Jupiter-Family Comet
LAFFT	Laser Ablation-Fast Flow Tube
LIF	Laser Induced Fluorescence
MASI	Meteoric Ablation Simulator
MAVEN	Mars Atmosphere and Volatile Evolution
MFC	Mass Flow Controller
MIF	Meteoric Input Function
MLT	Mesosphere Lower Thermosphere
MOZART	Model for OZone And Related chemical Tracers
MSP	Meteoric Smoke Particle
Nd-YAG	Neodymium-doped Yttrium Aluminium Garnet
NLC	NoctiLucent Cloud
OCC	Oort Cloud Comets

OSIRIS	Optical Spectrograph and InfraRed Imager System
PLP	Pulse Laser Photolysis
PMC	Polar Mesospheric Cloud
PMT	Photo-Multiplier Tube
PTP	p-Terphenyl
QMS	Quadrupole Mass Spectrometer
RMR	Rayleigh-Mie-Raman
RRKM	Rice-Ramsperger-Kassell-Markus
SCCM	Standard Cubic Centimetres Per Minute
SLM	Standard litres per minute
SCIAMACHY	Scanning Imaging Absorption Spectrometer for Atmospheric CHartographY
TMA	Tri-methyl aluminium
TOF-MS	Time-Of-Flight Mass Spectrometer
WACCM	Whole Atmospheric Community Climate Model
ZoDY	Zodiacal Cloud Model

1 Introduction to cosmic dust in the upper atmosphere of Earth

This chapter gives a general introduction to the mesosphere lower thermosphere (MLT), the meteoric metals that ablate in this region and the subsequent metal layers that form between 70 – 110 km. As well as this, the techniques used to measure these species will be discussed along with the atmospheric models used to simulate the meteoric input and metal layers; the two metals specific to this thesis, Ni and Al; and the aims of the research.

1.1 The Mesosphere and Lower Thermosphere

The Earth's atmosphere consists of several 'layers' segregated by altitude and temperature profile. Each area, spanning from the troposphere to the exosphere consists of a unique set of atmospheric conditions. The region of interest in this project is the mesosphere and lower thermosphere layer. Within this area resides the turbopause at 105 km which represents the boundary between the atmosphere and space. This region receives high-energy inputs from space such as solar electro-magnetic radiation and the solar wind [*Marsh et al.*, 2007] as well as the daily injection of extra-terrestrial cosmic dust. The MLT also exhibits a similar energetic impact from the lower atmosphere in the form of gravity waves, tides and planetary waves [*Fritts and Alexander*, 2003].

The beginning of the mesosphere is expressed by a local temperature maximum at the stratopause at ~50 km, which results from stratospheric ozone absorbing incident radiation above 200 nm, leading to a heating effect

[*Barnett et al.*, 1975; *Hiroshi*, 1989]. Figure 1.1 illustrates a temperature plot during the January (a) and July (b) period of this region from 50 – 110 km. The plot data consists of an average output from the Whole Atmosphere Community Climate Model (WACCM) from 2004 to 2011, a total averaging period of 8 years [*Marsh et al.*, 2013b; *Plane et al.*, 2015]:

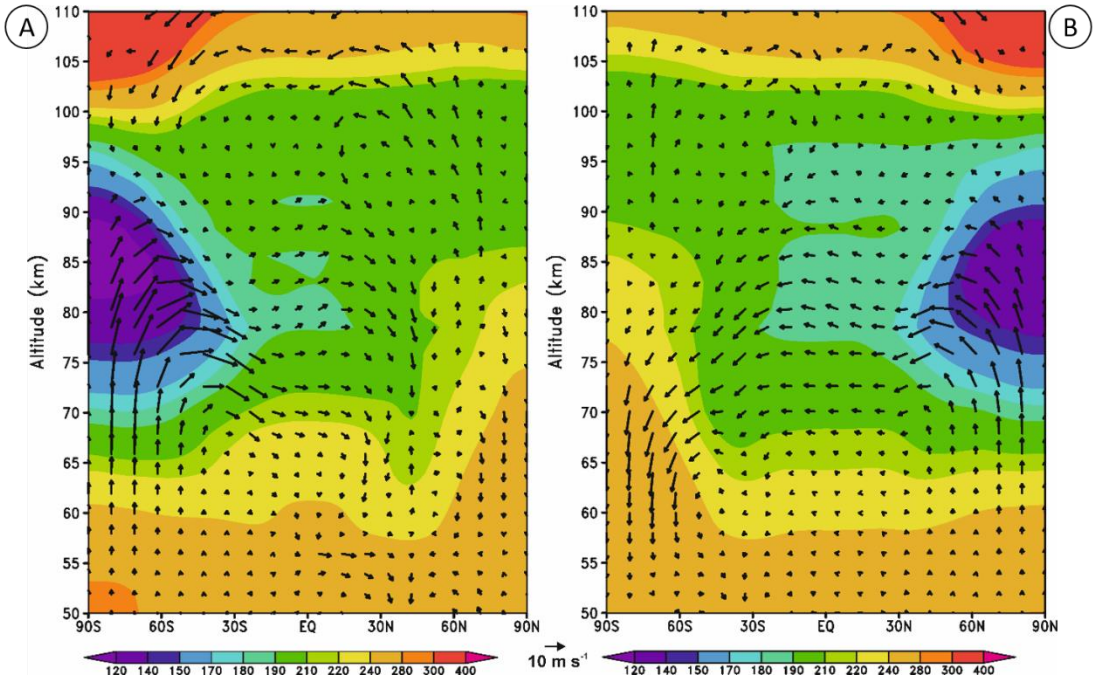

Figure 1.1: Contour plot of the temperature profile (colour) as a function of latitude (bottom-ordinate) and height (left-ordinate) in the MLT for January (a) and July (b) from WACCM. [*Plane et al.*, 2015]

The profile of figure 1.1 illustrates the temperature decrease with altitude from the mesosphere (orange region) to the mesopause (purple-green region). The mesopause height varies seasonally, residing at ~85 km in summer and ~100 km during the winter period. From there, the thermosphere begins and leads to a rapid warming with increasing altitude, because of extreme UV radiation

absorption, mostly by O_2, at wavelengths below 180 nm. These temperatures in the thermosphere can exceed 1000 K during solar storms [*Brasseur and Solomon*, 2005]. It should be noted that because pressure in this region is extremely low ($<10^{-7}$ bar above 110 km), the vibrational and rotational modes of the molecules residing there are generally not in thermodynamic equilibrium [*Brasseur and Solomon*, 2005].

The MLT resides between 70 and 110 km in the atmosphere [*Portnyagin*, 2006]. The turbopause, which can be defined as the boundary between the atmosphere and space, occurs at an altitude of 105 km, therefore residing in the MLT [*Teitelbaum and Blamont*, 1977]. At this boundary point, pressures fall to less than 5×10^{-7} bar and the mean free path of air molecules there approaches 1 m. The result is that bulk turbulent motion and thus eddy diffusion is limited, leaving molecular diffusion as the primary influence on transport of chemical species. Gravitational separation of molecules by mass now occurs, leaving heavier species such as Ar and CO_2 to reside in the lower thermosphere while lighter species such as H, H_2 and He occur in higher concentrations above 500 km [*Brasseur and Solomon*, 2005].

The MLT receives high-energy inputs from space, in the form of solar electromagnetic radiation and energetic particles i.e. protons and electrons from solar activity [*Marsh et al.*, 2007]. The result is the generation of radical and ion species due to photo-dissociation, photoionization, and high-energy collisions of species in the MLT. The most important of these processes is the photodissociation of O_2 through absorption of incident radiation in the Schumann-Runge continuum (130-175 nm) as well as the Schumann-Runge bands (175-195 nm) [*Nee and Lee*, 1997]. A small contribution is also made

through the photolysis of O_3 [*Mlynczak et al.*, 2013]. The O atoms released by photolysis are a major influence in the MLT since they drive much of the chemistry in this region, as shown in Figure 1.2 below, controlling the concentrations of various species such as H, OH and HO_2 and being responsible for the formation of the metal layers.

Atomic oxygen is principally removed through the following reaction sequence, R1.1 to R1.4:

$O + O_2 (+M) \rightarrow O_3$ (where M = third body, N_2 and O_2) (R1.1)

$H + O_3 \rightarrow OH + O_2$ (R1.2)

$H + O_2 (+M) \rightarrow HO_2 + M$ (R1.3)

$O + HO_2 \rightarrow OH + O_2$ (R1.4)

$H + HO_2 \rightarrow H_2 + O_2$ (R1.5)

These reactions control the concentrations of various species in the upper atmosphere. Figure 1.2 below illustrates the modelled mixing ratios of atmospheric constituents in a vertical profile of the MLT. As stated previously, atomic O in Figure 1.2(b) is the dominate species. However, there is a considerable difference in the estimated levels of O below 82 km during daytime and night-time, with over three orders of magnitude difference between the night-time atomic O (blue-dashed line in Figure 1.2(b)) and the daytime estimates (solid-blue line). The recombination of atomic O with O_2 to form O_3 in R1.1 contributes to this reduction in atomic oxygen. Above 82 km, the diurnal variation is less pronounced as the chemical energy from solar UV absorption during the day builds up and is stored, being slowly released throughout the night.

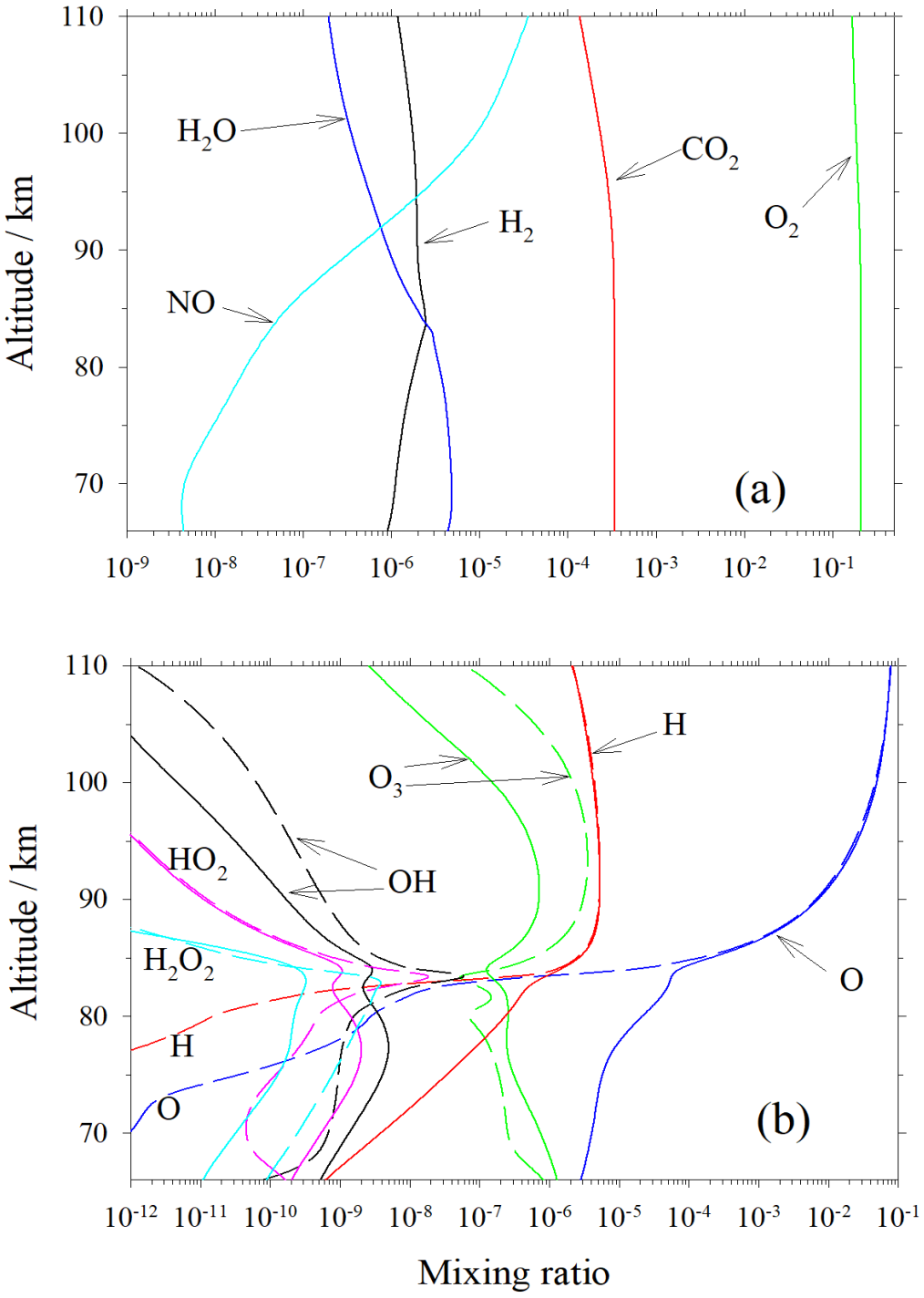

Figure 1.2: Relative abundance output of atmospheric constituents in the MLT as a function of altitude (km) and mixing ratio, calculated using the UEA 1-dimensional mesospheric model [*Plane*, 2003]

Methane that propagates up from the stratosphere undergoes oxidation to H_2O in the lower mesosphere. This is followed by photolysis of the water molecule (by Lyman-alpha radiation at 121.6 nm which penetrate to as low as 80 km) leading to the production of atomic H [*Chandra et al.*, 1997; *Plane*, 2003]. In Figure 1.2(a) this reduction in H_2O can be observed as a result of photolysis and subsequent increase in atomic H [*Solomon et al.*, 1982]. With a similar upper atmospheric profile to O, H has a pronounced diurnal variation below 82 km as shown in figure 1.2(b). Up at higher altitudes (>90 km) there is a decrease in H due to formation of H_2 as a result of reaction with the hydroperoxyl radical (R1.5) [*Solomon et al.*, 1982]. This in turn leads to an increase in H_2 mixing ratio up to ~90 km. O_3 exhibits a night-time maximum above 80 km according to figure 1.2(b) but from altitudes above >95 km, its mixing ratio decreases due to catalytic loss from atomic H (R1.2). Figure 1.2(a) shows that nitric oxide (NO) increases significantly from the mesosphere to the lower thermosphere, by ~3 orders of magnitude. The reason for this sharp increase is mainly due to reaction R1.6 [*Duff et al.*, 2003]:

$$N(^2D) + O_2 \rightarrow NO + O \qquad \text{(R1.6)}$$

$$N_2^+ + O \rightarrow N(^2D) + NO^+ \qquad \text{(R1.7)}$$

The $N(^2D)$ is formed from a variety of exothermic ion-molecule reactions such as interaction between the N_2^+ ion and atomic oxygen (R1.7) [Brown, Brown, 1973]. The presence of ionized species in the upper atmosphere is due to the region receiving high exposure from solar photons which are energetic enough to ionize molecules and atoms. This leads to increased plasma concentrations above 70 km, marking the beginning of the ionosphere [*Plane*, 2003]. This area of atmospheric space has historically been divided into three

regions with distinctly different plasma characteristics. In the D region (70 - 95 km), proton hydrates and negative ions are most prevalent. In the E region (95 – 170 km) O_2^+ and NO^+ ions are the dominant species along with free electrons [*Monro*, 1970]. Finally, in the F region (170 - 500 km), O^+ and N^+ ions are the positive ions with the highest concentration [*Pavlov*, 2012].

1.2 Ablation of cosmic dust

The main sources of cosmic dust that enters the terrestrial atmosphere are the dust trails formed by the sublimation of comets orbiting the sun. These events are the origin of the well-known meteor showers such as the Leonids and Perseids. The second input relates to fragments that travel from the asteroid belt between Mars and Jupiter, as well as dust particles from cometary trails that have long since decayed [*Ceplecha et al.*, 1998]. All planets in the solar system encounter interplanetary dust (IDP) as they move in their respective orbits [*Borin et al.*, 2017]. When these dust particles enter a planetary atmosphere at orbital velocity, they undergo rapid frictional heating due to collision with air molecules of that atmosphere, leading to flash vaporization of the particle. For example, in Earth's atmosphere, the dust particles enter at extremely high velocities (11 – 72 km s^{-1}) and ablate, leading to the formation of the meteoric neutral metal atom layers (Na, Fe, Mg, etc.) residing from 75 – 110 km, and metal ion layers which reside between 85 – 130 km. The average daily input of cosmic dust into the terrestrial atmosphere has been debated for decades. The primary reason for this is that no single technique is available to observe particles over the mass range of 10^{-12} – 1 g (bulk of the incoming material) [*Ceplecha et al.*, 1998; *Vondrak et al.*, 2008].

Up until the 1990's, the mostly accepted figure for daily mass input was in the region of 44 t d^{-1}, an estimate averaged over the entire planet [*Vondrak et al.*, 2008]. This value was evaluated through extrapolating between visual meteoric records with masses > 10 mg as well as satellite impact data, masses <1µg. Using conventional meteor radar measurements to monitor specular reflections from the ion trails caused by ablating meteoroids was ignored as the measurements were regarded as a lower limit to the flux [*Hughes*, 1997]. New methods for estimating the cosmic dust flux were then developed such as the Long Duration Exposure Facility (an orbital impact detector), an orbital facility with a number of exposed panels on which particle impact craters could be measured after its return to Earth. The estimate from this technique was 110 ± 55 t d^{-1} [*Love and Brownlee*, 1993; *McBride et al.*, 1999]. Following the turn of the Millennium, further studies led to an increase in the range of estimates of the cosmic flux input rate. Single-particle analyses of stratospheric sulfate aerosol have shown that up to half of the particles in the lower stratosphere consist of 0.5 - 1% weight of meteoric Fe, from which a flux between 22 – 104 t d^{-1} was deduced [*Cziczo et al.*, 2001]. Measurement of the accumulation of Ir and Pt in polar ice cores in Greenland indicated an input of 214 ± 82 t d^{-1} [*Gabrielli et al.*, 2004]. Depending on the method used to make the estimate, the mass influx of metallic cosmic dust entering the atmosphere ranges from 5 to 270 t d^{-1} [*Plane*, 2012]. Work by *Carrillo-Sánchez et al.* [2016] yielded a value of the order of 43 ± 14 t d^{-1}, a value close to estimates prior to the 1990's. This was evaluated by applying the mass, velocity and radiant distributions of the cosmic dust populations from four known sources: Jupiter family comets (JFCs), asteroid belt (AST), Halley-Type comets (HTCs) and the Oort Cloud comets (OOCs), constrained by lidar

measurements of the vertical fluxes of Na and Fe atoms in the upper mesosphere and accumulation rate of cosmic spherules at the South Pole. *Borin et al.* [2017] evaluated a mass input of 15.3 ± 2.6 t d^{-1} through the use of an astronomical dust model which numerically integrated asteroidal dust particles. The most recent estimate for the mass input was calculated by *Carrillo-Sánchez et al.* [2020], which is an updated study from the work done by *Carrillo-Sánchez et al.* [2016], where the new version of the Chemical ABlation MODel (CABMOD) (see Section 1.4.1) was used to provide the input for Earth (28 ± 16 t d^{-1}), Mars (2 ± 1 t d^{-1}) and Venus (31 ± 18 t d^{-1}).

Initially when the input of meteoric metals into the atmosphere was estimated, the relative metallic abundances in the ablated vapour were assumed to match their meteoric abundances in chondritic meteorites [*Fegley Jr and Cameron*, 1987; *Vondrak et al.*, 2008]. In recent years, a more realistic method has been applied which considers the thermodynamics of a silicate melt, and explicitly describes the evaporation kinetics of the individual elements by applying Langmuir evaporation. This shows that the more volatile elements such as Na evaporate first, followed by the major elements Fe, Mg and Si and leaving the most refractory elements such as Ca and Al to evaporate last. This process is known as differential ablation [*Carrillo-Sánchez et al.*, 2015; *Vondrak et al.*, 2008]. CABMOD has been deployed to investigate this phenomena by including a series of ablative processes, such as sputtering, particle melting and vaporization [*Carrillo-Sánchez et al.*, 2020; *Carrillo-Sánchez et al.*, 2015]. Details of the model are described in Section 1.4.1. Figure 1.3 is an example of the ablation profile output for all major metal constituents entering Earth's atmosphere from three main cosmic dust

sources: JFCs, AST and HTCs, along with the combined total input [*Carrillo-Sánchez et al.*, 2020].

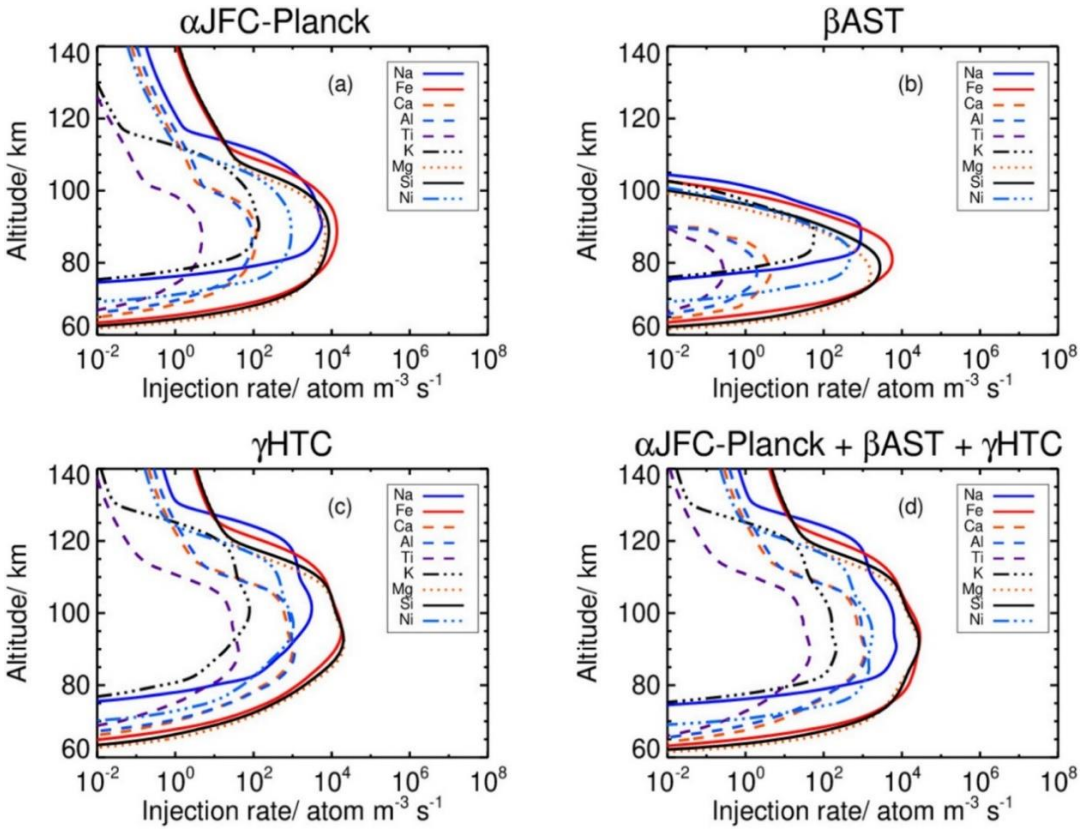

Figure 1.3: Injection profiles for the metal constituents that are injected into Earth's atmosphere where (a) represents the dust source from JFCs; (b) AST; (c) HTC sources; and (d) the global ablation rates for Earth's atmosphere which is a summation of all 3. Source: [*Carrillo-Sánchez et al.*, 2020]

According to Figure 1.3(d), Na (blue line) and K (black dashed line) are the first elements to ablate between 75 - 130 km, since both are relatively volatile. Mg, Fe and Si are more distributed throughout the MLT, starting just below 100 km and finishing at ~75-80 km, due to the elements being more resistant to vaporisation. Ca, Al and Ti are the most refractory elements, and therefore start to ablate below the main elements.

Once the metals have vaporized into the atmosphere, their interactions with air molecules in the atmosphere lead to a variety of ion molecule and neutral reactions. Note that the chemistry of each species is significantly different, with K behaving more similarly to Na, Mg behaving like Fe, and Ca acting somewhere in-between. Silicon on the other hand reacts quite differently to the other meteoric elements, since it is a metalloid (both metal and non-metal) [*Plane et al.*, 2015]. The majority of the individual reactions for Na, K, Mg, Fe and Ca have been studied in the laboratory under pressures that are higher than the pressures of the MLT ($<10^{-5}$ bar), since those conditions are extremely difficult to reproduce. The method entails measuring the reactions over a range of pressures and temperatures so that their rate coefficients can then be extrapolated to the pressures of the MLT [*Broadley et al.*, 2007; *Vondrak et al.*, 2006; *Whalley et al.*, 2011], with termolecular reactions being pressure-independent. Measurements of the rate coefficients for these meteoric metals can then be compiled in a chemistry scheme reflective of the expected reactions in the MLT. From there they can be inserted into global chemistry climate models (see Section 1.4.2), to better understand the chemical behaviour of the metallic species in the MLT [*Feng et al.*, 2013; *Plane and Whalley*, 2012]. Figure 1.4 illustrates the reaction scheme for Fe, one of the meteoric metals that has been studied most extensively.

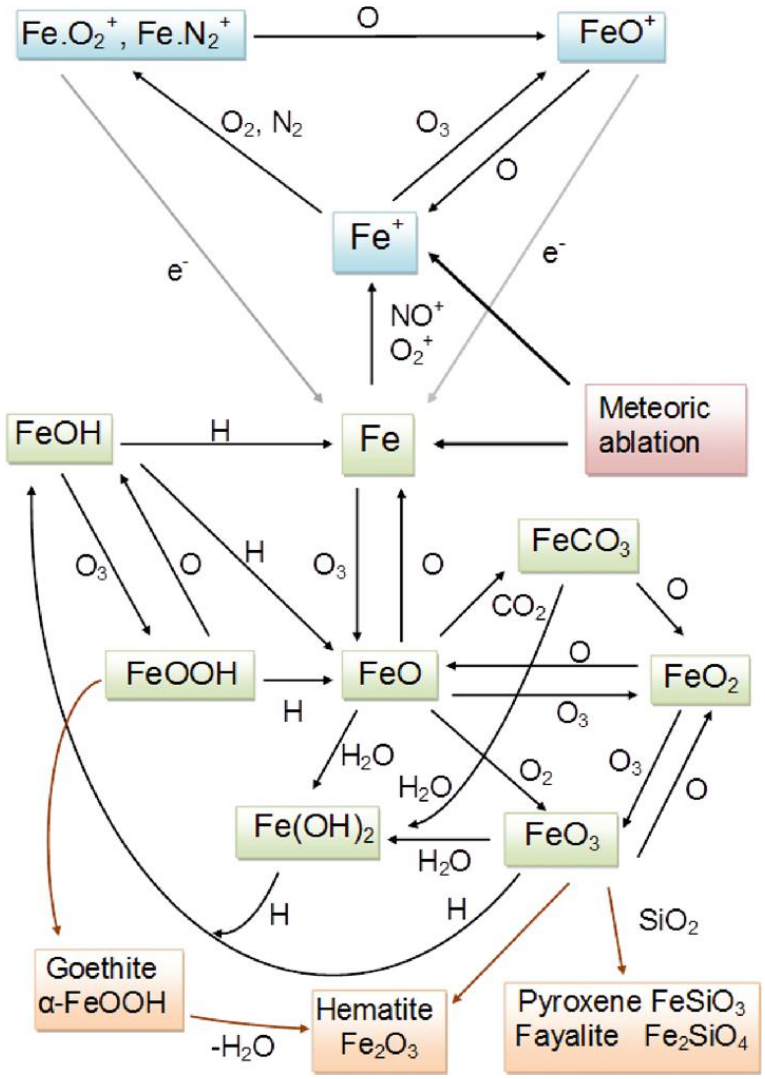

Figure 1.4: Schematic of the chemistry of Fe in the mesosphere and lower thermosphere [*Feng et al.*, 2013]. The blue, green and orange boxes indicate the ion molecule, neutral and polymerization chemistry, respectively.

Ionized metallic species (blue shaded boxes in Figure 1.4) are species that tend to dominate above 100 km i.e. in the lower E region. During meteoric ablation, the metal atoms which evaporate initially travel at high velocities similar to that of the parent meteoroid, resulting in hyperthermal collisions with air molecules which may ionize them. Applying the Fe chemistry of Figure 1.4 for example, the following metal ions can form through photoionization of Fe

or charge transfer with the important ambient E region ions (Fe = Mt) [*Bones et al.*, 2016b; *Brown*, 1973]:

$Mt + h\nu \rightarrow Mt^+ + e^-$ R1.8

$Mt + NO^+ \rightarrow Mt^+ + NO$ R1.9

$Mt + O_2^+ \rightarrow Mt^+ + O_2$ R1.10

According to Figure 1.4, these charged Fe atoms can further react with O_3, to form MtO^+ [*Woodcock et al.*, 2006]. Neutralization of atomic metal ions (Mt^+) such as Fe^+ takes place through the formation of a molecular ion, which is then followed by dissociative recombination with electrons [*Bones et al.*, 2016b]. Neutralization of Mt^+ can also take place through the process of radiative recombination, whereby the metal ion absorbs an incoming electron and releases a photon, thereby stabilizing the resulting neutral atom. Dielectronic recombination, through which a free electron is captured by the metal ion and this simultaneously excites a core electron in the ion, only applies to high temperatures above 10,000 K. The exception is for ground states that have fine-structure splitting such as Si^+ and Fe^+ [*Bryans et al.*, 2009]. This may explain why small concentrations of neutral Fe have been measured up to ~155 km [*Chu et al.*, 2011], an area of very low pressure and high kinetic temperature.

For the neutral chemistry (green-shaded boxes in figure 1.4), all metal atoms that have been measured to this point, react rapidly with O_3:

$Mt + O_3 \rightarrow MtO + O_2$ R1.11

It is also possible for superoxides (MtO_2) to form through recombination between the metal, O_2 and a third body; however, this is restricted to Na, K

and Ca. This reaction is pressure-dependent, however, and therefore only becomes a competing reaction with R1.11 below 85 km. Once the metal oxide is formed, it can react with an array of molecules such as CO_2 to form metal bicarbonates ($MtCO_3$) [*Gómez Martín et al.*, 2016], H_2O to form metal hydroxides ($Mt(OH)_x$) [*Broadley and Plane*, 2010] and O_3 to produce higher oxides (MtO_x, $x > 1$) [*Self and Plane*, 2003].

Silicon chemistry is quite different from the other metals such as Fe, Ca and Na. The main reason for this is the very strong SiO bond, which enables rapid oxidation of ablated Si atoms by O_2 [*Gómez Martín et al.*, 2009]. Silicon is a highly abundant (~20%) element [*Gómez Martín et al.*, 2009] in cosmic dust and is injected through ablation into the atmosphere above 80 km. A number of silicon species have been studied recently (SiO, SiO2, Si^+, etc) and these have been implemented into a new model for silicon chemistry in the MLT [*Plane et al.*, 2016].

The brown-shaded boxes in Figure 1.4 indicate the formation of Meteoric Smoke Particles (MSPs) through polymerization of Fe- and other metal-containing species and SiO_2 [*Aylett et al.*, 2019]. MSPs are regarded as sinks for the metallic species below the atom metal layers. First proposed by *Rosinski and Snow* [1961], subsequent growth of the particle would take place by coagulation [*Saunders and Plane*, 2006]. Experimental studies have illustrated that they quickly polymerize, especially if the molecules contain Fe so that the collisions are controlled by long-range magnetic dipole forces [*Saunders and Plane*, 2006]. These particles are too small to sediment gravitationally, therefore are transported downwards through residual atmospheric circulation [*Dhomse et al.*, 2013]. Because of their small size

range and low concentration, detecting MSPs in the MLT is very challenging and it is even more difficult to measure their composition. Measuring their interactions is vital as they potentially play an important role in the formation of Polar Mesospheric Clouds (PMCs), acting as ice nuclei [*Plane et al.*, 2015]. They may also affect the balance of odd oxygen and hydrogen through heterogeneous chemistry as well as influencing the mesospheric charge balance [*Murray and Plane*, 2003]. Another potentially important impact of MSPs involves transport into the stratosphere where the particles act as condensation nuclei for sulfate aerosol and affect the freezing properties of polar stratospheric clouds, thus affecting stratospheric ozone levels [*James et al.*, 2018].

1.3 Observations of metal species in the Mesosphere Lower Thermosphere

1.3.1 Remote sensing methods

Metal species in the upper atmosphere have been observed for decades. The earliest work can be traced back to *Slipher* [1929] where the Na layer were observed through radiation at 589 nm in the night sky spectrum. Quantitative metal atom measurements in the MLT were first made in the 1950's using ground-based photometers. Using this technique, resonance fluorescence measurements are made from spectroscopic transitions of the metal atoms, through excitation by solar radiation. By applying this technique, emission lines from Na, Fe, K and Ca^+ in the MLT were categorized due to these metals having very large resonant scattering cross-sections [*Baggaley*, 1980; *Hunten*, 1967]. From there use of tuneable laser sources allowed for the

development of a resonance technique known as ‘light imaging, detection and ranging’ (lidar). The Na layer was the first to be measured using this new lidar detected by *Bowman et al.* [1969] due to its large effective backscatter cross section as well as large column abundance. From there on photometry-based operations were disbanded in the 1970’s due to the rapid introduction of tuneable laser sources [*Gardner et al.*, 2005; *Plane et al.*, 2015]. The method entails tuning the wavelength of a pulsed laser beam to correspond to an intense spectroscopic transition of the species being analysed. This beam is then transmitted upward to the mesosphere to the metal analyte of interest, followed by resonant scattering of the pulse by the metal atoms. Most of the scattering is lost; however, a small fraction resonantly scattered light returns to the surface. From here it can be collected by a telescope and quantified by time-resolved photon counting. The recorded altitude of the incoming signal is determined by the time it spent in the atmosphere before returning. The absolute metal density is then calculated through calibration with a Raleigh-scattered signal at a lower altitude of known density [*Abo*, 2005].

1.3.2 Satellite observations and remote-sensing

The dawning of the space age led to numerous satellite launch and rocket sounding campaigns. Some of the earliest satellite launches for atmospheric observations include Ariel I, launched in April 1962, which was designed to measure various properties of the ionosphere including electron density, ion concentrations, as well the intensity of the solar spectrum near the Lyman-α line at 1216 Å [*Willmore*, 1965]; Explorer 12 launched in August 1961 and designed to measure cosmic-ray particles, solar wind protons and

magnetospheric magnetic fields [*Bryant et al.*, 1962; *Sonnerup and Cahill Jr.*, 1968]; OGO-6 which launched in June 1969 and detected Mg^+ and Fe^+ ion species [*Kumar and Hanson*, 1980]; and the Nimbus-4 Backscatter Ultraviolet (BUV) satellite that was placed into orbit in April 1970 for the purpose of global atmospheric ozone measurements [*Heath et al.*, 1973].

The introduction of an analytical device in spatial orbit has helped to provide an extra dimension for analysis of the MLT by downward detection, compared to the usual lidar measurements upwards from the Earth's surface. Over the last two decades, substantial progress in monitoring the MLT using satellites have been made. In particular, the determination of the vertical profiles of metal atoms and ions in the upper atmosphere through the deployment of space-borne limb-scanning spectrometers. Two satellites in particular have been used for terrestrial upper atmosphere observations of meteoric metals, Odin and Envisat. The Odin satellite was equipped with the Optical Spectrograph and Infrared Imager System (OSIRIS) spectrometer designed for the detection of Na [*Fan et al.*, 2007] and K [*Dawkins et al.*, 2014]. Envisat includes both the Scanning Imaging Absorption Spectrometer for Atmospheric Cartography (SCIAMACHY) for measuring Mg and Mg^+ [*Langowski et al.*, 2014; *Langowski et al.*, 2015] and the Global Ozone Measurement by Occultation of Stars (GOMOS) spectrometer for Na [*Fussen et al.*, 2010]. Both the OSIRIS and SCIAMACHY instruments measure dayglow radiance profiles that are produced by solar-excited resonance fluorescence.

More recently, the Mars Atmosphere and Volatile Evolution (MAVEN) mission was developed to analyse the upper atmosphere of Mars [*Crismani et al.*, 2017]. The spacecraft launched in November 2013, arrived at the Martian

atmosphere in September 2014 and initiated its one-year mission in November 2014. The objectives of the study were as follows: Investigate the interactions between the Sun and solar wind with the magnetosphere and upper atmosphere of Mars; to analyse the upper atmosphere and ionosphere composition as well as the dictating processes involved; to evaluate the escape rates from the Martian upper atmosphere to space; and to use these escape rates to extrapolate the total atmospheric gaseous loss to space from past to present [*Jakosky et al.*, 2015]. The most notable discovery during the campaign in relation to IDPs was the detection of a Mg^+ ion layer near an altitude of 90 km. The Mg^+ emission at 280 nm (Figure 1.5) is a result of resonant scattering of solar UV photon excitation rather than direct excitation as a result of ablation. The surprising lack of a detectable Mg layer was later investigated (see Section 1.4.2).

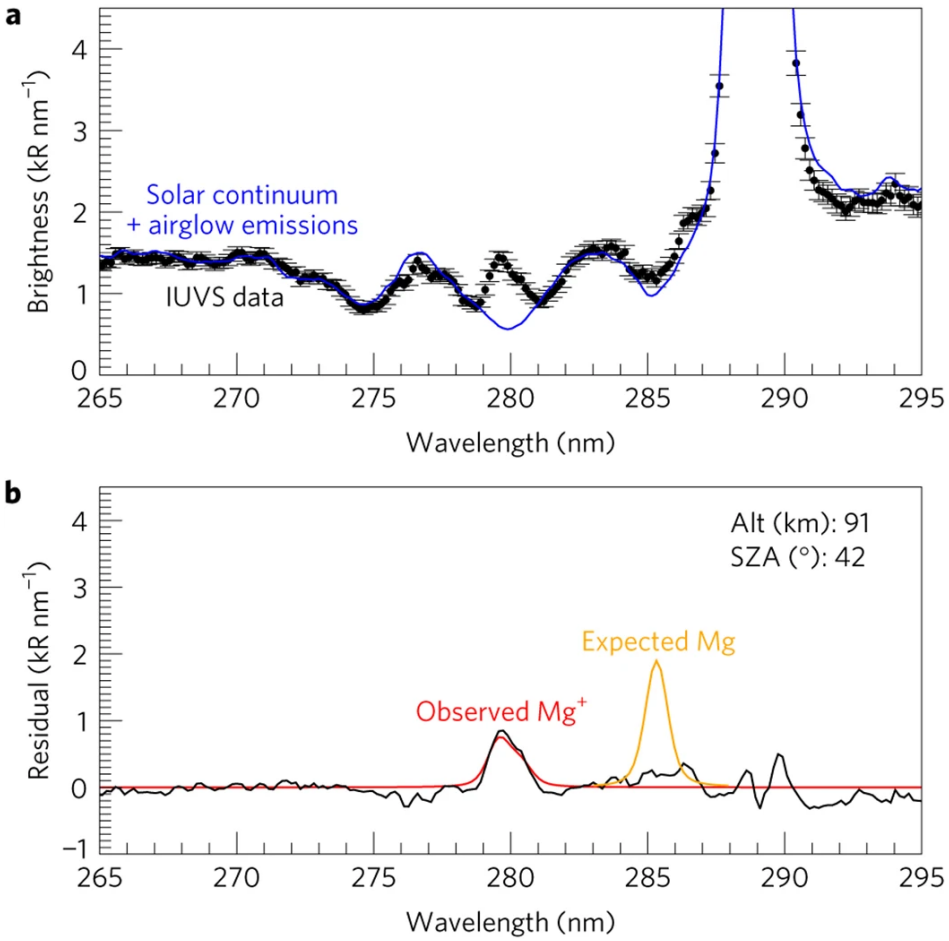

Figure 1.5: Scan taken from MAVEN (10-15 hr local time) in the northern hemisphere (50^{o}-70^{o}N) of Mars on April 22nd, where (a) represents the averaged spectrum and 1σ uncertainties of the Poisson noise of the data with (b) showing the residual from (a) as the black line along with the Mg^{+} peak (red line) and expected Mg peak at 285 nm (orange line). Source: [*Crismani et al.*, 2017]

1.3.3 Rocket-borne sounding with mass spectrometry

During the same period as the early observational satellite launches, rocket-borne soundings began operation [*Krankowsky et al.*, 1972] and would continue throughout the 1970's and 1980's [*Kopp*, 1997]. The objectives of these soundings were to measure the positive and negative ion composition

in the upper atmosphere, specifically the lower *E*-region. The main difficulty with the initial measurements was designing a mass spectrometer that could: meet the requirements for a small payload in a rocket; include a high speed pump with a large capacity; fast mass sweep; ability to detect positive and negative ions; better sensitivity than 10 ion cm^{-3}; and a mass range that would extend up to 150 a.m.u [*Krankowsky et al.*, 1972]. The recorded species varied from meteoric metals (e.g. Na^+, Mg^+, Al^+, Ca^+, Fe^+, Co^+, Ni^+) to metal containing compounds (e.g. $Fe^+.(H_2O)$, $CaOH^+$, MgO^+). The rocket soundings also recorded several non-metallic species such as O_2^+, NO^+, O^+ and N^+ [*Grebowsky and Aikin*, 2002; *Kopp et al.*, 1985a]. These flights have been very useful in ion metal comparison studies done at the University of Leeds in recent years for Si [*Plane et al.*, 2016], Ca [*Plane et al.*, 2018b] and Fe [*Feng et al.*, 2013]. Further details of rocket flights used in this study are described in Chapter 5.

1.4 Atmospheric modelling of meteoric metals

For modelling the metallic layers in the MLT, three components are required for an atmospheric model. First, the meteoric input function (MIF) describes the injection rate into the atmosphere of each element (e.g. Na or Fe) as a function of time and latitude [*Carrillo-Sánchez et al.*, 2020]. From there, a meteoric metal chemistry module needs to be incorporated into the general atmospheric chemistry scheme in the model [*Feng et al.*, 2013; *Marsh et al.*, 2013a]. The final component entails insertion of a gas-phase species removal function through the formation of MSPs. Model outputs can then be compared

to observations and the chemical scheme iterated, if necessary [*Plane et al.*, 2015].

1.4.1 Meteoric input function and the chemical ablation model

The main purpose of the Chemical Ablation MODel (CABMOD), developed at the University of Leeds, is to predict the thermal heating of a meteoric particles from collisions with air molecules in the terrestrial atmosphere [*Vondrak et al.*, 2008]. With the assumption of Langmuir evaporation, the model applies the vapour pressure calculated by the MAGMA thermodynamic code [*Fegley Jr and Cameron*, 1987; *Schaefer and Fegley*, 2004] to yield an evaporation rate of each element as a function of altitude, taking account of changes in the particle mass and composition changes as ablation occurs. At the melting range of the particle (since they contain multiple heterogeneous components), the micrometeoroid begins the process of ablation as the metals and metals oxide quickly evaporate. The early versions of CABMOD (CABMOD-1 and 2) assumed that all micrometeoroids were of a homogeneous oxide composition. The rate of evaporation was determined with the use of the Hertz-Knudsen equation:

$$\frac{dm_i}{dt} = f(T)\,\gamma_i p_i S \sqrt{\frac{M_i}{2\pi k_B T}} \qquad \text{E1.1}$$

where T is the temperature, S the particle surface area, p_i the gas-liquid equilibrium vapour pressure, γ_i denotes the evaporation coefficient, k_B the Boltzmann constant and $f(T)$ represents the phase transition factor which accounts for any non-instantaneous melting. γ_i is assumed to be 1, to maintain

simplicity since there is a lack of experimental data. The phase transition factor, $f(T)$, is presented as a sigmoidal function:

$$f(T) = \frac{1}{1 + \exp\left(\frac{-(T - T_{mp})}{\tau}\right)} \qquad \text{E1.2}$$

with T_{mp} representing the mean melting point of the assumed homogeneous phase, with τ as the width of sigmoid profile. This function allows for melting to occur over a temperature range, with the most immediate melting occurring at T_{mp}. τ was determined to be 51 K for Allende and carbonaceous chondrites similar to that type, and 108 K for ordinary chondrites (Chergach) [*Gómez Martín et al.*, 2017].

The latest version of CABMOD (CABMOD-3) assumes that the cosmic dust particles have two components, silicate bulk and metal grains, which is supported by the density differences between the phases: the silicate bulk density at 2200 kg m^{-3} and a density of 4710 kg m^{-3} for the sulfide grains [*Bones et al.*, 2019]. Previous studies relating to Na, Fe and Ca ablation also supported this update, since it was concluded that a pure metal phase separate to the bulk silicate phase would explain the observed early release of Fe during the heating process, particularly in Chergach where a high metallic Fe abundance lead to doubly peaked profiles [*Bones et al.*, 2019; *Gómez Martín et al.*, 2017]. Since this update also addresses Ni in these phases, further details will be discussed in Section 1.5.1.

CABMOD is combined with the astronomical Zodiacal Cloud Model (ZoDY) to produce the MIF. The ZoDy is a dynamical model which describes both the temporal and orbital evolution of dust particles in the sub-mm range from the respective sources: Jupiter Family Comets, Asteroids, Halley Type Comets,

and Oort Type Comets. It also specifies the sinks for these particles, such as collisional fragmentation, exiting the solar system due to solar photon pressure, or atmospheric entry [*Nesvorný et al.*, 2011; *Nesvorný et al.*, 2010]. ZoDy provides to CABMOD the meteoric mass (10^{-8}-10^{3} µg) [*Ceplecha et al.*, 1998], entry velocity (11-72 km s^{-1}) and radiant distributions (0 – 90˚) for Earth [*Carrillo-Sánchez et al.*, 2015; *Nesvorný et al.*, 2011]. CABMOD then predicts the ablation rate for the meteoric metals of interest. Figure 1.3 above is an example of the ablation profile output for Na, K, Mg, Fe, Ni, Si, Ca, Al and Ti.

1.4.2 The Whole Atmosphere Community Climate Model

After determination of the MIF for the metal of interest, it is then combined with a list of potential reactions the metal is expected to have in the MLT and further added to an atmospheric model. Over the last decade, the research group at the University of Leeds has used WACCM, with altitudes ranging from the Earth's surface to the thermosphere at ~140 km [*Feng et al.*, 2013; *Plane et al.*, 2018b] and uses the framework developed from the fully coupled Community Earth System Model (CESM) [*Hurrell et al.*, 2013]. The standard horizontal resolution of the model is 1.9º x 2.5º (latitude x longitude) and 88 vertical model layers (with a height resolution of ~3.5 km in the MLT). WACCM provides a detailed description of atmospheric processes in the mesosphere and lower thermosphere. These include auroral processes, non-local thermodynamic equilibrium, ion drag, radiative transfer, molecular diffusion of major and minor species as well as an interactive chemistry module [*Marsh et al.*, 2007]. Iterations 1 to 4 of WACCM employed the standard model chemistry Model for OZone And Related chemical Tracers-version 3 (MOZART-3)

package [*Kinnison et al.*, 2007], which has 59 chemical species and 217 gas-phase reactions including the *E* region ion chemistry for O^+, O_2^+, N^+, N_2^+, NO^+ and electrons [*Marsh et al.*, 2013a]. For altitudes below 60 km, WACCM has a specified dynamics option where the temperature and wind field at each time step is nudged with meteorological reanalysis data. Above 60 km, the model is free-running. Several improvements have been made in recent years since the WACCM4 version described by [*Marsh et al.*, 2013b]. WACCM5 [*Gettelman et al.*, 2019; *Mills et al.*, 2017] applies WACCM4 chemistry WACCM5 also operates at a higher vertical and horizontal resolution. The latest version of WACCM used for metal chemistry is WACCM6 which is part of the second iteration of the coupled Earth System Model, CESM2 [*Gettelman et al.*, 2019]. A lower resolution of WACCM6 is still available which can run metal layer simulations that are consistent with previous iterations of WACCM [*Plane et al.*, 2015]. WACCM-X is a separate development of WACCM which incorporates the same features but extends up to ~500 km in altitude, covering the majority of thermosphere [*Liu et al.*, 2010].

In terms of meteoric metals, the neutral and ion chemical reactions of Na [*Marsh et al.*, 2013a], K [*Plane et al.*, 2014], Mg [*Langowski et al.*, 2015], Fe [*Feng et al.*, 2013] and Ca [*Plane et al.*, 2018b] have been added to WACCM. The Fe chemistry scheme illustrated in Figure 1.4 above is an example of how extensive the reaction catalogue added to WACCM is. WACCM-Ca is the most recent work relating to modelling work chemistry. For this model the MIF profiles (see Section 1.4.1) for Ca and Na used in the study were initially reduced by a factor of 5 [*Plane et al.*, 2018b]. This factor compensates for the fact that global models such as WACCM underestimate the vertical transport of minor species in the MLT, because short wavelength gravity waves are not

resolved on the model horizontal grid scale (~150 km). These sub-grid waves contribute to chemical and dynamical transport while dissipating, and this can exceed transport driven along mixing ratio gradients by the turbulent eddy diffusion produced once the waves break [*Gardner et al.*, 2017]. Since these additional vertical transport mechanisms are underestimated, the MIF needs to be reduced in order to simulate the observed metal density [*Plane et al.*, 2018b]. Figure 1.6 shows a monthly comparison example between the observations and model simulations of Ca and Na using WACCM-Ca, with both metals showing satisfactory agreement each month.

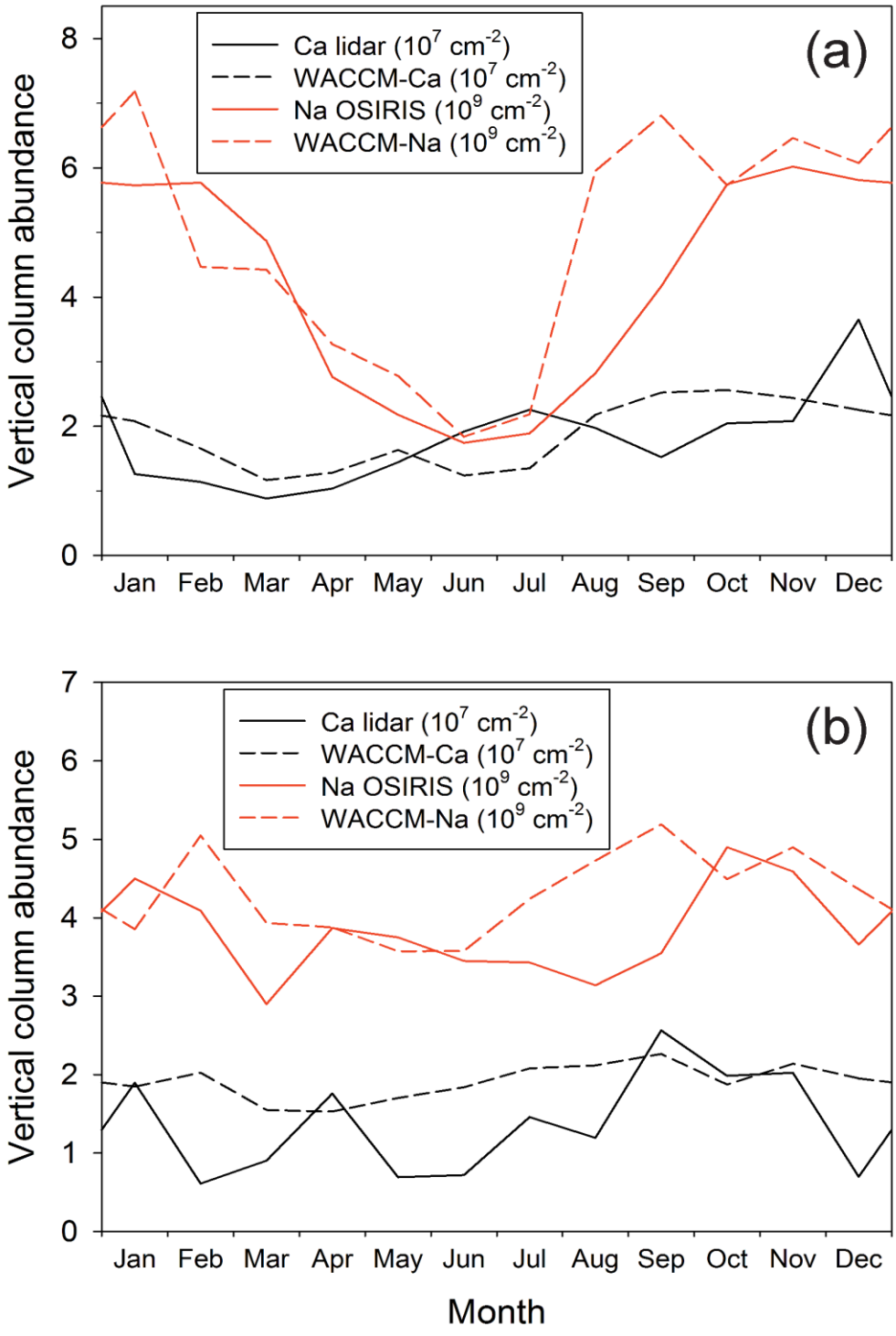

Figure 1.6: Comparison between the observed and modelled profiles of Ca and Na vertical column abundances where (a) located at Kühlungsborn (54°N) and (b) located at Arecibo (18°N). The data points are monthly averages from January to December. The Na observations are taken from the OSIRIS spectrometer on the ODIN satellite [*Fan et al.*, 2007], with the Ca lidar data

taken from Kühlungsborn between 1996 – 2000 [*Gerding et al.*, 2000] and Arecibo Observatory from 2002 – 2003. Source: [*Plane et al.*, 2018b]

The formation of MSPs through the polymerization of metal reservoir species is currently represented in WACCM by a “dimerization” reaction representing permanent removal. The dimerization rate constants are estimated using dipole-dipole capture theory [*Feng et al.*, 2013; *Plane*, 2004]. For minor metal species such as K, the dimerization process of the $KHCO_3$ species increases by a factor of 270, due to the ability of $KHCO_3$ to polymerize with any of the major metallic species such as $NaHCO_3$ and FeOH [*Plane et al.*, 2014].

Most observations of meteoric metals are done on Earth but the recent deployment of MAVEN to Mars [*McClintock et al.*, 2015] enabled the detection of a Mg^+ ion layer at ~90 km (though no Mg layer was observed) [*Crismani et al.*, 2017]. A 1-D model was constructed to investigate this, which used CABMOD and ZoDy to estimate the Mg MIF for Mars [*Plane et al.*, 2018a]. This study suggested that the absence of a detectable Mg layer is attributed to ~50% of the ablated Mg atoms ionizing with CO_2 molecules in the Martian atmosphere due to hyperthermal collisions, as well as MgO^+ ions forming cluster ions with CO_2 which dissociatively recombine with electrons to form $MgCO_3$ rather than Mg Future versions of WACCM – e.g. for Mars - could be developed to describe other planetary atmospheres once the appropriate chemistry scheme and atmospheric conditions are achieved.

1.5 Ni and Al

Both species represent part of the total cosmic dust input into Earth's atmosphere and are the specific focus of this thesis. Therefore, it is important to identify what is currently known about the two meteoric metals.

1.5.1 Ni

Techniques for isolating Ni in Fe meteorites have been developed since the 1940's e.g. breaking off and powdering a fragment of the impacted sample, dissolving it in dilute HNO_3 and adding NH_4OH. This results in the precipitation of the Fe component in the meteorite in the form of ferric hydroxide. Decantation of the clear liquid mixture from the precipitate followed by addition of ethanol and dimethylglyoxime leads to the isolation of a scarlet-red precipitate. This was indicative of Ni and the probability that the specimen was a meteorite [*Ashbrook.*, 1945]. In terms of atmospheric measurements of Ni in the upper atmosphere, Ni^+ ions ($^{58}Ni^+$ & $^{60}Ni^+$) were first observed with the use of a quadrupole mass spectrometer flown from a sounding rocket at the Andoya Rocket Range, Norway, on 26th November 1969 [*Krankowsky et al.*, 1972]. Following this, several measurements were carried out during the 1970's and 1980's [*Grebowsky and Aikin*, 2002; *Kopp*, 1997]. From there, chemiluminescence from the electronically excited NiO molecule, formed from the reaction between Ni and O_3, was detected by *Evans et al.* [2011] as a broad continuum in the visible section of the nightglow spectrum, ranging from 440 – 670 nm. This detection was done using the OSIRIS spectrograph on the Odin satellite [*Llewellyn et al.*, 2004] and the Arizona Airglow Instrument (GLO-1) spectrograph on the Space Shuttle [*Broadfoot and Bellaire Jr.*, 1999].

The first observations of the Ni layer were made at the Poker Flat Research Range at Chatanika. Alaska (65^{o}N, 147^{o}W) by *Collins et al.* [2015], on two nights during midwinter (27 - 28th Nov & 20 - 21st Dec 2012) by probing the Ni($^{3}F_4$ – ^{3}D) transition at λ_{air} = 336.96 nm. The Ni resonance lidar consisted of an excimer-pumped dye laser and a 1.04 m diameter telescope that was previously used for Na and Fe mesospheric layer measurements [*Gelinas et al.*, 2005]. The concentration of Ni atoms was determined by applying resonance absorption at one wavelength (λ_1 = 337.054 nm) following by measuring emissions at two wavelengths (λ_1 = 337.054 nm and λ_2 = 339.396 nm). E.13 was applied to determine the ratio of the Ni resonance signal at altitude z (N_{Ni} (z)) to the Rayleigh scattering signal at altitude z_R (N_RZ_R):

$$\frac{N_{Ni}(z)}{N_R(z_R)} = \frac{\sigma_{abs}(\lambda_1)\,\rho_{Ni}(z)}{\sigma^{\pi}{}_R(\lambda_1)\rho(z_R)} \frac{[\gamma_1\eta_1T_1+\gamma_2\eta_2T_2]}{[\eta_1 T_1]} \frac{1}{4\pi} \frac{{z_R}^2}{z^2} \qquad \text{(E1.3)}$$

where σ_{abs} is the resonance cross section at wavelength (λ_1), ρ_{Ni} the concentration of Ni, $\sigma^{\pi}{}_R$ the Rayleigh backscatter cross section at λ_1, ρ is the concentration of air at altitude (z_R), $\gamma_{1,2}$ as the branching ratios of each wavelength transition, $\eta_{1,2}$ the receiver efficiencies and T_1 and T_2 are the one-way atmospheric transmission coefficient at wavelengths λ_1 and λ_2. Equation 1.4 can be rearranged to calculate the concentration of Ni:

$$\rho_{Ni}(z) = \frac{N_{Ni}(z)}{N_R(z_R)} \frac{\sigma^{\pi}{}_R(\lambda_1)\rho(z_R)}{\sigma_{abs}(\lambda_1)} \frac{1}{[\gamma_1+\gamma_2[\frac{\eta_2T_2}{\eta_1T_1}]]} 4\pi \frac{z^2}{{z_R}^2} \qquad \text{(E1.4)}$$

One challenge with measuring the Ni concentrations was that the element has several isotopes: ^{58}Ni (68%), ^{60}Ni (26%), ^{62}Ni (4%), ^{61}Ni (1%) and ^{64}Ni (1%). However, since the isotope shift in the spectral lines was smaller than the linewidth of the laser [*Schroeder and Mack*, 1961], it was possible to designate Ni as a single isotope for retrieving the Ni concentrations.

The peak density was 1.6 × 10^4 cm^{-3} at 87 km, with a column abundance of 2.7 × 10^{10} cm^{-2}. Figure 1.7 illustrates the Ni layer profile measured by *Collins et al.* [2015], compared against Fe layer lidar soundings during the same period.

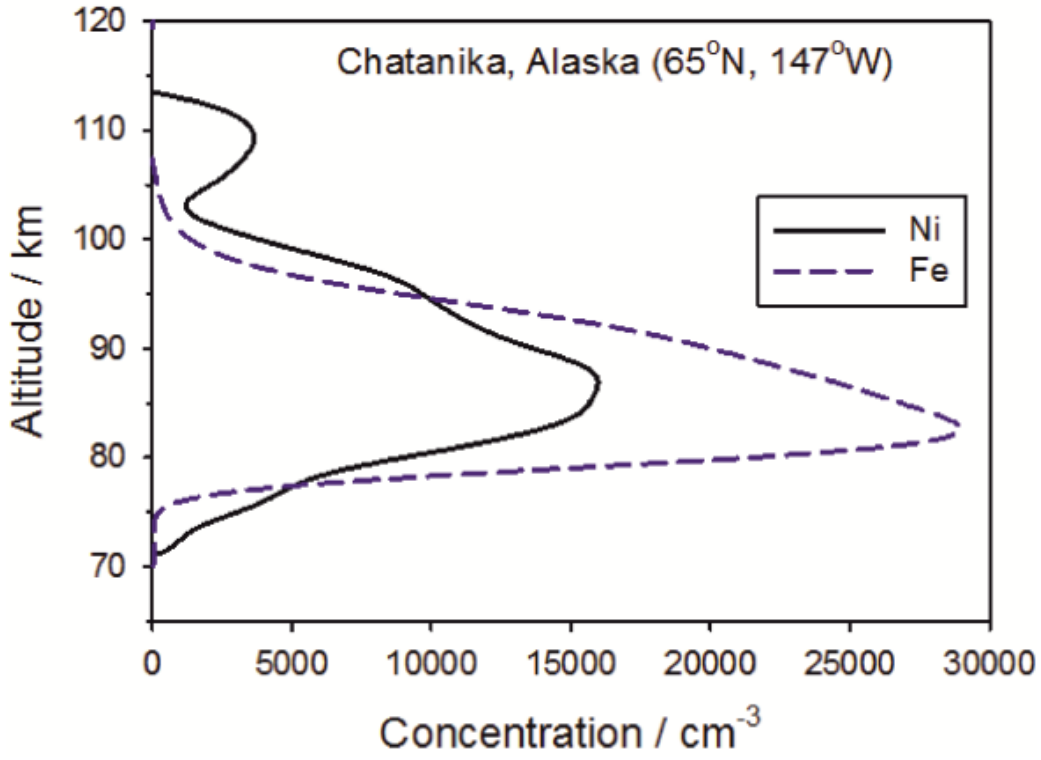

Figure 1.7: A comparison between the vertical profiles of the Ni and Fe atom layers. Adapted from *Collins et al.* [2015] with Fe lidar measurements from the same location.

When compared to Fe, another transition metal that should be injected into Earth's atmosphere through meteoric ablation over a similar altitude range [*Carrillo-Sánchez et al.*, 2020], the Fe:Ni column abundance interpreted from Figure 1.7 is only 1.2 which is much smaller than the carbonaceous Ivuna (CI) chondritic ratio of 18 [*Asplund et al.*, 2009]. The CI ratio is chosen here as it is regarded as the closest in composition to IDPs [*Jessberger et al.*, 2001].

Recently, the ablation of Ni from meteoric fragments using the Meteoric Ablation Simulator (MASI) at the University of Leeds, which has been previously used to study Fe, Na and Ca meteoric fragments [*Bones et al.*, 2016a]. In the recent work, the evaporation of Ni and Na were measured through laser induced fluorescence (LIF) as meteoric fragments in several different size ranges were heated at a rate that would simulate atmospheric entry [*Bones et al.*, 2019]. The experimental results from this study were then applied to the new version of CABMOD (CABMOD-3) (see Section 1.4.1). In this new iteration, the Ni is treated ase part of the Ni-Fe-S metallic grain composition, but absent from the bulk Fe-Mg-SiO_4 phase [*Carrillo-Sánchez et al.*, 2020]. The experimental data from MASI and the CABMOD-3 simulations showed that the ablation of Ni occurs rapidly at a relatively low temperature (~2200 K), with the same observed for metallic or sulfide Fe, before the bulk silicate of Fe eventually ablates.

The MIF ratio of Fe:Ni predicted by the CABMOD-ZoDy coupled model was 16:1, which is in close agreement with the CI ratio of 18. However, this is still ~13 times larger than the ratio determined from the lidar soundings of *Collins et al.* [2015]. This would indicate a large Ni enrichment in cosmic dust particles entering Earth's atmosphere, although this would also contradict recent meteoric fragment analysis done in the laboratory at Leeds [*Bones et al.*, 2019] as well as the Fe:Ni ratio from cosmic dust particles which survived atmospheric entry, measured by *Arndt et al.* [1996]. Further examination of Figure 1.7 shows that that the Ni layer exhibits a much broader layer profile than Fe, both top-side and bottom-side, ranging from 70 – 115 km. This may suggest that the neutral and ion-molecule chemistry of Ni is different to that of Fe, despite the elements being first row transition metals.

In terms of kinetic measurements, Ni + O_2 has been measured previously with Ar as the carrier gas and acting third body [*Brown et al.*, 1991], yielding a rate coefficient of k(Ni + O_2, T = 296 K) = (1.7 ± 0.3) × 10^{-30} cm^6 $molecule^{-2}$ s^{-1}. The reaction of Ni^+ + O_3 has been studied previously by *McDonald et al.* [2018] with the use of a selected-ion flow tube, with a rate coefficient of k(Ni^+ + O_3, T = 300 - 500 K) = (11 ± 2) × 10^{-10} cm^3 $molecule^{-1}$ s^{-1}. The subsequent higher oxide reactions, NiO^+ + O_3 and NiO_2^+ + O_3, were measured to be (9.5 ± 3.0) × 10^{-10} cm^3 $molecule^{-1}$ s^{-1} and (10 ± 7) × 10^{-10} cm^3 $molecule^{-1}$ s^{-1}, respectively.

1.5.2 Al

Al^+ ions have been in the MLT by mass spectrometry from sounding rockets, similar to Ni^+ (see section 1.3.3) [*Kopp*, 1997; *Krankowsky et al.*, 1972] and have also been detected in the Martian atmosphere using the Neutral Gas Ion Mass Spectrometer which was part of the MAVEN satellite [*Benna et al.*, 2015]. Solar-induced fluorescence of the $B_2\Sigma^+ \leftarrow X_2\Sigma^+$ transition for AlO has been observed during atmospheric turbulence experiments during twilight hours involving the release of tri-methyl-aluminium (TMA) [*Golomb et al.*, 1967; *Johnson*, 1965], with observed lifetimes ranging from seconds to 30 minutes [*Golomb et al.*, 1967; *Roberts and Larsen*, 2014]. FeO and NiO have also been measured in the airglow spectrum [*Evans et al.*, 2011] but no meteoric metal molecular species has been actively detected (i.e. by resonance lidar) since the transition probabilities between molecular states are orders of magnitude less than fully allowed atomic transitions.

Three measurements of this rate constant have been previously made, with two of the rate coefficients measured by Pulsed Laser Photolysis – Laser

Induced Fluorescence (PLP-LIF) agreeing with each other [*Garland and Nelson*, 1992; *Le Picard et al.*, 1997] at $k(Al + O_2)$ = ~1.7 × 10^{-10} cm^3 $molecule^{-1}$ s^{-1}, but disagreeing with the first published value of $k(Al + O_2)$ [*Fontijn et al.*, 1977]. The work done by *Fontijn et al.* [1977] entailed using absorption and resonance fluorescence detection of Al in a High Temperature Fast Flow Reactor (HTFFR), reporting their value for $k(Al + O_2)$ = 3.2 × 10^{-10} cm^3 $molecule^{-1}$ s^{-1}. The reason why the reaction proceeds so rapidly is due to the formation of a strong Al-O bond, similar to what is seen for two other meteoric species Ti [*Ritter and Weisshaar*, 1990] and Si [*Gómez Martín et al.*, 2009].

Other neutral reactions of Al that have been studied include Al + CO_2 [*Fontijn and Felder*, 1977; *Garland*, 1992]; AlO + O_2 [*Belyung and Fontijn*, 1995]; and AlO + CO_2, along with the back reactions of AlO with CO [*Parnis et al.*, 1989] and O [*Cohen and Westberg*, 1983]. The atom abstraction reaction of k(AlO + H_2, 296 K) was measured to have an upper limit of 5.0 × 10^{-14} cm^3 $molecule^{-1}$ s^{-1} by *Parnis et al.* [1989] in a static pressure gas cell with LIF detection.

The ionization energy of AlO has also been determined previously by *Weber et al.* [1986] to be ≤ 9.75 eV, using a guided-ion beam setup. This value is further supported with a recently calculated value of 9.70 eV using *ab initio* theory [*Sghaier et al.*, 2016]. Considering the ionization energies of NO and O_2 to be to be 9.26 and 12.07 eV [*Lide*, 2006], respectively, it seems likely that AlO will only charge transfer with O_2^+ and not NO^+ to form AlO^+.

1.6 Thesis Overview

The primary objectives of this thesis study are as follows:

A two-month campaign at the Leibniz-Institute of Atmospheric Physics, Kühlungsborn, Germany (54^{o}N, 12^{o}E) to operate a metal resonance lidar in an attempt to observe the AlO layer. The cross section for AlO at the bandhead of the B(0)-X(0) transition will be measured initially in the laboratory at the University of Leeds. The flow tube for this measurement will be downscaled for transport to Kühlungsborn to act as a calibration cell for the lidar so that the observations are done at the bandhead peak.

The Ni layer column abundance observed by *Collins et al.* [2015] was surprisingly high, giving an Fe:Ni ratio of only 1.2:1 compared to the CI ratio of 18:1. This would require a factor of 15 increase in enrichment of Ni which is highly unlikely. Therefore, further observations are required to verify the densities observed at Alaska. These lidar soundings will also take place at Kühlungsborn.

Several neutral and ion-molecule reactions of Ni and Al will be measured in this study, using a fast flow tube system. Metal atoms and ions are produced by ablation of a metal rod using a 532 nm Nd-YAG laser [*Self and Plane*, 2003; *Whalley et al.*, 2011]. The reactants are later injected into the flow tube with the products detected by either Laser Induced Fluorescence (LIF) for neutral species [*Gómez Martín and Plane*, 2017] or by Mass Spectrometry (MS) [*Broadley et al.*, 2007] for ion species.

Finally, the complete set of measure Ni kinetics will be inserted into a global chemistry-climate model along with an experimentally-derived MIF for Ni, similar to what was done for previous metals [*Feng et al.*, 2013; *Marsh et al.*, 2013a]. The purpose of this model would be to simulate the expected

densities and profile of the Ni layer to see how they compare with the measurements made in Alaska and Kühlungsborn.

2 Materials & Methods

This chapter details the range of experimental apparatus used throughout this thesis study, to help achieve the objectives detailed in Chapter 1.

2.1 Laboratory Kinetic instruments

As stated in chapter 1, the reaction kinetics of several Ni and Al species were studied and then later applied to a global climate model to simulate both metals in the MLT. A series of techniques have been developed over the last few decades for studying these types of reactions. These methods are varied in terms of the species under study (charged or neutral), the mode of injection and the detection of the reactants/products. One of the aims of this study was to attempt lidar observations of AlO. A molecular metal layer has never been detected previously, so to ensure the possibility of detection, the optical absorption cross section of AlO needed to be established since a molecular metal would exhibit a band emission rather than a line emission. To get an accurate measurement of this, a Laser Ablation-Fast Flow Tube (LA-FFT) setup was used. The results of these kinetic experiments using this instrument will be discussed in Chapter 4.

2.1.1 Laser Ablation-Fast Flow Tube/Time-of-Flight Mass Spectrometry for Al + O_2 kinetics

The system has remained largely unchanged for over a decade [*Gómez Martín and Plane*, 2011; *Self and Plane*, 2003] with the exception of the introduction of the Time-of-Flight Mass Spectrometer (ToF-MS) [*Gómez Martín et al.*, 2016] and a number of minor modifications. The tube itself is made from stainless steel, with an internal diameter of 37.5 mm. To allow for a stable low vacuum in the tube, different sections of the tube were fitted with 70 mm conflat flanges and sealed with copper gaskets. Figure 2.1 below illustrates the schematic for the LA-FFT:

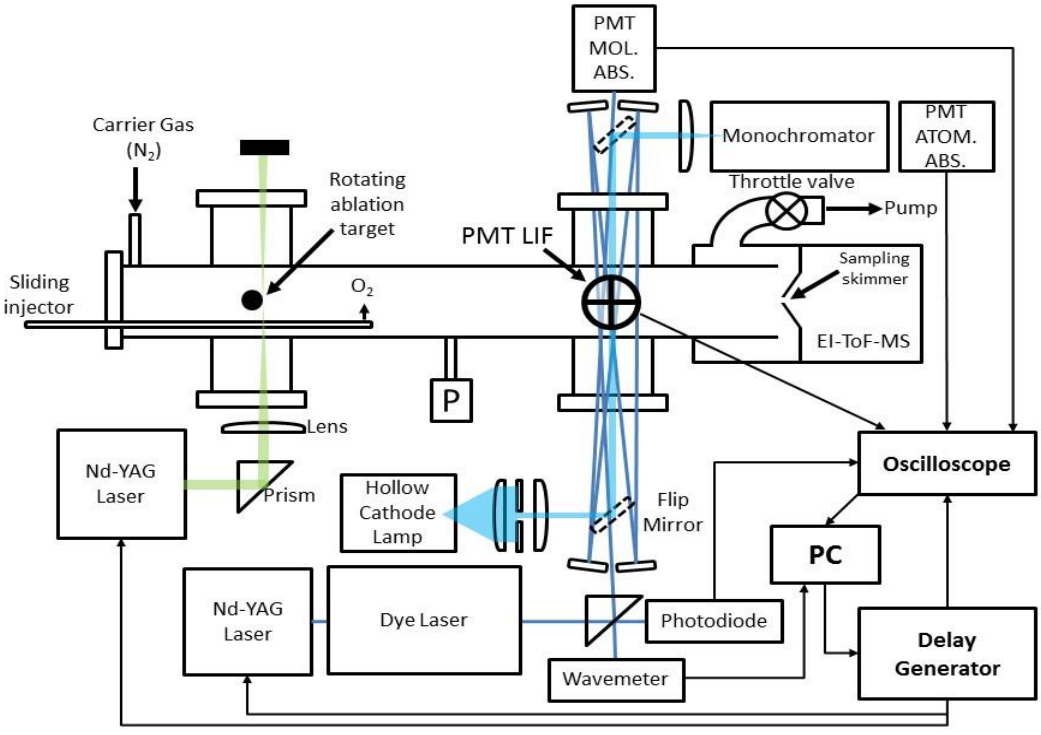

Figure 2.1: The LA-FFT schematic diagram for the Al + O_2 kinetics reaction. The flip mirror allowed for alteration between the Al and AlO measurements. The O_2 and N_2 flows were introduced using calibration mass flow controllers.

A pulsed 532 nm Nd-YAG laser (Continuum Minilite) was used for the ablation of the rotating cylindrical Al metal target. This laser emits fundamental 1064 nm light in the infrared [*Continuum*, 1996] but was frequency-doubled to 532 nm (repetition rate = 10 Hz, pulse energies = ~25 mJ). The importance of mounting the metal target on a rotary feedthrough powered by a DC motor was to allow for a fresh surface for each laser pulse [*Self and Plane*, 2003]. An external power supply was used to power the rotating motor. A flow of O_2 was then added via a ¼ in. (6 mm) glass sliding injector downstream of the ablation source. A modified ConFlat flange with a Cajon vacuum fitting was used to allow the movable injector to be inserted into the flow tube. The O_2 concentration was adjusted through balancing the flow with addition of N_2. Adjustment of the sliding injector changes the contact time between O_2 and the Al ablated atoms. If the species were injected too soon, the AlO would not be detected due to further reaction of AlO with O_2. The contact times between the ablated Al atoms and O_2 was varied between 0.5 – 2.5 ms during the experiment. Typical carrier flows of N_2 during the experiment were 3-4 standard litres a minute (slm) at a pressure of 0.7 Torr. Two MKS baratron units were installed during the experiment, with one operating up to 10 Torr and the other up to 1000 Torr. Pressure control was maintained with a throttle valve connected to a 80 $m^3\ hr^{-1}$ rotary pump (Edwards, Model E2M80) backed by a roots blower (Edwards, Model EH500A). This produced the high flow speeds required in the tube.

Once the pulse of Al/AlO passed down the flow tube and reached the spectroscopic cell, the Al atoms and AlO molecules were quantified separately. First, Al atoms were measured using Atomic Resonance Absorption Spectrometry (ARAS), to measure the absolute concentration of

Al atoms, through absorption of the 396.15 line of Al ($^2S_{1/2} \leftarrow {}^2P^o_{3/2}$), emitted by a hollow cathode lamp (HCL) (Perkin Elmer). The non-absorbed light exiting the spectroscopic cell was measured using a monochromator (resolution of 1.9 nm Full Width at Half Maximum [FWHM]) and a photomultiplier tube (PMT) (Hamamatsu H7710-12).

For the measurement of AlO absorption and fluorescence, pulsed laser radiation was generated through a combination of Sirah Cobra Stretch dye laser pumped by a Continuum Surelite Nd-YAG laser (λ = 532 nm; 10 Hz). For this experiment, the dye laser used a solution of Coumarin 102 in ethanol, spanning a spectral range of 455 – 495 nm. The width of the laser pulse was 6 ns and had a linewidth of 0.003 nm. A wavemeter (Coherent Wavemaster) was used to monitor the wavelength of the dye laser beam during spectral scans. A HeNe laser was used to calibrate the wavemeter to 3 decimal places as an extra check.

The AlO fluorescence in the optical port was collected perpendicular to the dye laser beam, though a set of lenses and interference filters (depending on whether the measurement was resonance or off-resonance) by a photo-multiplier tube (PMT) (Electron Tubes, 9816QB). For measurement of the resonance fluorescence from the B(0)-X(0) and B(1)-X(1) bands, a band-pass filter centred at 482 nm (Ealing 35-3441, 10 nm FWHM) was installed before the PMT. To check the transmission curve of the filter before use, a UV-Vis absorption spectrometer (Perkin Elmer, Lambda 900) was used. Off-resonance fluorescence was also observed by applying a yellow high pass filter (Comar 495GY25, with a cut-on wavelength of 495 nm) and by pumping the B(1)-X(0) or B(2)-X(1) transitions. The better signal was observed with the

resonance detection of AlO at the B(0)-X(0) band, with the signal at least two orders of magnitude larger than the scattered light from the laser. Therefore, this band was used for the kinetics studies. Care had to be taken to avoid saturating the PMT at the bandhead of the 0-0 transition due to intense fluorescence release. This was achieved by reducing the PMT voltage from the usual voltage of 1 kV to ~800 V, as well as reducing the pulse laser energies of the dye laser to ~0.5 mJ.

The dye laser radiation passed through the same optical port as the Al absorption lamp. Two glass tubes were attached to either side of the spectroscopic cell with each edge cut to fit a fused silica window at Brewster's angle (57^{o}), to ensure that the incident light entering was transmitted to through the spectroscopic cell with minimal reflections causing scattered light. Black tape was applied to the glass tubes to limit scattered room light affecting the PMT. Since the LIF PMT was positioned above the cell and the absorption PMT was directed to one side of the cell, opposite to the lamp and laser, a flip mirror was deployed to alternate between each measurement. This way, the methods did not interfere with each other. The AlO absorption from its B-X electronic transition was quantified using a multi-pass arrangement. This entailed passing the dye laser beam back and forth several times through the cell using mirrors to compensate for the small diameter of the flow tube by increasing the AlO absorption pathlength, in accordance with the Beer-Lambert law. The resulting laser pulse energy from this multi-pass system was monitored on exit by a PMT through a stacking of neutral density filters.

Downstream of the 6-way crossing spectroscopic cell was a TOF-MS with electron impact ionization (Kore Technology). This was coupled to the end of

the flow tube and was used to identify Al reaction products and to measure the purity of the N_2. The signals from the internal detector of the TOF-MS were quantified using a digital oscilloscope (LeCroy LT342), followed by interpretation of the data with the instrument's software. From there, subsequent data collection and analysis was carried out. All laser triggering and acquisition of oscilloscope data were synchronized by a Quantum digital delay pulse generator (model 9518). The TOF-MS had its own backing pump (Edwards XDS 35 Dry Pump, 44 m^3 hr^{-1}) which operated continuously, even when the flow tube was not in operation.

For the lidar measurements discussed later in section 2.2, this flow tube was re-purposed and condensed to a smaller portable system to act as a calibration cell for AlO to ensure the lidar wavelength was measured accurately. Details of this cell are discussed in section 2.2.4.

Materials

Oxygen-free-nitrogen (OFN, 99.998%, BOC) cylinder was used to supply the main carrier gas. For the O_2 supply for the sliding injector, an Ultra-High-Purity (UHP) O_2 (BOC) cylinder was used, either directly or in a diluted bulb mixture with N_2. For the metal ablation target, a cylindrical rod (diameter = 6 mm) of industrial grade Al was manufactured. Calibration of the OFN N_2 cylinder was made with the TOF-MS to check the purity. This was done by investigating the relative abundance of other m/z ratios, such as O_2 at 16 m/z.

2.1.2 Ion-Fast flow tube/Quadrupole Mass Spectrometry for Ni^+ and Al^+ kinetics

The schematic diagram of the IFT/QMS system used to study the reactions of Al^+ is shown in figure 2.2 below. Although this setup is similar in some respects to that of the LA-FFT used for the Al + O_2 kinetics discussed earlier in this chapter, the ion-molecule version was based on previous studies of the reactions of Fe^+ [*Vondrak et al.*, 2006], Ca^+ [*Broadley et al.*, 2008] and Mg^+ ions [*Whalley et al.*, 2011]. The stainless-steel flow tube length from ablation to detection was 972.5 mm, with 111 mm separating the entry to the flow tube and the ablation point. The flow tube consisted of cross-pieces and nipple sections, which were all connected by ConFlat flanges and then were sealed with Viton or copper gaskets, depending on vacuum requirements. The flow tube had an internal diameter of 350 mm. A roots blower (Edwards, Model EH500A) which was backed up by an 80 $m^3\ hr^{-1}$ rotary pump (Edwards, Model E2M80), allowed for the high gas flow velocities required in the flow tube.

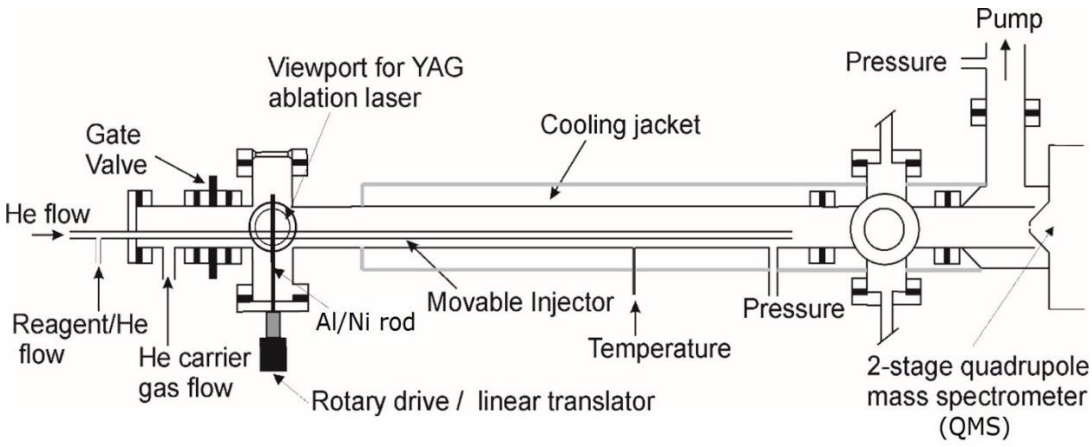

Figure 2.2: Schematic diagram of the fast flow tube with a laser ablation ion source, coupled to a differentially pumped quadrupole mass spectrometer. Reagents were admitted via a sliding injector and kinetics were measured by

either altering the contact time between the sliding injector and the detection point or by adjusting the reagent concentration at a fixed contact time. The cooling jacket allowed for solid CO_2 pellets to be packed in for low temperature experiments.

Al^+ and Ni^+ ions for the reaction were produced through laser ablation of a solid Al or Ni rod using a 532 nm Nd:YAG laser, which operated at a repetition rate of 10 Hz with a pulse energy of ~25 mJ per pulse. Both rods were 5 mm in diameter with varying lengths. Rubber gloves were worn when the Ni rod was handled to avoid any skin contact. The laser beam was loosely focused onto the target rod using a quartz lens with a focal length of 150 mm. A beam dump was positioned after the ablation cell to remove the residual 532 nm laser light. The metal rod was mounted on an adjustable rotary feedthrough which was powered by a DC motor. The rod was positioned into the centre of the cylindrical axis of the flow tube as shown in figure 2.2. The rotation rate of the rod was at of 2 – 4 Hz to ensure the laser was always hitting a fresh metal surface, maintaining a uniform M^+ signal [*Vondrak et al.*, 2006]. In terms of signal counts, Ni^+ ions were 3-4 times less abundant than Al^+ ions under the same ablation conditions which indicated that the Al rod was much easier to ablate/ionize.

The metal ion pulses were carried in a flow of He which entered the flow tube upstream of the ablation target. Reactants for both ions (N_2, O_2, H_2O, CO_2, O_3) were injected into the flow tube through a sliding glass injector positioned along the floor of the tube (Figure 2.2). A 5 slm Mass Flow Controller (MFC) was used for the main carrier flow (He), with a 100 Standard Cubic Per

Minute (sccm) MFC installed for the O_3/O_2 mixture and a 200 sccm MFC for addition of another reactant (H_2O, CO_2, etc), with an extra 200 sccm MFC to balance the amount of H_2O or CO_2 put in with a flow of He. The typical gas flow rate overall used was ~4200 sccm per experiment. This was divided into increments of 4000 - 4200 sccm of carrier gas He, 10 - 20 sccm O_3/O_2 mixture and 0-200 sccm ratio for the balanced CO_2/H_2O with He flows. Pressures were of the order of 1 - 4 torr, which was controlled by a throttle valve situated on the exhaust. This yielded flow velocities that ranged from 55 - 14 m s^{-1} with the Reynolds number always less than 80, ensuring laminar flow conditions [*Gómez Martín et al.*, 2016].

To generate the O_3 required for reaction with M^+, O_2 was flowed through the high voltage corona in a commercial ozoniser (Fischer Technology Ozone Generator 500 Series). This produced a 5-8 % mixture of O_3 in O_2. The O_3 flow was then passed through the MFC and the O_3 concentration was monitored in a 300 mm pathlength optical cell downstream of the ozoniser, by optical absorption of the 253.7 nm emission line from a Hg lamp [*Broadley et al.*, 2007; *Whalley et al.*, 2011]. Both the lamp and cell were covered in thick black cloth to avoid any interference from room lighting. Voltage settings for the ozoniser were set in the range of 30-41 V, depending on the O_3 concentration required. At the end of each experiment, 100 sccm of O_2 was passed through the system with the ozoniser off to purge the flow tube of O_3. For pressure monitoring, two pressure transducers (MKS Baratron) were attached adjacent to the gate valve, with upper limits of 10 Torr and 1000 Torr.

The metal ions and their molecular products were detected using a differentially pumped 2-stage quadrupole mass spectrometer (QMS) which was run in positive ion mode (Hiden Analytical, HPR60). Since the metal atoms were already ionized, there was no need for electron impact or photoionization. The QMS was backed up with an Edwards RV5 (5.8 m^3 hr^{-1}) which kept the system at low pressure when the flow tube was not operating. If the QMS suddenly was exposed to atmospheric pressure, the turbo and backing pumps automatically shut down, stabilizing the sytem for restart. The sample or skimmer cone that was between the flow tube and the first stage of the MS had a 0.4 mm orifice biased at −17 V. These skimmer cones were designed to admit the ions from the flow tube into the quadrupole. The skimmer cone that was between the first and second stage of the MS had a 1.8 mm orifice biased at −86 V. Time-resolved ion pulses were then recorded with a multichannel scaler (ORTEC) that was synchronized to the Q switch of the YAG laser by using a digital delay generator (Quantum model 9518). For each experiment, 500 - 1000 laser shots of Al^+ and Ni^+ pulses were then signal-averaged and saved in the '.mcs' format. MS software supplied from Hiden (MASsoft) was also used in conjunction with the multichannel scaler. This program allows for a real-time measurement from the MS of a specific mass of interest during the experiment. It also has a scanning functionality, allowing for a set range of masses to be scanned for over a designated time. This is essential for identifying the products that were detected and from there focusing solely on specific individual masses for long duration scans. During this study, the desktop computer that operated the multichannel scaler software stopped working and was too old to be replaced

easily, so MASsoft was then primarily used. Signal was then recorded from 3-minute averaged intervals.

Materials

He (99.995%, BOC gases) was used as the main carrier flow. To avoid contamination with H_2O and CO_2, it was purified by passing through a liquid N_2 molecular sieve maintained at 63 - 77K (4 Å, 1 – 2 mm, Alfa Aesar). H_2O (Milli-Q pure) and CO_2 vapour was prepared by purification through three freeze-pump-thaw cycles. These were then made up into 10% bulbs in a glass vacuum line, with He as the diluting factor. The initial CO_2 added for the bulb before the purification was from a CO_2 (99.995%, BOC gases) cylinder. N_2 (99.995%, BOC gases) and O_2 (99.999%, BOC gases) were used without purification.

2.1.3 Ion-Fast flow tube/Quadrupole Mass Spectrometry for molecular metal kinetics of NiO^+, AlO^+ and NiO

After measuring the metal atomic ion reaction rates with CO_2, N_2, O_2, H_2O and O_3, the next step was to investigate the reactivity of their metal oxide ions with O, CO and O_3. When the metal oxide ion (MO^+) is formed in the lower thermosphere, it can undergo dissociative recombination to form the neutral metal [*Bones et al.*, 2016b]. The rate at which the metal is neutralized plays an important role in the top-side layer shape and abundance. However, reactions that compete with dissociative recombination by reducing MO^+ back to M^+ can play an important role in slowing the rate of neutralization. O and CO react with MO^+ to form M^+ and O_2 or CO_2, respectively. O_3 can react in a forward direction to form higher oxides (MO_2^+) or in a backward direction to

form $M^+ + 2O_2$ [*Broadley et al.*, 2007]. For neutral NiO, its reactions with O and CO were examined to try to explain the broad bottomside of the Ni layer profile measured by *Collins et al.* [2015] at Poker Flat, Alaska, compared with Fe.

The reactions of neutral Ni were performed by [*Mangan et al.*, 2019] separately to the ion studies done in this thesis. However, the kinetics of NiO with O and CO and NiO_2 with O were not addressed in that study and were instead determined in this work. Figure 2.3 below shows the series of modifications that were made to the flow tube discussed earlier in figure 2.2, to construct the Ion Molecule Fast flow tube/Quadrupole Mass Spectrometry (IMFT/QMS) system. The colour scheme indicates the distinctions between the neutral and ion molecule experiments.

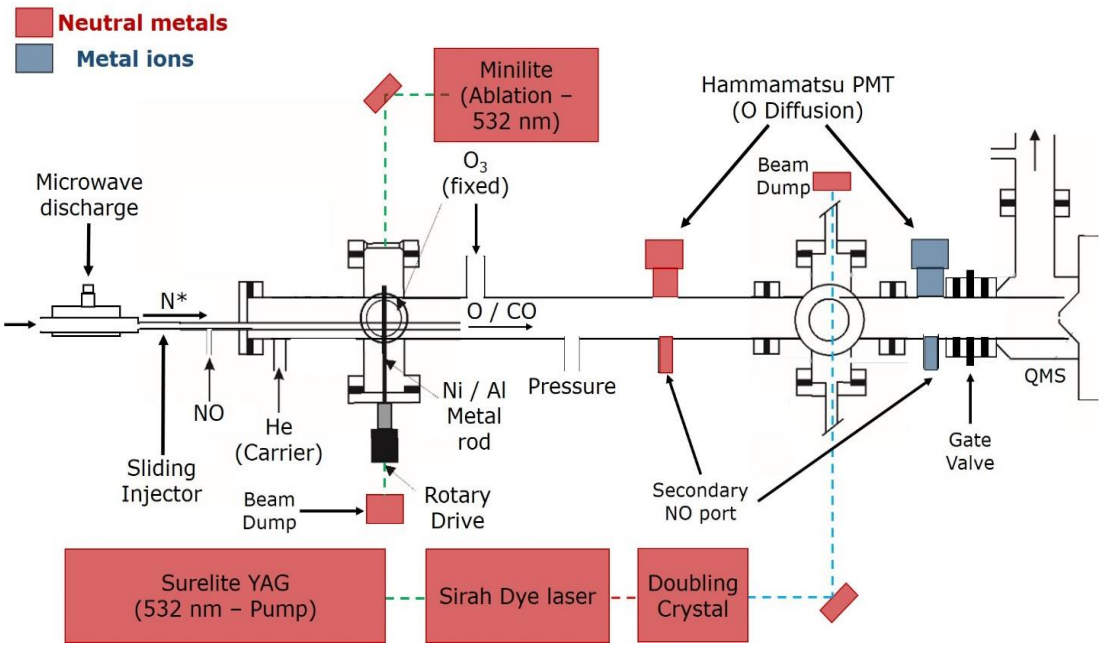

Figure 2.3 Schematic diagram of the modified LAFFT/QMS system with additional port for the LIF detection of the metal, microwave discharge

connection to the sliding injector, fixed O_3 side arm port and secondary PMT for measurement of O chemiluminescence. Neutral Ni atoms were probed at 341.476 nm [Ni($z^3F_4^0$−a^3D_3)] by using a frequency-doubled dye laser (Sirah Cobra Stretch) pumped with a Nd:YAG laser. The QMS was used to quantify Ni^+ and NiO^+ ions but was also used for NO calibration at mass 30 in all the experiments of this section.

O_3 was fixed at an injection point 70 mm downstream of the ablation cell. The sliding injector was still the primary entry point for the reactants (O and CO). The main difference with this setup from the previously described flow tubes was the addition of a microwave discharge cavity (McCarroll cavity - Opthos). The purpose of the cavity was to generate N atoms by discharging N_2 that was flowed through it. These excited atoms were then titrated with NO (N + NO → O + N_2 [*Self and Plane*, 2003]) The cavity consisted of a 150 mm quartz tube that was connected to the sliding injector used in previous experiments, by a Teflon fitting. Teflon was used instead of a standard metal cajon fitting as the newly formed O would have adsorbed and then recombined on the metal surface. The quartz tube was mounted on an adjustable stand to allow for a level of flexibility to the sliding injector and avoid breakage while changing the length to the flow tube.

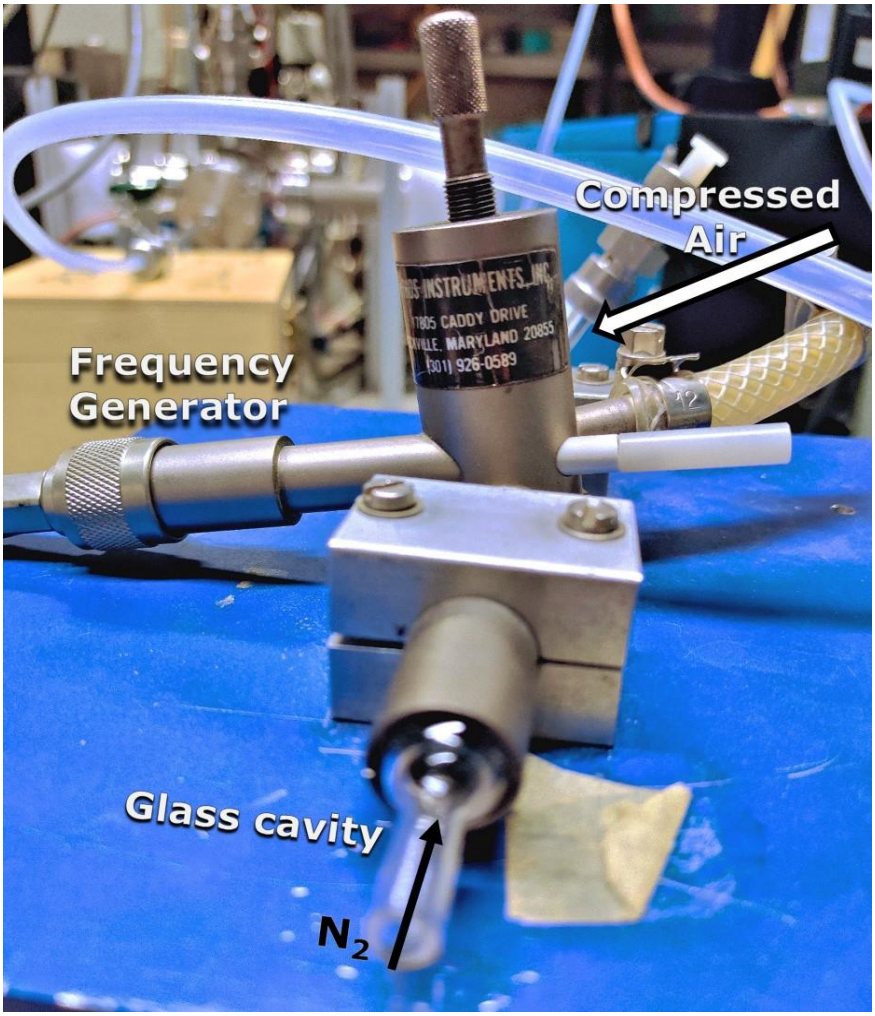

Figure 2.4: The microwave discharge cavity. Compressed air was used to prevent the cavity from overheating. This was especially important when the cavity was glass and not quartz, as glass softens at 427 K and melts at 727 K [*Karazi et al.*, 2017] compared with quartz at 1127K [*Ainslie et al.*, 1961]. Forward wattage of the frequency generator was between 192 – 194 W. Reflected wattage for the majority of the experiments remained < 5 W. A low reflected wattage was vital to ensure a more efficient conversion of N_2 to excited N atoms.

The forward wattage of the discharge was maintained between 192 - 194 W. A Tesla coil was used to initiate the spark for the discharge. Once the cavity was tuned, the reflected wattage for the majority of the experiments remained

< 5 W. A low reflected wattage was vital to ensure a more efficient conversion of N_2 to excited N atoms. The O concentration was measured by titration with NO_2 [*Self and Plane*, 2003]. Reaction of NO with O leads to formation of excited NO_2^*; the chemiluminescence was measured through a PMT (Hamamatsu Type H9306-13) with an interference filter at 590 ± 5 nm. The PMT was situated upstream of the QMS for the ion experiments, and the LIF PMT for the neutral component.

O diffusion to the flow tube walls and subsequent removal was an important factor to account for. The first-order loss of O to the walls of the flow tube was measured by measuring [O] at differing flow times, achieved by changing the flow velocity while maintaining a constant pressure. This was done by varying the total carrier flow and adjusting the pressure accordingly. A secondary addition of NO was made just upstream of the detection point to measure the relative intensity of the NO_2^* chemiluminescence, and from this the change in relative [O] could be determined.

2.1.4 Neutral kinetics of NiO

For studying the kinetics of NiO, LIF was reintroduced (see section 2.1.1). Ni atoms were probed at 341.476 nm [Ni($z^3F_4^0$−a^3D_3)] through the use of a frequency-doubled dye laser (Sirah Cobra Stretch) that was pumped with a Nd:YAG laser (Continuum Surelite). The dye solution used was pyridine 1 which was then doubled using a Beta barium borate (BBO) crystal. A Nd:YAG laser (Continuum Minilite) was used for the ablation of the Ni metal rod. A focusing lens (250 mm) was used for the ablation. The Ni LIF signal was collected using a PMT (Electron tubes, PM30D) with an interference filter (λ_{max}

= 340 nm, fwhm = 10 nm). The distance from ablation to detection by LIF was 455 mm. The QMS was still deployed for calibration of NO before the O was made to react with NiO.

The main carrier gas was changed from He to N_2, as clustering reactions with the neutral Ni was not an issue. N_2 was more readily accessible and economical, and diffusional loss to the flow tubes walls is also reduced. Flows of 3000 sccm for the N_2 carrier MFC, and 300 sccm for the MFC flowing through the discharge, were used for all the experiments.

Initially Teflon tubing was used to connect the N_2 flow to the microwave cavity. However, there was some evidence of air contamination leaking into the N_2, and so the Teflon was replaced with copper tubing and a flexible stainless-steel bellows. The copper tubing was placed in a dewer and filled with a solid CO_2 pellet/acetone mixture to freeze out any H_2O or CO_2 contaminants. Liquid N_2 was not used to avoid the possibility of freezing down N_2 in the line.

The analogue output from the PMT was sent to a gated boxcar averager (SRS – Model SR 280) and converted to a digital output. A CompactRIO controller (National Instruments interpreted the signal for the desktop LabVIEW software to record the output.

O, CO and O_3 were prepared and admitted to the flow tube in the same way as the NiO^+ kinetic study, apart from making up CO and NO bulb mixtures in N_2 rather than He. O diffusion was also measured the same way but the PMT measuring the chemiluminescence of O was placed upstream of the LIF detection point.

Diffusion of Ni in the flow (k_{diff}) was measured by varying the total flow of N_2 and adjusting the delay between ablation and downstream LIF detection.

2.1.5 Materials

He (99.995%, BOC Gases) was supplied for the ion molecule kinetics with N_2 (99.9999%, N6.0, BOC Gases) used for the neutral experiments. O_2 (99.999%, BOC gases) was used without purification. CO bulbs were prepared from a CO (99.5% pure, Argo International) lecture bottle without any further purification and diluted to 10% mixtures using He or N_2.

Atomic O was prepared by reacting discharged N atoms with NO. The NO bulb was prepared from a NO cylinder mixture (99.95%, air products). The cylinder had both an O_2 and NO_2 impurity so purification was needed. The following degassing method was applied to purify the NO in three steps. First, just under 1 atm from the cylinder was admitted to the gas line and frozen down in a glass cold finger held at 77 K (liquid N_2). Both the NO (Freezing point = 109 K) and NO_2 (Freezing point = 262 K) froze down, with a trace amount of O_2 also. The liquid oxygen was indicated by a pale blue colour in the cold finger. The pump was closed off during this process. Second, the sample was then warmed back to room temperature. The O_2 came off first since it has a similar boiling point to N_2. The cold finger was open to vacuum during this time to pump off the O_2 impurity but was closed off before the NO evaporated. This cycle was repeated 2 to 3 times. The final step was to remove the NO from the NO_2. After freezing down the last time, the liquid N_2 dewer was swapped with a container filled with solid CO_2 pellets mixed with acetone to slightly liquify the pellets and allow for better surface contact with the cold finger since the pellets alone did not sufficiently cool the glass finger. The temperature of dry ice (Boiling point ~195 K) was low enough to keep the

NO_2 in liquid form but not the NO. The NO was then transferred to another evacuated bulb. The purification was successful if the final bulb was colourless. The NO that was transferred was then made into a 5-10% bulb mixture using N_2 or He.

2.2 Lidar Observations

2.2.1 Monitoring site

For all lidar systems, the essential components are a transmitter (i.e. a pulsed nanosecond laser) and a receiver. Many of these systems apply the use of a beam expander in the transmitter unit to reduce the divergence of the laser beam in the atmosphere. If the laser is tuned to a strong atomic resonance line of the species of interest, the laser light will be resonantly scattered. Photons will also be backscattered by aerosols (Mie scattering) and molecules (Rayleigh scattering), and a small fraction of the scattered light can be detected in a ground-based telescope adjacent to the transmitter. The elapsed time from the outgoing laser trigger to collection provides the altitude from which the photons are scattered. Following collection in the telescope, the photons can be detected by a PMT and recorded with a multichannel scalar i.e. time-resolved photon counting [*Wandinger*, 2005].

A collaboration was established with Dr Michael Gerding at the Leibniz Institute of Atmospheric Physics (IAP), Germany, to perform lidar observations of Ni and AlO. The IAP is a world leader in lidar observations of metallic species including Fe, Ca and Ca^+ in the MLT [*Alpers et al.*, 1996; *Alpers et al.*, 1990; *Gerding et al.*, 2000]. The institute is located ~4 km south-

east of the town of Kühlungsborn (54°N, 12°E), a tourist seaside resort on the Baltic sea and ~24 km west of the closest city, Rostock. The institute was strategically located because of the very low light pollution levels from the nearby town of Kühlungsborn. This ensured the lowest possible interference to atmospheric measurements that are sensitive to external light sources. The institute is also an active weather station, therefore most of the meteorological data required during observations was acquired on-site.

Two lidar systems at the IAP were deployed for this study, a metal resonance lidar and a Rayleigh/Mie/Raman (RMR) lidar. Table 2.1 below shows the dates the lidar operated on for each metal:

Table 2.1: Dates when Ni and AlO lidar measurements were made at the IAP, Kühlungsborn

Metal	Date	Comments
AlO	January 2016	Initial observation attempt
	April 2017	AlO calibration cell and attempted monitoring
Ni	April/May 2017	Attempted lasing at 337 nm for Ni
	September-October 2017	Change in laser and attempted observations at 337 nm
	January-March 2018	Observations of Ni at 337 nm and 341 nm

2.2.2 Rayleigh-Mie-Raman lidar

A Rayleigh-Mie-Raman (RMR) lidar was operated in conjunction with the resonance lidar system. Since 2009/2010, a new RMR lidar (with a Quanta-Ray PRO290-30 Nd-YAG laser) was installed on site for the purpose of soundings of middle atmospheric temperatures and NoctiLucent Cloud (NLCs) during both daytime and night-time periods, with initial operations in summer 2010 [*Gerding et al.*, 2013a; *Gerding et al.*, 2016; *Kopp et al.*, 2011]. For this experiment, the RMR lidar was utilized as a reference instrument for the resonance dye lidar as it could provide an off-resonance measurement of the atmospheric background. Since it was the most important lidar system at the institute due to the necessity of quantifying upper atmospheric temperatures and NLCs, it was operated frequently and had constant maintenance.

During operation, the YAG reached pulse energies of 650-700 mJ per pulse at 30 Hz. One fixed mirror and two steering mirrors were used to guide the laser light into atmosphere and were co-axial with the receiving telescope. Backscattered light from the atmosphere is now collected by a 32 inch (812.8 mm) parabolic *f*/4 mirror with a focal length of 3.25 m, compared to the previous 5 telescopes of 500 mm diameter [*Gerding et al.*, 2013b; *Gerding et al.*, 2016]. During operation, 90% of the received photons are for lidar detection, with the latter 10% used for beam stabilization. A chopper was installed to prevent unwanted entry of large photon quantities scattered from the lower atmosphere, through specific timing with the fired laser pulse. The measured photon counts are recorded by transient recorders and were accumulated over 1000 laser pulses (equates to ~30 s). A new function known

as ‘cloud mode’ allows for lidar operation during periods of ‘broken clouds’. During this mode, the data would be pre-integrated over 50 laser pulses and only used for final integration if the observed SNR was at a satisfactory level. Just a few seconds of increased background from cloud interference would contaminate the entire measurement. With cloud mode, operation can continue even during periods of fast cloud travel, without the issue of recording that data [*Gerding et al.*, 2016]. Generally, 30 minutes of high background from cloud passage was the institute standard during lidar practice before operations were terminated.

2.2.3 Metal Resonance lidar

For assessing metal species in the MLT, more flexibility was required as each metal is detected by a specific wavelength. Operating the metal dye lidar was similar to that of the RMR-lidar with the main exception of dye changes every 1.5/2 hours during operation.

The original setup in the lidar bay consisted of two dye lasers, each with their own oscillator and two amplifier stages. Rather than both setups having their own pumping source, an excimer laser beam was split 50:50% to each dye laser [*Alpers et al.*, 1996; *Gerding et al.*, 2000]. The system was quite robust, maintaining functionality even after being shut down for several months. For this reason, the dye lidar has remained mostly unchanged over the years. The system was first deployed for atmospheric observations of Ca at 423 nm and Ca^+ at 393 nm in the MLT [*Alpers et al.*, 1996]. This was the reason for having a dual dye laser setup as both species could be measured simultaneously. Since 1997, the backscattered photons from the upper atmosphere were

collected in the receiver system consisting of 7 parabolic mirrors, each of 500 mm diameter [*Gerding et al.*, 2000].

For this study, a few modifications were made to the system. A 308 nm XeCl Lambda Physik LPX 300 excimer laser was the pumping source for the dye laser, with pulse energies between 400-500 mJ per pulse. Both dye lasers could not be used as one had deteriorated to the extent that conversion efficiency of the pumping laser light to the dye beam was very low. Therefore, only one dye laser was required, allowing 100% of the pumping energy to pump the one dye and increase the overall lidar pulse energy. This way, following the fundamental principle of the Power-Aperture product, $P_{av}A$, which relates the received signal to the laser power and the area of the receiving telescope, a larger backscatter signal should be observed [*She*, 2005].

For Ni, p-Terphenyl (PTP) in propylene carbonate was used first, covering a spectral range of 330 – 349 nm. The solvent was chosen as a less toxic alternative to p-Dioxane, the dye solvent used by *Collins et al.* [2015] but eventually the solvent had to be changed back to the original p-Dioxane as the propylene carbonate was not efficient enough [*Brackmann*, 1994; *Gerding et al.*, 2019]. Concentrations were of the order of ~0.2 g/L for the PTP. The initial wavelength that was considered for observations was λ_{air} = 336.9563 nm, since this was previously used for the initial observations of Ni (Collins et al., 2015) for pumping ground state Ni(^{3}F). In late 2017, laboratory kinetics of Ni showed a more favourable transition at λ_{air} = 341.4764 nm probing the low-lying Ni(^{3}D) state [Ni($z^3F_4^0$–a^3D_3)] (Mangan et al., 2019). This wavelength was closer to the PTP laser dye's emission maximum than the ground state

transition Ni(^{3}F) at 337 nm. As a result, this yielded a larger laser power, less broadband emission, and more wavelength stability. For AlO, Coumarin 102 in ethanol was used as the laser dye, spanning a spectral range of 455 to 495 nm, which is within range of the bandhead of the B(0)-X(0) band of AlO at 484 nm.

For the receiver, instead of 7 parabolic mirrors of 500 mm diameter to reduce losses from the optic connections between the mirrors, a single 30 in. (760 mm) mirror was used for the observations, shown in figure 2.5 below. A quartz fibre was then used to guide the backscattered light to the detection point.

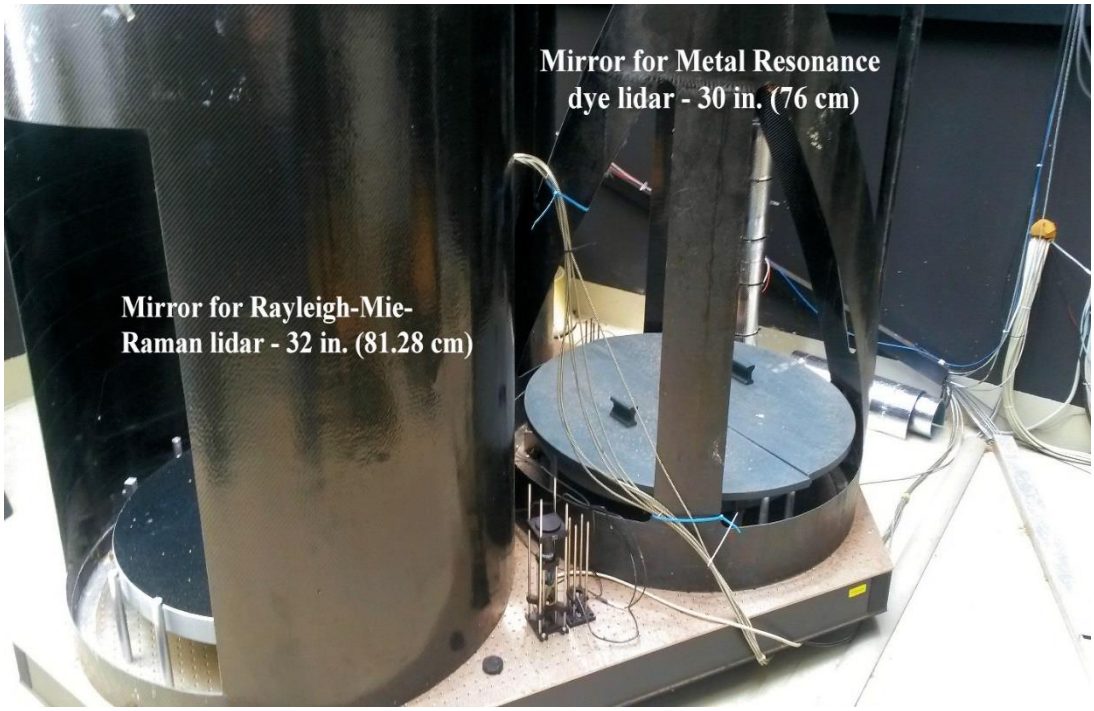

Figure 2.5: The receiver system for the RMR and dye lidar in the telescope bay of the IAP. Both systems were in operation for all the measurements made. Instead of 7 parabolic mirrors of 500 mm diameter to reduce losses from the optic connections between the mirrors, a single 30 in. (760 mm) mirror was applied for the dye lidar observations.

The quartz fibre used was an Optran UV with a transmission of ~90% for both states of Ni and AlO. The wavemeter deployed for the wavelength calibration and adjustment was the High Finesse WSU-30-MC, with a spectral range of 330-1180 nm. This range ensured that the laser could be tuned to both Ni at 337 nm and AlO at 484 nm. The detector was equipped with a 29-nm (full width at half maximum) Interference filter (IF) that had ~85% transmission at both wavelengths observed, and a Hamamatsu R7600U-200 PMT that was cooled to achieve ~40% quantum efficiency. The wideband IF had the potential issue of large background noise, so the lidar soundings required moonless nights; however, with high transmission and the PMT specification, a larger signal-to-noise ratio was achieved. For the AlO soundings, a 10 nm interference filter was used, as the higher laser power achieved at 484 nm was enough to compensate for the signal.

The operating software for the system is unique to the IAP, although it has remained largely unchanged for over two decades. Therefore, the saved matrix format for the lidar data was less user friendly than data recorded from the institute's more modern equipment, such as the RMR-lidar. Extraction of the appropriate dataset required written scripts from the program's designer. The data was then recorded into altitude bins of 200 m, with each bin corresponding to 4000 laser pulses at 30 Hz. During analysis, only datasets with low noise were used to give a stronger profile. Background scans of the noise were run during the lidar observations. The noise was then quantified in Hz against the time measured along with an indication of sunset and sunrise using solar elevation in degrees.

For metal resonance dye lidar monitoring, a set number of atmospheric conditions were required. These included the following:

During lidar operation, these weather parameters needed to be monitored as they could interfere with the signal. Sudden drops in outside temperature can cause thermal small shifts in the beam-steering mirrors and hence slight misalignment of the laser. Higher relative humidity with cold temperatures produced a similar effect to cloud coverage, with enhanced laser scattering in the boundary layer. The automated weather station at the institute provided real-time measurements of the temperature, pressure, humidity and wind speed. Once a potential clear day was predicted by weather reports, on-line satellite data was required during a lidar run to provide a close to real-time profile of cloud movements near the area, as clouds were the primary potential interference. Unfortunately, this method lacks consistency for more low-lying cloud formations, a common issue around coastal regions. To resolve this, multiple high-resolution cameras were installed around and on top of the institute to provide detailed coverage of low-lying cloud movements in the general vicinity. There were further problems with this as the four main cameras on-site were each delayed by a set number of minutes, with the most responsive delayed by 5 minutes. This made immediate response to cloud interference difficult. However, the employment of the near instantaneous RMR-lidar reading in conjunction with the satellite data and high-resolution cameras resolved this issue.

Since the institute is located in mainland Europe, numerous aircraft fly through the general area. To ensure the safety of pilots and passengers, a radar

monitoring system was set up in the lidar bay to detect incoming airplanes. Upon detection, the lidar was programmed to self-terminate operation.

2.2.4 Flow Tube Calibration Cell for use in observations at 484 nm

For measuring a metal species, the standard metal lidar operation entailed firing the laser at the wavelength of interest (either calculated theoretically or measured experimentally) without a constant point of reference. From there, a wavelength scan over a set number of picometers was applied and appropriate wavelength tuning of the dye laser would follow until the desired signal was observed, assuming that signal was even the species of interest in the first place. With this method, there was high uncertainty in the efficiency of detection. This issue was less severe with atomic layer species such as Na and Fe, as they yield specific line emissions and all the currently discovered metal layers are in atomic form around their layer peak [*Plane*, 2003]. Even Ni exhibited a line emission and was already observed for reference [*Collins et al.*, 2015]. But if a metal molecular layer were to reside in the MLT, the level of difficulty would increase, as the line spectrum would instead be a band spectrum. This was the justification behind experimentally measuring the cross section of AlO (see section 2.1) to find the most suitable wavelength for performing lidar observations. To assist the measurement of AlO by lidar, a Flow-tube calibration cell (FTCC) was built and deployed at Kühlungsborn to reference the wavelength output before attempted observations of AlO were performed. The setup represented a small-scale flow tube based on that used for the kinetic studies of Al + O_2 (section 2.1.1). Viton gaskets were used instead of copper caskets, as the ultimate vacuum required for the small-scale

did not need to be as good, since the focus was detection of the species rather than measuring kinetics. The method allowed a near real time reference for the AlO band to maintain the ideal wavelength for measuring AlO, and to avoid drift. The system was also tested before being transported to Germany. This was to check the minimum requirements needed to see an AlO signal. Figure 2.6 (A) below illustrates a schematic diagram of the FTCC:

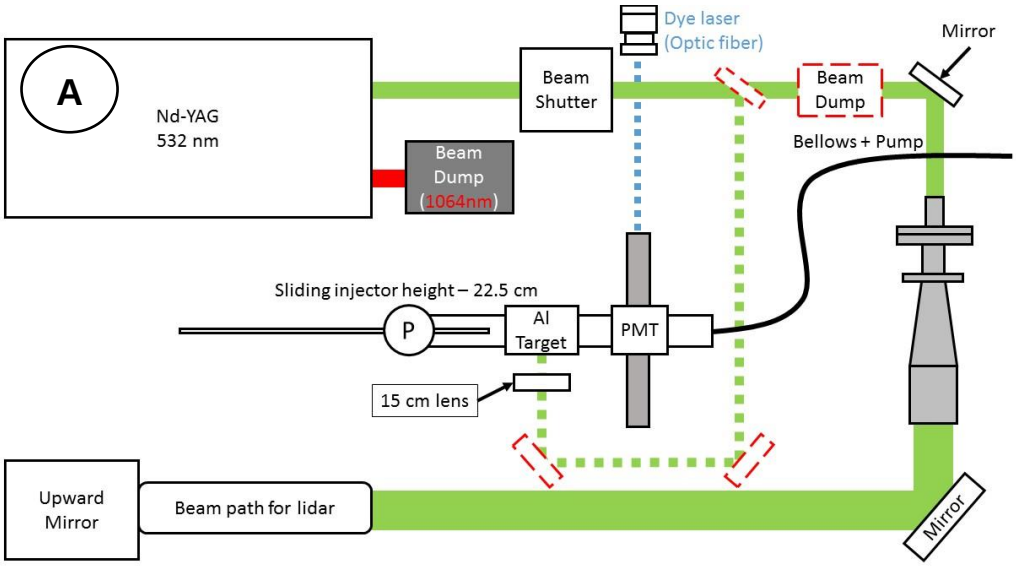

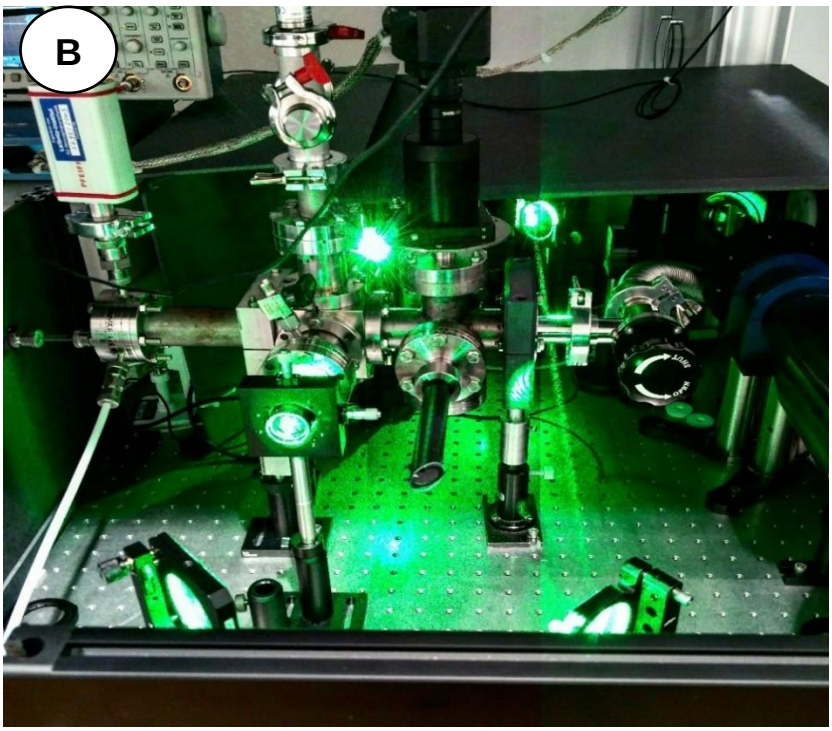

Figure 2.6: Schematic diagram of the calibration cell in the RMR-lidar bay (A) and the cell during operation (B). During operation, the mirror directing the 532 nm laser light to the calibration cell had to be removed from the path of the lidar beam. The YAG was set to a low pulse energy and beam-splitted for the calibration since the maximum pulse energy would likely damage the flow tube window and rod. The bellows connecting the cell to the pump was placed in a fixed position to avoid contact with telescope and subsequent misalignment of the lidar beam.

As shown in figure 2.6, the cell was small enough to be positioned in the centre of the RMR-lidar bay. The system was initially pumped with an EcoDry M20 pump (15 m^3/hr^{-1}, with an ultimate pressure 5.5 x 10^{-2} mbar) but unfortunately this was not capable of creating a sufficient vacuum, compared to the Edwards M28 used in the initial testing (ultimate pressure of 1 x 10^{-3} mbar). Following this, a Leybold Trivac D65B pump was borrowed from the University of Rostock which had the suitable specifications to achieve adequate vacuum (volume flow rate of 65 m^3 hr^{-1} and an ultimate pressure of <1 x 10^{-4} mbar). Further pressure control was achieved with an angle valve, as illustrated in figure 2.6 (B). The metal target rotation motor was powered at 1V by an external power supply. To align with the lidar beam, the cell centre line was elevated to a height of 225 mm. Since the cell required a 532 nm YAG laser for ablation of the Al rod, a fraction of the total lidar light was diverted to the ablation cell. Three beam dumps were installed in the system, one to remove the fundamental 1064 nm light from the Nd-YAG and the second dump removes the majority of the 532 nm light. The third was for residual light from

the 532 nm laser after it passed through the cell. With the laser operating at extremely high pulse energies (~650 mJ, 20W at 30 Hz), the YAG was set to a low pulse energy to avoid damaging the metal rod and flow tube windows. This along with three mirrors to guide the beam to the cell, reduced the total output to 20 mJ per pulse. A 150 mm lens was applied to the 532 nm laser to focus the beam to the rotating metal target. However, due to space constraints, only one of the two systems could be activated at once. Therefore, when the lidar required operation, part of the calibration cell needed to be removed temporally. Overall, it was not an issue changing the optics for checking the wavelength of the dye laser before and after lidar measurements, to ensure it was maintained on the most intense Al-O band down to the nearest picometer.

Unfortunately, since the dye laser was in the room next door, an optic fibre was required to pass the dye laser light through to the calibration cell. This initially caused a number of issues as the required pulse laser energies led to the fibres burning out. ~5 mJ of laser pulse energy was measured before the fibre, with 2 mJ per pulse after the fibre. Since there was a risk of damaging the fibre with this pulse and only 0.2 mJ was required to successfully see a signal (measured at the University of Leeds before departure), the input into the fibre was reduced using 50% density filters which were installed in front of the fibre. Combining the optical density filter after the fibre, the total energy pulse was in the range of 0.2 - 0.5 mJ. The N_2 and O_2 cylinders were provided by the IAP's rocket department.

The cell was operated under the following conditions during wavelength scanning around the band head of the AlO B(0) – X(0) band. The pressure in

the cell was typically2.1 Torr, with a N_2 flow of 2000 sccm and an O_2 flow of 4 sccm. Since Al was very reactive with O_2, k = (1.68 ± 0.24) x 10^{-10} cm^3 $molecule^{-1}$ s^{-1} [*Le Picard et al.*, 1997]) only a trace concentration was required. The contact length of the sliding injector after ablation was 80 mm and the time delay from ablation to the LIF cell was 5.1 ms. After a series of scans, λ = 484.3646 nm yielded the maximum signal intensity with a signal:scatter ratio of 9:1.

2.3 Atmospheric Modelling

Once the laboratory kinetics of Ni and Al were completed and observations of the species by lidar sounding were performed, the final objective was to investigate if the measurements were reproducible in a global climate model. For this work, a 3-D global model of meteoric Ni was developed by adding the measured reaction rates of both species into the Whole Atmospheric Community Climate Model (WACCM) described in Chapter 1. The horizontal resolution of the model was 1.9º latitude x 2.5º longitude [*Feng et al.*, 2013; *Marsh et al.*, 2013a; *Plane et al.*, 2018b]. The global model of meteoric Al was still in development during the writing of this thesis, therefore will not be included in the study.

Injection profiles, also known as meteoric input functions (MIFs), specify the temporal and geographical input of meteoric metals into the MLT. The Ni was added to WACCM-Ni. This MIF were calculated from three sources of cosmic dust particles that enter Earth's atmosphere: Jupiter family comets (JFCs), the asteroid belt (ASTs) and long-period comets (here treated as Halley type comets, HTCs) [*Carrillo-Sánchez et al.*, 2020; *Carrillo-Sánchez et al.*, 2016].

The mean injection profiles of Ni (dash/dot blue line) into the Earth's atmosphere, along with the other major meteoric metals is illustrated in Chapter 1 (Figure 1.3). Applying the MIFs shown in Figure 1.3 for global models such as WACCM leads to a large overestimation of all the metal layers in the MLT [*Plane et al.*, 2018b]. This is most likely due to WACCM underestimating the vertical transport of minor species through the MLT [*Gardner et al.*, 2017]. Models with coarse horizontal grid scales such as WACCM (~200 km resolution) are unable to resolve short wavelength gravity waves. Therefore, the model does not capture much of the wave spectrum that causes dynamical or chemical transport [*Plane et al.*, 2018b]. Since WACCM does not account for these vertical transport components, the MIF need to be reduced by a factor of ~5 to reproduce the observed metal densities. Since this has already been applied for Fe [*Feng et al.*, 2013], Ca [*Plane et al.*, 2018b] and Na [*Marsh et al.*, 2013a], both Al and Ni were given the same correction.

For each metal, a metal layer that was previously studied was chosen for comparison. For Ni, a WACCM-Fe simulation was used, as Fe is well studied both by observation and modelling [*Alpers et al.*, 1990; *Feng et al.*, 2013]. Fe and Ni are both transition metals that reside next to each other in the periodic table (atomic numbers 26 and 28, respectively), so a comparison of these metals is of particular interest. The chondritic ratio of Fe:Ni is 18:1 [*Lodders and Fegley*, 2011], and the modelled ablation ratio is 16:1 [*Bones et al.*, 2019; *Carrillo-Sánchez et al.*, 2020]. WACCM-Ca was the preferred comparison for WACCM-Al, as both metals are highly refractory. They also have similar abundances, with a chondritic and ablation ratios of Ca:Al of 1.4:1 [*Lodders*

and Fegley, 2011] and 0.9:1 [*Carrillo-Sánchez et al.*, 2020], respectively. Details of the reaction list for Ni and Al are discussed later in Chapters 5 & 6.

The modelled neutral and ion profiles of Ni and Al were then compared to observational data. For the neutral metals, all data was taken from the lidar soundings at Kühlungsborn (54°N), which were discussed earlier in this chapter. Therefore, the modelled output that was analysed was focused at 54^{o} N. Further analysis was done for output at the Arecibo and Beijing locations as both are in the process of executing or developing the infrastructure for lidar soundings for Ni.

For the ion observations, mass spectrometry data was collected from 8 rocket flights detailed in Table 2.2 below:

Table 2.2: The 8 rocket flights used for metal ion measurements.

Payload	Location	Latitude	Date & Time (UTC)	Reference
Ue06	Wallops Islands, USA	37.8^{o}N	12/08/1976 16:58	[*Herrmann et al.*, 1978]
Ue08	Wallops Islands, USA	37.8^{o}N	01/01/1977 19:03	[*Meister et al.*, 1977]
S261	Kiruna, Sweden	68^{o}N	30/07/1978 00:32	*[Kopp et al., 1985b]*
S262	Kiruna, Sweden	68^{o}N	13/08/1978 00:38	*[Kopp et al., 1985b]*
Ue20	Red Lake, Canada	51^{o}N	25/02/1979 11:44	*[Kopp and Herrmann, 1984]*
Ue21	Red Lake, Canada	51^{o}N	27/02/1979 11:50	[*Kopp*, 1997]
Ue10	Kiruna, Sweden	68^{o}N	16/11/1980 03:50	[*Kopp et al.*, 1985a]

Ue09	Kiruna, Sweden	68°N	30/11/1980 00:44	[*Kopp et al.*, 1985a]

There were ~150 text files for flight with masses ranging from 14 to 176 a.m.u. Each text file had a list of altitudes and masses but the altitudes were not evenly spaced between each other and don't match from file to file. Therefore an R script was used to extract the data corresponding to the masses needed (m/z – Al: 27; Fe: 56; Ni: 58) and to interpolate the data gaps so they could be compared with each other. The geometric mean and standard deviation was then calculated for each density and Fe^+:Al^+/Fe^+:Ni^+ ratios were determined for comparison with WACCM output. Flights were initially compared individually to identify and remove any outlining dataset that would affect the overall average.

Running the model

To initiate a model run, a case was first setup using the using the MobaXterm terminal software. A number of parameters were edited before the case was configured and the job was built: reaction list source mods; number of cores required for the run; length of the model (days, months, years) and the recorded timestamp lengths; whether the run was nudged or free-running.

Once the job was successfully built, it was then submitted to High Performance Computing resource cluster in the University of Leeds known as the Advanced Research Computing (ARC) cluster. The second iteration, ARC2 was used from 2017-2019 and was followed by ARC3 from 2019 onwards. For the majority of model runs, any errors present would lead to a

crash of the run at the building stage before submission. Free-running global climate models were allowed to freely develop atmospheric structures as they are not constrained but take longer to run. The first few days in the run would then be dedicated to the growth of the species before useable data was recorded. This was to reduce the risk of crashing the model while it was in the preliminary stage of development. Later the model runs could be nudged by starting from an initialization file making use of all the data in the model run from day 1. *Nudging*, which is also known as *Newtonian relaxation*, is a form of data assimilation that allows adjustment to the dynamical variables of free running Global Climate Models. The use of nudging gave a more realistic representation of the atmosphere at a specific time as they can align a climate model to real meteorology to compare with observations [*Feng et al.*, 2013; *Smith et al.*, 2017].

GEOV [*NCAR*, 2020] was used for immediate viewing of WACCM output as data did not need to be extracted from the server. However, its functionality was limited to plotting only the variables output from the model and plotted pressure on the y-axis rather than altitude. For offline analysis, Panoply (Version 4.11.2) [*Schmunk*, 2020] was used. Unfortunately, the program was only capable of reading one NETCDF4 (Network Commom Data Form) file at a time, therefore the files required concatenation before been opened. A script in the IDL language (Interactive Data Language) was created for this task and to specifically extract the variables wanted from the WACCM run, since the output ranged from CO_2 concentration to e density. The script also included a function to convert the atmospheric pressure output into altitude in km so it could be plotted against rocket and lidar data.

3 The neutral and ion kinetics of Al

The only observed Al species in Earth's upper atmosphere have been Al^+ ions by rocket borne mass spectrometry, with a neutral Al layer yet to be quantified. Therefore, a catalogue of neutral and ion-molecule Al reactions required measurement, similar to those used in WACCM-Ca [*Plane et al.*, 2018b] and WACCM-Fe [*Feng et al.*, 2013], if an Al iteration of WACCM is to be developed to simulate the potential densities of Al, AlO and Al^+. In this chapter, the neutral kinetics for Al + O_2 are examined along with the absorption cross section of AlO (the energetics of R3.1 – R3.12 were calculated using CBS-QB3 theory [*Frisch et al.*, 2016]):

$Al + O_2 \rightarrow AlO + O$ $\quad \Delta H^o = -14 \pm 9$ kJ mol^{-1} (R3.1)

$AlO + AlO \rightarrow Al_2O + O$ $\quad \Delta H^o = -81$ kJ mol^{-1} (R3.2a)

$AlO + AlO + M \rightarrow Al_2O_2 + M$ $\quad \Delta H^o = -516$ kJ mol^{-1} (R3.2b)

Probable reactions of Al^+ and AlO^+, in the Mesosphere Lower Thermosphere (MLT) were also investigated:

$Al^+ + O_3 \rightarrow AlO^+ + O_2$ $\quad \Delta H^o = -17$ kJ mol^{-1} (R3.3)

$Al^+ + N_2 + M \rightarrow Al{\cdot}N_2^+ + M$ $\quad \Delta H^o = -19$ kJ mol^{-1} (R3.4)

$Al^+ + O_2 + M \rightarrow Al.O_2^+ + M$ $\quad \Delta H^o = -12$ kJ mol^{-1} (R3.5)

$Al^+ + CO_2 + M \rightarrow Al{\cdot}CO_2^+ + M$ $\quad \Delta H^o = -45$ kJ mol^{-1} (R3.6)

$Al^+ + H_2O + M \rightarrow Al{\cdot}H_2O^+ + M$ $\quad \Delta H^o = -111$ kJ mol^{-1} (R3.7)

$AlO^+ + O \rightarrow Al^+ + O_2$ $\Delta H^o = -17$ kJ mol^{-1} (R3.8)

$AlO^+ + CO \rightarrow Al^+ + CO_2$ $\Delta H^o = -17$ kJ mol^{-1} (R3.9)

$AlO^+ + O_3 \rightarrow Al^+ + 2O_2$ $\Delta H^o = -226$ kJ mol^{-1} (R3.10a)

$AlO_2^+ + O_2$ $\Delta H^o = -273$ kJ mol^{-1} (R3.10b)

$AlO^+ + H_2O \rightarrow AlOH^+ + OH$ $\Delta H^o = -65$ kJ mol^{-1} (R3.11)

$AlO^+ + O_2 \rightarrow AlO_3^+$ (R3.12)

A similar set of reactions measured for Al^+ were also applied to the neutral Al atom. Those were measured by Dr. Thomas Mangan. All electronic structure calculations (CBS-QB3 theory [*Frisch et al.*, 2016]) along with Rice-Ramsperger-Kassell-Markus (RRKM) theory [*De Avillez Pereira et al.*, 1997] were carried out by Prof. John Plane. Work involving the PGOPHER spectroscopy program was performed by Dr. James Brooke.

3.1 Neutral kinetics and cross section of Al + O_2

Before observations of neutral Al could be attempted in the MLT, it was important to understand what species were likely to be present (e.g. Al, AlO, AlOH). The following section presents the kinetics of Al reacting with O_2 using both the Laser Induced Fluorescence (LIF) and Atomic Resonance Absorption Spectroscopy (ARAS) techniques, which measured the growth of AlO molecules and the decay of Al atoms, respectively. R1 has been measured previously [*Fontijn et al.*, 1977; *Garland and Nelson*, 1992; *Le Picard et al.*, 1997]. The three measurements indicate a rate coefficient between 1.7×10^{-10} cm^3 molecule^{-1} s^{-1} to 3.2×10^{-10} cm^3 molecule^{-1} s^{-1}. Since the rate of

formation of AlO is fast, the species is potentially more abundant than Al in the upper atmosphere, in contrast to previously measured metals and their oxides in the MLT (e.g. Fe, Ca, Na). Therefore, it was necessary to know the cross section of the resonance band of AlO if ground-based lidar operations were to take place. For the Al + O_2 experiments (experimental details in chapter 2), the contact time was fixed and the change in concentration of O_2 yielded both the growth and decay profiles by LIF and ARAS, respectively. The contact time for each experiment was adjusted by placing the sliding injector at different contact lengths between the ablation cell and the spectroscopic cell. The signal intensity for each concentration was calculated by taking a mean of recorded points (15-20 points). The mean intensities of AlO production were then referenced to the chamber conditions during the specific measurement (flows, pressure, etc.) to calculate the O_2 concentration. The AlO profile was then plotted against [O_2] multiplied by the contact time (molecule cm^{-3} s) to retrieve the growth rate (k_{growth}) (Figure 3.1 is one example of a LIF measured AlO signal growth):

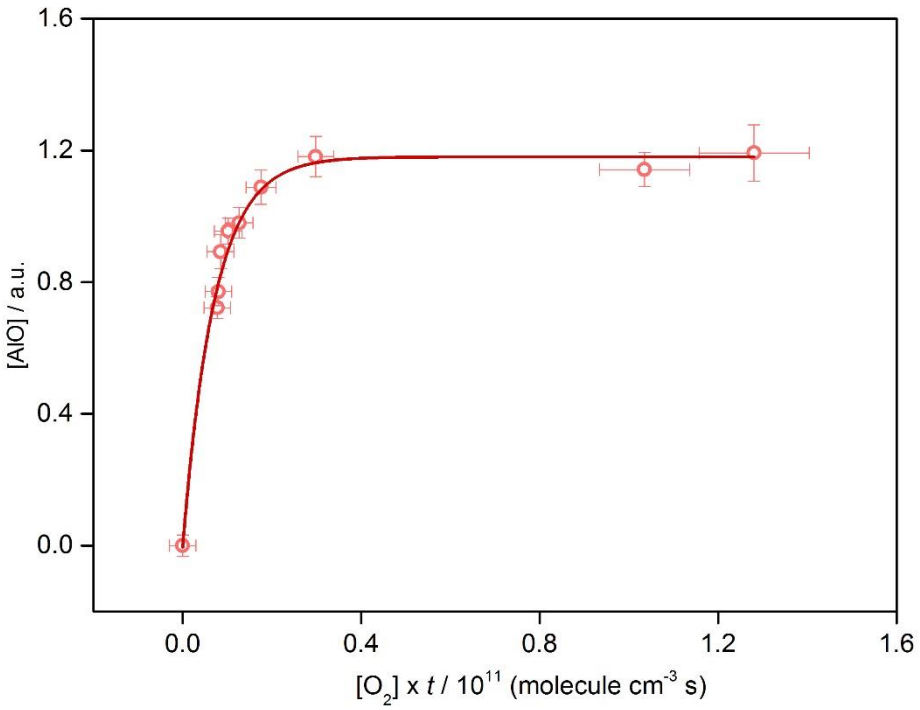

Figure 3.1: A LIF profile of AlO growth, where the LIF intensity was plotted against the O_2 concentration multiplied by a fixed reaction time of 3.4 ms (molecule cm^{-3} s). The growth was fitted with a 'monomolecular' exponential model to measure the rate constant.

The contact length was set to x = 10 cm, giving a reaction time between ablation and O_2 injection of 3.4 ms at 0.8 Torr and a total flow of 3 slm. The profile of Figure 3.1 shows a clear exponential growth and could be fitted with the following exponential 'monomolecular' growth model (Matlab) to give k_{growth}:

$$[AlO] = [Al](1 - \exp(-k^*([O_2]-x_c)) \quad \text{(E3.1)}$$

where [AlO] and [Al] represent the concentrations at the detection region and x_c is the concentration. This fit was not applicable at all fixed lengths. If the O_2

was injected too soon, the AlO species would reside in the flow tube for longer, allowing for further reactions to occur and the LIF signal to decrease. A similar pattern was also observed for higher O_2 concentrations.

3.1.1 Further reactions of AlO with O_2

LIF Growth and decay

To account for further product formation in the flow tube and therefore loss of AlO, the model fit was modified to a bi-exponential expression with psuedo-first order growth and decay terms:

$$[AlO] = [Al] (\exp(-k'_{AlO\ decay} [O_2] - \exp(-k'_{AlO\ growth} [O_2])) \quad \text{(E3.2)}$$

For this fit, it was assumed that Al and AlO showed a similar diffusion rate in N_2. The diffusion rate of Al was measured separately and was of the order of 300 s^{-1} at 0.8 Torr.

For the AlO datasets showing decay, only the first section of the decay was included in the fits. The reason for this was that the whole trace did not exhibit single exponential behaviour as indicated in equation (I). With only the first section taken into the account, the k_{decay} was set to 0 and the bi-exponential expression of E3.2 was simplified back to the monomolecular growth model (equation 3.1). Figure 3.2 shows the fitted AlO growth:

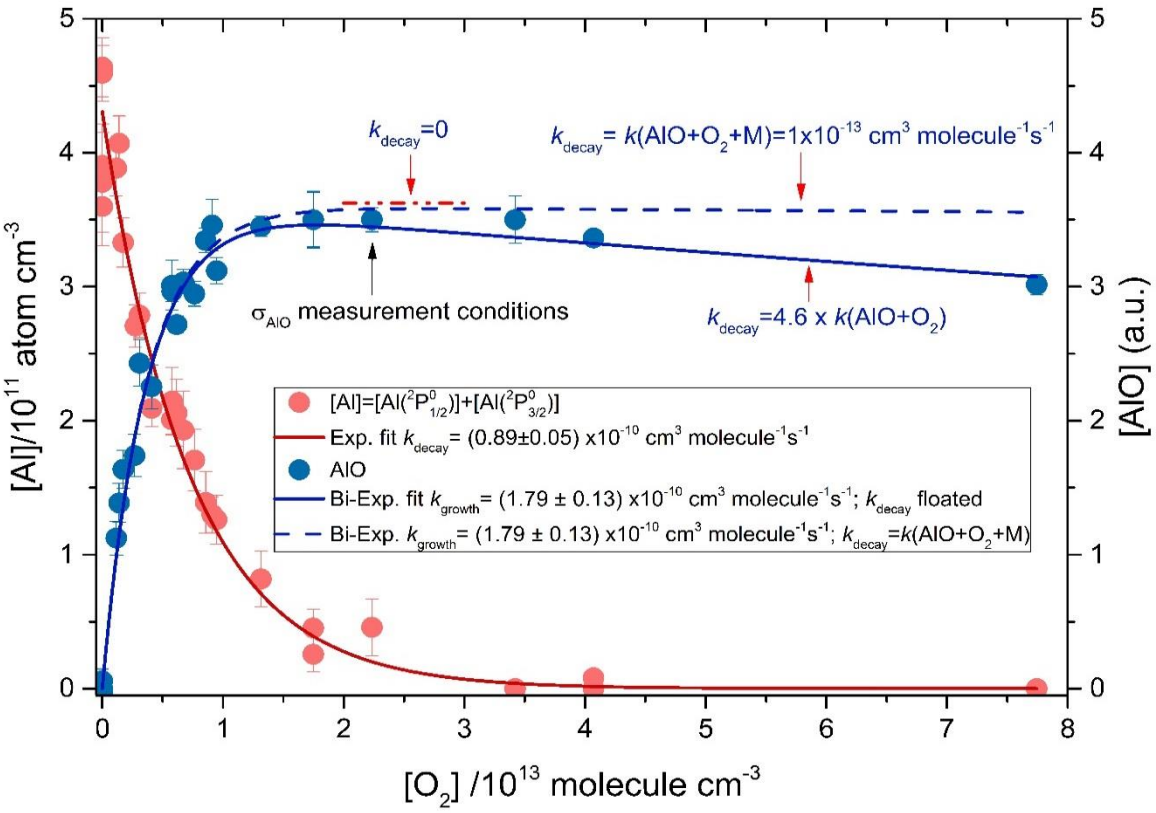

Figure 3.2: Rate plots of the Al decay (red line) and the AlO growths (blue line) for increasing O_2 concentration at a fixed contact time of 1.5 ms. The plot shows the subsequent Al and AlO atom concentrations (cm^{-3}) against O_2 concentration (molecule cm^{-3}). The AlO LIF signal is faster than the Al decay rate, as the former is measured at the well mixed centre point of the laminar flow, whereas the latter covers a larger area and thus includes unreacted Al atoms. The solid blue line shows the bi-exponential fit of the AlO decay whereas the red dashed line follows the same fit but with k_{decay} = 0. The dashed blue line is an evaluation of the bi-exponential expression, using the estimated AlO decay rate constant of AlO + O_2 at 0.8 [*Belyung and Fontijn*, 1995]

The AlO growth rate constant was then determined by linear regression of the growth rates against the contact time *t*, as shown in E3.3:

$$k' = k_1 \times t + c \qquad \text{(E3.3)}$$

The contact time was calculated from the injection distance, flow and pressure, and accounts for parabolic flow correction in the flow tube. The calculated contact times were in close agreement (within 5%) with the observed flight time of the Al and AlO pulses between ablation and detection in spectroscopic cell. The LIF plot of k'_{growth} vs *t* (blue symbols) is illustrated in Figure 3.4. Applying the linear fit (blue line) showed that the line goes through the origin, within error, and has a slope of $k_1 = (1.73 \pm 0.26) \times 10^{-10}$ cm^3 $molecule^{-1}$ s^{-1}.

With the LIF rate constant now measured, the decay of the LIF signal required investigation. Figure 4.3 below shows each experimental run that had a trace of AlO decay against increasing O_2 concentration at different contact times. The AlO dataset has been scaled to the Al concentration, which was determined by ARAS (further details below), and have been multiplied by the average correction factor for the laminar flow parabolic profile (0.63) [*Gómez Martín et al.*, 2016]. This was because the it is the AlO at the core of the laminar flow which is detected by the LIF laser. The solid line fits in Figure 3.3 show the numerical solutions of the system of differential equations (zero-dimensional) from a kinetic model [*Gómez Martín et al.*, 2016; *Gómez Martín and Plane*, 2011], through which “X” (See equations in Figure 3.3) can be defined as a species in excess over AlO. O_2 can react with AlO, illustrated in R3.13 below. The electronic structure calculations carried out for each reaction were done at the CBS-QB3 level of theory [*Frisch et al.*, 2016]:

$AlO + O_2 + M \rightarrow AlO_3 + M$ $\Delta H = -217.8$ kJ mol^{-1} (R3.13)

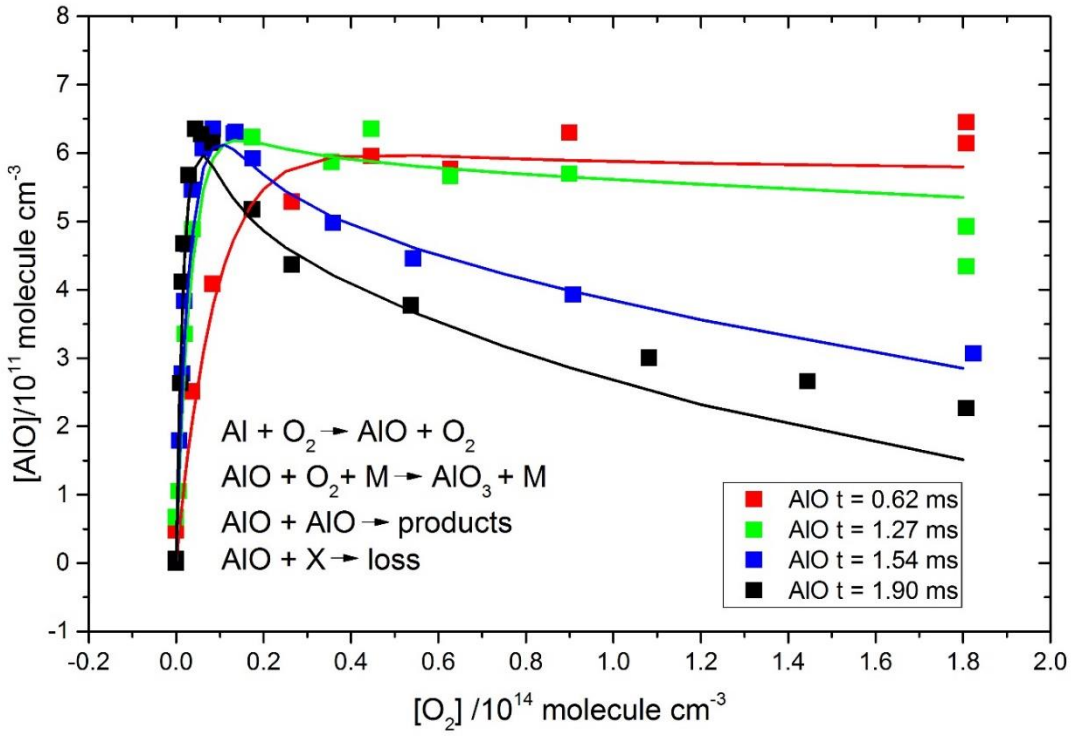

Figure 3.3: Measurements of AlO decay for increasing O_2 concentrations at varying contact times, showing the AlO density (molecule cm^{-3}) against the O_2 concentration (molecule cm^{-3}). At longer contact times, the decay of the AlO signal was more pronounced.

The rate constant for R14 at 0.8 Torr and 298 K had been determined by *Belyung and Fontijn* [1995] using the Troe expression to be $k_2 = 1\times10^{-13}$ cm^3 molecule^{-1} s^{-1} (indicated in Figure 3.3). Comparing this to the observed removal of AlO in Figure 3.3 above, it is apparent that this rate constant does not account for the total removal of AlO. The observed rates are contact time dependent, with the decay more pronounced at longer times. Another possibility relates to the X (Figure 3.3) variable, suggestive that it could be an

impurity in the introduced O_2 supply. However, the gas lines were leak tested, the O_2 supply was UHP and there was no measurable evidence of an impurity detected from the mass spectra measured. To validate this, X should be of the same order as O_2 but the sum of several higher aluminium oxides does not account for the fast removal. Therefore, an AlO self-reaction was considered (see R2a and R2b above). Both R2a and R2b are energetically favourable, with the third body reaction being highly exothermic. However, Al_2O_2 was not measured in the mass spectrometer but the Al_2O product was detected at m/z 70, which suggests that R2a is the dominant pathway. Investigation of the potential energy surface of the AlO self-reaction (using CBS-QB3 theory) [*Frisch et al.*, 2016] was made, with no energy barrier found between the linear AlO dimer and the Al-O-Al + O exit channel. Therefore, both R2a and R2b could be addressed together as they ultimately result in the same product. An assumed rate constant of ~ 3×10^{-10} cm^3 $molecule^{-1}$ s^{-1} was applied to the combined reactions, which can explain the AlO decays observed for $[O_2] < 5 \times 10^{13}$ molecule cm^{-3}. For larger O_2 concentrations, however, this value was not sufficient, so a secondary AlO loss process needed consideration. Species clustering was considered as suggested in the mass spectra, where a m/z 97 peak was observed, potentially indicative of Al_3O^+. The clusters may be initiated by the AlO self-reaction and therefore need a longer contact time. However, insufficient evidence was available to support this theory.

Al decay – Atomic Resonance Absorption Spectroscopy

By applying the same data treatment to the ARAS data that was used to plot the LIF intensities, , the calculated k'_{decay} for each contact time was found to

be significantly slower than the LIF counterpart. Figure 3.3 above gives an example of the Al atom decay corresponding to opposing AlO growth. For suitable comparison, the column density measured by absorbance across the flow tube was scaled to concentration using the flow tube diameter. Although the Al decays appear to be well fitted by single exponential decays, the decay constants are a factor of 2 smaller than the corresponding AlO growth constants. This difference relates to the radiation from the Al Hallow Cathode Lamp (HCL) passing through the laminar flow profile. The Al absorption from the HCL lamp samples a large area of the spectroscopic cell and averages the Al concentration at the core and outer laminae of the flow, where unreacted Al resides due to lower O_2 concentration. In contrast, the focused beam of the LIF laser collects fluorescence at the core of the laminar flow, where adequate mixing between Al and O_2 has been achieved after injection, leaving the AlO growth rate unaffected by diffusion.

To resolve this issue, the ARAS data was analysed by equating the observed relative absorptions $(I_0\text{-}I)/I_0$ to the difference of integrated absorption and emission lines profiles, where the exponential dependence of the absorption coefficient was approximated through use of a Taylor series [*Laimer et al.*, 1996; *Laimer et al.*, 1995; *Spietz et al.*, 2001]. The temperature of the emission lamp and detector were important for the correction as this determines the level of broadening of the emitted radiation and the absorption losses at the detector. The ratio between the temperature of absorption and emission is λ, illustrated in E3.4:

$$\gamma = \frac{T_A}{T_E} \qquad \text{(E3.4)}$$

A 1-D box model was created relating the observed relative absorptions at varying λ against the Al column density (L x [Al] in cm^{-2}) where L (~ 3.75 cm) is the optical path. This model then functioned as a reference table for the measured relative absorptions, whereby the absorption intensities are computed into the model to a corresponding γ to retrieve the Al column density. The Doppler temperature of the Al HCL was assumed to be of the order of 600 K (γ = 2), as indicated in previous studies [*L'Vov et al.*, 1976; *Wagenaar et al.*, 1974].

Weighted average rate constant

With the ARAS temperature correction applied, the resulting column density values can be plotted against [O_2] to obtain the Al decay rate (k_{decay}). The individual decay rates from each experiment were then plotted against contact time, as indicated in Figure 3.4 below (red points). Applying the linear regression fit (Equation III) to the plotted points gave a measured rate constant $k_{4.1}$ = (1.63 ± 0.22) × 10^{-10} cm^3 $molecule^{-1}$ s^{-1}, very close to the measured rate constant for the LIF kinetics of AlO growth (blue points of Figure 3.4) of (1.73 ± 0.26) × 10^{-10} cm^3 $molecule^{-1}$ s^{-1}. However, the intercept for the Al decay was 0.75 ms. This result reflects the mixing time of O_2 in the laminar flow to the walls, as discussed above. Hence, the radial diffusion time of O_2 is of the same order as the contact time. However, the k' vs t plot allowed for correction of the radial mixing and an average rate constant was calculated to be k_1(298 K) = (1.68 ± 0.24) × 10^{-10} cm^3 $molecule^{-1}$ s^{-1} using the LIF and ARAS datasets.

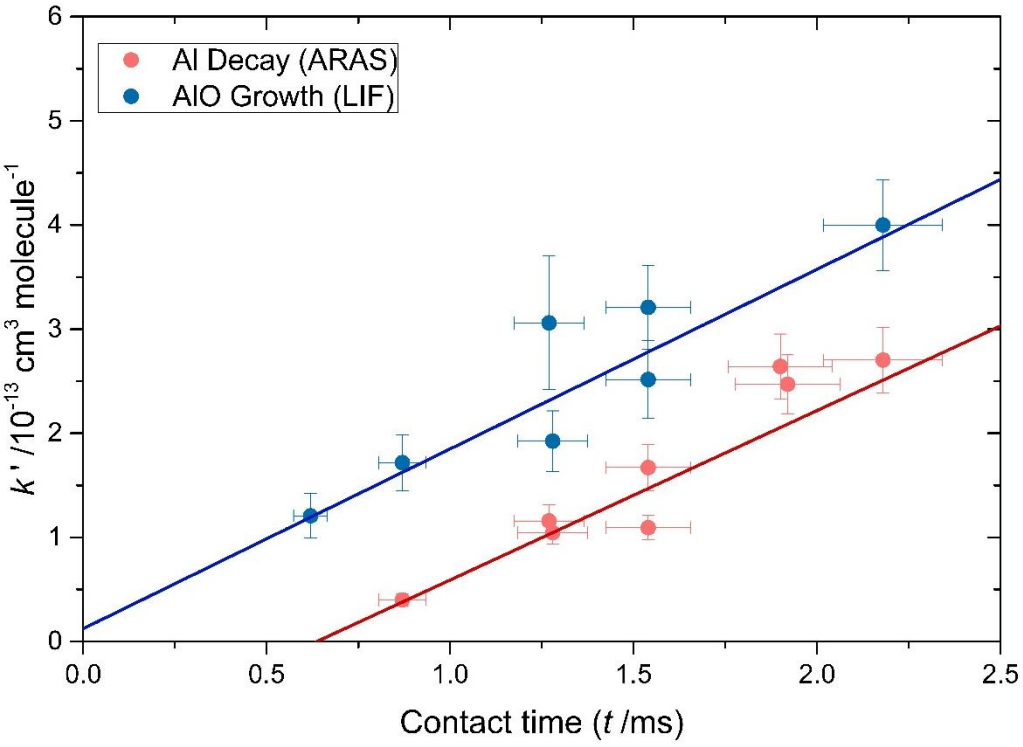

Figure 3.4: AlO growth rates (blue) and the Al decay rates (red). The individual points were derived from the LIF growth and ARAS decay plots in cm^3 $molecule^{-1}$ against contact time (ms). The LIF intercept is within the Origin but the non-zero of the Al scatterplot intercept is reflective of the radial mixing time of O_2 in the laminar flow.

3.1.2 Absorption cross section of AlO

With the kinetics completed, the next task was to measure an experimental cross section of AlO for use in future lidar observations. Resonance fluorescence of the AlO $B^2\Sigma^+ \leftarrow X^2\Sigma^+$ transition was recorded as a function of excitation laser wavelength, illustrated in Figure 3.5:

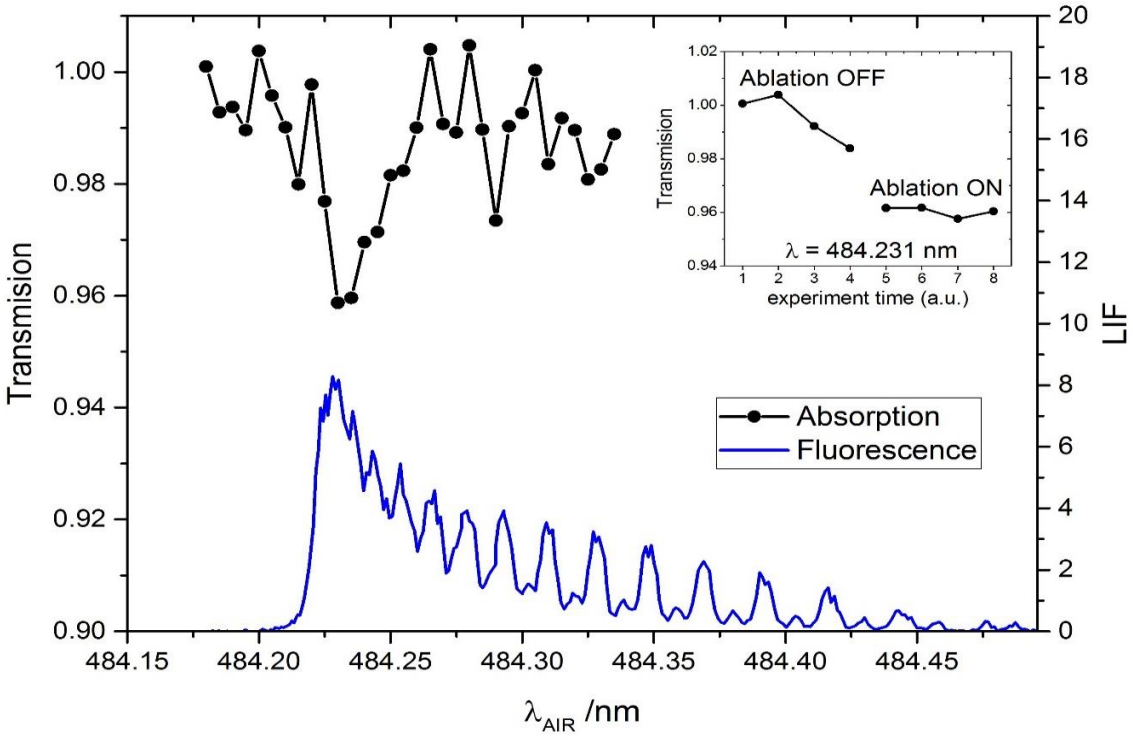

Figure 3.5: Absorption in flow tube as a function of wavelength around the band head of the B(0)-X(0) band of AlO with the reference LIF spectrum. The absorption insert in the top right corner shows the drop in transmitted intensity at the AlO fixed wavelength.

The fluorescence spectrum was also normalized to the measured dye efficiency and filter transmission curves. Since the measured spectrum was limited to a small range, the spectral efficiency of the PMT detector did not change significantly. The absorption spectrum (black line) in Figure 3.5 was measured under the same conditions as the absorption experiments indicated previously in Figure 3.3, with 5 laser passes through the flow tube to increase the absorption pathlength.

Eventually a measurable band was retrieved from the noise at the desired wavelength, with reference to the measured LIF spectrum and was recorded with sufficient signal-to-noise. To add more weight to these observations, further measurements were taken whereby the dye laser was fixed at the 0-0 bandhead and under continuous flow, the ablation laser was switched on and off to see if any observable change occurred. The observed change is shown in the top right corner of Figure 3.5. It was clear that the transmission intensity was unchanged (transmission = ~1) when the ablation laser was off, but when ablation commenced, the intensity decreased (transmission = 0.96), indicative of absorbing AlO.

To determine the absorption cross section of AlO, a modified Beer-Lambert Law was applied. Consideration of the near to stoichiometric conversion of Al into AlO gives E3.5:

$$\sigma_{AlO} = \frac{OD}{n\ x\ L\ x\ [AlO]} = \frac{\ln\left(\frac{I_o}{I}\right)}{n\ x\ L\ x\ [Al]\ x\ \phi} \qquad \text{(E3.5)}$$

where the optical density of AlO (OD) = ln (I_0/I), with I_0 and I as the laser intensities transmitted through the tube without and with AlO respectively, n represents the number of beam passes through the tube, $L \times [Al]$ is the column density of ground state Al atoms in the absence of O_2 measured by ARAS, and ϕ is a correction factor encompassing the AlO losses through reactions R2a,b and R14. It also accounted for the incomplete conversion of Al into AlO due to the slow diffusion of O_2 towards the outer area of the laminar flow. Through this method, the optical path length was the same for both species.

First, the column density of Al($^2P_{3/2}$) measured at 392.15 nm with no addition of O_2 and under the same conditions (flow, pressure) as the absorption

experiments, was calculated to be $L \times [\mathrm{Al}\ (^2P_{3/2})] = (8.0 \pm 1.4) \times 10^{11}$ atom cm^{-3}. The equilibrium populations of the Al ground state doublet (at 298 K) were of the order of the 0.46 for J=1/2 and 0.54 for J=3/2. Therefore, the $L \times [\mathrm{Al}]$ (where $L \times [\mathrm{Al}] = L \times [\mathrm{Al}\ (^2P_{1/2}) + \mathrm{Al}\ (^2P_{3/2})]$) was calculated to be $(1.47 \pm 0.25) \times 10^{12}$ atom cm^{-3}. The added uncertainty was to accommodate the scatter in the atomic absorption observations and the estimated Doppler temperature range (450 – 750 K). ϕ was calculated using the kinetics plots by estimating the fraction of Al in the absorption path that did not convert to AlO and the AlO loss by secondary processes, yielding a value of 0.76 ± 0.06. With OD at air wavelength (λ_{air} = 484.23 nm) = 0.037 ± 0.005 (as obtained from Figure 3.7) and constant path length, the absorption cross section for AlO $\sigma(\lambda_{air}$=484.23 nm) = $(6.7 \pm 1.6) \times 10^{-15}$ cm^2 $molecule^{-1}$ at 0.0027 nm resolution.

3.1.3 Modelled AlO spectra

Theoretical spectra of the 0-0 and 1-0 absorption bands were simulated using PGOPHER, a general purpose program for simulating and fitting molecular spectra [*Western*, 2016; 2017]. The resulting output was then compared with the observed measurements of the bands in figure 3.6 below, to investigate for correlation:

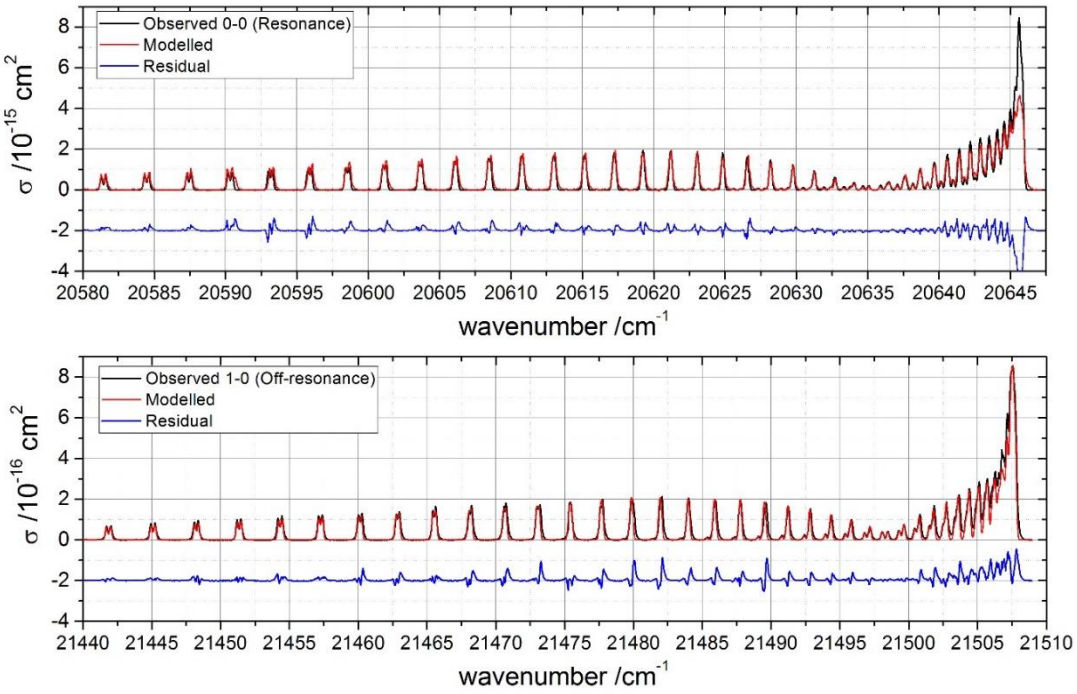

Figure 3.6: Cross section (cm^2 $molecule^{-1}$) against wavenumber (cm^{-1}) for the observable spectra of the 0-0 and 1-0 bands with their corresponding simulations from PGOPHER

The ideal match with the observed spectra was made by convolving the simulated spectra with a 0.18 cm^{-1} Gaussian, accounting for both pressure broadening and the spectral resolution. The residual component (blue line) represents the difference between both the modelled and the observed spectra. The trace features in the residual are the result of imprecision in calibration of the experimental wavelength and how a simple Gaussian function is limited in its description of pressure broadening. In terms of the cross section, the calculation for the bandhead of the 0-0 band was of the order of 8.5×10^{-15} cm^2 $molecule^{-1}$. This was in close agreement with the experimentally measured form of $(6.7 \pm 1.6) \times 10^{-15}$ cm^2 $molecule^{-1}$. The 0-0

bandhead of the measured LIF spectrum appears to be saturated compared to the modelled form (factor of 2 larger), but the rest of the resolved rotational lines outside the bandhead are simulated correctly. In contrast, the simulated 1-0 band (bottom of Figure 3.6) using PGOPHER fits very well with the measured spectra. Although there was a significant difference in the measured and simulated bandhead of the 0-0 band, the very good agreement with the relative intensities of 1-0 band shows the extensive capability of PGOPHER in generating spectra for molecular species.

Further analysis with PGOPHER was performed to estimate the change in the rotational level populations in relation to temperature. Figure 3.7 below shows the simulated spectra of the B(0) ← X(0) band of AlO at two temperatures, 298 and 200 K.

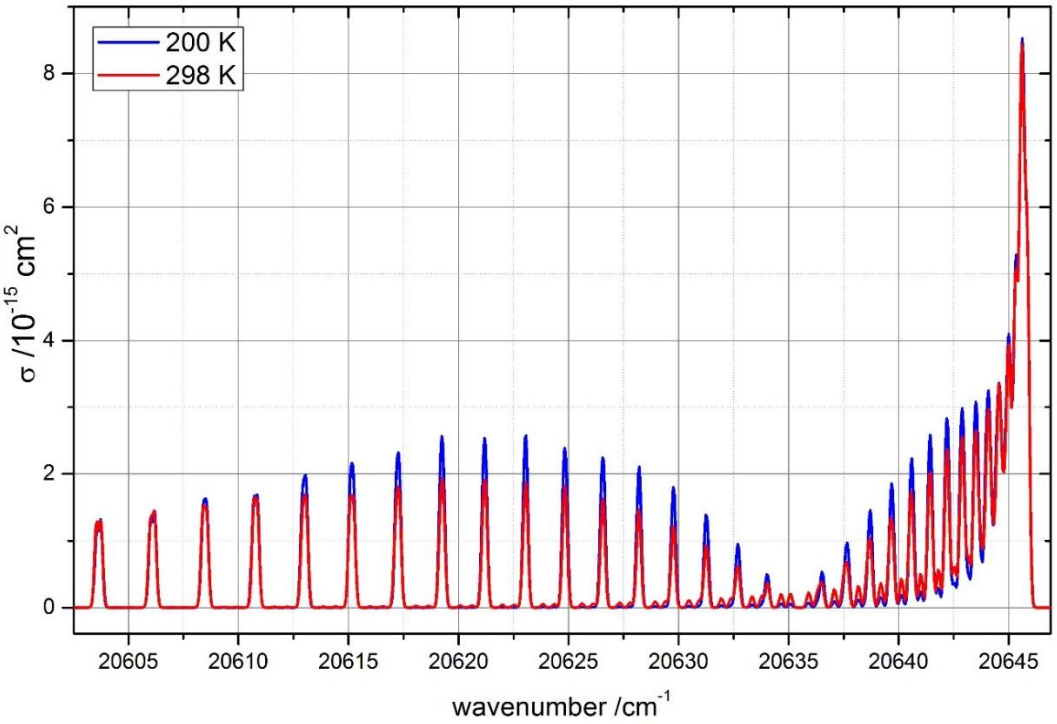

Figure 3.7: Cross section (cm^2 $molecule^{-1}$) against wavenumber (cm^{-1}) for simulated spectra of the B(0) ← X(0) band of AlO at 200 and 298 K

It was clear that there was a change in population of the rotational levels at the different temperatures. This is due to the higher population densities occupying the lower J levels at lower temperatures (as expected from the Boltzmann distribution), and thus the peak branch transitions at lower J levels are larger. In contrast to the rest of the spectra, the cross section at the bandhead does not change much. This is because of the turn-over of the R branch which occurs around J = 15, where de-population of higher J levels compensates for the populations of lower levels as well as the heavy band overlap contributing to minimize the spectral effect of changing populations [*Kraus et al.*, 2002]. This is convenient for the atmospheric retrieval of absolute AlO densities, since the low temperatures of the MLT (< 220 K) should not interfere with observed intensity at the band-head.

3.2 Kinetics of Al^+ and AlO^+

Laser ablation of an Al rod using a 532 nm laser (discussed earlier in this chapter) produces Al atoms and Al^+ ions. The kinetics of Al+ and AlO+ were measured using the Ion-Fast flow tube/Quadrupole Mass Spectrometry technique described in Section 2.1.3. One concern is that if metastable excited states of Al^+ were produced and were sufficiently long-lived, they would potentially interfere with the kinetic measurements (and would also be recorded by the mass spectrometer at m/z 27). The metastable state that would potentially be most problematic is the $Al^+(3^3P)$ state, which is 4.64 eV above the $Al^+(3^1S)$ ground state. However, the radiative lifetime of the excited state is 304 μs (0.3 ms) [*Kramida et al.*, 2018]. This was more than an order

of magnitude shorter than the flow time from the metal rod where ablation occurs to the point where the other reactants are injected into the flow tube, which ranged from 5 – 40 ms, depending on total flow and reaction distance. Therefore, by the time the other reactants entered the flow tube, all the Al^+ in the higher metastable state would have radiated or been quenched to the ground state $Al^+(^1S)$.

The kinetics measurements of Al^+ were made by adjusting the injector length in the flow tube, which allowed reactants to be injected between 11 and 43 cm upstream of the skimmer cone of the mass spectrometer. The AlO^+ kinetics was measured at fixed contact lengths with varied concentration of the reactant (CO, O_3 etc). The loss of Al^+ by R3.3 – R3.7 was described by a pseudo first-order decay coefficient, *k'*, since the concentrations of the reactants, as well as the carrier gas in the case of R3.4 – R3.7, were in large excess of the Al^+ concentration. The diffusional loss of Al^+ to the flow tube walls, $k_{\mathrm{diff,Al^+}}$, was also first-order. Therefore, the total removal of Al^+ when studying R3.3 is given by E3.6:

$$k'_{total} = \left(k_{\mathrm{diff,Al^+}} + k_3[\mathrm{O_3}] + k_5[\mathrm{O_2}][\mathrm{M}]\right) \qquad \text{(E3.6)}$$

and for R3.4 to R3.7:

$$k'_{total} = \left(k_{\mathrm{diff,Al^+}} + k_{\mathrm{X}}[\mathrm{X}]\right) \qquad \text{(E3.7)}$$

where k_X represented the pressure-dependent rate coefficient for the recombination of Al^+ with X = N_2, O_2, CO_2 or H_2O. Equation (VI) accounts for the recombination of Al^+ with O_2 since this species was always present in the O_3 flow. However, in this case k_5 was extremely slow (see below) and so in

practice could be ignored. In the absence of reactants, Al^+ concentration at the skimmer cone, $[Al^+]_0^t$, was given by:

$$ln[Al^+]_0^t = ln[Al^+]^{t=0} - t.k_{diff,Al^+} \quad \text{(E3.8)}$$

where $[Al^+]_X^{t=0}$ was the Al^+ concentration up until the injection point of reagent X, a flow time *t* upstream of the skimmer cone. When reactant X was added to the flow tube, the Al^+ density at the skimmer cone was then given by:

$$ln[Al^+]_X^t = ln[Al^+]^{t=0} - t\left(k_{diff,Al^+} + k_X[X]\right) \quad \text{(E3.9)}$$

Subtracting E3.8 from E3.9 generates an expression for *k′* which describes the reactive loss of Al^+ only:

$$k' = k_X[X] = \frac{ln\left(\frac{[Al^+]_X^t}{[Al^+]_0^t}\right)}{t} \quad \text{(E3.10)}$$

The main advantage of using E3.10 is that the diffusion rate of Al^+ was not required to obtain *k′*. Note that the flow times *t* referred to below have been corrected for the parabolic velocity profile in the flow tube [*Brown*, 1978]. The velocity along the axis of the flow tube, which was where the ions were sampled, was 1.6 times the uniform plug flow velocity – confirmed in the present experiment by measuring the arrival time of the pulse at the skimmer cone, shown in Figure 3.8 below.

3.2.1 Diffusion of Al^+

Before the kinetics of reactions of R3 - R12 were measured, the diffusional loss of Al^+ to the walls of the flow tube was determined. Figure 3.8 below shows a series of Al^+ pulses detected by the mass spectrometer at different

flight times. This was done by varying the flow times but maintaining constant pressure.

Note that the time in the x-axis of Figure 3.8 was between 30 – 70 ms, which is different to the reaction times of the experiment (5 – 40 ms). The time difference accounts for the distance from the ablation source to the skimmer cone, which is longer than the reaction time which started from the point of injection of the reagent to mass spectrometer. The flight time was dependent on the flow velocity. At the longer flight times, the pulse widths would increase due to axial diffusion, and the pulse height and integrated area of the ion pulses decreased due to radial diffusion and loss on the flow tube walls. Applying a log-plot of the integrated pulse area against flight time gives a linear trend (Figure 3.8) with a measured slope equal to the first-order loss on the flow tube walls, $k_{\text{diff,Al}^+}$. This was then applied to the diffusion coefficient of Al^+ in He by the expression for diffusion out of a cylinder [*Crank*, 1986]:

$$D_{Al^+-He} \geq k_{\text{diff},Al^+} P \frac{r^2}{5.81} \qquad \text{(E3.11)}$$

where *P* was the pressure of the flow tube and *r* was the radius of the tube. The inequality applies if the metal ion was not removed with 100% collision efficiency with the flow tube walls. The value for D_{Al^+-He} was ≥ 146 Torr cm^2 s^{-1} using E3.11. For comparison, D_{Al^+-He} was also estimated to be 221 Torr cm^2 s^{-1} at 298 K from the following E3.12 [*Rees*, 1989]:

$$D_{Al^+-He} = \frac{k_B T}{2.21\, n\pi\mu} \sqrt{\frac{\mu}{\alpha e^2}} \qquad \text{(E3.12)}$$

where *n* is the concentration of He, k_B is the Boltzmann constant, μ is the reduced mass of the Al^+ -He collision, α the polarizability of He (0.205 Å^3) and *e* the elemental charge. The experimental lower limit was close to this

estimate, indicative of efficient removal on the electrically earthed flow tube walls. Over time the probability of removal may become reduced due to coating of the flow tube walls with a partially insulting metal oxide layer.

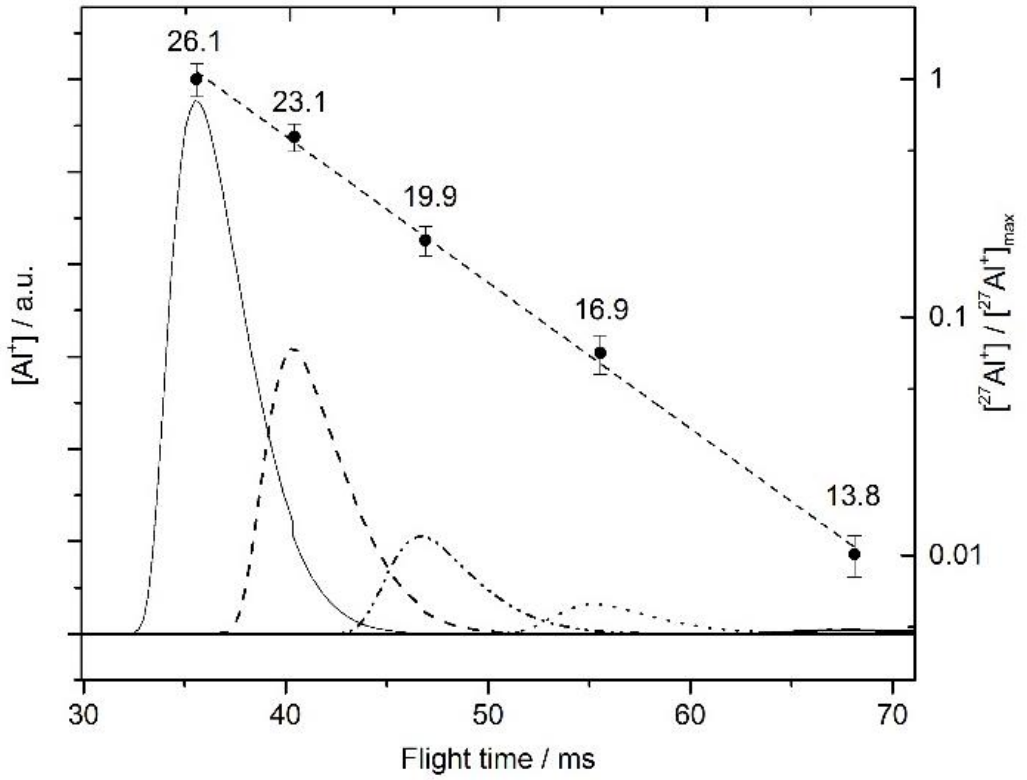

Figure 3.8: Al^+ ion pulses (left-hand axis) in arbitrary units against flight time in ms, altered for five different flow velocities (shown as numbers above each peak, each number in m s^{-1}) at 3 Torr pressure of He. Each point represents the ratio of each pulse area to that of the largest pulse area measured in the plot at 26 m s^{-1} (right-hand log scale). The line was a linear regression fit through the points. The 1σ error bars were determined from recording 3 repeated measurements at same flow.

3.2.2 $Al^+ + O_3$

The solid circle data-points in figure 3.9 were the initial measurement of R3 with $k_3 = (1.6 \pm 0.9) \times 10^{-10}$ cm^3 $molecule^{-1}$ s^{-1}. However, the linear regression line through these points did not pass through the origin as shown by equation (X). This was the result of a reaction between AlO^+ and O_3 which recycles AlO^+ to Al^+ (reaction R10a), and thus hinders the overall removal of Al^+ at higher O_3 concentrations. This phenomenon has also been discussed recently for the analogous reaction $Fe^+ + O_3$ [*Melko et al.*, 2017]. The solution was addition of H_2O along with the O_3 to remove AlO^+ via reaction R11. This then inhibited recycling of AlO^+ to Al^+ through reaction R10a. Figure 3.10 shows the effect on *k'* with increasing H_2O concentration at three different fixed O_3 concentrations. *k'* initially increases with increased H_2O but reaches a plateau when more than ~2×10^{12} molecule cm^{-3} of H_2O was added to the flow tube. The measurement of k_1 as a function of $[O_3]$ was now repeated at a higher $[H_2O]$ fixed at 3.5×10^{12} cm^{-3}. The resulting *k'* values were plotted as the open triangle points shown in Figure 3.9. A regression fit through these points was reapplied and now passed through the origin as expected, yielding $k_1 = (1.4 \pm 0.1) \times 10^{-9}$ cm^3 $molecule^{-1}$ s^{-1}.

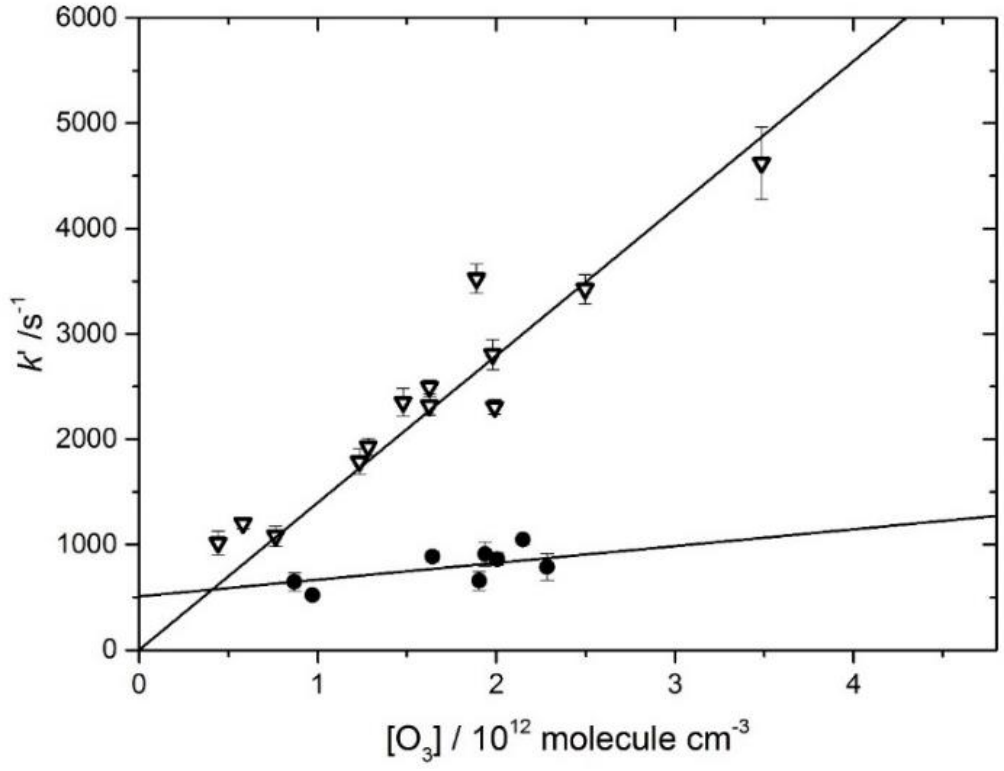

Figure 3.9. Plot of *k'* versus [O_3] for the study of R3. The data-points shown with open triangles were measured with a fixed [H_2O] at 3.5×10^{12} molecule cm^{-3}. The data-points depicted with solid circles are measured in the absence of H_2O. The effect of the addition of H_2O was shown by the intercept differences between the two fits, with the line fit without H_2O having a non-zero intercept. This was a result of a back reaction between AlO^+ and O_3 to retrieve Al^+.

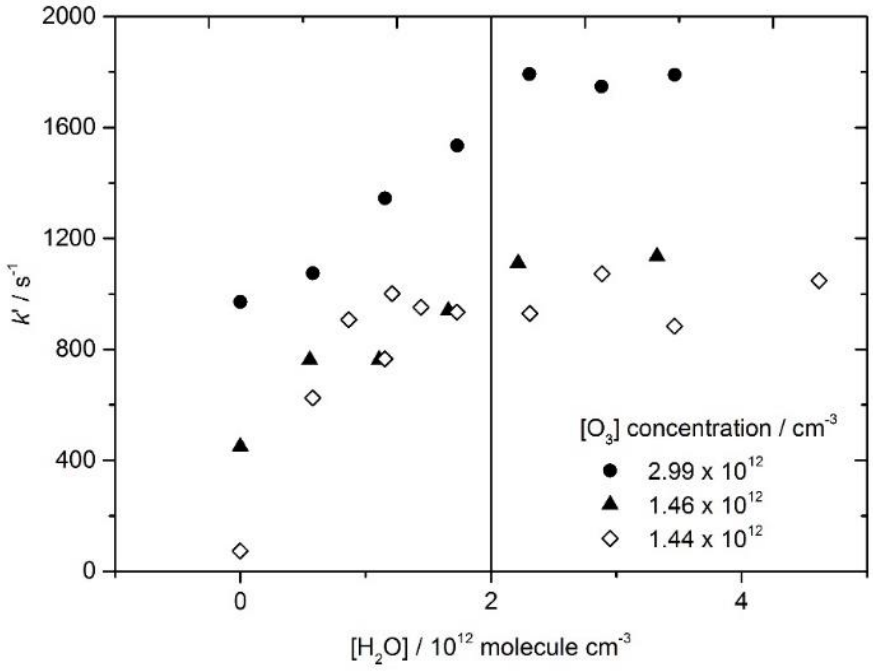

Figure 3.10. *k'* plotted against [H_2O] at three fixed [O_3] (see figure legend). The vertical line indicates the point (H_2O = 2 x 10^{12} molecule cm^{-3}) whereby R11 dominates R10a so that *k'* reaches a plateau and no longer increases with H_2O concentration. Therefore, for the final measurements of $Al^+ + O_3$, a concentration of 3.5 x 10^{12} molecule cm^{-3} was chosen as it was a safe margin after the plateau.

3.2.3 $Al^+ + CO_2$, N_2, O_2 and H_2O

Figure 3.11 shows plots of $ln\left(\frac{[Al^+]_X^t}{[Al^+]_0^t}\right)$ versus t (ms) at three different He pressures from 3 – 4 Torr for reaction R6. The plot fits were both linear and pass through the origin, as expected from equation (X). The measured slope of each plot gave the second-order recombination rate coefficient, k_{rec}, which showed an increasing relationship with pressure. R6 was measured at two

different temperatures (206 K and 293 K) and figure 3.12 shows the fitted slopes of k_{rec} versus [He] for R6 at each temperature. The calculated slopes of these plots gave rates of k_6 (206 K) = (1.5 ± 0.2) × 10^{-29} cm^6 $molecule^{-2}$ s^{-1} and k_6 (293 K) = (5.0 ± 0.6) × 10^{-30} cm^6 $molecule^{-2}$ s^{-1}.

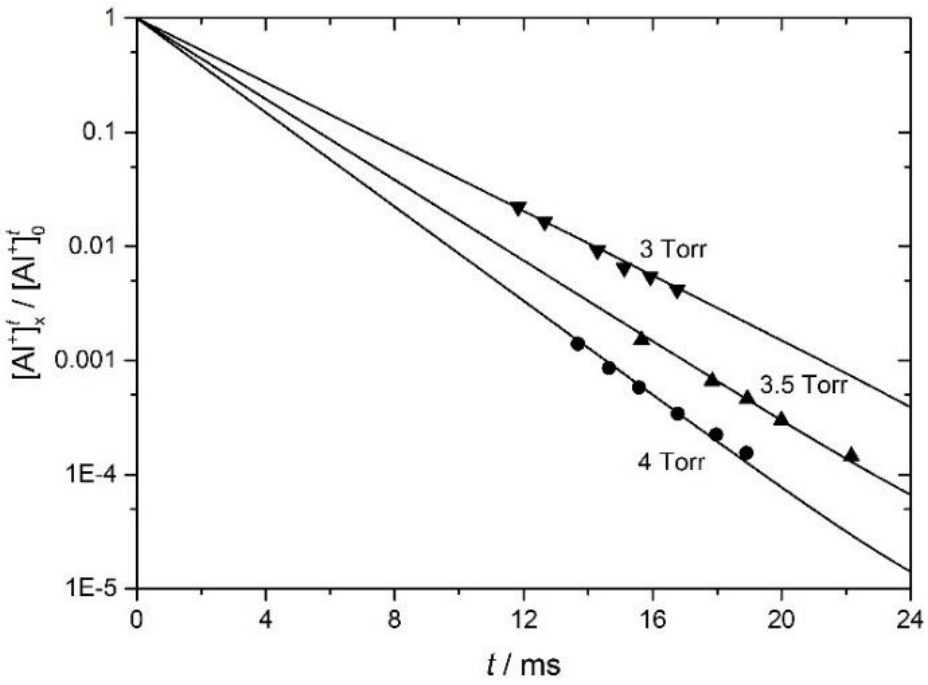

Figure 3.11. First-order decays of Al^+ in the presence of CO_2 (CO_2 concentration of 6.0 × 10^{14} molecule cm^{-3}) at 293 K, at three different pressures of He. The y-axis represented the signal ratio of reacted Al^+ to initial Al^+ against reaction time *t* (ms) in the x-axis.

The reaction of Al^+ + H_2O (R7) was only measured at 293K because of the hindrance of H_2O condensing on the flow tube walls at lower temperatures. As illustrated in Figure 3.12, R7 has the largest rate coefficient of the four recombination reactions, with k_7 (293 K) = (2.36 ± 0.32) × 10^{-29} cm^6 $molecule^{-2}$ s^{-1}. This trend with H_2O has been observed with previously measured metals.

The reaction of $Al^+ + N_2$ (R4) was very slow and could only be observed at 200 K giving k_4 (200 K) = (8.4 ± 0.9) × 10^{-32} cm^6 $molecule^{-2}$ s^{-1} removing the possibility of measuring an experimental temperature dependence for the reaction. The right-hand axis of figure 3.12 corresponds to R4 in this case. The reaction of $Al^+ + O_2$ (R5) was too slow to measure even at low temperatures, so an upper limit of k_5(205 K) < 2.8 × 10^{-32} cm^6 $molecule^{-2}$ s^{-1} was obtained from the experimental data. This was a marked contrast with previous measurements of metal ions with O_2, such as Fe^+ (8.3 x 10^{-30} $(T/300)^{-1.52}$ cm^3 $molecule^{-1}$ s^{-1}) [*Feng et al.*, 2013; *Vondrak et al.*, 2006] and Ca^+ (4.2 x $10^{-29}(T/200)^{-2.37}$ cm^3 $molecule^{-1}$ s^{-1}) [*Broadley et al.*, 2007; *Plane et al.*, 2018b].

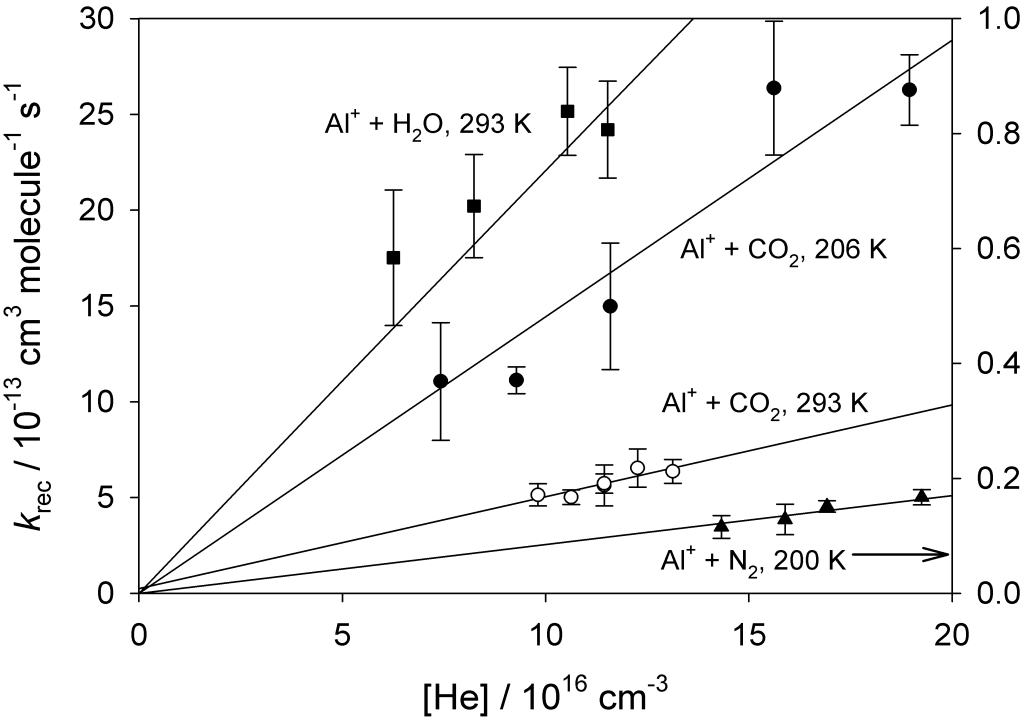

Figure 3.12. Second-order rate coefficients k_{rec} versus He concentration for the recombination of Al^+ with H_2O, CO_2 and N_2 (note the right-hand axis for the N_2 reaction). The rate of $Al^+ + N_2$ was notably slow at 200 K therefore no

temperature dependence was experimentally retrieved since reaction was not observed at 293 K. Reaction with H_2O was limited to 293 K since it would likely condense to the flow tube walls at lower temperatures.

3.2.4 $AlO^+ + O_3$ and H_2O

Removal of Al^+ in the presence of O_3 was examined (R3.3, R3.10a/b, R3.11) as a function of *t* at 293 K. Figure 3.13 below shows the four data-sets of $\left(\frac{[Al^+]^t_{O_3}}{[Al^+]^t_0}\right)$ versus *t* that were obtained. A model of the flow tube kinetics was developed, which had included $k_{3.3}$, the wall loss of Al^+, and the two unknowns, $k_{3.10}$ and the branching ratio $f_{3.10a}$ (where $f_{3.10a} = k_{3.10a}/k_{3.10}$ i.e. the fraction representing the total removal rate that was a result of recycling back to Al^+). This was then used to fit each dataset by minimizing the χ^2 residual between the experimental and modelled points. This analysis lead to weighted means of $k_{3.10}$ (293 K) at $(1.3 \pm 0.6) \times 10^{-9}$ cm^3 $molecule^{-1}$ s^{-1} and $f_{3.10a}$ at (63 ± 9)%. The fitting procedure proved to be far more sensitive to $f_{3.10a}$ than $k_{3.10}$, because it was the branching ratio that influenced the amount of Al^+ present rather than the absolute rate of reaction of AlO^+ with O_3. This was shown by the relative uncertainties of the two parameters represented as dashed lines in Figure 3.13.

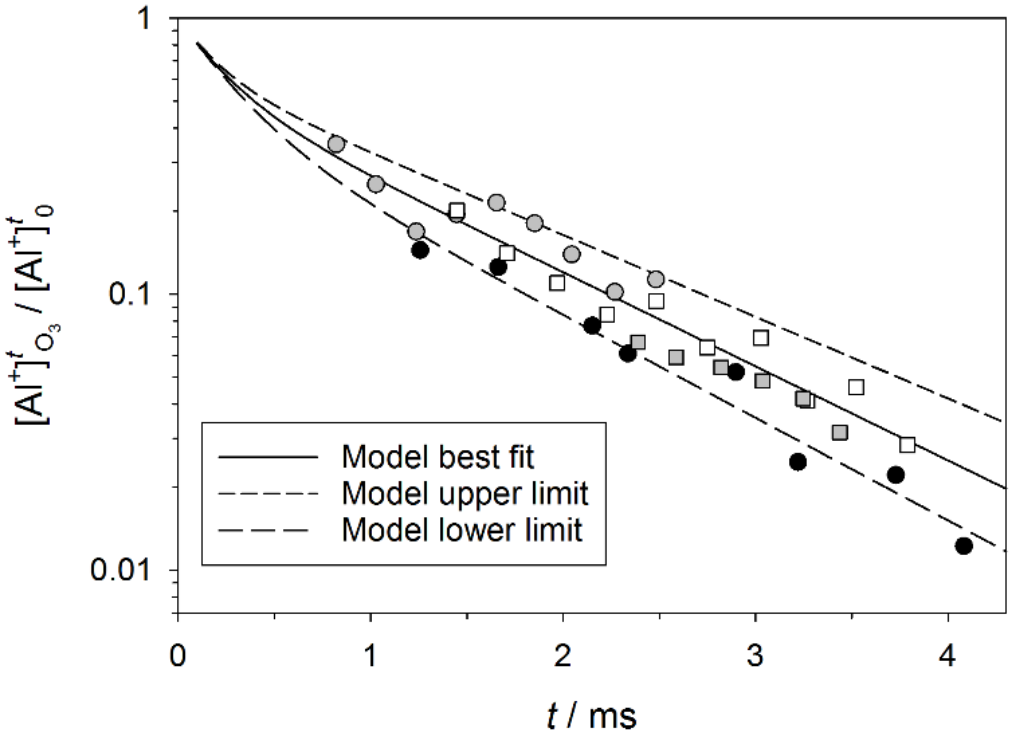

Figure 3.13. A plot showing the log scale of $\left(\frac{[Al^+]^t_{O_3}}{[Al^+]^t_0}\right)$ as a function of *t*, with an O_3 concentration = 1.2×10^{12} cm^{-3} at 1.0 Torr and 293 K. The model fit was represented as the solid black line, with upper and lower error limits illustrated by the dashed lines. Four experimental data sets were shown here with their own individual symbols.

The reaction between AlO^+ and H_2O (R3.11) was then studied by monitoring the AlO^+ ion with the mass spectrometer (m/z = 43), as a function of $[H_2O]$ at a fixed $[O_3]$ of 1.2 x 10^{12} molecule cm^{-3}. Plots of $\left(\frac{[AlO^+]^t_{H_2O}}{[AlO^+]^t_0}\right)$ versus *t* (ms) were then fitted with the kinetic model using the now measured $k_{3.3}$, $k_{3.10a}$ and $k_{3.10b}$. Fitting each of the four data sets with 5 to 10 data-points resulted in a value of $k_{3.11}$ (293 K) = (9 ± 4) × 10^{-10} cm^3 $molecule^{-1}$ s^{-1}. The successful

measurement of $Al^+ + O_3$ and the branching ratios of $AlO^+ + O_3$ were later essential for further reaction involving CO and O.

3.2.5 $AlO^+ + CO$

The AlO^+ ions were produced by reaction R3.3 through addition of O_3 downstream of the ablation point at a fixed point. The rate coefficient, $k_{3.9}$, for this reaction was determined earlier in this chapter. CO was diluted in He (10% bulb) and was injected 35.5 cm downstream of the metal rod. This gave a reaction time of 7.5 ms from the sliding injector to the mass spectrometer. The rate coefficient, $k_{3.9}$, for R3.9 was studied by varying the ratio of CO concentration to O_3 concentration and observing the change in ratio $[Al^+]/[Al^+]_0$, where $[Al^+]_0$ represents the Al^+ signal with no CO present. The experimental data was then fitted with a modified form of E3.6 to account for regeneration of Al^+ from AlO^+ by O_3 and CO:

$$\frac{d[Al^+]}{dt} - k_{diff,\,Al^+}[Al^+] - k_{O_3}[Al^+][O_3] - k_{O_2}[Al^+][O_2][M] + k_3[AlO^+][O_3] + k_{16}[AlO^+][CO] \quad \text{(E3.13)}$$

In the model run, Al^+ concentration was initially simulation over the reaction time of 7.5 ms using $k_{\text{diff, Al}^+}$, followed by addition of O_3 at 2.73 x 10^{11} molecule cm^{-3} with the remaining Al^+ trace acting as $[Al^+]_0$ before increments of CO were added. Reaction R11 between $AlO^+ + H_2O$ was included for the modelled fit since there was a trace leak in the system (~30 mTorr min^{-1}) and the rate of R3.11 was very fast (measured earlier in this chapter). However, the estimated concentration was low (5×10^9 molecule cm^{-3}) therefore, the effect on the model fit was minimal overall.

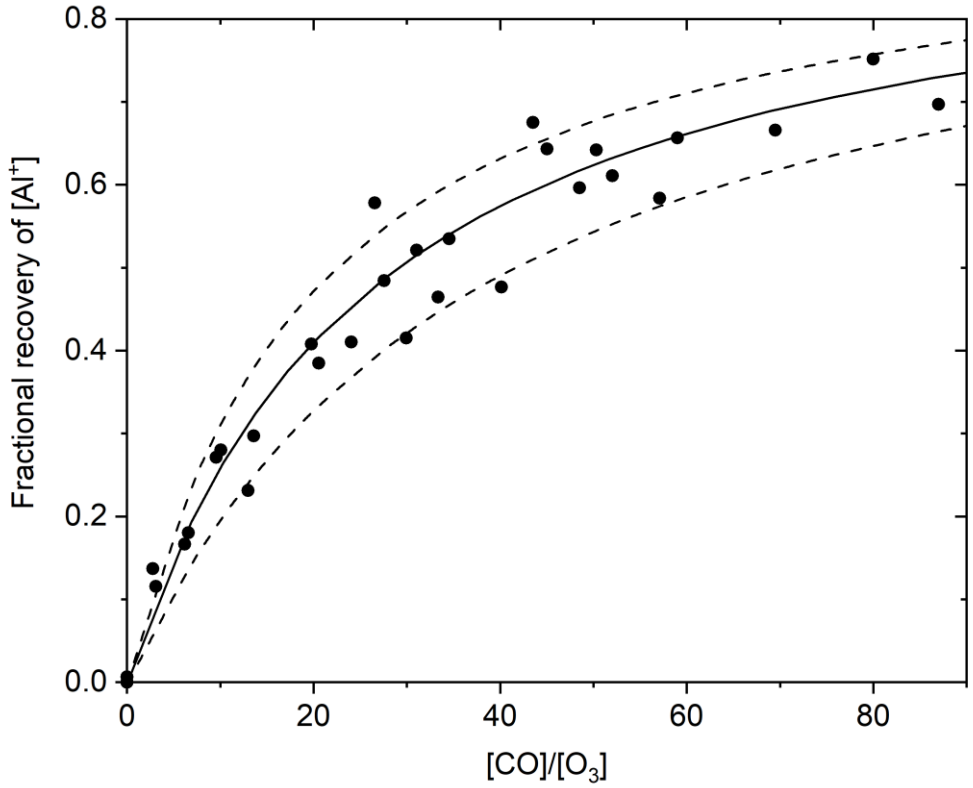

Figure 3.14: Ratio of signal recovery plotted against [CO] / [O_3], where the CO concentration was varied against a fixed concentration of O_3. The dashed lines represent the ± 1σ of the fit, calculated by individually fitting the rate fit to each data point. Signal recovery of Al^+ was plateauing at ~75% at [CO] / [O_3] ratios greater than 80.

As shown in figure 3.14, the fitted value of k represented by the solid line gives an acceptable fit to the experimental data. The error of the fit was determined by fitting to each individual experimental point, giving a series of k values from which, the standard deviation was calculated. The percentage recovery of the $^{27}Al^+$ signal in both the experimental data and modelled fit plateaued between 70-75%, when the ratio of [CO] / [O_3] was greater than 80. The calculated rate for k_9 from the model was [3.7 ± 1.1] × 10^{-10} cm^3 $molecule^{-1}$ s^{-1}, more than a factor of 2 times the rate of FeO^+ + CO at [1.59 ± 0.34] × 10^{-10} cm^3 $molecule^{-}$

^{1} s^{-1} [*Woodcock et al.*, 2006] and 25% more than CaO^{+} + CO at [2.8 ± 1.5] × 10^{-10} cm^{3} $molecule^{-1}$ s^{-1} [*Broadley et al.*, 2008].

3.2.6 AlO^{+} + O

Initially varying the O concentration at a fixed O_3 was attempted. However, both the large diffusion of O and the lack of consistent conversion of NO to O made it difficult to vary. Therefore, [O] was fixed to 1.36 x 10^{13} molecule cm^{-3} against a range of [O_3] (0.4 – 3.5 × 10^{11} molecule cm^{-3}), following the method applied in [*Whalley and Plane*, 2010]. The solid circle points of figure 3.15 are Al^{+} ions with only O_3 present at a fixed reaction distance, with the rates of $k_{3.3}$, $k_{3.10a}$ and $k_{3.10b}$ included. $k_{3.11}$ was also included but the H_2O concentration from the system leak was too low to affect measurements. The open circles were the Al^{+} ions in the presence of O_3 and fixed O. The rate of Al^{+} recovery was fitted using a modified form of E3.13 to incorporate O instead of CO. Similar to R3.9, the error of the fit was determined by fitting to each individual experimental point measured.

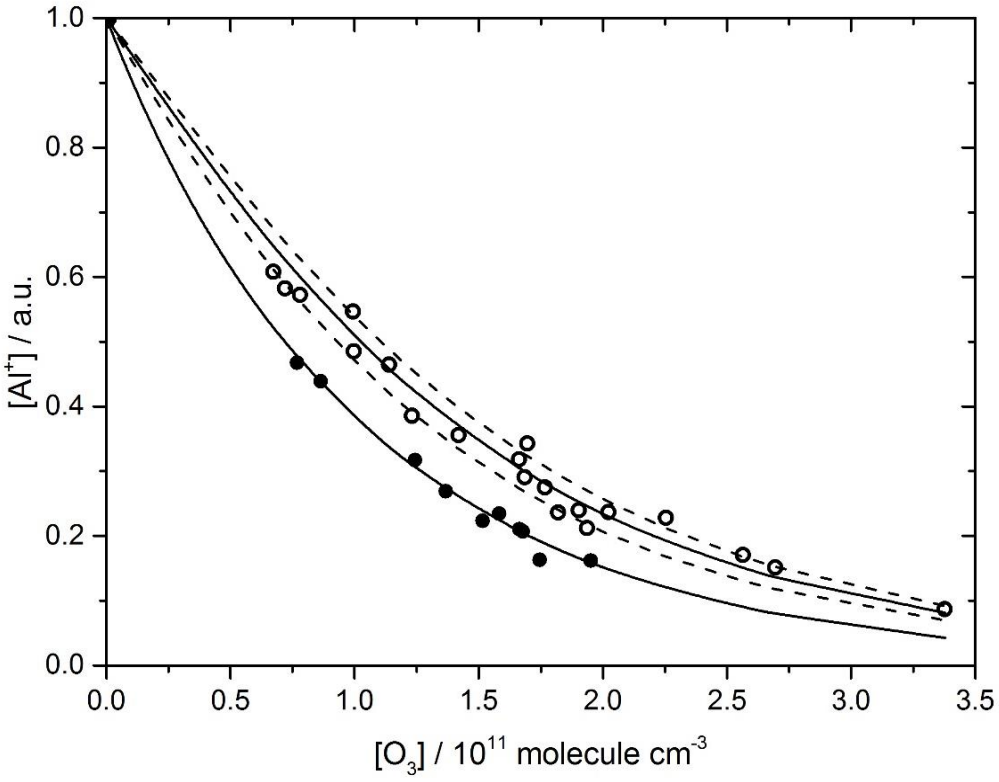

Figure 3.15: Reaction of AlO^+ + O at 294 K, using the 27 m/z channel for Al^+. The solid circles are the experimental points of Al^+ in the presence of O_3 and absence of a fixed [O] = 1.36×10^{13} molecule cm^{-3}, with the solid line through the points representing the modelled fit. The open circles with solid line are the experimental and modelled data for Al^+ in the presence of O. The dashed lines represent the uncertainty.

The O_3 was varied from 0.5 – 3.5×10^{11} molecule cm^{-3} but the O concentration was fixed at 1.36×10^{13}. The rate of $k_{3.8}$ = [1.7 ± 0.7] $\times 10^{-10}$ cm^3 $molecule^{-1}$ s^{-1}. Nearly the same as the recorded value for NiO^+ + O discussed in Chapter 3. This was a factor of 4 times larger than the measured rate of CaO^+ + O at 4.2×10^{-11} cm^3 $molecule^{-1}$ s^{-1} [*Broadley et al.*, 2008; *Plane et al.*, 2018b] and nearly 6 times larger than FeO^+ + O at 3.0×10^{-11} cm^3 $molecule^{-1}$ s^{-1} [*Feng et*

al., 2013; *Woodcock et al.*, 2006]. The rate of $AlO^+ + O_2$ was retrieved from the model runs of AlO^+ with CO and O and calculated to be 6×10^{12} cm^3 $molecule^{-1}$ s^{-1}. The reaction of $Al^+.N_2 + O$ was not included in the model since the formation of $Al^+.N_2$ by R3.4 was very slow.

3.2.7 Discussion

The rate of $Al^+ + O_3$ (R3.3) was found to be ~40% faster than the calculated Langevin capture rate of 1.0×10^{-9} cm^3 $molecule^{-1}$ s^{-1}. It may be indicative that the reasonable dipole moment of O_3 (0.53 D [*Lide*, 2006] was enough to promote Al^+ capture. Applying the statistical adiabatic channel model (SACM) of Troe [*Troe*, 1985] with a rotational constant for O_3 of 0.428 cm^{-1}, estimated by applying a geometric mean of the rotation constants for rotation orthogonal to the point group C_{2v} axis of the molecule along which the dipole lies, yielded a value of $k_1(293\ K) = 1.39 \times 10^{-9}$ cm^3 $molecule^{-1}$ s^{-1}, which showed better agreement with the experimental measurement. Finally, the temperature dependence of the reaction was then theoretical estimated to be $k_{3.1}(100 – 300\ K) = 1.48 \times 10^{-9} (T/200)^{-0.164}$ cm^3 $molecule^{-1}$ s^{-1}.

Applying SACM for the reaction between $AlO^+ + O_3$ (R3.10) yielded a value of $k_{10}(100 - 300\ K) = 1.20 \times 10^{-9} (T/293)^{-0.175}$ cm^3 $molecule^{-1}$ s^{-1}, agrees with the measured value within error. For R3.11, the larger dipole moment of H_2O of 1.85 D [*Clough et al.*, 1973] increased the SACM estimate to $k_{3.11}(100 - 300\ K) = 2.30 \times 10^{-9} (T/293)^{-0.309}$ cm^3 $molecule^{-1}$ s^{-1}, nearly double the experimental rate.

The cluster reactions of Al^+ with N_2, O_2, CO_2 and H_2O required extrapolation to the temperatures and pressures of the MLT which were not possible experimentally. To do this RRKM theory was applied using a solution of the Master Equation based on the inverse Laplace transform method [*De Avillez Pereira et al.*, 1997]. This method has been applied previously to recombination reactions of metallic species [*Broadley et al.*, 2007; *Vondrak et al.*, 2006; *Whalley et al.*, 2011]. The low-pressure limiting rate coefficients calculated using this method, $k_{rec,0}$, were then fitted through the experimentally measured data points, followed by extrapolation between 100 and 600 K, shown in Figure 3.16 below. R3.5 was nearly 3 orders of magnitude faster than R3.2 (at the same temperature). Table 3.1 below shows the expressions for the low-pressure limit rates. It is noted that low-pressure limiting rate coefficients are suitable for the meteoric ablation region in planetary atmospheres where the pressure is < 10^{-5} bar.

Table 3.1. Low-pressure limiting rate coefficients for the addition of a single ligand to an Al^+ ion using RRKM theory

Reaction	**$\log_{10}(k_{rec,0}$/ cm^6 molecule^{-2} s^{-1}) T = 100 – 600 K**
$Al^+ + N_2$	$-27.9739 + 0.05036\log_{10}(T) - 0.60987(\log_{10}(T))^2$
$Al^+ + CO_2$	$-33.6387 + 7.0522\log_{10}(T) - 2.1467(\log_{10}(T))^2$
$Al^+ + H_2O$	$-24.7835 + 0.018833\log_{10}(T) - 0.6436(\log_{10}(T))^2$

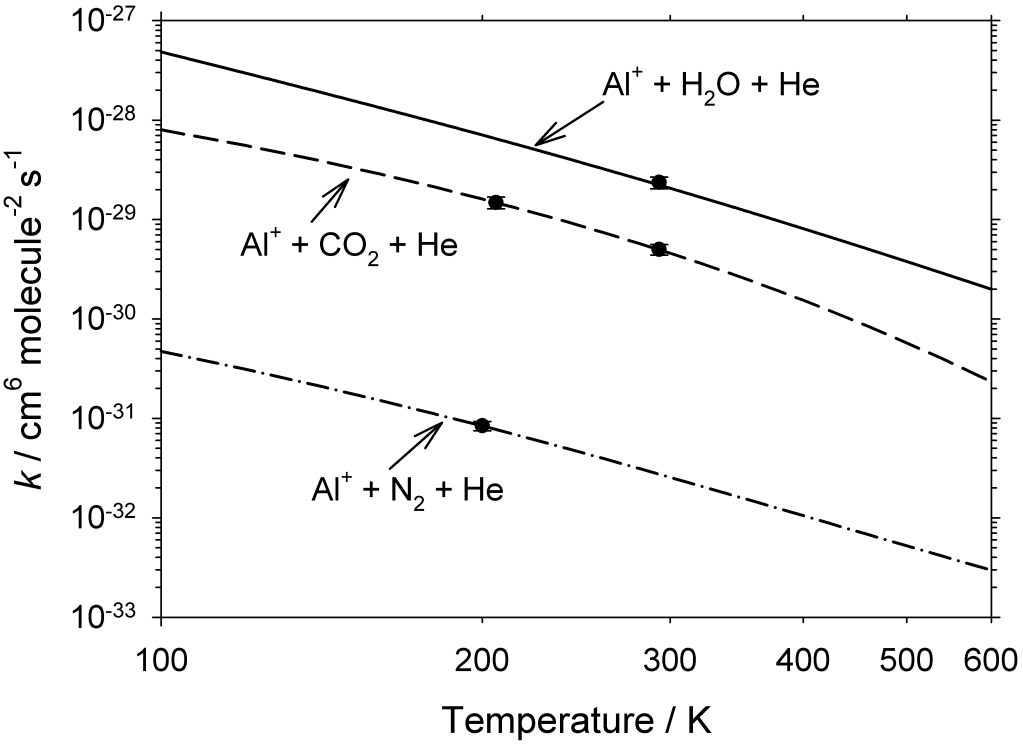

Figure 3.16: RRKM fits through the experimental data points (solid circles) for the recombination reactions of Al^+ with N_2, CO_2 and H_2O over a temperature range form 100 – 600 K. Note the log scale applied for *k* on the left hand axis to properly illustrate the 3 reactions separated by up to 3 orders of magnitude.

Some of the ion reactions addressed in this chapter have been measured previously. *Leuchtner et al.* [1991] found an upper limit of $k_{3.3}(300\ K) \leq 1.3 \times 10^{-32}$ cm^6 molecule^{-2} s^{-1} for $Al^+ + O_2$ in a selected ion flow tube at 0.25 Torr pressure, which was consistent with the upper limit of 2.8×10^{-32} cm^6 molecule^{-2} s^{-1} achieved in this study. For $Al^+ + CO_2$, work by *Clemmer et al.* [1992] reported a $k_{3.6}(300\ K) \leq 2.0 \times 10^{-27}$ cm^6 molecule^{-2} s^{-1} in a guided ion beam instrument with a maximum pressure of 0.3 mTorr. Although the actual measurement here of $k_{3.5}(293\ K) = (5.0 \pm 0.6) \times 10^{-30}$ cm^6 molecule^{-2} s^{-1} is 3 orders of magnitude less, it is still less than the upper limit.

3.2.8 Atmospheric Implications

To be able to apply the cluster reaction rate coefficients for modelling in planetary atmospheres, a level of adjustment is required to account for the relative efficiency of the main species of each atmosphere instead of He, which was used as the main carrier and third body source in the kinetic measurements. If N_2 and O_2 are the third body in an ion-molecule recombination reaction, as in the case of the Earth's atmosphere, the rate coefficients $k_{3.4}$, $k_{3.6}$ and $k_{3.7}$ would require an increase by a factor of 3 [*Plane et al.*, 2015]. For Mars' atmosphere, CO_2 is the dominant species and would require a factor of 8 increase [*Whalley and Plane*, 2010]. Figure 3.17 below demonstrates the vertical profiles for removal of Al^+ ions in the atmospheres of Earth and Mars. For Earth, the vertical profiles of *T*, pressure and the mixing ratios of O_3, N_2, CO_2, H_2O, CO and O were taken from the Whole Atmosphere Community Climate Model (WACCM4) [*Garcia*, 2007; *Marsh et al.*, 2013a]. They are represented as monthly zonal averages at 40^{o}N in April, at local midnight. The top panel of Figure 3.17 below shows that reaction R3.3 with O_3 dominated between the altitudes of 80 and 140 km. During daytime the O_3 concentration would decrease by around 1 order of magnitude due to photolysis [*Plane et al.*, 2015] but R3.3 will still dominate as the rate was still ~5 orders of magnitude higher than the N_2 equivalent (R3.4). R3.5 was the least important removal process because of the low mixing ratio of H_2O, less than a few ppm above 80 km [*Plane*, 2003; *Plane et al.*, 2015]

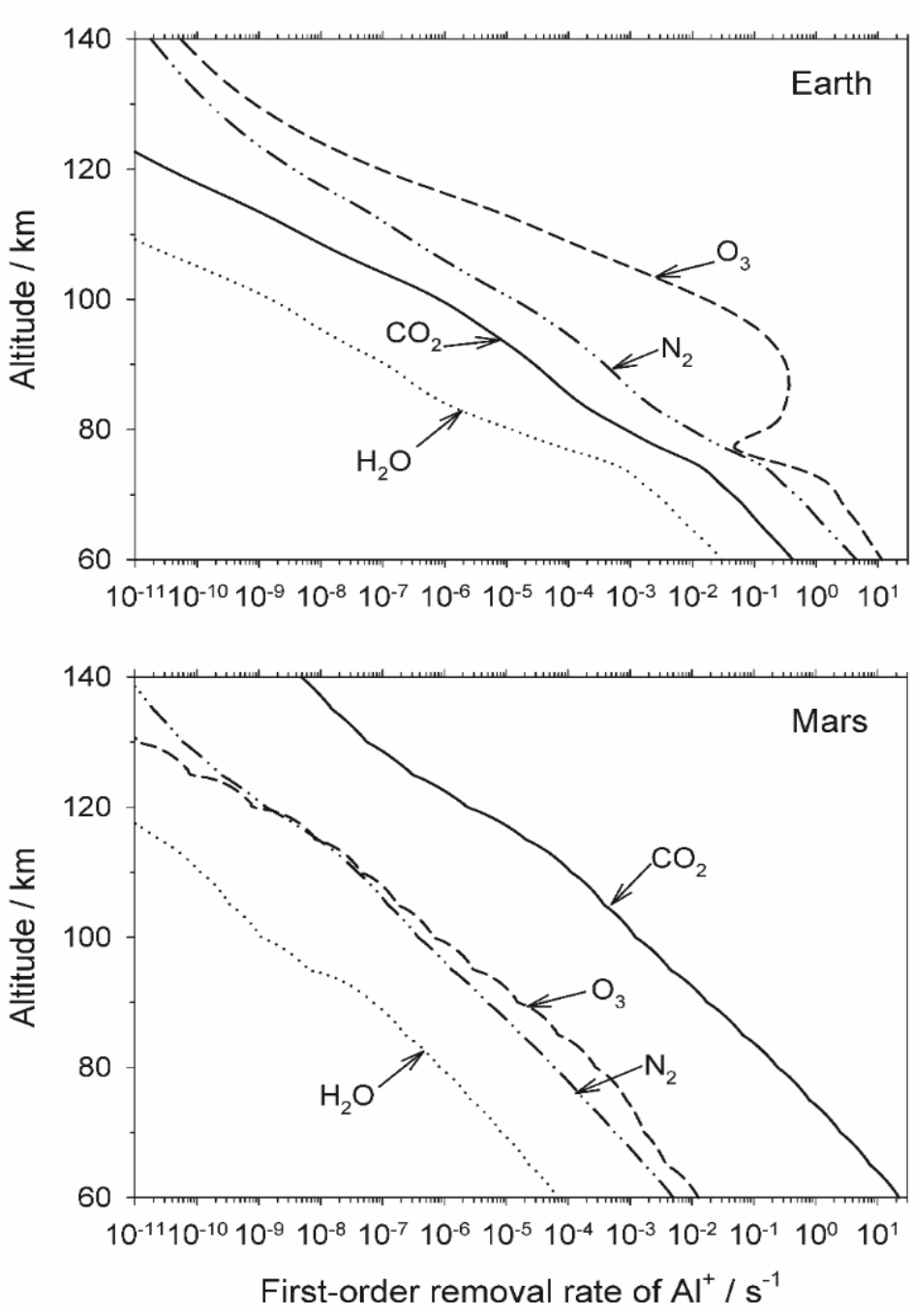

Figure 3.17: Removal rates of Al^+ ions in Earth and Mars' atmosphere. Earth: Latitude at 40ºN, time at local midnight, April (top panel); Mars at local noon with latitude = 0º, solar longitude L_s = 85º (bottom panel).

The vertical profiles of the CO_2, O_3, N_2 and H_2O (O_2, CO and O in figure 3.18 below) species and *T* for Mars' atmosphere were taken from the Mars Climate

Database v.5.3 (http://www-mars.lmd.jussieu.fr/mcd_python/)[*Forget et al.*, 1999] for the conditions at latitude = 0^o, with time at local noon and solar longitude set to $L_s = 85^o$ (northern hemisphere summer). O_3 concentration was much lower than in Mars compared to Earth's atmosphere (e.g. 500 times lower at 80 km) because the Martian atmosphere consists of ~95% CO_2. Therefore, R6 dominates by ~3 orders of magnitude.

On Earth, the metallic ion layers (i.e. Fe^+ [*Feng et al.*, 2013] and Mg^+ [*Langowski et al.*, 2015] peak at ~95 km, where Figure 3.17 (top panel) shows that the e-folding lifetime of Al^+ was only ~10 s. Recent measurements by the MAVEN spacecraft on Mars show that the Mg^+ layer peaks around 90 km [*Crismani et al.*, 2017]. At this altitude, the e-folding lifetime of Al^+ ions will be around 1 minute. Al^+ would thus rapidly disappear on either planet. However, since the R3.8 ($AlO^+ + O \rightarrow Al^+ + O_2$) was measured to be quite fast ($[1.7 \pm 0.7] \times 10^{-10}$ cm^3 $molecule^{-1}$ s^{-1}), AlO^+ was much more likely to recycle to the Al^+ ion rather than undergo dissociative recombination with an electron [*Bones et al.*, 2016b]. CO may also play a similar role to O in reducing AlO^+ back to Al^+ as suggested by R9 [*Woodcock et al.*, 2006]. To test this a similar plot of removal rates was prepared for AlO^+, as shown in Figure 3.18 below:

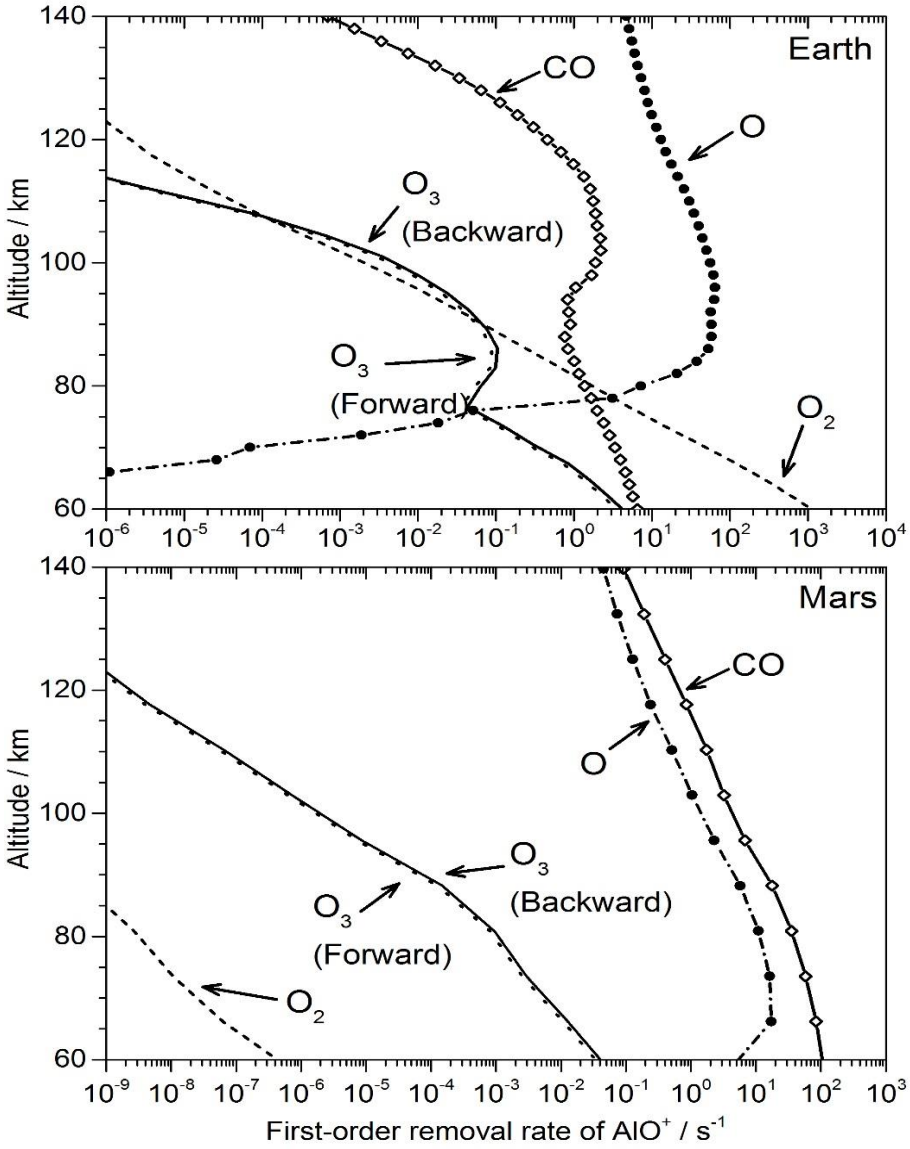

Figure 3.18: Ion Removal rates of AlO^+ in planetary atmospheres of Earth and Mars: Earth, 40ºN, at local midnight (top panel); Mars, local noon, latitude = 0º, solar longitude L_s = 85º (bottom panel). The species addressed are reaction with O, CO, O_3 and O_2. At >80 km in Earth's atmosphere, both the O and CO densities were the dominant sources of AlO^+ removal and dominant for the whole plotted range on Mars's atmosphere.

For both atmospheres in figure 3.18, loss by CO and O dominates the AlO^+ removal process above 80 km on Earth, and 60 km on Mars. Therefore,

recycling to Al^+ is very likely, reducing the amount of AlO^+ available to undergo dissociative recombination to Al. In Mars, removal by O_3 was ~5 orders of magnitude less than O and O_2 drops more than 9 orders of magnitude by 80 km due to the low concentrations of the species.

In Mars' atmosphere, AlO^+ could potentially be formed from the CO_2 cluster ion by the reaction with atomic O. Since the concentrations of O_3 are much less on the Martian atmosphere as indicated earlier, CO_2 would represent a likely pathway.

$$Al^+.CO_2 + O \rightarrow AlO^+ + CO_2 \qquad \Delta H^o = -81 \text{ kJ mol}^{-1} \qquad \text{(R13)}$$

Currently the already established metal models (WACCM-Na, WACCM-Ca, WACCM-Fe) do not account for the ion molecule metal reaction with CO, since CO is much less abundant than O at the ion altitudes. Figure 3.18 however, suggests that AlO^+ removal by CO is significant and should be included.

3.3 Conclusion

The first measurement of the rate constant for Al + O_2 over a range of temperatures was carried out using absorption and resonance fluorescence detection of Al in a high temperature fast flow reactor [*Fontijn et al.*, 1977]. The literature value was of the order of $k_1 = 3.2 \times 10^{-10}$ cm^3 $molecule^{-1}$ s^{-1} at 298 K. It was later agreed that this value of AlO formation (k_1) was in error [*Garland and Nelson*, 1992]. Following this, two subsequent measurements with application of the PLP-LIF technique in a conventional slow flow reactor [*Garland and Nelson*, 1992] and in a CRESU apparatus [*Le Picard et al.*, 1997]

were carried out. The reported rate constant in this instance at 298 K was ~1.7 × 10^{-10} cm^3 $molecule^{-1}$ s^{-1}. The result presented here was in excellent agreement with the two PLP-LIF experimental determinations, firmly establishing the rate constant of Al + O_2. As well as this, newly found evidence for the AlO self-reaction was made, whereby the reaction appears to proceed via the Al_2O + O product channel. The first experimental determination of the absorption cross section (σ) of AlO was made, with a value of (6.7 ± 1.6) × 10^{-15} cm^2 $molecule^{-1}$ at 298 K and 0.8 Torr (0.003 nm resolution). The experimentally measured cross section at the 0-0 band head was compared with the ro-vibrational spectral model PGOPHER, showing very good agreement between the two. As well as this, PGOPHER excellently reproduces the intensities of the J-level rotational lines, even with varying temperature. Therefore, the program holds credibility for generating reference spectra of various molecular species as well as gaining understanding of the cross-section's temperature dependence. With the newly measured cross section of AlO, the first attempted lidar observations of a molecular species in the MLT could be made.

The reaction kinetics of Al^+ with O_3, N_2, CO_2 and H_2O (R3, R4, R6, R7) have been measured for the first time using a laser ablation fast flow tube technique, and an upper limit obtained to recombination with O_2 (R5). Further reactions with the oxide form, AlO^+, were also investigated with CO, O and O_3 (R8, R9, R10a, R10b). Al^+ was particularly slow at reacting with the main constituents of Earth's atmosphere (N_2, O_2, CO_2). The recombination reaction with CO_2 was measured at room temperature, however, the N_2 reaction was only be observed at lower temperatures. Reaction between Al^+ and O_3 was close to the ion-molecule capture rate which was also enhanced by the small

dipole moment of O_3. This reaction then dominated removal of Al^+ in the terrestrial atmosphere because of the reasonably high concentrations of O_3 in the MLT. However, in the Martian atmosphere, recombination with CO_2 was about 3 orders of magnitude faster. Reaction of AlO^+ with CO had the highest observed reaction rate compared to other previously measured metal analogues. The fast rates of AlO^+ with O and CO would affect the levels of neutralization to Al by dissociative recombination since the species would be recycled to Al^+.

4 Neutral and ion-molecule kinetics of Ni

In 2015, the mesospheric Ni layer was observed for the first time by resonance lidar near Fairbanks, Alaska [*Collins et al.*, 2015], reporting a peak density of ~16,000 atoms cm^{-3} at a height of 87 km, which is within a factor of 2 of the Fe layer peak at the same location/season. The low ratio of Fe and Ni was unexpected because the relative Fe to Ni ratio quantified in carbonaceous chondrites is 18:1. [*Asplund et al.*, 2009]. Metallic Ni^+ ions in the Mesosphere-Lower Thermosphere (MLT) have mostly been observed by mass spectrometry from rocket soundings [*Kopp*, 1997] and have been compared to the most recent ablation ratio estimate predicted by *Carrillo-Sánchez et al.* [2020], yielding Fe^+/Ni^+ ratios of 20^{+13}_{-8} and 16 respectively which is very close to the chondritic ratio. To explore the highly contrasting neutral ratio measured

by lidar soundings, kinetic studies of neutral (Ni, NiO, NiO_2) and ion-molecule (Ni^+, NiO^+) species were carried out in this chapter. The kinetics would also provide an insight into the upper atmosphere of Mars, where Ni^+ ion have been measured using the MAVEN spacecraft [*Carrillo-Sánchez et al.*, 2020; *Grebowsky et al.*, 2017].

Based on the chemistry of other meteoric metals such as Fe^+, Mg^+ and Ca^+ [*Plane et al.*, 2015], Ni^+ ions are initially produced in the MLT through either charge transfer of Ni atoms with ambient NO^+ and O_2^+ ions, photo-ionization, or by direct ionization through atmospheric entry when the freshly ablated Ni can ionize through hyperthermal collisions with air molecules residing in the upper atmosphere [*Plane et al.*, 2015]. NiO^+ can also be formed directly through the reaction of Ni with ambient O_2^+ ions [*Schlemmer et al.*, 2003]. Note that all electronic structure calculations (B3LYP/aug-cc-pVQZ theory [*Frisch et al.*, 2016]; statistical adiabatic channel model (SACM) [*Troe*, 1985], etc); trajectory calculations [*Su and Chesnavich*, 1982] along with Rice-Ramsperger-Kassell-Markus (RRKM) theory [*De Avillez Pereira et al.*, 1997] were carried out by Prof. John Plane in this chapter.

The oxidation of Ni^+ to NiO^+ would proceed via reaction with O_3:

$$Ni^+ + O_3 \rightarrow NiO^+ + O_2 \qquad \Delta H^o = -125\ [-157 \pm 19]\ kJ\ mol^{-1} \qquad (R4.1)$$

The NiO^+ ion can then react further with O_3 to create higher oxides, or be recycled back to the Ni^+ ion by reaction with O_3, CO or O:

$$NiO^+ + O_3 \rightarrow Ni^+ + 2O_2 \qquad \Delta H^o = -184\ [-136 \pm 19]\ kJ\ mol^{-1} \qquad (R4.2a)$$

$$\rightarrow NiO_2^+ + O_2 \qquad \Delta H^o = -259\ kJ\ mol^{-1} \qquad (R4.2b)$$

$$NiO_2^+ + O_3 \rightarrow NiO^+ + 2O_2 \qquad \Delta H^o = -61\ kJ\ mol^{-1} \qquad (R4.3a)$$

$\rightarrow ONiO_2^+ + O_2$ ΔH^o = -142 kJ mol^{-1} (R4.3b)

$NiO^+ + O \rightarrow Ni^+ + O_2$ ΔH^o = -284 [-237 ± 19] kJ mol^{-1} (R4.4)

$NiO^+ + CO \rightarrow Ni^+ + CO_2$ ΔH^o = -195 [-269 ± 19] kJ mol^{-1} (R4.5)

with the reaction enthalpies been calculated at the B3LYP/aug-cc-pVQZ level of theory (at 0 K), where the enthalpies shown in parentheses apply the experimental bond energies of $D_0(Ni^+\text{-}OH)$ = 235 ± 19 kJ mol^{-1} and $D_0(Ni^+\text{-}O)$ = 257 ± 19 kJ mol^{-1} [*Armentrout et al.*, 1982; *Vardhan et al.*, 2003]. As well as this, Ni^+ can undergo recombination reactions with several atmospherically relevant species:

$Ni^+ + N_2$ (+ M) $\rightarrow Ni^+.N_2$ ΔH^o = -112 kJ mol^{-1} (R4.6)

$Ni^+ + O_2$ (+ M) $\rightarrow NiO_2^+$ ΔH^o = -74 kJ mol^{-1} (R4.7)

$Ni^+ + CO_2$ (+ M) $\rightarrow Ni^+.CO_2$ ΔH^o = -109 kJ mol^{-1} (R4.8)

$Ni^+ + H_2O$ (+ M) $\rightarrow Ni^+.H_2O$ ΔH^o = -168 kJ mol^{-1} (R4.9)

where M represents a third body, and the dot notation is to signify a cluster ion. The Ni^+ bond in this regard is electrostatic in nature (i.e. ion-induced dipole) rather than a chemical one. From there, these molecular ions can undergo dissociative recombination with electrons, which will lead to production of neutral Ni atoms. It is noted that radiative (or dielectronic) recombination of Ni^+ with electrons should only be significant in the thermosphere above 120 km where the atmospheric pressure is very low, based off the work done with Fe^+ [*Chu et al.*, 2011; *Plane et al.*, 2015].

In addition to the ion molecule kinetics, several neutral reactions for NiO and NiO_2 were examined:

$NiO + O \rightarrow Ni + O_2$ (R4.13)

$NiO + CO \rightarrow Ni + CO_2$ (R4.14)

$NiO_2 + O \rightarrow NiO + O_2$ (R4.15)

NiO and NiO_2 can undergo reaction with O_3, O_2, CO_2 and H_2O to form further higher oxides, carbonates as well as hydroxides [*Mangan et al.*, 2019]. R4.13 – R4.15 reaction pathways play an important role in hindering the formation of $ONiO_2$, $NiCO_3$ and $Ni(OH)_2$, therefore play a central role in controlling the shape of the neutral Ni layer. R4.14 has been studied previously by *Mangan et al.* [2019] using a pulsed laser photolysis-laser-induced fluorescence (PLP-LIF) technique in a slow flow reactor cell.

In this chapter we report the experimental kinetics of reactions R4.1 – R4.16, with additional theory to extrapolate the measured rates to temperature and pressure conditions of the upper atmosphere. Finally, the relative importance of these reactions in the upper atmospheres of Earth and Mars was examined.

4.1 Kinetics of Ni^+

4.1.1 Recombination reactions of Ni^+ with N_2, O_2, CO_2 and H_2O

As described in Chapter 2, laser ablation of a Ni metal rod produces Ni atoms and Ni^+ ions and this became the active source for Ni molecular ion species in the flow tube, to be later detected downstream using a Quadruple Mass Spectrometer. The kinetics of Ni^+ were measured by adjusting the sliding injector length in the flow tube which carried the reactant, yielding reaction times of 8 – 40 ms at 294 K. In contrast, for NiO^+, the sliding injector was fixed

to certain contact lengths with the concentration of the reactants varied (O_2, O_3, O, CO). The depletion in Ni^+ was measured in the presence and absence of the reactant of interest, which is designated here as X. For R4.6 – R4.9, the generalized three body reaction is represented as:

$$Ni^+ + X\ (+M) \rightarrow Ni^+.X \qquad \text{(R4.16)}$$

a plot of $\ln\left(\frac{[Ni^+]_X^t}{[Ni^+]_0^t}\right)$ vs. reaction time t yields the pseudo first-order rate coefficient k', as shown in E4.1, since the reactant concentrations and the carrier gas were in large excess of the Ni^+ concentration coming from the rod:

$$k' = k_X[X] = \frac{ln\left(\frac{[Ni^+]_X^t}{[Ni^+]_0^t}\right)}{t} \qquad \text{(E4.1)}$$

Generation of the expression for k' has been detailed in Chapter 3, where the kinetics of Al^+ were examined. Here, $[Ni^+]_X^t$ is the Ni^+ signal at the detector at time t in the presence of reactant X, and $[Ni^+]_0^t$ represents the Ni^+ signal in the absence of X. Note that the contact time t is measured directly from the arrival time of the Ni^+ pulses at the skimmer cone of the mass spectrometer (see Figure 3.8 in Chapter 3).

Figure 4.1 shows examples of pseudo first order kinetic plots for R4.7 (Ni^+ + O_2). Typical Ni^+ concentrations in the upstream section of the tube are estimated at ~5×10^6 cm^{-3}, whereas [X] is > 1×10^{11} molecule cm^{-3}, giving the excess required to achieve the pseudo first order conditions with the linearity of these kinetics plots confirming this assumption. The advantage of using this method is that k' could be determined without needing to know the rate of loss of Ni^+ to the tube walls (k_{diff}) (discussed in Chapter 3) [*Vondrak et al.*, 2006].

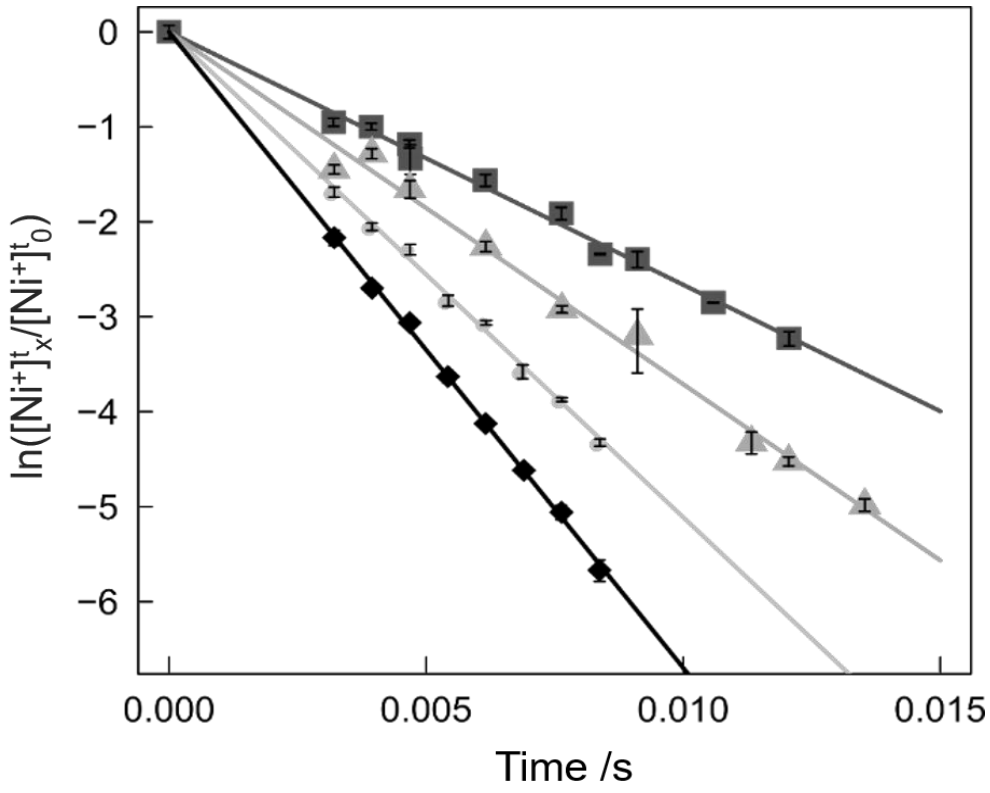

Figure 4.1. Plot of $\ln\left(\frac{[Ni^+]_X^t}{[Ni^+]_0^t}\right)$ against reaction time, where [O_2] = 1.5 × 10^{14} molecule cm^{-3} (dark grey squares), 5.5 × 10^{14} molecule cm^{-3} (grey triangles), 1.1 × 10^{15} molecule cm^{-3} (light grey circles), 2.2 × 10^{15} molecule cm^{-3} (black diamonds). Experimental conditions: P = 2.5 Torr, *T* = 294 K. The lines fitted through the experimental data are exponential fits where the slope yields *k′*.

When *k′* is plotted against [X], the second-order rate coefficients can then be determined. These are then plotted further as a function of [He] as shown in Figure 4.2, with the fitted slopes of these plots (R4.6 – R4.9) yielding the third-order rate coefficients. The 1σ uncertainties are determined from the standard errors of the slopes of the regression lines, combined with the additional uncertainty in [X].

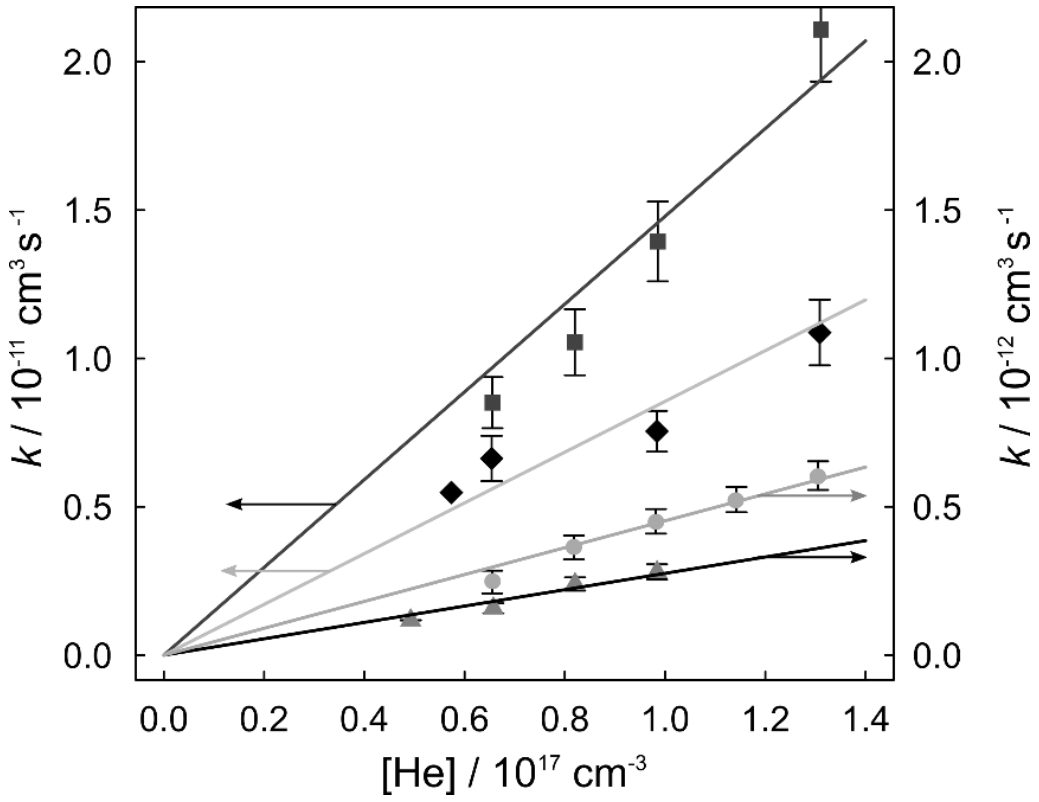

Figure 4.2. Recombination rate coefficients plotted as a function of pressure, in relation to [He]. Dark grey squares: R4.6 ($Ni^+ + H_2O$); black diamonds: R4.9 ($Ni^+ + CO_2$); Grey circles: R4.8 ($Ni^+ + N_2$); grey triangles: R4.7 ($Ni^+ + O_2$). Note there are two different ordinates: the left-hand ordinate scales for reactions R4.6 and R4.9; while the right-hand ordinate scales for R4.7 and R4.8 (indicated with arrows). The fitted lines through the experimental points are linear regression fits, where the slopes of each fit provide the 3rd order rate coefficients. Experimental conditions: T = 294 K.

The measured rate coefficients for the 4 reactions addressed in Figure 4.2 were as follows (cm^6 $molecule^{-2}$ s^{-1}): $k_{4.6}(Ni^+ + N_2) = (3.5 \pm 0.5) \times 10^{-30}$; $k_{4.7}(Ni^+ + O_2) = (2.8 \pm 0.5) \times 10^{-30}$; $k_{4.8}(Ni^+ + CO_2) = (7.7 \pm 1.0) \times 10^{-29}$; $k_{4.9}(Ni^+ + H_2O) = (1.3 \pm 0.2) \times 10^{-28}$.

4.1.2 $Ni^+ + O_3$

Initial measurements of the pseudo first-order reaction of Ni^+ with O_3 (R4.1) gave a lower than expected rate coefficient of ~3×10^{-10} cm^3 $molecules^{-1}$ s^{-1}, illustrated in Figure 4.3 below (the experimental points shown as grey diamonds). A similar issue was observed for the analogous reaction of $Al^+ + O_3$ (described in Chapter 3) as well as the Fe counterpart ($Fe^+ + O_3$) measured by *Melko et al.* [2017]. In both those studies, significant recycling of the metal oxide ion back to the atomic ion through reaction with O_3 was discovered. Therefore, it was highly likely that the recycling was repeating here via $NiO^+ + O_3$ (reaction R4.2a). To account for this, a constant concentration of H_2O was added into the flow tube, since the recombination reaction shown as follows:

$$NiO^+ + H_2O\ (+ M) \rightarrow NiO^+.H_2O \qquad \Delta H^o = -212\ kJ\ mol^{-1} \qquad (R4.11a)$$

It is also noted that the bimolecular reaction pathway is as follows using B3LYP/aug-cc-pVQZ level of theory:

$$NiO^+ + H_2O \rightarrow NiOH^+ + OH \qquad \Delta H^o = +22\ kJ\ mol^{-1} \qquad (R4.11b)$$

which is too endothermic. If the experimental values for both $D_0(Ni^+\text{-}OH) = 235 \pm 19$ kJ mol^{-1} and $D_0(Ni^+\text{-}O) = 257 \pm 19$ kJ mol^{-1} [*Vardhan et al.*, 2003] are taken into account, the reaction may be even more endothermic, $\Delta H^{\ominus} = +(92 \pm 27)$ kJ mol^{-1}. The rearrangement of the $NiO^+.H_2O$ to produce the di-hydroxide ion $Ni(OH)_2^+$:

$$NiO^+.H_2O \rightarrow Ni(OH)_2^+ \qquad \Delta H^o = +13\ kJ\ mol^{-1} \qquad (R4.11c)$$

has a barrier of 128 kJ mol^{-1} with respect to $NiO^+ + H_2O$. Therefore, only reaction channel R4.11a would be the primary pathway for removal of NiO^+,

preventing its reaction with O_3. As illustrated in Figure 4.3 (black triangles), the measured k' increased significantly in the presence of H_2O, suggesting inhibition of the O_3 recycling. However, even with the addition of H_2O and subsequent increase in k', applying a linear fit of k' vs. [O_3] does not go through the origin with clear curvature observed past [O_3] > 1×10^{12} molecule cm^{-3} in Figure 4.3. It was clear that the H_2O does not completely prevent recycling of NiO^+ to Ni^+ when [O_3] was greater than this limit. However, this could not be resolved experimentally since the upper limit of [H_2O] we could add to the flow tube was constrained by the vapour pressure of the molecule at 294 K. Therefore, a full kinetic model was developed to fit $k_{4.1}$, $k_{4.2}$, $k_{4.3}$ and $k_{4.11}$ to the measurements from different experiments. Since R4.4 and R4.5 also required these reactions, a compromise was established for the rate coefficients used in the kinetic models for each of these reactions. The final rate for R4.1 came to value of $k_{4.1}(294\ K) = (9.7 \pm 2.1) \times 10^{-10}$ cm^3 $molecule^{-1}$ s^{-1}. Note that the converted [O_3] from [O_2] during the experiments ranged from 1.5 to 4% when passed through the high voltage corona in the commercial ozoniser.

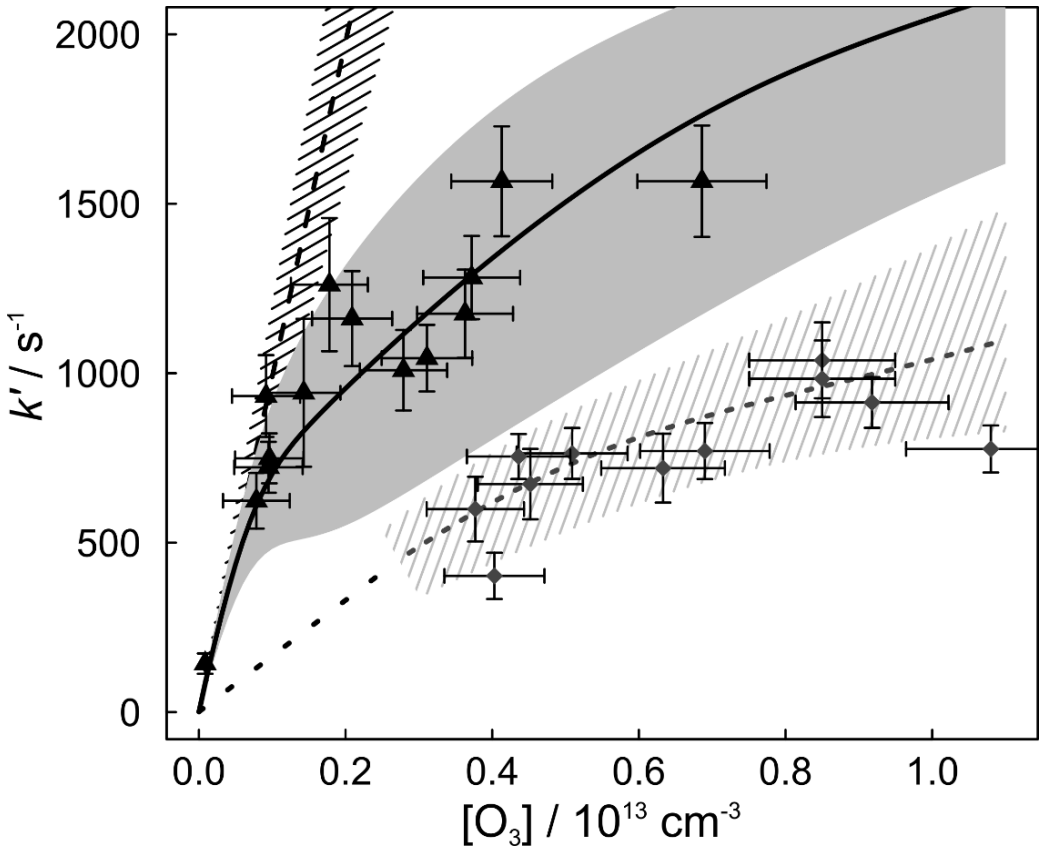

Figure 4.3. Plot of k' for R4.1 as a function of $[O_3]$, for 3 separate cases: a) $Ni^+ + O_3$ with full recycling of NiO^+ by reaction R4.2a (measurements shown as grey diamonds, with the dotted line as the model fit, extrapolated to $[O_3] = 0$ with the sparse dotted line and 1σ error illustrated as dashed lines); b) $Ni^+ + O_3$ with a fixed $[H_2O] = 3 \times 10^{12}$ cm^{-3}, which helped reduce the recycling of NiO^+) (experimental data shown as black triangles, with the black solid line as the model fit); and finally c) the limiting case of $Ni^+ + O_3$ if no recycling back to Ni via R4.2a took place (black dashed line). Experimental conditions: pressure = 1.0 Torr, T = 294 K.

4.2 Kinetics of NiO^+

4.2.1 Flow tube model

The kinetic model was constructed to detail both the gas-phase reactions of the ions (and the neutral atom equivalent) as well as their loss on the flow tube walls. The wall loss rate for each ion was computed from its diffusion coefficient (k_{diff}) in He [*Rees*, 1989]:

$$D = \frac{k_B T}{2.21 n \pi \mu} \sqrt{\frac{\mu}{\alpha e^2}} \quad \text{(E4.2)}$$

with the wall loss rate then given by

$$k_{\text{diff}} = D \frac{5.81}{Pr^2} \quad \text{(E4.3)}$$

where in E4.2, T is temperature of the system, μ is the reduced mass of the ion and He, α represents the polarizability of He, e is the charge, n is the He concentration, and in E4.3, P is the pressure in the tube and r is the radius of the flow tube [*Woodcock et al.*, 2006]. The wall losses for Ni^+, NiO^+ and NiO_2^+ (k_{diff}) were 661, 656 and 653 s^{-1}, respectively, at conditions of 1 Torr and 294 K. The Ordinary Differential Equations (ODEs) (E4.4 – 4.6) which describe the wall loss processes and reactions R4.1 - R4.3 were solved numerically with the use of a 4th-order Runge-Kutta algorithm.

$$\frac{d[Ni^+]}{dt} = -k_1[Ni^+][O_3] + k_{2a}[NiO^+][O_3] - k_{diff[Ni^+]}[Ni^+] - k_9[Ni^+][H_2O] - k_7[Ni^+][O_2] \quad \text{(E4.4)}$$

$$\frac{d[NiO^+]}{dt} = +k_1[Ni^+][O_3] - (k_{2a} + k_{2b})[NiO^+][O_3] - k_{diff[NiO^+]}[NiO^+] - k_{11}[NiO^+][H_2O] + k_{14}[NiO^+][O_2] \quad \text{(E4.5)}$$

$$\frac{d[NiO_2{}^+]}{dt} = +k_{2b}[NiO^+][O_3] - (k_{3a} + k_{3b})[NiO_2{}^+][O_3] - k_{diff[NiO_2{}^+]}[NiO_2{}^+] + k_7[Ni^+][O_2] \quad \text{(E4.6)}$$

E4.4 – E4.6 represent the key coupled rate coefficients deployed in the kinetic model. The complete model also includes coupled rate equations for all the reagents studied. This was allowed because the concentrations of the reagents are orders of magnitude higher than the ablated Ni^+ (and Ni for the neutral kinetics). Therefore, they can be considered constant and their corresponding coupled equations are excluded here.

To adequately replicate the conditions of the experiment as closely as possible (i.e. sampling over a set range of times, several ms after injection of O_3 into the Ni^+/He flow) the slope of $ln\left(\frac{[Ni_t^+]_X}{[Ni_t^+]_0}\right)$ against *t* was applied to retrieve *k′* for each measured [O_3]. *k′* was determined from model output sampled at *t* = 3.75 and 5.00 ms, which were the set reaction times of the experiment by varying the sliding injector distance in relation to the skimmer cone of the mass spectrometer. The reason for choosing these times was that over this time interval the Ni^+ decay was observed to be first-order, except for when low [O_3] (<10^{12} cm^{-3}) was present in the absence of H_2O. From there a comparison was made between the modelled *k′* values and the experimental data, for experiments measured both with and without H_2O (shown as the solid and dotted lines in Figure 4.3). A third fit in (dashed straight line) Figure 4.3 was also included where the only reaction is $Ni^+ + O_3 \rightarrow$ products i.e. there is no recycling effect by reaction R4.2a. This fit passes through the steepest part of the curve of the experimental data with added H_2O, at [O_3] less than 1×10^{12} molecule cm^{-3}.

The kinetic model was fitted to the experimental data both manually and through use of a Monte Carlo method. The rate coefficient for reaction $Ni^+ + O_3$, k_1, was first increased until the initial steep part of the model curve matched up with the experimental data. In this range, R4.11 with H_2O shuts down the recycling process of NiO^+. To help reinforce the fitted rate of k_1, it was combined with similar fits obtained in experiments that also use k_1, $NiO^+ + CO$ (R4.4) and $NiO^+ + O$ (R4.5) (Sections 4.3.2 and 4.3.4). The combination of all 3 experiments yielded a $k_{4.1}(294\ K) = (9.7 \pm 2.1) \times 10^{-10}\ cm^3\ molecule^{-1}\ s^{-1}$. As well as this, the second-order rate coefficient for $NiO^+ + H_2O$ at 1 Torr was determined to be $(6.2 \pm 3.0) \times 10^{-10}\ cm^3\ molecule^{-1}\ s^{-1}$ (close agreement to the theoretical estimate of this reaction discussed in Section 4.6).

If there was significant recycling of the higher oxides, NiO_x^+ (x = 2, 3 …), occurring through reaction with O_3, then the model fits would lose all correlation to the data with and without H_2O. To allow the model to fit the data, only (16 ± 9%) of NiO_2^+ recycling to NiO^+ through R4.3 was allowed, and (29 ± 20%) of NiO^+ recycling to Ni^+ through R4.2 was used. The final uncertainties for the rate coefficients $k_{4.2a}$, $k_{4.2b}$, $k_{4.3a}$ and $k_{4.3b}$ were determined by fitting each individual data point and from there calculating the mean and standard deviation of the fitted values (final value shown in Table 4.1).

The model examining the neutral kinetics of NiO has largely a similar structure to the NiO^+ model discussed here. The main difference for the neutral species is the lack of clustering that is present for the Ni^+ and NiO^+ ions. For example, with the Ni^+ model involving atomic O, formation of $Ni^+.N_2$ ion and reaction of this species with O needs to be accounted for since N_2 is required for the

discharge. However, this reaction is not an issue for neutral Ni, therefore this reaction is not included in the model list.

4.2.2 Reaction of NiO^+ with CO

R4.5 was studied by injecting CO using the sliding injector 0.5 cm upstream of the fixed O_3 injection into the carrier gas flow. In order to measure $k_{4.5}$, the ratio of [CO]/[O_3] was varied against each other, a similar methodology to that done for FeO^+ + CO and CaO^+ + CO, with the N_2O substituted for O_3 in this experiment [*Broadley et al.*, 2008; *Woodcock et al.*, 2006]. The recycling of Ni^+ was modelled with the use of the rate coefficients and branching ratios for R4.1 – R4.3 that were fitted in Section 4.2 of this Chapter. Figure 4.4 below illustrates the fractional recovery in Ni^+ signal (where 0 represents the Ni^+ signal when [CO] = 0) against the ratio of [CO]/[O_3]. With the ratio increasing >50, the percentage recovery starts to plateau around 75-80%, evident in the experimental data and was reproducible in the modelled data. $k_{4.5}$(NiO + CO) was then obtained by fitting the model rate to each individual data point in Figure 4.4. After the model fits to each data point, the average and standard deviation of the fitted values was calculated, yielding $k_{4.5}$(NiO + CO, T = 294 K) = (7.4 ± 1.3) × 10^{-11} cm^3 $molecule^{-1}$ s^{-1}. For the kinetics of NiO^+ and NiO in this chapter, there was a trace leak of H_2O in the system of ~30 mTorr min^{-1}. Therefore, an additional reaction step between the metal oxide and H_2O was included in each model to view its effect but the computed leak was too low (5 × 10^9 molecule cm^{-3}) to affect the model fit.

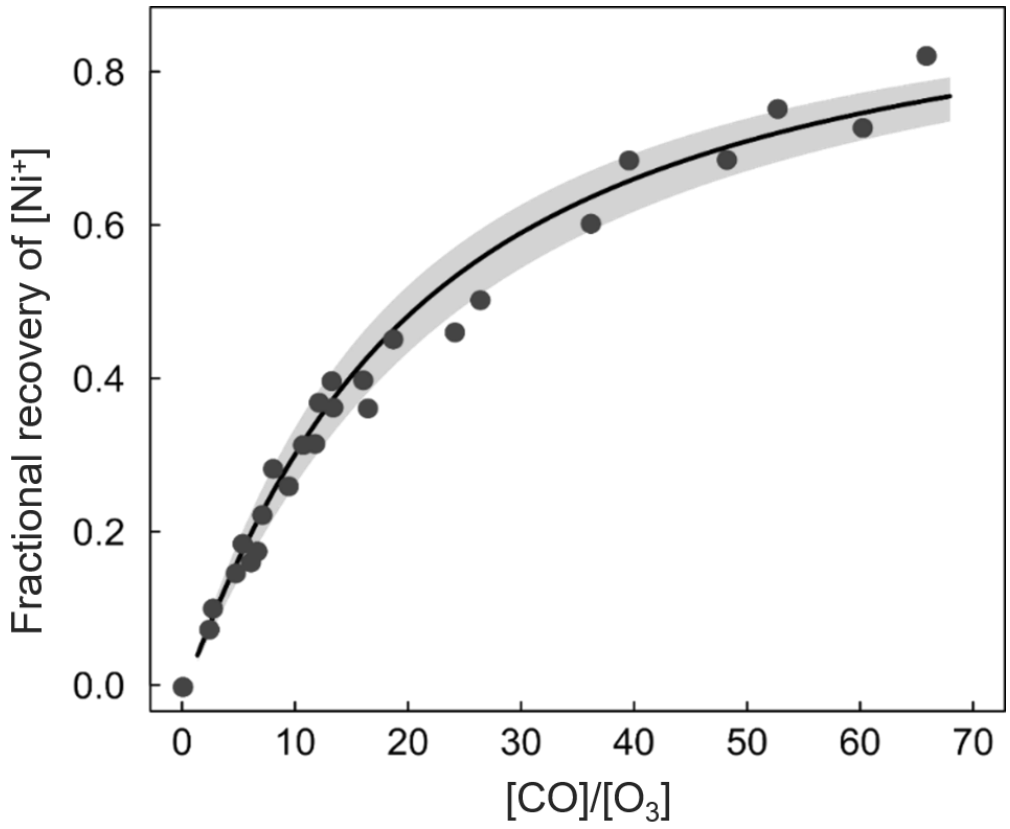

Figure 4.4. Plot of the fractional recovery in [Ni^+] against ratio of [CO]/[O_3]. The solid points are the measured experimental points, and the solid black line is the model fit with the ±1σ uncertainty shown by the shaded region. Experimental conditions: P = 1 Torr; *T* = 294 K.

4.2.3 Reaction of NiO^+ with O

Reacting NiO^+ with atomic O recycles the molecular ion back to Ni^+. The NiO^+ ions are first created in the presence of O_3 via R4.1, leading to depletion of [Ni^+] which is then followed by an increase in [Ni^+] when O is injected. This difference can be used to obtain $k_{4.4}$(NiO + O). Following previous work done by *Whalley and Plane* [2010], it is much easier to maintain a constant [O], accurately measuring the set concentration and wall loss rate (discussed in Chapter 2) the change in Ni^+ signal was measured for a range of [O_3]. Applying

a fixed [O_3] with varied [O] would prove more difficult as there is much less control in varying atomic O. The [O_3] is largely stable 2 - 3 minutes after the O_2 flow is changed. The O concentration in Figure 4.5 was maintained at 9.2 × 10^{12} molecules cm^{-3}. Similar to NiO + CO, the recycling of Ni^+ was modelled using the both rate coefficients and branching ratios for R4.1 – R4.3, but also accounting for the measured wall loss of O (470 ± 65 s^{-1}).

As discussed in Chapter 2, the atomic O is generated from the microwave discharge of N_2 in a glass/quartz cavity. The amount passed through the discharge tube was ~300 sccm which is 8-11% of the total flow. Ni^+ ions do undergo recombination reaction with N_2 to form $Ni^+.N_2$ through reaction R6. This ion can then react further with atomic O:

$$Ni^+.N_2 + O \rightarrow NiO^+ + N_2 \qquad \Delta H^o = -112 \text{ kJ mol}^{-1} \qquad \text{(R4.12)}$$

The contribution of R4.12 is significant enough, that at the low end [O_3] range in Figure 4.5, the $Ni^+ + N_2$ reaction was faster than $Ni^+ + O_3$, with the $Ni^+.N_2$ ion becoming a significant reservoir species. The flow tube model described in Section 4.3.1 was modified to accommodate the rate of R4.4 ($NiO^+ + O$) to the ODE's of E4.4 and E4.5, followed by addition of another ODE to detail the formation and removal of the $Ni^+.N_2$ ion reactions R4.6 and R4.12. To be able to measure both rates, $k_{4.4}$ and $k_{4.12}$ were fitted to each data point in Figure 4.5 separately using the flow tube kinetic model. The mean and standard deviation of the fitted data points was calculated, yielding $k_{4.4}$($NiO^+ + O$, 294 K) = (1.7 ± 1.2) × 10^{-10} cm^3 $molecule^{-1}$ s^{-1}, and $k_{4.12}$($Ni^+.N_2 + O$, 294 K) = (7 ± 4) × 10^{-12} cm^3 $molecule^{-1}$ s^{-1}.

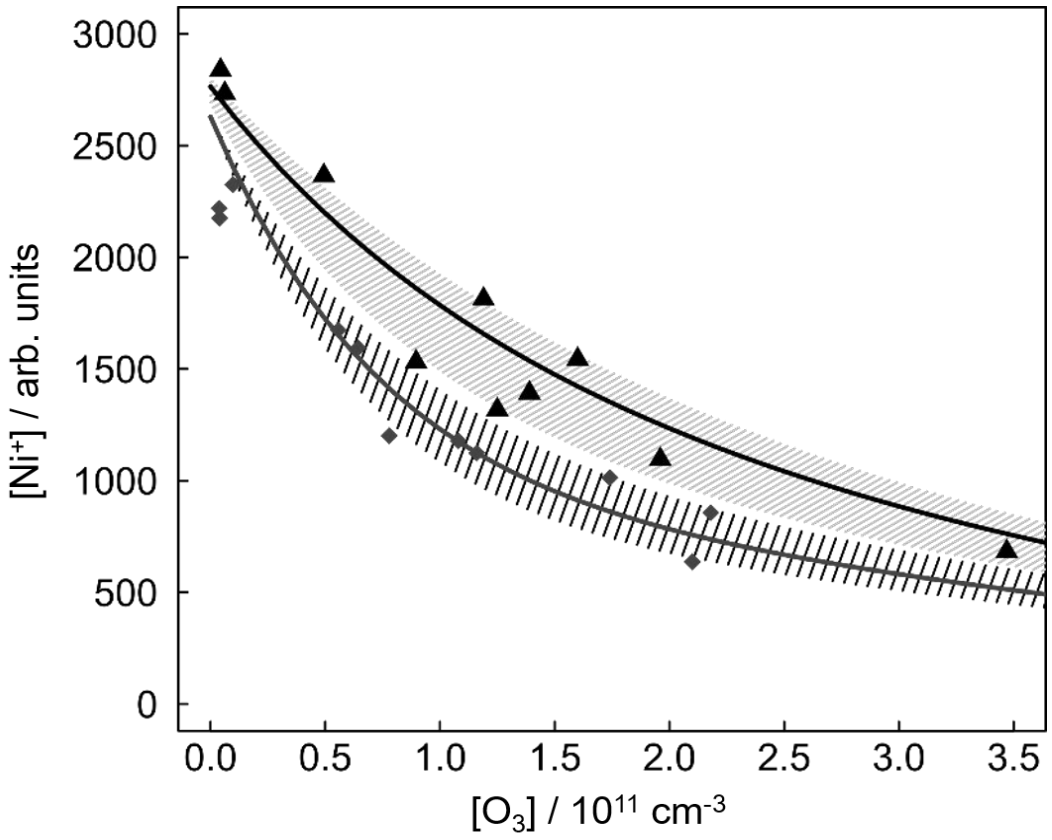

Figure 4.5. $[Ni^+]$ as a function of increasing $[O_3]$, showing the increased recycling of Ni^+ when [O] is present. The experimental points (black triangles) and model fit (black line) show the $[Ni^+]$ amount in the presence of fixed [O] = 9.2×10^{12} molecule cm^{-3}. This was then compared to the experimental points (grey diamonds) and model fit (grey line) with no [O]. The shades envelopes (thick grey lines for $[Ni^+]$ with no O present and thin light grey lines for $[Ni^+]$ in the presence of [O]) depict the ±1σ uncertainties of the model fits. Experimental conditions: 1 Torr; T = 294 K; $[N_2] = 3 \times 10^{15}$ cm^{-3}

4.3 Neutral kinetics of NiO and NiO_2

A similar kinetic model to that used for the NiO^+ kinetics was deployed here for NiO. As discussed in Section 4.3.1, clustering with N_2 is not an issue with neutral Ni, therefore N_2 was used as a carrier flow for the experiment instead of He. The Ni first-order wall loss rate was quantified to be 150 ± 22 s^{-1}. For the oxides, NiO and NiO_2, an estimated loss rate of 130 s^{-1} was calculated based from the long-range capture forces between these oxides and N_2, a method described by *Self and Plane* [2003]. The atomic O wall loss rate for these experiments was measured to be (231 ± 31 s^{-1}), taken from 7 separate O diffusion measurements (see Chapter 2). Determination of the rate coefficient here was done similarly to the molecule ion reactions (see Section 4.3), by evaluating the average value and uncertainty of each reaction rate coefficient through independently fitting to each experimental data point in the reaction, and then calculating the mean and standard deviation.

4.3.1 Reaction of NiO with CO

Ni atoms were initially ablated from a Ni rod, followed by addition of O_3 at a point 7 cm downstream of the metal rod to form the NiO molecule through reaction between Ni and O_3 [*Mangan et al.*, 2019]. CO was then added 0.5 cm upstream of the O_3 point of injection via sliding injector. This resulted in a reaction time of 5 ms from the sliding injector to the LIF detection point. The same method used to measure $k_{4.5}$ is used here to measure $k_{4.14}$, by varying [CO] at a fixed [O_3] and observing the resulting change in fractional recovery of [Ni^+]. The experimental points with model line fit and uncertainty envelope

are shown in Figure 4.6 below. The recycling of Ni was modelled out by using the rate coefficients and branching ratios for Ni and NiO reacting with O_2 and O_3 determined previously by *Mangan et al.* [2019] (in cm^3 $molecule^{-1}$ s^{-1}): k(Ni + O_3, 294 K) = (6.5 ± 0.7) × 10^{-10}; k(NiO + O_3 → Ni + $2O_2$, 294 K) = (1.4 ± 0.5) × 10^{-10}; k(NiO + O_3 → NiO_2 + O_2, 294 K) = (2.5 ± 0.7) × 10^{-10}; k(Ni + O_2 + N_2, 1 Torr, 294 K) = (1.2 ± 0.1) × 10^{-13}; k(NiO + O_2 + N_2, 1 Torr, 294K) = (4.0 ± 0.9) × 10^{-14}. The model fit accurately fits to the experimental data, yielding a value $k_{4.14}$(NiO + CO, 294 K) = (3.0 ± 0.5) × 10^{-11} cm^3 $molecule^{-1}$ s^{-1}, shown in Figure 4.6. This measured rate is also in very good agreement with the only previous study of R14 done using a pulsed laser photolysis-laser induced fluorescence (PLP-LIF) technique in a slow flow reactor [*Mangan et al.*, 2019]. The value reported there was $k_{4.14}$(NiO + CO, 190−377 K) = (3.2 ± 0.6) × 10^{-11} (T/200)$^{-0.19\pm0.05}$ cm^3 $molecule^{-1}$ s^{-1}. When applying the same temperature for both rate coefficients, $k_{4.14}$(NiO + CO, 294 K) = (3.0 ± 0.6) × 10^{-11} cm^3 $molecule^{-1}$ s^{-1}, the same number measured in the fast flow tube here, with slightly larger uncertainty.

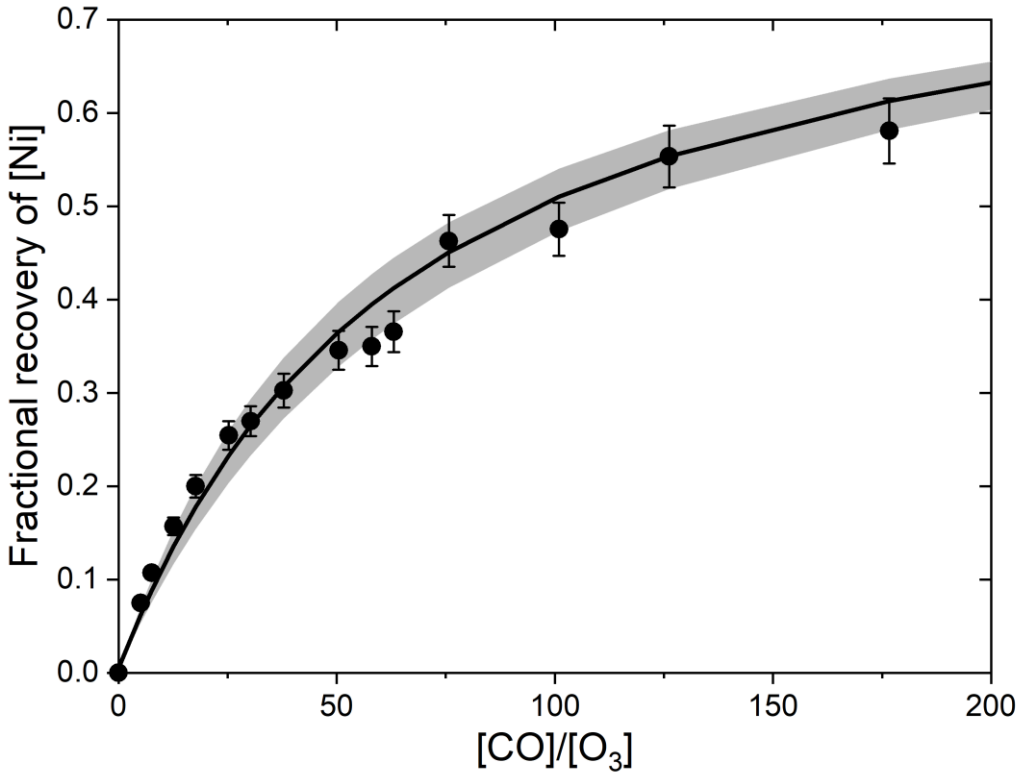

Figure 4.6. Fractional recovery of [Ni] plotted against [CO]/[O_3], where [O_3] is fixed at 1.8 × 10^{12} cm^{-3}. The solid black points are the experimental data with their individual error bars, while the solid black line is the model fit with ±1σ uncertainty (shaded region). Conditions: P: 1 Torr; *T* = 294 K.

4.3.2 Reactions of NiO and NiO_2 with O

Following a similar reaction method to NiO^+ + O (section 4.3.3), a constant [O] was injected against a range of [O_3], illustrated in Figure 4.7 below. NiO was formed first by reaction of the ablated Ni and O_3, with the open triangles in Figure 4.7(b) indicating the Ni signal decay with O_3 (varied from (0.3 – 1.3) × 10^{12} molecule cm^{-3} with an uncertainty of ~±10%). Figure 4.7(a) shows the Ni decay (open triangles) over a range of [O_2] to form NiO_2 [*Mangan et al.*, 2019]. The solid black points of both Figure 4.7 (a) and (b) are the experimental points with a fixed value of 9.2 × 10^{12} molecule cm^{-3} added at the point of

injection, with both plots showing a level of Ni signal recovery. NiO_2 is also formed through reaction of NiO with O_3, therefore the rate, $k_{4.15}(NiO_2 + O)$, needing measuring first in order to fit $k_{4.13}(NiO + O)$ in the flow tube model. Since the O_3 was injected through a side port of the flow tube, a mixing time of 1.5 ms was accounted for in the model, which was estimated as the time it took for O_3 to diffuse 1 cm across the flow tube with $D(O_3\text{-}N_2 = 134$ cm^2 s^{-1} at 1 Torr [*Langenberg et al.*, 2019]. The model fit through the experimental points of Figure 4.7(a) yielded a rate of $k_{4.15}(NiO_2 + O, 294\ K) = (2.5 \pm 1.2) \times 10^{-11}$ cm^{-3} molecule s^{-1}. For Figure 4.7(b), the model fit computed a value of $k_{4.13}(NiO + O, 294\ K) = (4.6 \pm 1.4) \times 10^{-11}$ cm^3 molecule^{-1} s^{-1}.

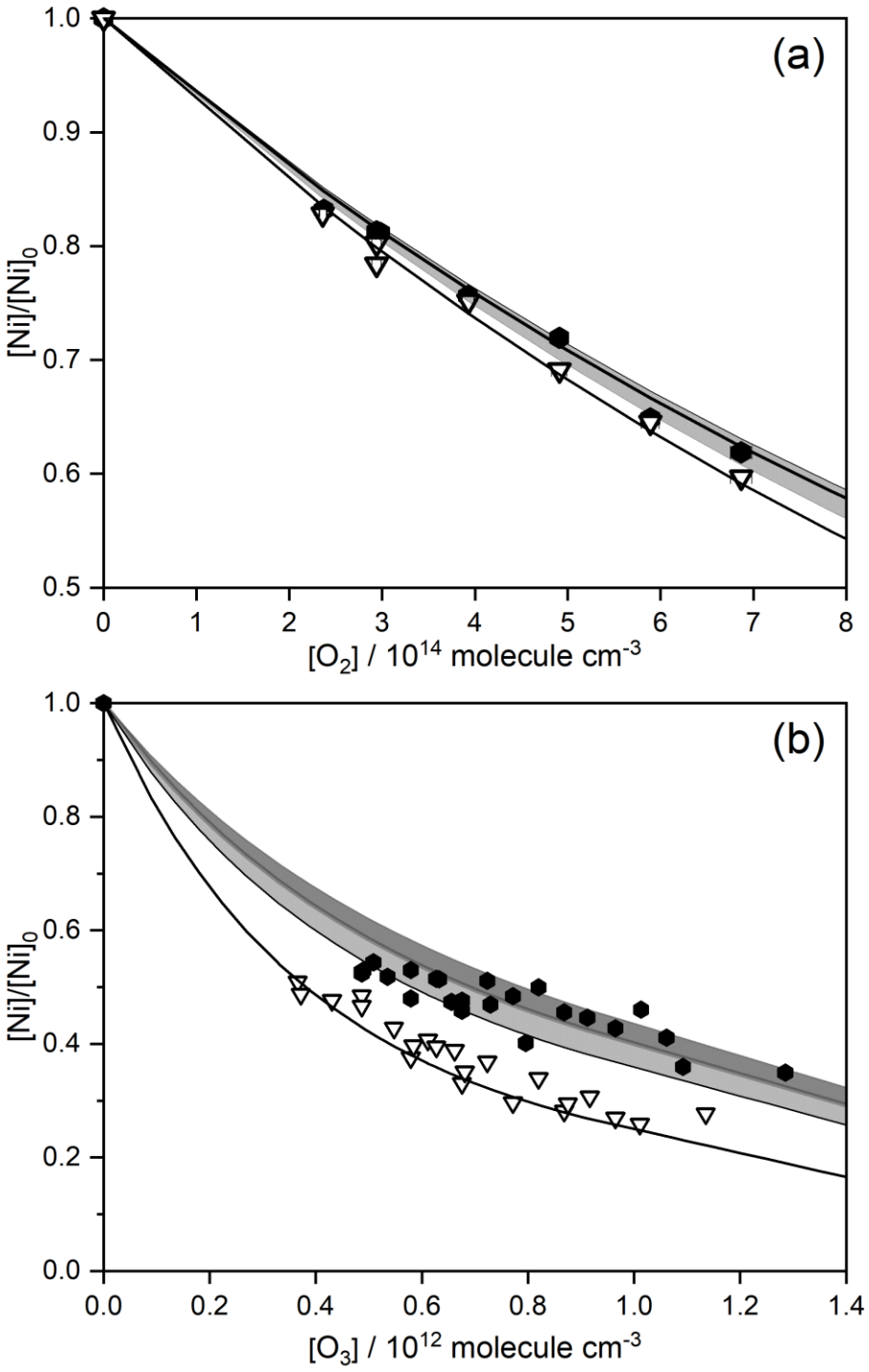

Figure 4.7. (a) Plot of $[Ni]/[Ni]_0$ against $[O_2]$, where $[Ni]_0$ is the concentration at $[O_2] = 0$. The $[O_2]$ was varied from 2 – 7 × 10^{14} cm^{-3}, while (b) shows a plot of [Ni] as a function of $[O_3]$, ranging from ~4 – 13 × 10^{11} cm^{-3}. The symbols indicate the same treatment in both plots, with the solid black points as the experimental data with a fixed addition of atomic O ([O] = 9.2 × 10^{12} molecule

cm^{-3} at injection point); while the open triangles show data in the absence of O. The solid black lines represent the model fits through each dataset while the shaded area of the model fit in the presence of O represents the ±1σ limits. Conditions: 1 Torr, *T* = 294 K.

Table 4.1 below summarizes all the reactions measured in this study which will subsequently be added into the WACCM-Ni model.

Table 4.1. Summary of reaction ion molecule (R4.1 – R4.12) and neutral (R4.13 – R4.15) rate coefficients measured in the present study (*T* = 294 K).

No.	Reaction	Rate coefficient [a]
R4.1	$Ni^+ + O_3 \rightarrow NiO^+ + O_2$	$(9.7 \pm 2.1) \times 10^{-10}$
R4.2a	$NiO^+ + O_3 \rightarrow Ni^+ + 2O_2$	$(7.8 \pm 2.9) \times 10^{-11}$
R4.2b	$NiO^+ + O_3 \rightarrow NiO_2^+ + O_2$	$(1.9 \pm 0.7) \times 10^{-10}$
R4.3a	$NiO_2^+ + O_3 \rightarrow NiO^+ + 2O_2$	$(4.6 \pm 2.2) \times 10^{-11}$
R4.3b	$NiO_2^+ + O_3 \rightarrow ONiO_2^+ + O_2$	$(2.4 \pm 1.2) \times 10^{-10}$
R4.4	$NiO^+ + O \rightarrow Ni^+ + O_2$	$(1.7 \pm 1.2) \times 10^{-10}$
R4.5	$NiO^+ + CO \rightarrow Ni^+ + CO_2$	$(7.4 \pm 1.3) \times 10^{-11}$
R4.6	$Ni^+ + N_2$ (+He) $\rightarrow Ni^+.N_2$	$(3.5 \pm 0.5) \times 10^{-30}$
R4.7	$Ni^+ + O_2$ (+He) $\rightarrow Ni^+.O_2$	$(2.8 \pm 0.5) \times 10^{-30}$
R4.8	$Ni^+ + CO_2$ (+He) $\rightarrow Ni^+.CO_2$	$(7.7 \pm 1.0) \times 10^{-29}$
R4.9	$Ni^+ + H_2O$ (+He) $\rightarrow Ni^+.H_2O$	$(1.3 \pm 0.2) \times 10^{-28}$
R4.11	$NiO^+ + H_2O \rightarrow NiO^+.H_2O$	$(6.2 \pm 3.0) \times 10^{-10}$
R4.12	$Ni^+.N_2 + O \rightarrow NiO^+ + N_2$	$(7 \pm 4) \times 10^{-12}$

R4.13	$NiO + O \rightarrow Ni + O_2$	$(4.6 \pm 1.4) \times 10^{-11}$
R4.14	$NiO + CO \rightarrow Ni + CO_2$	$(3.0 \pm 0.5) \times 10^{-11}$
R4.15	$NiO_2 + O \rightarrow NiO + O_2$	$(2.5 \pm 1.2) \times 10^{-11}$

[a] Units for bimolecular reactions: cm^3 $molecule^{-1}$ s^{-1}. Units for termolecular reactions: cm^6 $molecule^{-2}$ s^{-1}. The stated uncertainties are 1σ.

4.4 Discussion

To help better under the experimental results and extrapolate to the conditions of both Earth and Mars' atmospheres, a series of electronic structure calculations were performed with the use of b3lyp/aug-cc-pVQZ theory within the Gaussian 16 suite of programs [*Frisch et al.*, 2016].

4.4.1 $Ni^+ + O_3$, $NiO^+ + O_3$, $NiO^+ + CO$, and $NiO^+ + O$

The measured rate of R4.1 ($Ni^+ + O_3$) in this chapter was very fast, with $k_{4.1}(294\ K) = (9.7 \pm 2.1) \times 10^{-10}$ cm^3 $molecule^{-1}$ s^{-1}. The reaction is ~20% faster than the Langevin capture rate of 8.1×10^{-10} cm^3 $molecule^{-1}$ s^{-1}, but within the experimental uncertainty recorded. The modest dipole moment of O_3 of 0.53 D [*Lide*, 2006] may helped enhanced its capture by Ni^+ leading to a value faster than the capture rate. This effect was also observed for $Al^+ + O_3$ in Chapter 3. Two methods have been used to try predict this higher rate coefficient. Firstly, the effect of the charge-permanent dipole interaction could be estimated using the method formulated by [*Su and Chesnavich*, 1982], based on trajectory calculations, yielding a $k_{4.1}(Ni^+ + O_3, 294\ K) = 9.8 \times 10^{-10}$ cm^3 $molecule^{-1}$ s^{-1}, which closely agrees with the measured value. The

statistical adiabatic channel model of *Troe* [1985] with application of the rotational constant for O_3 of 0.428 cm^{-1} (estimation of this discussed in Chapter 3), gave a value of $k_{4.1}(294\ K) = 1.1 \times 10^{-9}\ cm^3\ molecule^{-1}\ s^{-1}$, which was slightly higher than the measured rate but still within the uncertainty. Both methods also predict a slight negative temperature dependence for the reaction. Combining that with the experimental value measured at 294 K yielded a rate of: $k_{4.1}(100 – 300\ K) = 9.7 \times 10^{-10}\ (T/200)^{-0.16}\ cm^3\ molecule^{-1}\ s^{-1}$.

R4.1 is very exothermic at 125 kJ mol^{-1}, with the NiO^+ product potentially being produced in 9 low-lying electronic states, in addition to the its ground state [*Sakellaris and Mavridis*, 2013]. When determining the rate coefficients for the NiO^+ reactions, the kinetic model had to assume that the NiO^+ is largely ablated in the ground state or the alternative was rapidly quenching of the higher electronic states in 1 Torr of N_2. The rate coefficient, $k_{4.2}(NiO^+ + O_3)$ was determined to be about 35% of the Langevin capture rate for that reaction. Both branching ratios of the reaction are exothermic (see bond energy calculations in Section 4.1); with the higher exothermic channel of R4.2b yielding the $NiO_2^+ + O_2$ product and producing a larger branching ratio ($f_{4.2b}$ = 71%). When compared to other metal analogues, the branching ratio producing FeO_2^+ from $FeO^+ + O_3$ is the least dominant of the two channels at 39% [*Melko et al.*, 2017], and for MgO_2^+ formed from the reaction of $MgO^+ + O_3$, the ratio measures in at 65% [*Whalley et al.*, 2011]. For the higher oxides, the more exothermic channel of the NiO_2^+ and O_3 reaction (R4.3) produced $ONiO_2^+ + O_2$ (Section 4.1 again) with an even higher branching ratio (f_{3b} = 84%). This is highly contrasting to the Fe counterpart, where the $FeO_3^+ + O_2$

product from the analogues reaction is close to thermoneutral, with the resulting branching ratio as only 21% [*Melko et al.*, 2017]. The rate coefficients and branching ratios of R4.1 – 4.3 been studied previously in a selected-ion flow tube by *McDonald et al.* [2018]. In their study, a measured rate of $k_{4.1}$(300 – 500 K) = (11 ± 2) × 10^{-10} cm^3 $molecule^{-1}$ s^{-1} was achieved, which is in close agreement with the measured rate of $k_{4.1}$ in this chapter. An earlier study by *Božović et al.* [2010] stated that $k_{4.1}$ proceeded at 40% of the collisional rate at room temperature but further examination by *McDonald et al.* [2018] showed that the other group did not account for the recycling of NiO^+ with O_3 (R4.2a) which is accounted for in this study, justifying the difference in rate. The branching ratio for R4.2a in this work was $f_{4.2a}$ = (29 ± 14%), which is in the range of the uncertainty determined by *McDonald et al.* [2018] at (40 ± 20)%. For the higher oxide rates however, there are differences between the two experimental works. The combined rate of $k_{4.2}$ in this work is (2.7 ± 0.8) × 10^{-10} cm^3 $molecule^{-1}$ s^{-1} which is outside the uncertainty range of the very fast rate of (9.5 ± 3.0) × 10^{-10} cm^3 $molecule^{-1}$ s^{-1} measured by *McDonald et al.* [2018]. For R4.3, the rate $k_{4.3}$ = (2.9 ± 1.2) × 10^{-10} cm^3 $molecule^{-1}$ s^{-1} just about agrees with the lower limit of (10 ± 7) × 10^{-10} cm^3 $molecule^{-1}$ s^{-1} measured by *McDonald et al.* [2018], however the branching ratios of that reaction do not, with their $NiO^+ + 2O_2$ product channel, $f_{4.3a} = 85^{+10}_{-40}$, whereas the same channel $f_{4.3a}$ in this study is much lower at (16 ± 10)% but with a much lower uncertainty.

If the rate coefficients and branching ratios for R4.1 – 4.3 are taken from the study by *McDonald et al.* [2018] and applied to the kinetic model used in this study (see Figure 4.8 below), the newly *k′* modelled values do achieve a fit to the experimental data when [H_2O] is added (black triangle symbols of Figure

4.3), largely down to the similar $k_{4.1}$ values and the near inhibition of R4.2 – R4.3. However, when [H_2O] is absent (grey diamond symbols of Figure 4.3), no match between the modelled and experimental data is achieved since the new *k′* modelled values in relation to O_3 are much higher in rate than the experimental points due to the differences in rate of the higher oxides reactions in both studies.

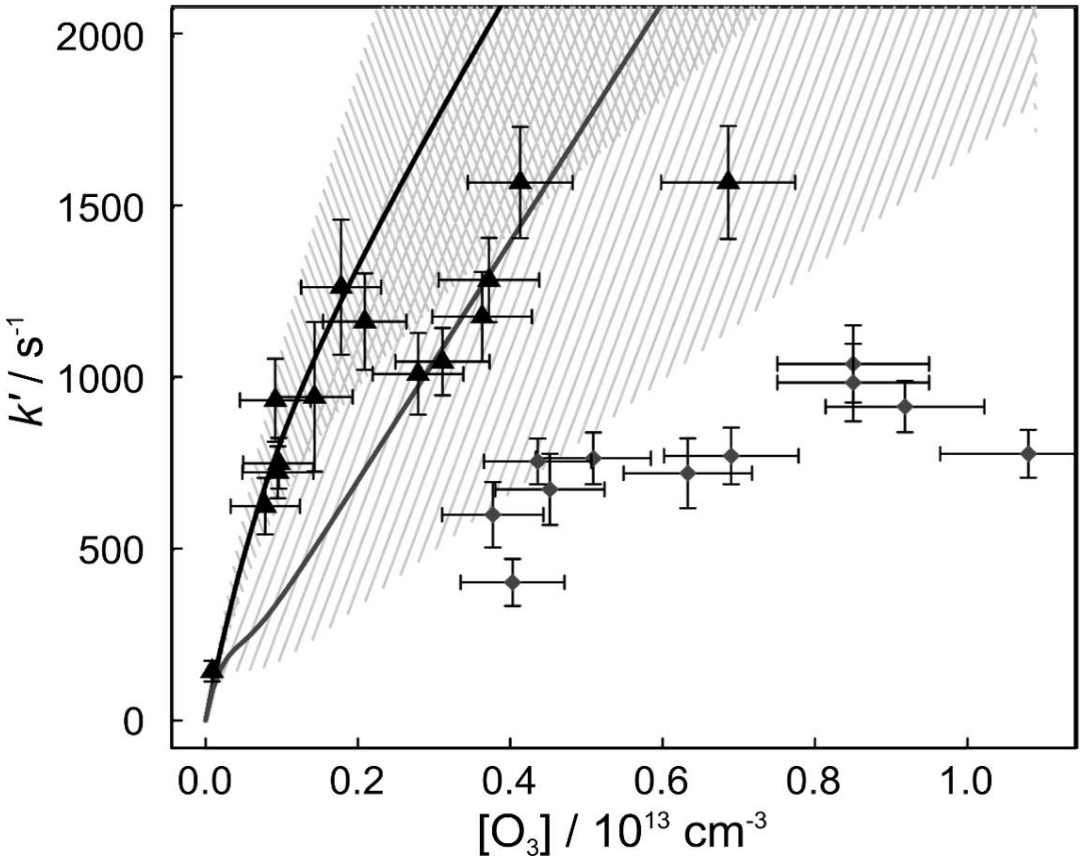

Figure 4.8. Kinetic plot of experimental data from this study of R4.1, compared with the flow tube kinetic model with the rate coefficients from *McDonald et al.* [2018] substituted in (original fitted rate coefficients shown in Figure 4.3). Lower grey line indicates the model fit with no [H_2O] added; upper grey line illustrates the fit with [H_2O] added. The shaded envelopes represent the possible range in the modelled values if the uncertainties for the R4.1 and

R4.2 coefficients plus that of the branching ratio for R4.2 are included. See Figure 4.3 for further details of the plot.

The rate coefficient for NiO^+ + CO measured in this study came to $k_{4.5}$(294 K) = (7.4 ± 1.3) × 10^{-11} cm^3 $molecule^{-1}$ s^{-1}. When compared to other measured metallic ions: ~2.2 times slower than FeO^+ equivalent at k(FeO^+ + CO) = (1.59 ± 0.34) × 10^{-10} cm^3 $molecule^{-1}$ s^{-1} [*Woodcock et al.*, 2006] and ~3.8 times slower than k(CaO^+ + CO) = (2.8 ± 1.5) × 10^{-10} cm^3 $molecule^{-1}$ s^{-1} [*Broadley et al.*, 2008]. It is also 5 times slower than k(AlO^+ + CO) = (3.7 ± 1.1) × 10^{-10} cm^3 $molecule^{-1}$ s^{-1} measured in Chapter 3.

The reaction of NiO^+ + O was measured at a rate of $k_{4.4}$(294 K) = (1.7 ± 1.2) × 10^{-10} cm^3 $molecule^{-1}$ s^{-1}., which is almost exactly the same as the rate coefficient measured k(AlO^+ + O) in Chapter 3. This was 5.3 times faster the FeO^+ equivalent where k(FeO^+ + O) = ((3.2 ± 1.5) × 10^{-11} cm^3 $molecule^{-1}$ s^{-1}) [*Woodcock et al.*, 2006] and ~4 times the rate of CaO^+ with k(CaO^+ + O) = (4.2 ± 2.8) × 10^{-11} cm^3 $molecule^{-1}$ s^{-1} [*Broadley et al.*, 2008]. Only the MgO^+ analogue achieves a faster rate, with k(MgO^+ + O) = (5.9 ± 2.4) × 10^{-10} cm^3 $molecule^{-1}$ s^{-1} [*Whalley and Plane*, 2010].

4.4.2 NiO + O, NiO + CO, and NiO_2 + O

The reaction of $k_{4.14}$(NiO + CO) = (3.0 ± 0.5) × 10^{-11} cm^3 $molecule^{-1}$ s^{-1} is ~210 times faster than the analogues reaction of FeO + CO with a k(FeO + CO, 294 K) = 1.5 × 10^{-13} cm^3 $molecule^{-1}$ s^{-1}. The result is in very good agreement with the only previous study of R4.14 measured by *Mangan et al.* [2019], where

$k_5(190 - 377\ K) = (3.2 \pm 0.6) \times 10^{-11} (T/200)^{-0.19\pm0.05}$ cm^3 molecule^{-1} s^{-1}, i.e. at $k_5(294\ K) = (3.0 \pm 0.6) \times 10^{-11}$ cm^3 molecule^{-1} s^{-1}.

The reduction of NiO to Ni via atomic O yielded a rate, $k_{4.13}$(NiO + O, 294 K) = (4.6 ± 1.4) × 10^{-11} cm^3 molecule^{-1} s^{-1} is one of the slowest measured rates recorded from the meteoric metal range to date. It is ~3 times slower than the Fe equivalent at k(FeO + O, 294 K) = 1.4 × 10^{-10} cm^3 molecule^{-1} s^{-1} [*Self and Plane*, 2003], ~3.5 times slower than k(NaO + O) = 1.6 × 10^{-10} cm^3 molecule^{-1} s^{-1}, ~7 times slower than k(CaO + O) = 3.1 × 10^{-10} cm^3 molecule^{-1} s^{-1} [*Broadley and Plane*, 2010] and more than an order of magnitude slower than k(MgO + O) = 6.2 × 10^{-10} cm^3 molecule^{-1} s^{-1} measured by *Whalley and Plane* [2010]. In contrast, R4.15 yielded a rate of $k_{4.15}$(NiO$_2$ + O, 294 K) = (2.5 ± 1.2) × 10^{-11} cm^{-3} molecule s^{-1}. which is 24%, 20% and 12% faster than the respective analogue rates of Fe (1.9 × 10^{-11} cm^3 molecule^{-1} s^{-1}), Na (k(NaO$_2$ + O) = 2.0 × 10^{-11} cm^3 molecule^{-1} s^{-1}) and Ca (k(CaO$_2$ + O) = 2.2 × 10^{-11} cm^3 molecule^{-1} s^{-1}), with only the Mg equivalent coming out faster, k(MgO$_2$ + O) = 7.9 × 10^{-11} cm^3 molecule^{-1} s^{-1}, ~3 times faster than R4.15.

4.4.3 Ni$^+$ + N$_2$, O$_2$, CO$_2$ and H$_2$O

The recombination of Ni$^+$ with N$_2$ ($k_{4.6}$) does not appear to have a previously reported rate coefficient. However the formation of the product ion (Ni$^+$.N$_2$) has been reported in a separate study involving a ring electrode trap [*Schlemmer et al.*, 2003]. The equivalent reaction with O$_2$ has been studied however, with the use of a selected ion flow tube setup [*Koyanagi et al.*, 2002]. There, a bimolecular rate coefficient of 2.0 × 10^{-13} cm^3 molecule^{-1} s^{-1} was measured under conditions of 0.35 Torr of He. Converting the 2nd-order to a 3rd-order rate coefficient provided a value of $k_{4.7}$ = 1.7 × 10^{-29} cm^6 molecules^{-}

^{2} s^{-1}, ~6 times faster than the value from the study in this chapter of (2.8 ± 0.5) × 10^{-30} cm^6 $molecule^{-2}$ s^{-1}. It is not clear why there is such a large difference between the two rate, however for the study by [*Koyanagi et al.*, 2002], no pressure-dependence was reported.

There no previous study found for the cluster reactions of Ni^+ with CO_2 or H_2O. However, the reaction between Ni^+ and D_2O was studied by *Cheng et al.* [2007]. In their study, the measured rate of 1.7 × 10^{-12} cm^3 $molecule^{-1}$ s^{-1} in 0.35 Torr He yields a 3rd-order rate coefficient of 1.5 × 10^{-28} cm^6 $molecule^{-2}$ s^{-1}. This reported value is ~13% higher than the value for H_2O in this study, $k_{4.9}(Ni^+ + H_2O)$ = (1.3 ± 0.2) × 10^{-28} cm^6 $molecules^{-2}$ s^{-1}.

The cluster reactions of Ni^+ (R4.6 – R4.9) could only be measured at (294 K), the rate required extrapolation to the temperatures and pressures in the MLT that are outside the experimental range. This was done using RRKM theory, which was also done for the Al^+ cluster reactions in Chapter 3, using a solution of the Master Equation (ME) based on the inverse Laplace transform method [*De Avillez Pereira et al.*, 1997] This has been done for the recombination reactions of previous metallic ions studied, including Ca^+ [*Broadley et al.*, 2007], Fe^+ [*Vondrak et al.*, 2006] and Mg^+ [*Whalley et al.*, 2011].

Table 4.2. Low-pressure limiting rate coefficients for the addition of a single ligand to an Ni^+ ion with He as third body, using RRKM theory

Reaction	**$\log_{10}(k_{rec,0}$/ cm^6 $molecule^{-2}$ s^{-1})** ***T* = 100 – 600 K**
$Ni^+ + N_2$	$-27.5009 + 1.0667\log_{10}(T) - 0.74741(\log_{10}(T))^2$

$Ni^+ + O_2$	$-27.8098 + 1.3065\log_{10}(T) - 0.81136(\log_{10}(T))^2$
$Ni^+ + CO_2$	$-29.805 + 4.2282\log_{10}(T) - 1.4303(\log_{10}(T))^2$
$Ni^+ + H_2O$	$-24.318 + 0.20448\log_{10}(T) - 0.66676(\log_{10}(T))^2$

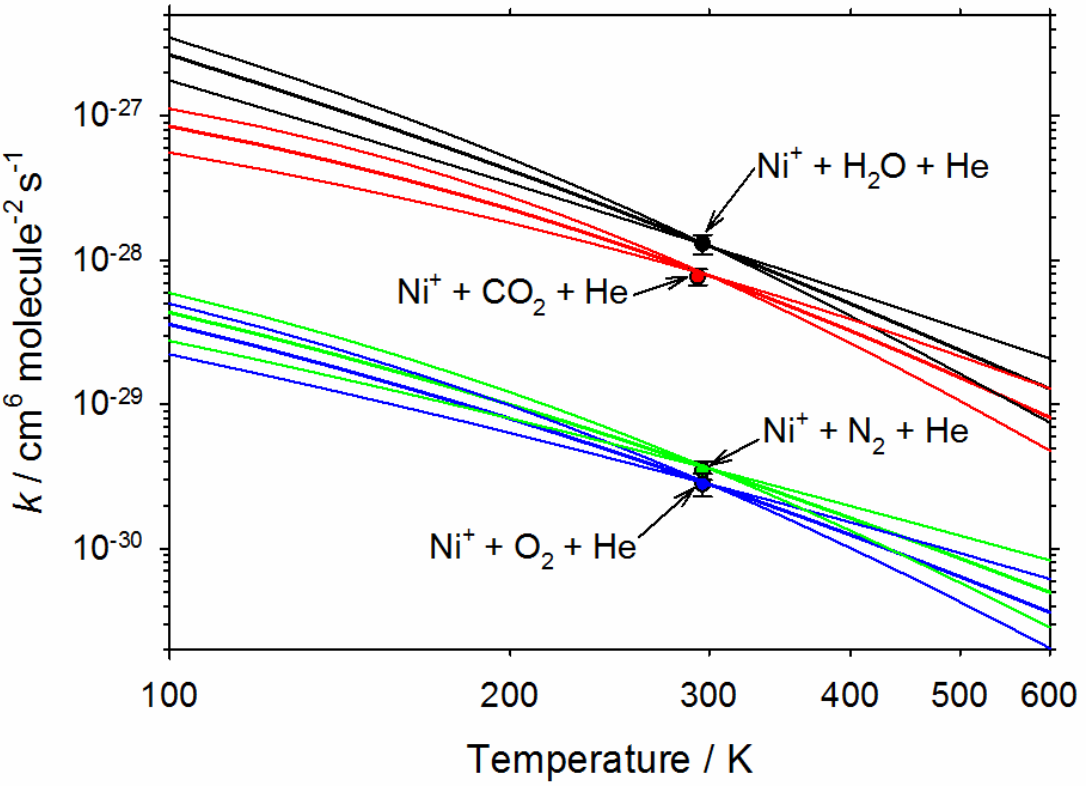

Figure 4.9. Plots of the RRKM fits (thick lines) through the experimentally measured data points (solid circles) for the recombination reactions of Ni^+ with N_2 (green), O_2 (blue), CO_2 (red) and H_2O (black) over a temperature range of 100 – 600 K. The faint lines indicate the sensitivity limits of each fit. Note that the left-hand ordinate is in log scale to better illustrate the separation of the 4 reactions by nearly 2 orders of magnitude.

4.5 Atmospheric Implications

Before the cluster reaction rate coefficients can be applied to a model in a planetary atmosphere, the $k_{rec,0}$ values require adjustment to account for the relative third body efficiencies of the major atmospheric species compared with the He used here in the kinetic measurements. For Earth's atmosphere, N_2 and O_2 are the primary atmospheric species, therefore acting as the third body in an ion-molecule recombination reaction. To account for those species, the rate coefficients k_6, k_7, k_8 and k_9 require an increase by a factor of 3 [*Plane et al.*, 2015]. For Mars, the primary constituent is CO_2, which requires a rate factor increase of 8 [*Whalley and Plane*, 2010].

Before the NiO^+ rate of removal in both atmospheres was examined, the rate coefficients of the molecular ion reacting with expected atmospheric species was estimated using the RRKM method. The molecular parameters for $ONiO_2^+$, $ONi^+.N_2$, $ONi^+.CO_2$ and $ONi^+.H_2O$ were determined separately using electronic structure calculations. The calculated rate coefficients in the range from 120 - 300 K were as follows:

$$k_{rec,0}(NiO^+ + N_2 + He) = 3.4 \times 10^{-30} (T/300)^{-3.38} \text{ cm}^6 \text{ molecule}^{-2} \text{ s}^{-1}$$

$$k_{rec,0}(NiO^+ + O_2 + He) = 1.1 \times 10^{-29} (T/300)^{-3.39} \text{ cm}^6 \text{ molecule}^{-2} \text{ s}^{-1}$$

$$k_{rec,0}(NiO^+ + CO_2 + He) = 1.2 \times 10^{-27} (T/300)^{-3.42} \text{ cm}^6 \text{ molecule}^{-2} \text{ s}^{-1}$$

$$k_{rec,0}(NiO^+ + H_2O + He) = 2.0 \times 10^{-26} (T/300)^{-2.90} \text{ cm}^6 \text{ molecule}^{-2} \text{ s}^{-1}$$

where the expected uncertainty is ~3 at 300 K. It is also noted that the calculated rate for $NiO^+ + H_2O$ here at 1 Torr and 294 K is 7.2×10^{-10} cm^3 molecule^{-1} s^{-1}, has decent agreement with the experimental fit (see Table 4.1 in Section 4.3).

Figure 4.10 below illustrates the computed vertical profiles for the removal rates of Ni^+ and NiO^+ ions in both the atmosphere of Earth and Mars. The vertical profiles of *T*, pressure and the mixing ratios of O_3, N_2, CO_2 and H_2O for Earth's atmosphere are taken out of output from the Whole Atmosphere Community Climate Model (WACCM4) [*Garcia*, 2007; *Marsh et al.*, 2013b]. The latitude taken for these conditions was 40ºN in April, at 00:00 L.T. In Figure 4.10a, the dominant removal process of Ni^+ appears to be from O_3 between the altitude range of 83-110 km. Mass spectrometric measurements from rocket soundings show that the peak of the Ni^+ ion density occurs between 95-105 km [*Carrillo-Sánchez et al.*, 2020]. During daytime, when the O_3 concentration decreases by ~1 order of magnitude to photolysis [*Plane et al.*, 2015], the reaction with O_3 is fast enough that it will still dominate over this altitude range. Outside of this altitude range (above 110 km and below 83 km) clustering with N_2 dominates the Ni^+ removal, with the recombination with O_2 ~7 times slower. Loss of Ni^+ by CO_2 should not be important for two reasons. Firstly, in Figure 4.10a, formation of the $Ni^+.CO_2$ ion in the terrestrial atmosphere is less competitive than O_2, O_3 and N_2 for the whole altitude range. Secondly, bond energies of the ion clusters were examined using B3LYP/aug-cc-pVQZ level of theory and was found that the $Ni^+.N_2$ cluster ion has a high bond energy of 112 kJ mol^{-1} (reasonable higher than the value of 99 kJ mol^{-1} measured by *Bauschlicher et al.* [1989]). Therefore it is unlikely to undergo ligand switching with CO_2, which contradicts behaviour seen from other metallic ions such as Fe^+ [*Vondrak et al.*, 2006], Ca^+ [*Broadley et al.*, 2008] and Mg^+ [*Whalley et al.*, 2011]. Despite having a faster rate than N_2, O_2, CO_2, the reaction of Ni^+ with H_2O is the least impactful in Earth's atmosphere

because the mixing ratio of H_2O is very low, i.e. less than a few ppm above 80 km [*Plane et al.*, 2015].

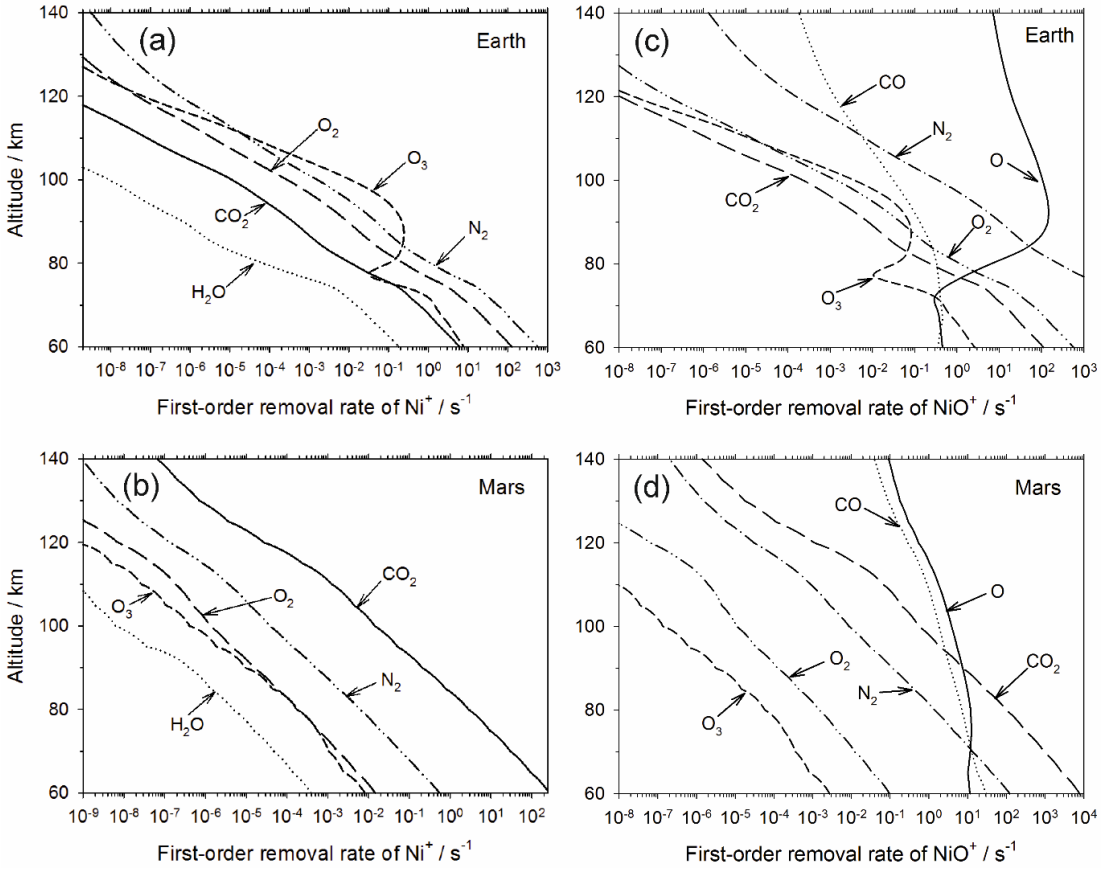

Figure 4.10. Plots of removal rates of Ni^+ and NiO^+ ions in planetary atmospheres from 60 – 140 km: (a) Ni^+ and (b) NiO^+ on Earth, 40ºN, local midnight, April (top panel); (c) Ni^+ and (d) NiO^+ on Mars, local noon, latitude = 0º, solar longitude L_S = 85º (bottom panel). Note the log scale used for the bottom ordinate to highlight the large differences in Ni^+ removal rate between each species.

The vertical profiles of the plotted species and *T* (K) for Mars' atmosphere are taken from the Mars Climate Database v.5.2 (http://www-mars.lmd.jussieu.fr/mcd_python/) [*Forget et al.*, 1999], under the following

conditions: latitude = 0°, local noon and solar longitude L_s = 85° (northern hemisphere summer). Mars' atmosphere largely consists of CO_2 (~95%), while the O_3 concentration is much lower than in Earth's atmosphere (e.g. a factor of 0.002 at 80 km). Therefore, in Figure 4.10b, recombination of Ni^+ with CO_2 dominates by more than 2 orders of magnitude across the entire plotted range of altitude from 60 to 140 km.

On Earth's atmosphere, the fast reaction of NiO^+ with O is the most dominant loss process above 85 km, according to Figure 4.10c, giving the NiO^+ ions a turnover lifetime of around 10 ms. However, below the 85 km mark, recombination with N_2 and O_2 can produce $NiO^+.N_2$ and $ONiO_2^+$ ions, which then can further ligand-switch with CO_2 or H_2O which are both more strongly bound cluster ions to Ni^+ (Calculated at the B3LYP/aug-cc-pVQZ level of theory). From there, any of these cluster ions can then react directly with atomic O e.g. for $NiO^+.H_2O$

$$NiO^+.H_2O + O \rightarrow NiO_2^+ + H_2O \qquad \Delta H^o = -136 \text{ kJ mol}^{-1} \qquad \text{(R4.17a)}$$

$$\rightarrow Ni^+.H_2O + O_2 \qquad \Delta H^o = -240 \text{ kJ mol}^{-1} \qquad \text{(R4.17b)}$$

For the loss of NiO^+ in Figure 4.10d, the reactions with O and CO dominate above 90 km, with the NiO^+ ion having a lifetime of ~100 ms. Below 90 km. clustering with CO_2 becomes more dominant, but the resulting $NiO^+.CO_2$ cluster ion will likely go on to react with O, CO, or H_2O.

4.6 Conclusion

The rate coefficients for the reactions of Ni^+ with O_3, N_2, O_2, CO_2 and H_2O, the reactions of NiO and NiO^+ with O, CO and O_3 and NiO_2 with O have been measured in this chapter. Only the reactions of Ni^+ with O_3, O_2, NiO^+ with O_3 and NiO with CO have been measured previously. The reaction of Ni^+ with O_3 to form NiO^+ is quite exothermic allowing it to react at the ion-molecule capture rate, with slight enhancement from the small dipole moment of O_3. This reaction dominates removal of Ni^+ in the terrestrial atmosphere because of the relatively high concentration of O_3 in the tertiary ozone maximum residing at ~87 km. However, NiO^+ is more likely to be quickly recycled by O atoms to Ni^+ since it ~5 times faster the Fe analogue of FeO^+, interrupting the dissociative recombination of NiO^+ by electrons to produce Ni. In contrast, on Mars' atmosphere the recombination of Ni^+ with CO_2 is the most rapid removal process by over 2 orders of magnitude, throughout Mars' mesosphere since CO_2 is the most abundance species there. For the neutral species in this study, k(NiO + CO) was measured at a rate of 3×10^{-11} molecule cm^{-3} s^{-1}, which was the same rate coefficient as the only previously made measurement of it in a PLP-LIF slow flow tube reactor system. The reaction with CO is also ~210 times faster than the FeO counterpart, which will likely influence the bottomside of the Ni layer. NiO and NiO_2 with O were also measured, with the NiO + O rate coefficient being ~3 times smaller than the Fe counterpart. These rate coefficients will now be added to the Whole Atmospheric Community Climate Model (WACCM) to simulate Ni and Ni^+ in the upper atmosphere.

5 Lidar observations of Ni and model simulations from WACCM-Ni

This chapter presents lidar observations of Ni made at Kühlungsborn, Germany in collaboration with Dr Michael Gerding of the Leibniz Institute of Atmospheric Physics. These measurements will be compared with previous measurements of Ni and Fe, and of Ni^+ ions from rocket-borne mass spectrometry. This chapter also describes the new iteration of the Whole Atmospheric Community Climate Model (WACCM) for Ni, incorporating the chemistry of Ni and Ni^+ (discussed in chapter 4) and a new meteoric input function for Ni. The model output is then compared with the lidar observations and rocket sounding measurements. Theoretical calculations (B3LYP/6-311+g(2d,p) level of theory [*Frisch et al.*, 2016] and time-dependent density function theory (TD-DFT) [*Bauernschmitt and Ahlrichs*, 1996]) made in this chapter were performed by Prof. John Plane.

5.1 LIDAR observations of Ni

For this chapter, lidar observations at Kühlungsborn will be used for comparison with the model output, as there was a much larger recorded dataset (~16 hours) compared to the integration time measured in Chatanika, Alaska (65ºN, 147ºW) (<1 hour over two days). The lidar system in Kühlungsborn used an excimer-pumped (XeCl) dye laser with a repetition rate of 30 Hz [*Gerding et al.*, 2000] with p-Terphenyl dye in p-Dioxane (the same dye used by *Collins et al.* [2015]) to operate at 337 nm to access the ground

state Ni(^{3}F) transition [Ni($z^3F_4^0$−a^3F_4)] and 341 nm to access the metastable state Ni(^{3}D) transition [Ni($z^3F_4^0$−a^3D_3)]. The lidar system here made successful soundings of Ni for six nights from January to March 2018 with off-resonance soundings made beforehand for initial tests. Observations at 341 nm were taken on January 7th, 8th, 14th and February 8th; with March 20th, 2018 as a comparative sounding between 341 nm and 337 nm. The other remaining date was the first test at 337 nm on the 18th March 2018.

For Fe lidar comparison, observational data was taken from Urbana (40^{o}N, 272^{o}E) from October 1989 to June 1992 [*Feng et al.*, 2013; *Helmer et al.*, 1998]. The data was collected with 41 vertical levels from 80 km at 0.5 km intervals. There was no adequate Fe lidar data available from Kühlungsborn for the comparison.

For comparison with the Ni^+ and Fe^+ densities from the model output, 8 vertical profiles of Ni^+ (*m/z* = 58) and Fe^+ (*m/z* = 56). The sounding rocket launches used for this study are discussed in Table 2.2 (see Chapter 2). A geometric mean and standard deviation of all the flights was determined for comparison with the Ni^+ model output.

5.1.1 Initial observation attempts of Ni – Kühlungsborn 2017

During the initial trip from March to May 2017, there was difficulty getting the dye laser to output at 337 nm, which was the wavelength used by *Collins et al.* [2015] to probe the ground state Ni(^{3}F) transition at λ_{air} = 336.9563 nm. The broadband light pulse before the etalon (wavelength filter) was measured at ~4 mJ, but after the etalon was applied, there was no detectable light. The main difference between this setup and the one in Alaska was the choice of solvent, with propylene carbonate used as a non-toxic solvent as an alternative to p-Dioxane to dissolve the p-Terphenyl (PTP) dye. Since this mixture was not producing adequate laser light, the solvent was returned to p-Dioxane for the return expedition from September to October 2017. Observations were attempted during this period at 337 nm but there was no metal layer detected. At the same time, the kinetics of Ni were been investigated with the research group back in Leeds. It was discovered that the first excited state of Ni (Ni(^{3}D)) probed at λ_{air} = 341.4764 nm gave a higher signal intensity, and this transition was not used by *Collins et al.* [2015]. Ni(^{3}D) is a low-lying metastable state (<500 cm^{-1}) close to the ground state and has an Einstein coefficient 3 times larger than the corresponding transition at 337 nm (see Figure 5.1).

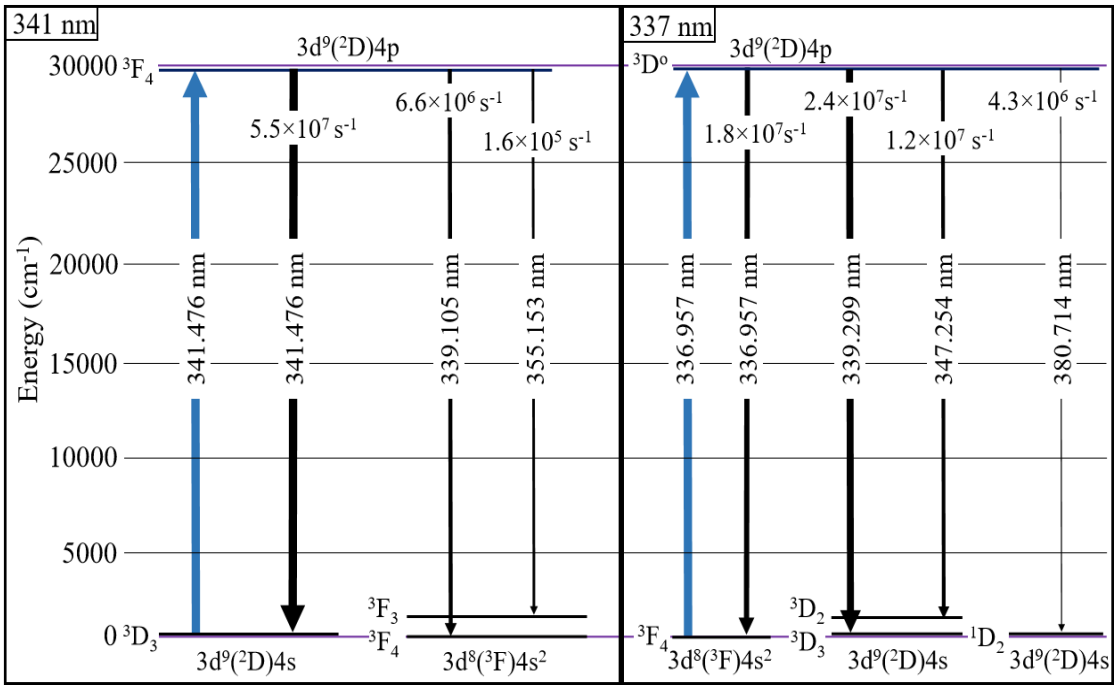

Figure 5.1. Energy level diagram for Ni with the most important transitions [*Kramida et al.*, 2018]. Wavelengths are given with respect to air. From the Einstein coefficients (shown horizontally at units of s^{-1}) we get branching fractions (i.e. relative emission intensities) for pumping at 341 nm of 11% and 89% at 339nm and 341nm, respectively. For pumping at 337nm the relative emission intensities are 31%, 41%, 20% and 7% at 337nm, 339nm, 347nm and 381nm, respectively.

5.1.2 Observations at 341 nm

Lidar operations were then resumed in January 2018 probing the Ni(^{3}D) transition at 341 nm and a layer was successfully observed on the 7th/8th January. This was then observed for another six nights from January to March (with successful observations in March at both 341 nm and 337 nm). In Leeds, the wavelength was produced by doubling 682 nm light from a pyridine 1 dye

but for the PTP dye, 341.476 nm was closer to the emission maximum. This provided more stability to the wavelength, with larger laser power and less broadband emission. The laser had operated on the night of the 7th for 40 minutes with a total 72,000 laser pulses. Photon counts were collected in 200-m altitude bins, which later were integrated to 1 km to improve signal-to-noise. The following night, the Ni layer was observed for ~2.5 hr with the same transition. Figure 5.2 illustrates the integrated raw profile from the night of the 8th January with the background count rate included (dashed line) and subtracted (solid blue line). The molecular backscatter (Rayleigh signal) is still visible above 50 km but decreasing with altitude with decreasing air density (indicated with the purple arrow of Figure 5.2).

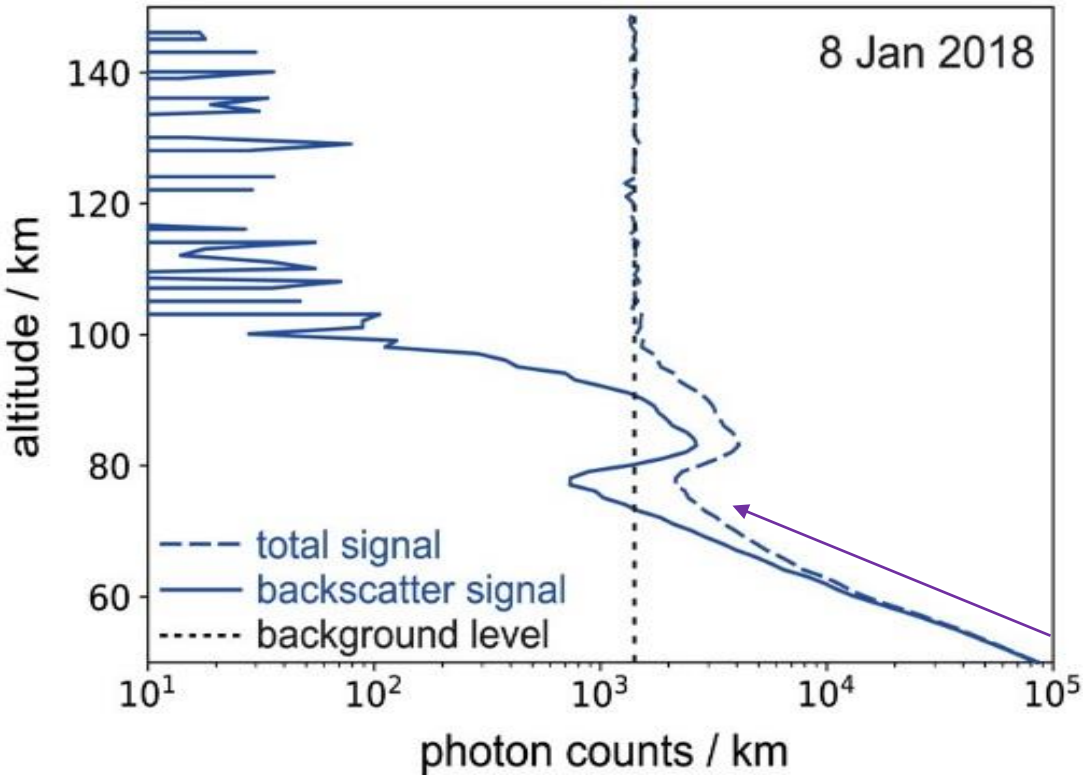

Figure 5.2. Integrated raw profile recorded by the resonance lidar at 341 nm for the evening of the 8th January 2018, before and after subtraction of the

background, as a function of altitude. The altitude resolution was set to 1 km bins.

Above ~78 km there is a clear Ni signal increase due to the present of resonance backscatter extending out from the Rayleigh scatter, with the layer being observed up to ~100 km. At altitudes higher than 100 km, the constant background counts are a result of detector noise and sky background, at ~1,400 counts / km. The background level is determined by averaging the signal at an altitude range above the Rayleigh signal (in this case from 120 – 140 km). Subtracting the layer in Figure 2 gives a much clearer view of the profile. At the altitude of the layer maximum, ~200 photon counts were recorded from Rayleigh signal, with 2,400 photon counts per kilometre attributed to the resonance signal. The signal requires further correction by removing the Rayleigh scatter before the layer peak density and abundance could be determined. The range-corrected Rayleigh scatter was extrapolated above 76 km with a normalized nightly density profile from the NRLMSISE-00 [*Picone et al.*, 2002], then was subtracted to get solely resonance counts.

The Rayleigh-subtracted backscatter profiles were then used to calculate the mean Ni density profiles. The Ni densities, ρ_{Ni}, at altitude z were calculated using the equation E5.1:

$$\rho_{Ni}(z) = \rho_{air}(z_R) \cdot \sigma_{Ray}/\sigma_{res} \cdot N_{res}^{corr}(z) / N_{Ray}^{corr}(z_R) \qquad \text{(E5.1)}$$

with $\rho_{air}(z_R)$ as the air density of the reference altitude taken from the NRLMSISE-00 atmospheric model [*Picone et al.*, 2002], with z_r set to the reference altitude of 50 km. At that altitude, there was no correction for stratospheric aerosol backscatter and ozone absorption required. The σ_{Ray}

and σ_{res} are the Rayleigh and effective backscatter cross sections, respectively, and are calculated as described by *Chu and Papen* [2005] and *Fricke and von Zahn* [1985], with oscillator strengths of 0.12 for Ni(^{3}D) and 0.024 for Ni(^{3}F) [*Kramida et al.*, 2018]. This yielded a calculated resonance cross section of 341 nm and 337 nm at σ_{res} = 1.08 × 10^{-17} m^2/sr and σ_{res} = 3.57 × 10^{-31} m^2/sr respectively. Note that the Ni(^{3}D) resonance cross section is ~5 times larger than the one measured for Ni(^{3}F), hence why this transition provided a much better signal in the kinetics experiments. The Rayleigh backscatter cross section, σ_{Ray} = 3.57 × 10^{-31} m^2/sr was the same for both 337 and 341 nm. The numbers are calculated for a 0.4 pm laser full width at half maximum (assuming Lorentz shape) and at ~90-km altitude in winter with an atmospheric temperature of 200 K.

N_{res}^{corr} (z) represented the range-corrected resonance photon counts with N_{Ray}^{corr} (z_R) as the range-corrected Rayleigh count rate at the reference altitude of 50 km. An additional factor was applied to the resonance photon counts to account for the thermal populations of the $^3D_3$ and $^3F_4$ states used, with the relative population of the Ni(^{3}D) state between 100 and 240 K varying from 3.9% to 18.5%. The temperature-dependent fraction of Ni in the $^3D_3$ state can calculated assuming a thermal population by E5.2:

$$0.570 \times \exp(-265.8/T) \qquad \text{(E5.2)}$$

The temperatures were retrieved from the Rayleigh-Mie-Raman lidar system (discussed in detail in Chapter 2) which operated in conjunction with the resonance lidar to provide both temperature measurements and real-time feedback from cloud interference [*Gerding et al.*, 2016]. The measured temperatures varied from 180 – 220 K at the peak of the Ni layer from 85-86

km. Referencing climatological data that was published for higher altitudes by *Gerding et al.* [2008] showed that similar were expected for the entire altitude range of the Ni layer during the January to March period. The fraction of Ni($^3D_3$) varied from 13.1% to 17% based off direct temperature measurements. Direct temperature measurements were not available for the whole altitude range therefore an average constant fraction of 15.1% was used. Further corrections for the density relating to the probability of relaxation at other wavelengths was then required, with the relaxation of the ^{3}F transition via emission at 380.7 nm given a 7% probability (illustrated in Figure 5.1). All the major contributors were in the transmission range of the interference filter, with 339.1 nm for the excitation of the Ni(^{3}D) state and 339.3 and 347.3 nm for the Ni(^{3}F) state [*Kramida et al.*, 2018]. Based on the differences in effective cross section and thermal population, a similar resonance signal was expected for both transitions.

For the statistical uncertainty of the calculated density, the square root of the original count rate at 1 km resolution was taken through the use of Poisson statistics. Figure 5.3 below illustrates the Ni density profile from both the observations done on the 7th and 8th January, with the additional nights included during the January to March period (January 14th, February 8th, March 20th, 2018). All the nights examined here were measurements at 341 nm, with the same statistical analysis, range correction and Rayleigh-subtraction discussed previously.

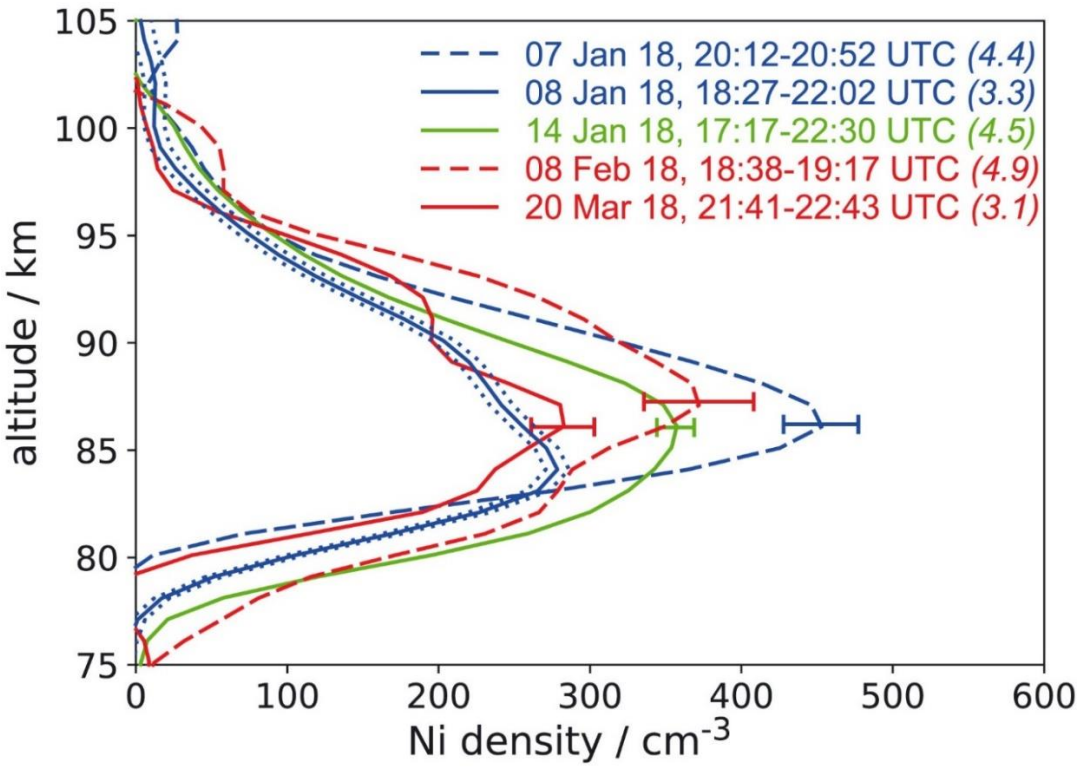

Figure 5.3. Nickel density profiles as a function of altitude (km) at the Ni(^{3}D) transition at 341 nm. The uncertainties are represented as either dotted lines or error bars at the layer maximum. The bracketed numbers in the legend represent the vertical column abundances in units of 10^8 cm^{-2}.

The layer peak varies from 84 – 87 km with observed nightly mean Ni peak densities ranging from ~280 to 450 cm^{-3}. The column abundance (cm^{-2}) can also be determined by retrieving the integrated area under the peak, by calculating the sum of resonance photon counts with altitude and applying the correction for the 1 km altitude bins (×1 km in cm). This gave column abundances ranging from 3.1 × 10^8 to 4.9 × 10^8 cm^{-2}. The bottom-side of the Ni layer showed a variance of as much as 5 km between the sounding nights, with the shape of the layer often differing from an ideal Gaussian.

The longer period of lidar sounding on the 8th/9th January provided a temporal evolution of the Ni layer, illustrated in Figure 5.4 below. This is the first temporal view of the Ni layer documented to date, even if it was only for a few hours. During the 3.5 hr sounding the layer was highly variable, with the peak density varying by up to 55% and the altitude of the peak changing by ~2 km within ~15 min timestamps. The bottom-side of the layer gradually ascends by 2 km over the period of the observations from ~18:30 to 22:00 UTC, bringing it from 78 – 80 km. The layer topside showed larger variability on much shorter timescales (~4 km over 15-30 min timestamps). Although this is only a single observation, the Ni layer appears to show a larger variability compared to the Fe layer [*Feng et al.*, 2013; *Kane and Gardner*, 1993]. Fe observations by [*Bills and Gardner*, 1990] showed typical Fe densities varying from 15,000 – 25,000 cm^{-3} (45% variance) over the course of 6 hr.

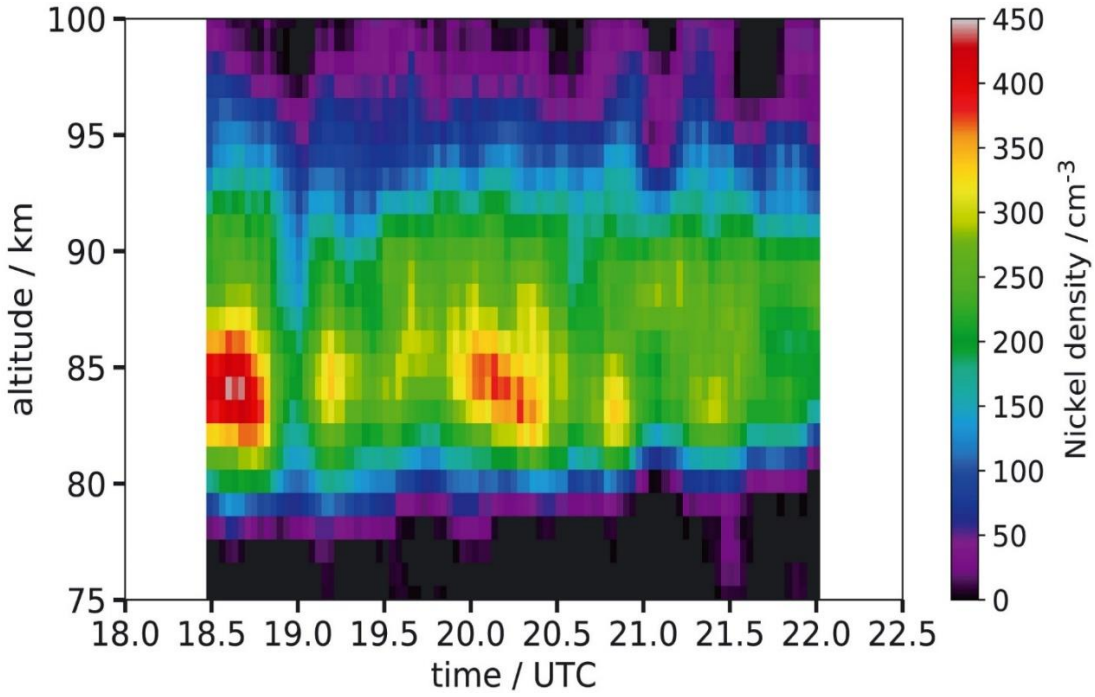

Figure 5.4. Temporal evolution of the Ni layer from a 3.5-hour lidar sounding done on the 8th January 2018, where the number density of Ni (colour scale

shown by the right-hand ordinate) is plotted as a function of altitude in km (left-hand ordinate) and time (bottom abscissa – UTC)

5.1.3 Observations at 337 nm and 341 nm

After successful lidar soundings of Ni probing the Ni(^{3}D) transition at 341 nm, the laser was also tuned to 337 nm to try to observe the Ni(^{3}F) state which was measured by *Collins et al.* [2015], since this would add more credibility to these measurements. Since the dye laser had a much lower pulse energy at this wavelength, the Rayleigh signal was also weaker. The backscatter cross section of the Ni(^{3}F) transition is also smaller, but the fraction of atoms occupying the ground state is larger. Through the use of a WS6-200 wavemeter received in March 2018, it was possible to adjust the laser to the Ni(^{3}F) transition at 337 nm and successfully observe a resonance signal at this wavelength. The first soundings of Ni(^{3}F) were carried out for 2.5 hr during the 18th / 19th March 2018. The measured Ni densities from the sounding were found to be lower than the observations done at 341 nm during the January/February observations. Following this, comparative soundings were made at both wavelengths on the 20th/21st March 2018. The laser was first set to 337 nm and collected Ni(^{3}F) resonance data from 19:04 – 21:22 UTC. The laser was then tuned back to 341 nm and operated from 21:41-22:43 UTC. The integrated raw data of both profiles is illustrated in Figure 5.5 with background subtraction and range correction included along with the uncorrected profile of 337 nm (background included).

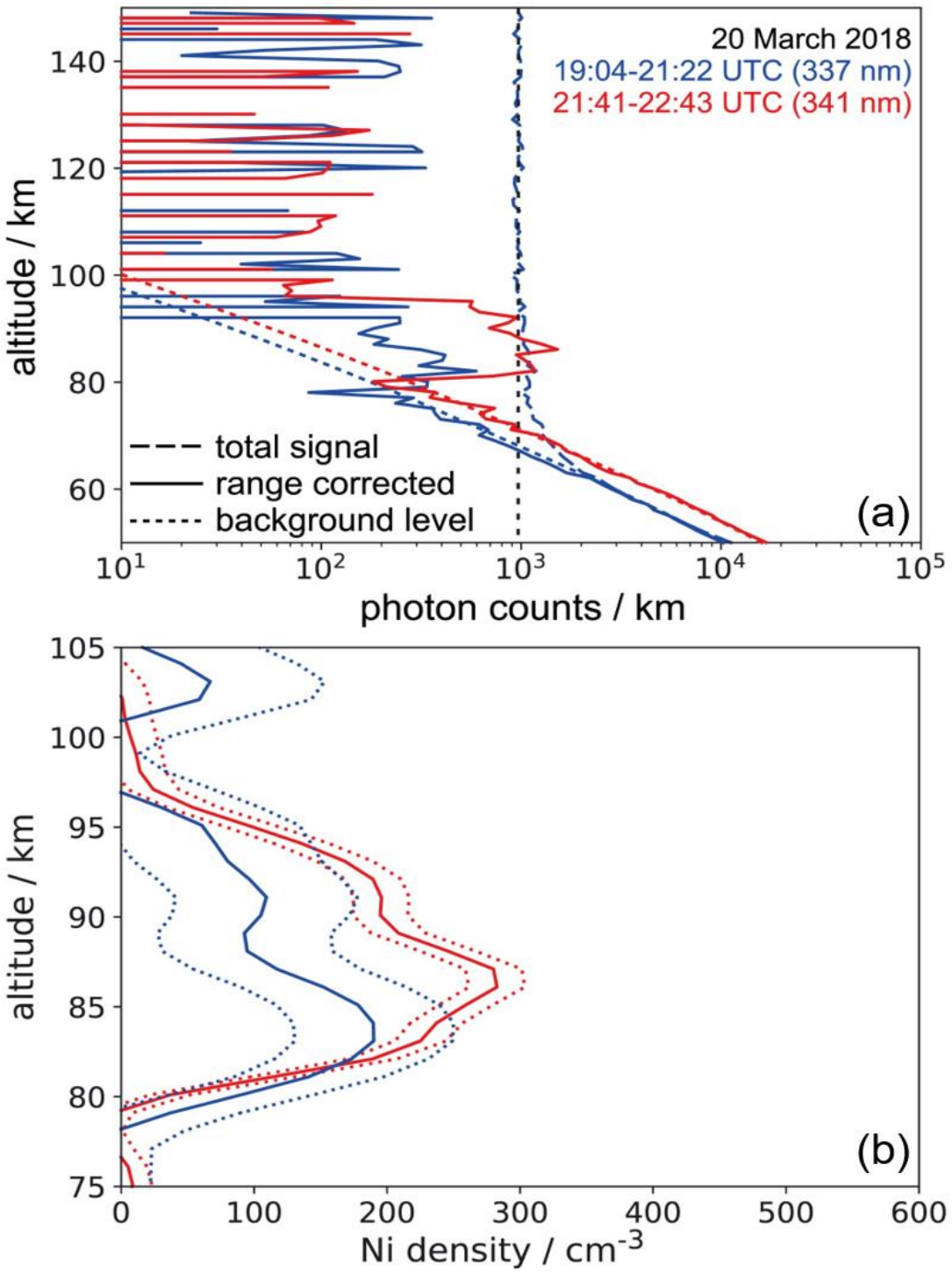

Figure 5.5. Lidar profiles on the 20th March 2018 where (a) is the raw data with background (dashed line) and profiles after background subtraction and range correction (solid lines), with the blue line showing the signal at 337 nm, red line showing 341 nm and the black showing the background level of 337 nm data. The blue/red dotted lines represent the normalized NRLMSISE-00

density profile used in the Rayleigh subtraction. (b) Ni density profiles of both 337 nm and 341 nm, calculated from the raw data, with the dotted lines representing the uncertainties.

The uncorrected profile at 337 nm has a weak resonance backscatter, similar to what was observed by *Collins et al.* [2015]. It is noted that the observations in Alaska applied a stronger smoothing of their profile. However, for the Ni(^{3}D) observation on the night of 20th/21st March, the 341-nm resonance signal was like that measured on the 8th January 2018. The Rayleigh scatter for both 337 and 341 nm reflect the differences in laser pulse energy (1:3) as well as integration time (2:1) but the resonance signal at 337 nm is still smaller than expected compared to the 341 nm counterpart. There were several technical limitations at 337 nm that would have contributed to this result. Since 337 nm was further from the dye fluorescent maximum than 341 nm, it was more sensitive to misalignment. At this wavelength, there was also a poorer contrast of the ring system generated from the external monitoring etalon which is generally the final laser check done before the dye laser is emitted into the atmosphere. The spectral resolution of the WS6-200 wavemeter was 0.2 pm (at 337 nm) and the minimum manual scan steps that could be achieved based on atmosphere return was also 0.2 nm. Therefore, potential systematic error of the laser to the center of the Ni resonance line at 337 nm could be ~0.1 pm, resulting in a possible underestimation of the true measured density at the very most 25%. There was also a larger fraction of broadband emission at 337 nm indicated by the wavemeter used. This could include Amplified Spontaneous Emission (ASE) (spontaneously emitted photons that are

amplified and adversely affects gain, efficiency and noise performance of the laser) [*Saifi*, 2001] and other broadband emission that contributed to the Rayleigh signal but not the resonance signal. However, a quantitative analysis of the broadband emission percentage was not possible with the wavemeter. Therefore a 33% fraction of amplified spontaneous emission was assumed. Taking both factors into accounts i.e. the 0.1 pm offset and 33% broadband emission, the effective backscatter cross section at 337 nm was estimated to be 1.42×10^{-18} m^2/sr. (Already accounted for in the density calculations of Figure 5.5).

In terms of the wavelength reading for the majority of the observations, an absolute wavelength reading was not available, a similar situation to the soundings done by *Collins et al.* [2015]. It was only in March 2018 that an accurate measurement of the pulsed laser light was retrieved through the use of the WS6-200 wavelength meter, with an accuracy of 0.2 pm in the wavelength range examined (in the range of the pulsed laser bandwidth). This was then cross-checked with the atmospheric return for both observations of the Ni(^{3}D) transition at 341 nm and Ni(^{3}F) transition at 337 nm.

To compensate for this in January when the first successful observations were made, the dye laser was rapidly scanned over a wavelength range of ~100 pm while continuously monitoring the backscatter signal. After initial coarse adjustment, the final wavelength was found through a detailed scanning across ~1 pm based on the post-analysis of the normalized resonance backscatter through integration of 4,000 laser pulses (~2.5 min) and 0.2 pm wavelength steps per profile. The following soundings night required only fine-tuning of the laser wavelength since the laser electronics was kept running

continuously and the laser rooms were temperature stabilized. During lidar operations, the wavelength was re-examined hourly to avoid wavelength drifts that can be caused by thermal adjustment of the laser resonator. The bandwidth of the laser was also checked hourly by inspection of the transmission from an external monitoring etalon.

The metastable ^{3}D state at 341 nm which produced a much better lidar resonance signal (as shown in Figure 5.5) than the ^{3}F ground state at 337 nm, was an unexpected result and the first example of a metal resonance lidar sounding where this is the case. Therefore, it was worth investigating if both states were existing in thermal equilibrium, which was assumed when the relative populations were calculated (see Section 5.2.2). Ni should be in a fast chemical steady state with its oxide form NiO, controlled specifically by the reactions of Ni with O_3 and NiO with O, as seen with other meteoric metals [*Plane et al.*, 2015]. The latter reaction with atomic O could initially produce Ni in a non-Boltzmann population which would support the non-thermal equilibrium case. But recent measurements by *Mangan et al.* [2019] included the rate coefficient for $k(\mathrm{Ni} + \mathrm{O_3} \rightarrow \mathrm{NiO} + \mathrm{O_2}) = (6.5 \pm 0.7) \times 10^{-10}$ cm^3 molecule^{-1} s^{-1}. Taking the O_3 concentration at 85 km near the Ni layer peak of 5×10^8 cm^{-3} [*Plane et al.*, 2015], the e-folding time for conversion of Ni to NiO is ~3.1 s, with the Ni atom experiencing an order of 10^5 collisions with air molecules. This number of collisions, combined with the low energy separation between the ^{3}D and ^{3}F states (204.8 cm^{-1}), makes it highly likely that both states are in equilibrium.

Finally, an important issue to address with the new measurements is how they compare to the well-studied mesospheric Fe layer and the CI chondritic ratio

of Fe:Ni. CI chondrites are chosen here as they are regarded as the closest in composition to interplanetary dust [*Jessberger et al.*, 2001]. Taking a standard Fe column abundance during the same January – March period at midlatitudes yields a value of 1.5×10^{10} cm^{-2} [*Kane and Gardner*, 1993]. This gives a Fe:Ni ratio of 38 ± 11. This ratio is 2.1 and 2.4 times larger than the ablation ratio calculated by the CABMOD-ZoDy (15.9) [*Carrillo-Sánchez et al.*, 2020] and the chondritic ratio (18) [*Asplund et al.*, 2009], respectively. This may suggest that Ni is converted to long-term atmospheric sinks more efficiently than Fe, or that the Ni in cometary dust particles is sub-chondritic. Accounting for the measurements made by *Collins et al.* [2015], the Fe:Ni ratio is 1.2 which is a factor of 13 and 15 times smaller than the ablation and CI ratio, which is an even larger difference. This would suggest that Ni is highly enriched in cosmic dust particles which contradicts the analysis of meteoric fragments done by *Bones et al.* [2019], as well as Fe:Ni ratio measured by *Arndt et al.* [1996] in cosmic dust particles which had survived atmospheric entry.

Unfortunately, there is no clear reason as to why there is a 50 – 70 factor difference between the lidar results in Kühlungsborn and the measurements made by *Collins et al.* [2015] in Alaska. Latitudinal differences could be considered, but this variance with latitude would be surprisingly large. Other metals typically exhibit abundance increases by no more than a factor of 2 when ranging from middle to high latitudes [*Feng et al.*, 2013; *Langowski et al.*, 2015]. Therefore, future soundings would be the logical way forward to resolve this discrepancy. Since the transition at 341 nm is comparatively easier to reach than 337 nm, it would be suggested to focus on this wavelength.

5.2 WACCM-Ni development

5.2.1 A Ni chemistry scheme for atmospheric modelling

Following the successful observations of Ni, the next objective entailed combining a global chemistry-climate model with the recently measured catalogue of Ni and Ni^+ reaction kinetics as well as addition of the experimentally supported meteoric input function (MIF) for Ni. The model simulations could then be compared to the lidar observations and ion measurements from rocket soundings. Additional objectives were to explain why the Ni layer exhibits a broader profile than Fe on the bottom side, and why the ratio of neutral Fe:Ni from the observations of Section 5.2 is more than double the chondritic and modelled ablation ratio. The reaction pathways for both the neutral and ion-molecule set of Ni reactions are illustrated by the schematic diagram in Figure 5.6 below with the assigned rate coefficients for each reaction in Table 5.1. The kinetics of many of the reactions discussed in Table 5.1 have now been measured, whether from the Ni kinetics of Chapter 4 or the work done by *Mangan et al.* [2019]. Rate coefficients to those for the analogous reactions of Fe were applied for the reactions that have not been yet measured for Ni. This is somewhat arbitrary, of course, since it has already been demonstrated how different both transitions metal behave kinetically in Chapter 4. It is noted that the important Ni reactions which have been set to their Fe analogues are all reasonably exothermic and the rates are quite fast (R5.10, R5.13, R5.16, R5.17, R5.36 and R5.42).

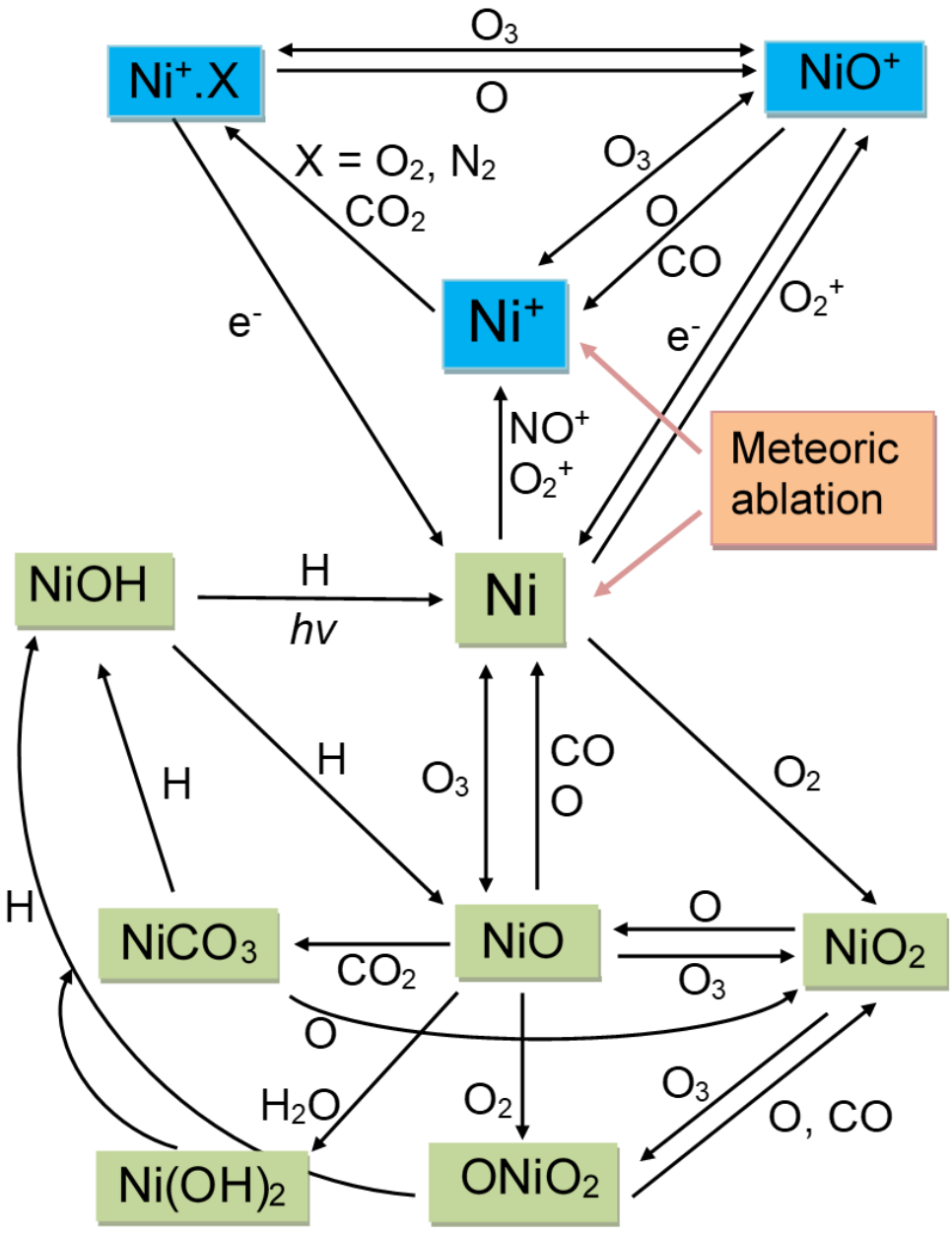

Figure 5.6: Schematic diagram of Ni and Ni^+ chemistry in the MLT following meteoric ablation into Earth's upper atmosphere. Ionized neutral Ni species are indicated in blue and green boxes, respectively.

R5.18 – R5.20 from Table 5.1 are polymerization reactions which detail the permanent loss of the important neutral reservoir species NiOH, $Ni(OH)_2$ and $NiCO_3$ which can react further to form meteoric smoke particles. This type of

reaction has been used previously for modelling the Fe, Na, Fe, Mg and Ca layers [*Feng et al.*, 2013; *Langowski et al.*, 2015; *Marsh et al.*, 2013a; *Plane et al.*, 2014; *Plane et al.*, 2018b]. The polymerization rates $k_{5.18\text{-}5.20}$ are set to 7×10^{-8} cm^3 s^{-1} for Ni, a factor of 80 times larger than a standard dipole-dipole capture rate for these metallic species. This is to account for the fact that the Ni reservoir species are not restricted to Ni-containing molecules and, therefore, can further polymerize with non-Ni containing meteoric molecules (e.g., FeOH, $Mg(OH)_2$ and $NaHCO_3$). There is also a large excess of the other ablated metals when compared to Ni (the elemental ablation ratio of Ni atoms to the summed amount of Na, Fe, Mg, Si, Al and K atoms is ~ 1/80) [*Carrillo-Sánchez et al.*, 2020]. This has been done previously for other minor meteoric metals i.e. Ca and K, with their respective dipole-dipole capture rates been increased by factors of 100 [*Plane et al.*, 2018b] and 270 [*Plane et al.*, 2014].

Table 5.1. Ni chemistry in the MLT

No.	Reaction	Rate coefficient [a]
		Neutral reactions
R5.1	$Ni + O_3 \rightarrow NiO + O_2$	$k_1 = 6.5 \times 10^{-10}(T/293)^{0.167}$ [b]
R5.2	$Ni + O_2 (+M) \rightarrow NiO_2$	$\log_{10}(k_2) = -37.592 + 7.168\log_{10}(T) - 1.565(\log_{10}(T))^2$ [b]
R5.3a	$NiO + O_3 \rightarrow NiO_2 + O_2$	$k_{3a} = 2.5 \times 10^{-10} (T/293)^{0.167}$ [b]
R5.3b	$NiO + O_3 \rightarrow Ni + 2O_2$	$k_{3b} = 1.4 \times 10^{-10} (T/293)^{0.167}$ [b]
R5.4	$NiO + O \rightarrow Ni + O_2$	$k_4 = 1.5 \times 10^{-10} \exp(-337/T)$ [c]
R5.5	$NiO + CO \rightarrow Ni + CO_2$	$k_5 = 3.2 \times 10^{-11} (T/200)^{-0.194}$ [b, c]
R5.6	$NiO_2 + O \rightarrow NiO + O_2$	$k_6 = 7.9 \times 10^{-11} \exp(-337/T)$ [c]
R5.7	$NiO + O_2 (+M) \rightarrow ONiO_2$	$\log_{10}(k_7) = -41.0913 + 10.1064\log_{10}(T) - 2.2610(\log_{10}(T))^2$ [b]
R5.8	$NiO + CO_2 (+M) \rightarrow NiCO_3$	$\log_{10}(k_8) = -41.4265 + 10.9640\log_{10}(T) - 2.5287(\log_{10}(T))^2$ [b]
R5.9	$NiO + H_2O (+M) \rightarrow Ni(OH)_2$	$\log_{10}(k_9) = -29.7651 + 5.2064\log_{10}(T) - 1.7118(\log_{10}(T))^2$ [b]
R5.10	$NiO_2 + O_3 \rightarrow ONiO_2 + O_2$	$k_{10} = 3.4 \times 10^{-10} \exp(-337/T)$ [d]
R5.11	$ONiO_2 + O \rightarrow NiO_2 + O_2$	$k_{11} = 2.3 \times 10^{-10} \exp(-2310/T)$ [d]
R5.12	$NiCO_3 + O \rightarrow NiO_2 + CO_2$	$k_{12} = 2.3 \times 10^{-10} \exp(-2310/T)$ [d]
R5.13	$ONiO_2 + H_2O \rightarrow Ni(OH)_2 + O_2$	$k_{13} = 5 \times 10^{-12}$ [d]
R5.14	$Ni(OH)_2 + H \rightarrow NiOH + H_2O$	$k_{14} = 3 \times 10^{-10} \exp(-796/T)$ [d]
R5.15	$NiCO_3 + H \rightarrow NiOH + CO_2$	$k_{15} = 3 \times 10^{-10} \exp(-796/T)$ [d]
R5.16	$ONiO_2 + H \rightarrow NiOH + O_2$	$k_{16} = 3 \times 10^{-10} \exp(-302/T)$ [d]

R5.17	$NiOH + H \rightarrow Ni + H_2O$	$k_{17} = 5 \times 10^{-11} \exp(-337/T)$ [d]
R5.18	$NiOH + NiOH \rightarrow (NiOH)_2$	$k_{18} = 7 \times 10^{-8}$ [e]
R5.19	$Ni(OH)_2 + Ni(OH)_2 \rightarrow (Ni(OH)_2)_2$	$k_{19} = 7 \times 10^{-8}$ [e]
R5.20	$NiCO_3 + NiCO_3 \rightarrow (NiCO_3)_2$	$k_{20} = 7 \times 10^{-8}$ [e]
R5.21	$NiOH + h\nu \rightarrow Ni + OH$	$k_{21} = 1.8 \times 10^{-2}$ [f]
		Ion-molecule reactions
R22	$Ni^+ + O_3 \rightarrow NiO^+ + O_2$	$k_{22} = 9.8 \times 10^{-10} (T/294)^{-0.16}$ [c]
R23	$Ni^+ + N_2 (+M) \rightarrow Ni^+.N_2$	$\log_{10}(k_{23}) = -27.5009 + 1.0667\log_{10}(T) - 0.74741(\log_{10}(T))^2$ [c]
R24	$Ni^+ + O_2 (+M) \rightarrow NiO_2^+$	$\log_{10}(k_{24}) = -27.8098 + 1.3065\log_{10}(T) - 0.81136(\log_{10}(T))^2$ [c]
R25	$Ni^+ + CO_2 (+M) \rightarrow Ni^+.CO_2$	$\log_{10}(k_{25}) = -29.805 + 4.2282\log_{10}(T) - 1.4303(\log_{10}(T))^2$ [c]
R26	$Ni^+ + H_2O (+M) \rightarrow Ni^+.H_2O$	$\log_{10}(k_{26}) = -24.318 + 0.20448\log_{10}(T) -0.66676(\log_{10}(T))^2$ [c]
R27	$NiO^+ + O \rightarrow Ni^+ + O_2$	$k_{27} = 1.7 \times 10^{-10}$ [c]
R28	$NiO^+ + CO \rightarrow Ni^+ + CO_2$	$k_{28} = 7.4 \times 10^{-11}$ [c]
R29a	$NiO^+ + O_3 \rightarrow Ni^+ + 2O_2$	$k_{29a} = 7.8 \times 10^{-11}$ [c]
R29b	$NiO^+ + O_3 \rightarrow NiO_2^+ + O_2$	$k_{29b} = 1.9 \times 10^{-10}$ [c]
R30	$NiO_2^+ + O_3 \rightarrow NiO^+ + 2O_2$	$k_{30} = 4.6 \times 10^{-11}$ [c]
R31	$Ni^+.N_2 + O \rightarrow NiO^+ + N_2$	$k_{31} = 7 \times 10^{-12}$ [c]
R32	$NiO_2^+ + O \rightarrow NiO^+ + O_2$	$k_{32} = 5 \times 10^{-11}$ [d]
R33	$Ni^+.CO_2 + O \rightarrow NiO^+ + CO_2$	$k_{33} = 2 \times 10^{-10}$ [d]

R34	$Ni^+.H_2O + O \rightarrow NiO^+ + H_2O$	$k_{34} = 2 \times 10^{-10}$ [d]
R35	$Ni^+ + e^- \rightarrow Ni + h\nu$	$k_{35} = 8 \times 10^{-12}(T/300)^{-0.51}$ [d]
R36	$NiO^+ + e^- \rightarrow Ni + O$	$k_{36} = 5.5 \times 10^{-7}(300/T)^{0.5}$ [d]
R37	$NiO_2^+ + e^- \rightarrow Ni + O_2$	$k_{37} = 3 \times 10^{-7}(T/200)^{-0.5}$ [d]
R38	$Ni^+.CO_2 + e^- \rightarrow Ni + CO_2$	$k_{38} = 3 \times 10^{-7}(T/200)^{-0.5}$ [d]
R39	$Ni^+.H_2O + e^- \rightarrow Ni + H_2O$	$k_{39} = 3 \times 10^{-7}(T/200)^{-0.5}$ [d]
R40	$Ni^+.N_2 + e^- \rightarrow Ni + N_2$	$k_{40} = 3 \times 10^{-7}(T/200)^{-0.5}$ [d]
R41a	$Ni + O_2^+ \rightarrow Ni^+ + O_2$	$k_{42a} = 3.1 \times 10^{-10}$ [g]
R41b	$Ni + O_2^+ \rightarrow NiO^+ + O$	$k_{42b} = 8.0 \times 10^{-10}$ [g]
R42	$Ni + NO^+ \rightarrow Ni^+ + NO$	$k_{43} = 9.2 \times 10^{-10}$ [d]
R43	$Ni + h\nu \rightarrow Ni^+ + e^-$	$k_{44} = 6.8 \times 10^{-8}$ [h]

[a] Units: s^{-1} for photolysis reactions; cm^3 $molecule^{-1}$ s^{-1} for bimolecular reactions; cm^6 $molecule^{-2}$ s^{-1} for termolecular reactions. [b] *Mangan et al.* [2019]. [c] Measured, Chapter 4 kinetics. [d] set to the analogous reaction for Fe [*Feng et al.*, 2013]. [e] See text. [f] Calculated for this study. [g] *Schlemmer et al.* [2003] measured the reaction channel producing $NiO^+ + O$; the channel to $Ni^+ + O_2$ is then set so the overall rate coefficient is at the Langevin capture rate. [h] Photoionization rate at 100 km, utilizing the photoionization cross sections from *Heays et al.* [2017].

5.2.2 Whole Atmosphere Community Climate Model for Ni

The Ni reaction list of Table 5.1 was then imported into the Whole Atmosphere Community Climate Model (WACCM6), where the framework of the model is taken from the fully coupled Community Earth System Model (CESM)

[*Gettelman et al.*, 2019]. WACCM6 extends over a large altitude range, going vertically from the Earth's surface to the lower thermosphere at ~140 km, which more than adequate for the 70 – 120 km requirements needed to simulate the Ni and Ni^+ densities. The same horizontal resolution (1.9^o latitude $\times$ 2.5^o longitude) and 88 vertical model layers (height resolution ~3.5 km in the MLT) was used similar to the earlier work on global meteoric metals discussed in Chapter 1 & 2 [*Plane et al.*, 2015], involving WACCM4 in CESM1 [*Hurrell et al.*, 2013]. The combination of WACCM6 with Ni chemistry is termed WACCM-Ni, based from the nomenclature of previous meteoric WACCM iterations. WACCM-Ni also uses a specific dynamics (SD) version of WACCM [*Feng et al.*, 2013; *Plane et al.*, 2018b], which is nudged with NASA's Modern-Era Retrospective Analysis for Research and Applications (MERRA2) [*Molod et al.*, 2015]. Since Fe and Fe^+ are well characterized from extensive observations in the MLT, the full set of Fe reactions in WACCM-Fe [*Bones et al.*, 2016b; *Feng et al.*, 2013; *Viehl et al.*, 2016] were included in the model run, to act a suitable comparison for Ni and Ni^+.

Figure 5.7 below illustrates the meteoric input functions (MIF) of meteoric Ni and Fe taken from the Chemical Ablation MODel-Zodiacal Cloud Model (CABMOD-ZoDy) complex (see Chapter 1) [*Carrillo-Sánchez et al.*, 2020]. Both the Ni and Fe profiles were initially reduced by a factor of 5 to compensate for the fact that global models like WACCM have underestimated the vertical transport of minor species in MLT [*Plane et al.*, 2018b] because short wavelength gravity waves are not resolved on the models horizontal grid scale (~150 km). These waves that are lower than the grid scale help contribute to chemical and dynamical transport while dissipating, and this can then surpass transport driven along mixing ratio gradients by the turbulent

eddy diffusion produced once these waves break [*Gardner et al.*, 2017]. This is why the MIF needs to be reduced in order to simulate the observed metal density because of the underestimation of these additional vertical transport mechanisms [*Plane et al.*, 2018b].

In CABMOD-3, the cosmic dust particles are parameterized to have 90 wt% Fe-Mg-SiO_4 phase and a 10 wt% metallic Fe-Ni phase, so that ~70% of the total Fe is embedded inside the silicate bulk phase [*Bones et al.*, 2019; *Carrillo-Sánchez et al.*, 2020]. From there, the elemental metallic phase Fe:Ni ratio is then set to 5.5, which then gives an overall Fe:Ni abundance ratio in the particle of 18:1, the same as the CI ratio [*Asplund et al.*, 2009]. The goal of this study was to scale the Ni MIF which in turn would optimise the WACCM-Ni modelled layer to the measured Ni layer by lidar. If the model output were to compare to the Ni measurements done at Chatanika, Alaska by *Collins et al.* [2015], the Ni MIF would have required an increase, relative to Fe, of up to a factor of 15 compared to the CI ratio [*Carrillo-Sánchez et al.*, 2020] which is an extremely large increase and therefore, unlikely to be valid. The measurements done in Kühlungsborn (Section 5.2) still require a change to the Ni MIF, but the amount is only a 2.1 decrease relative to the Fe MIF. This would be explicable if the Fe:Ni ratio in the metallic phase was ~12 rather than 5.5, or the Fe-Ni phase was ~5 wt% of the cosmic dust particles. A similar discrepancy was observed between the Fe^+:Ni^+ measurements recorded by MAVEN in the Martian thermosphere and the CABMOD-ZoDy prediction [*Carrillo-Sánchez et al.*, 2020]. The relative Ni MIF is not finalized, however, and will be revised following future lidar measurements. The seasonal and geographical variation of the Ni MIF was set to the variation determined for

the Fe MIF using an astronomical dust model [*Feng et al.*, 2013; *Fentzke and Janches*, 2008].

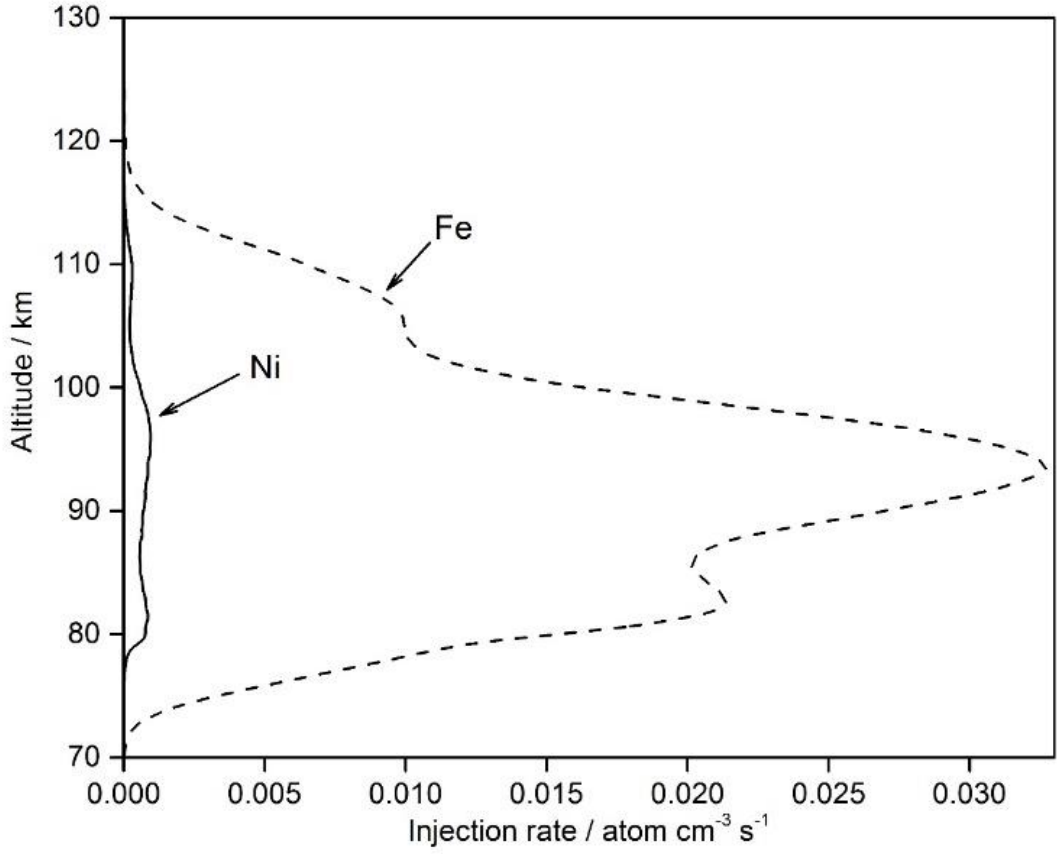

Figure 5.7. Meteoric injection rates of both Ni and Fe as a result of ablation. The injection profiles were taken from the work by [*Carrillo-Sánchez et al.*, 2020] and were subsequently divided by factors of 10.5 and 5.0, respectively (see main text for further details).

After setting the optimal Ni MIF during 2 years of model spin up, the WACCM-Ni model was run for a full year simulation from January to December 2012. The Ni observations in Section 5.2 were performed from January to March 2018, therefore performing the model simulation during the same time period would be ideal. However, several input files (solar input, CMIP6 emissions, chemical species at the surface) in the released CESM2_1_1 model have not

been made available for that particular year. Therefore, the choice of using 2012 output does not hold any significance, but the main aim of this study was to present the first atmospheric model of Ni and then compare the output to the very limited observational data currently available. As further observations are made in different monitoring sites worldwide, a deeper examination can be made into the latitudinal and seasonal dependence of the metal layer.

5.2.3 Observational Data for comparison

To explain the Ni layer measurements recorded by *Collins et al.* [2015], a very large Ni enrichment in cosmic dust would be required (see Section 5.3.2). As well as this, the measured Fe^+:Ni^+ ion ratio in the MLT was determined to be ~20:1 [*Carrillo-Sánchez et al.*, 2020], meaning that the neutral ratio cannot be explained by stating that most of the nickel is partitioned into Ni rather than Ni^+. Therefore, the Kühlungsborn observations were chosen for the model comparison (described in Section 5.2). The observation dates using the stronger Ni(a^3D_3 - $^3F_4$) transition at 341.48 nm (details in Section 5.2) were used averaged to give a single profile for comparison. Since Fe was also used for comparison, lidar observations from Urbana-Champaign (40°N, 272°E) between October 1989 and June 1992 were used [*Feng et al.*, 2013; *Helmer et al.*, 1998]. The fact this was another mid-latitude location with an extensive array of Fe lidar measurements made it a justified comparison. Rocket-borne mass spectrometric measurements of Ni^+ (*m/z* = 58) and Fe^+ (*m/z* = 56) density profiles (including a correction for their isotopic abundances) were taken from the 8 flights (see Table 5.1). A geometric mean and standard

deviation were applied to the 8 flights before comparison with the Ni^+ and Fe^+ model output.

5.3 WACCM-Ni results and comparison with observations

5.3.1 Mean profiles of Ni and Ni^+ WACCM-Ni output

Figure 5.8 denotes the profiles of the modelled Ni species around midnight, which were averaged over the same period (January – March) as the observations measured in Section 5.2. The observations and model simulations of Ni show a very good agreement, with both profiles peaking at an altitude of 86 km with peak densities at ~350 cm^{-3}. The profiles also have very similar top-side and bottom-side scale heights (75 – 102 km). The total concentration for Ni is mainly dictated by varying the Fe:Ni ratio in the metallic grain phase described in CABMOD-3 (see Section 5.3.2). However, factors such as the height of the layer peak and the scale heights provide a good test of the measured neutral and ion-molecule chemistry. Figure 5.8 also illustrates the major neutral reservoirs which are the hydroxides NiOH and $Ni(OH)_2$, and the sink for Ni is the $(NiOH)_2$ dimer which is acting as a surrogate for meteoric smoke. The metal oxides (NiO, NiO_2, $ONiO_2$) appear in narrow

layers peaking at ~10 cm^{-3} between 78 and 83 km. This is due to conversion to the more stable hydroxides by reaction of NiO with H_2O (R5.9), and $ONiO_2$ with H and H_2O (R5.13 & R5.16) [*Plane et al.*, 2015]. $NiCO_3$ is only a minor reservoir also because it is converted to NiOH by reaction with H (R5.15) with CO_2 as the by-product.

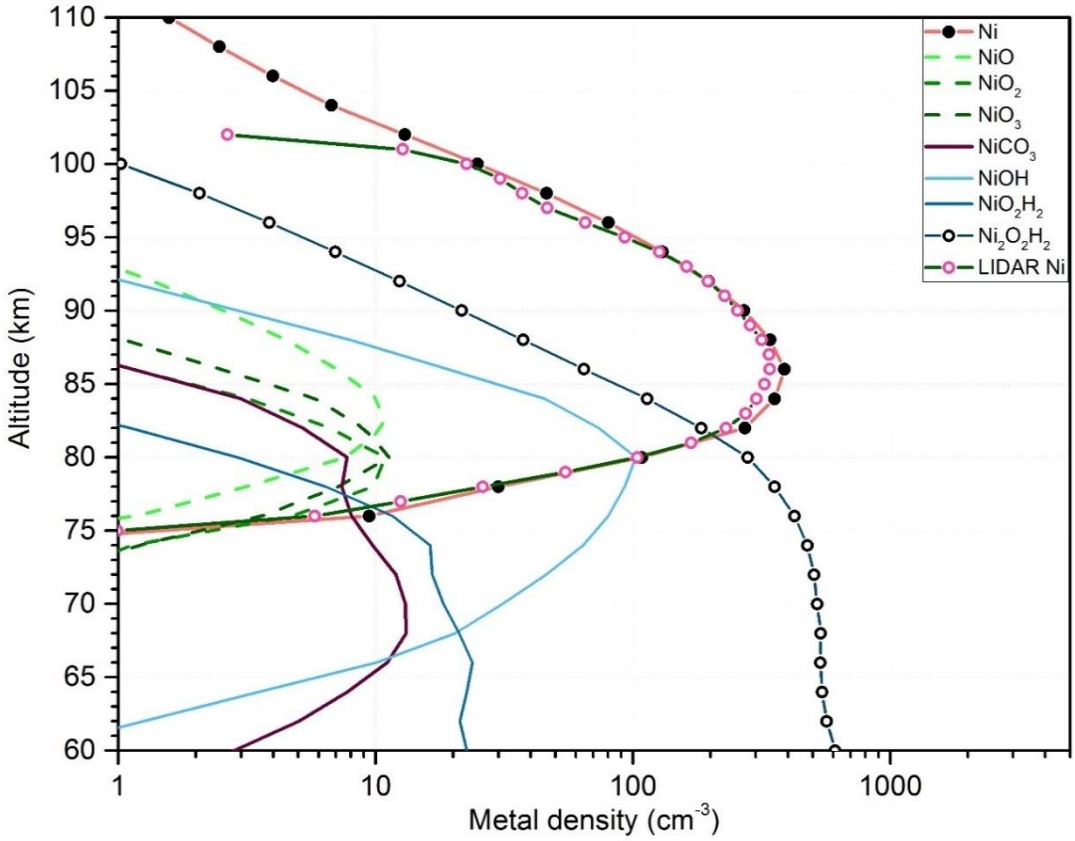

Figure 5.8: Mean altitude profiles of Ni species at 00:00 hours (Kühlungsborn local time) taken from WACCM-Ni output and compared with Ni lidar observations, between January and March 2018 at Kühlungsborn (54 N°, 12E°), with both plotted against altitude (km).

Figure 5.9 shows the mean vertical profiles of modelled Ni^+ species from WACCM-Ni in comparison with the geometric mean and standard deviation profile from the mass spectrometry measurements of Ni^+ by sounding rockets

(Table 5.1). The modelled density shows reasonable agreement with the measurements, fitting to the upper limit of the rocket average at the peak around 94 km. The modelled Ni^+ peak density is 95 cm^{-3}, compared with the observed peak of 70 cm^{-3}, with the upper limit at ~104 cm^{-3}. Calculating the column abundance between 80 and 110 km yielded a value of 1.5×10^8 cm^{-2} for the modelled Ni^+, compared with 9.7×10^7 cm^{-2} for the observed abundance. The molecular ions NiO^+, NiO_2^+ and $Ni^+.N_2$ (R5.23 – R5.24) are predicted to have much lower number densities than the Ni^+ ion (<1 cm^{-3}), with essentially no $Ni^+.H_2O$ and $Ni^+.CO_2$ species formed (see reactions R5.23 – R5.26 in Table 5.1).

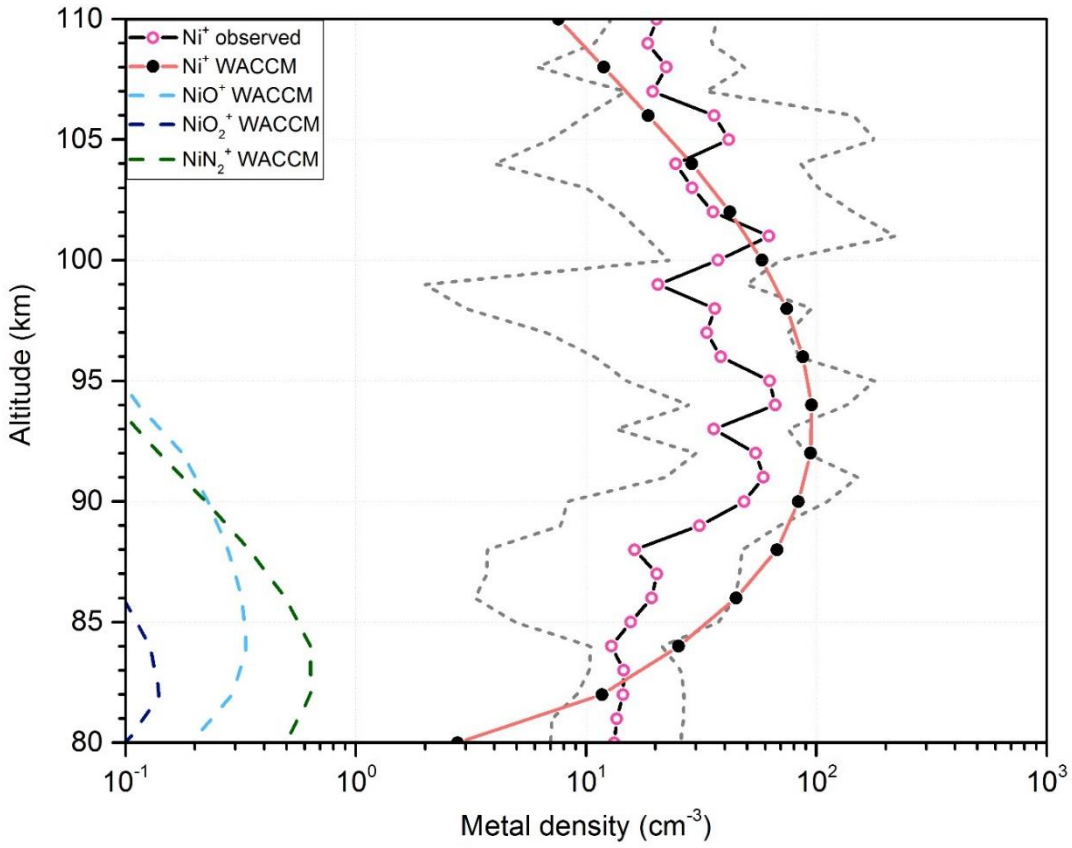

Figure 5.9: Mean altitude profiles of modelled Ni^+ species at 00:00 hours (Kühlungsborn local time) between January and March at Kühlungsborn (54 N°, 12E°). The density (log scale) was plotted as a function of altitude. The

solid black line with open pink circles represents geometric mean profile of observed Ni^+, with the geometric 1σ error limits denoted by the gray dotted lines, for the eight rocket flights described in Table 2.2

5.3.2 Diurnal variation of Ni and Ni^+ simulated by WACCM-Ni

Figure 5.10 illustrates Ni and Ni^+ densities as a function of time (in hours) and altitude (km), where the output from WACCM-Ni is sampled hourly and averaged for the whole month of April located at Kühlungsborn (54°N, 12°E). The Ni peak density in Figure 5.10a varies by ~30% throughout the averaged 24-hour period, with the peak altitude decreasing from 86 km at 00:00 to 84 km at 16:30 hrs. From 04:00 and 19:00 hrs an increase of Ni on the bottom-side of the layer was observed, whereby the density increases to 150 cm^{-3} at 80 km, and to 0.1 cm^{-3} at 72 km. These variances are a result of photolysis of NiOH (R5.21), as well as an increase of atomic O and H, and decrease of O_3, during daylight hours [*Plane et al.*, 2015].

The Ni^+ layer (Figure 5.10b) in contrast does not show any significant diurnal variation on the top- or bottom-sides. The main difference is a factor of 2 increase in the Ni^+ peak density between night and daytime hours (0900 – 1900 hrs). This can be attributed to the increase of ambient NO^+ and O_2^+ in the region due to photo-ionization; where these ions can then charge transfer with Ni (R5.41 and R5.42). It is also noted that R5.43 involving the photo-ionization of Ni is not competitive. Atomic O also increases during daytime hours by photolysis of O_2, therefore, efficiently recycling the NiO^+ molecular ion back to Ni^+ (R5.27). This leads to the prevention of the dissociative

recombination process of Ni^+ molecular ions with electrons to form neutral Ni (R5.36).

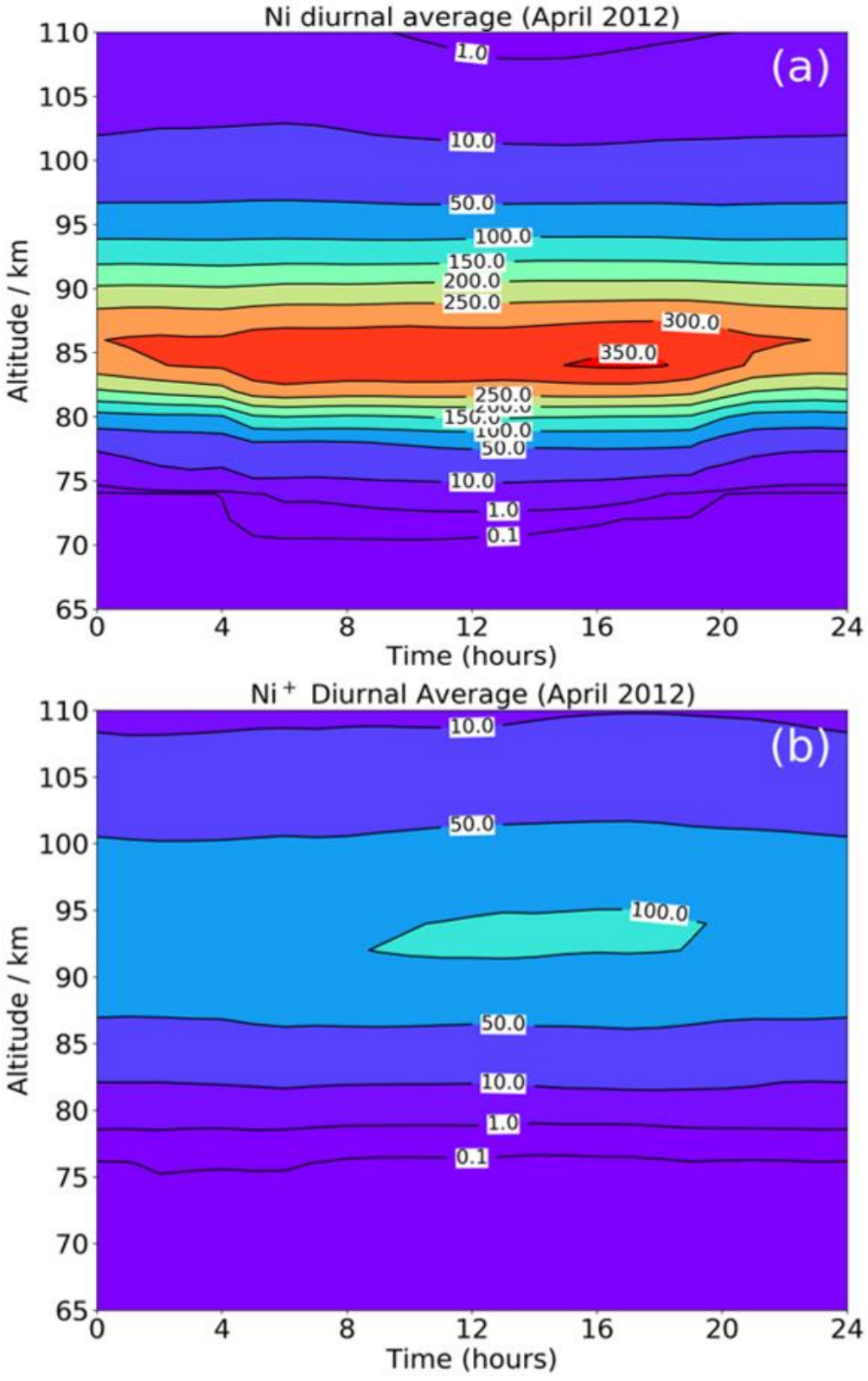

Figure 5.10: Plots showing the hourly average profiles of the (a) Ni and (b) Ni^+ densities (in cm^{-3}), as a function of altitude, simulated by WACCM-Ni for the whole month of April at 54° N, 12° E (Kühlungsborn).

5.3.3 Global column abundances of Ni and Fe

The contour plots in Figures 5.11a and 5.11b show the seasonal variation of the diurnally averaged Ni and Ni^+ column abundances, respectively, as a function of latitude and time in months. The Ni column denotes a wintertime maximum and summertime minimum, with the seasonal variation increasing with latitude. The highest abundance is observed over Antarctica during the winter period, which is likely attributed to the convergence of mesospheric air over the polar vortex [*Gardner et al.*, 2005]. This pattern has also been observed for other meteoric metals such as Fe [*Feng et al.*, 2013], Mg [*Langowski et al.*, 2015] and Na [*Marsh et al.*, 2013a]. At the Northern high latitudes, the increase in column abundance from summer to winter is a factor of ~7 for Ni, which is in close agreement to the ~6-fold increase observed for the other metals. However, in the Southern Hemisphere over Antarctica, an ~11-fold increase in Ni column abundance occurs which is quite high compared to other metals (which show a 6- to 8-fold increase). The column abundances measured at Kühlungsborn (see earlier in this Chapter) ranged from (3.1 – 4.9) × 10^8 cm^{-2} between January and March and show good agreement to the WACCM-Ni column abundance of (4.5 ± 1.5) × 10^8 cm^{-2} averaged over the same monthly period and location.

The seasonal variation of the simulated Ni^+ layer column abundance in Figure 5.11b is less extreme than Ni. The global seasonal Ni^+:Ni ratio from the model

output is 0.34. This ratio is lower than both the modelled Fe^+:Fe [*Feng et al.*, 2013] and Na^+:Na [*Marsh et al.*, 2013a] ratios, which have modelled seasonal averages close to unity. As well as this, the Ni^+:Ni ratio is far lower than the modelled Ca^+:Ca seasonal average of 11, but this ratio is a result of the unusually large photo-ionization rate of Ca and its charge transfer rate with NO^+ [*Plane et al.*, 2018b]. However, when these modelled ratios are compared to the rocket-borne observations, the Fe^+:Fe and Na^+:Na ratios are ~0.2 [*Feng et al.*, 2013; *Marsh et al.*, 2013a; *Plane*, 2004], a factor of 5 times smaller than the WACCM output, with the observed Ca^+:Ca ratio being a factor of ~2 smaller than its modelled equivalent. The observed Ni^+:Ni ratio in contrast (using the average Ni column abundance from Section 5.2, of 4.1×10^8 cm^{-2}) is 0.24, only 29% smaller than the ratio output from WACCM.

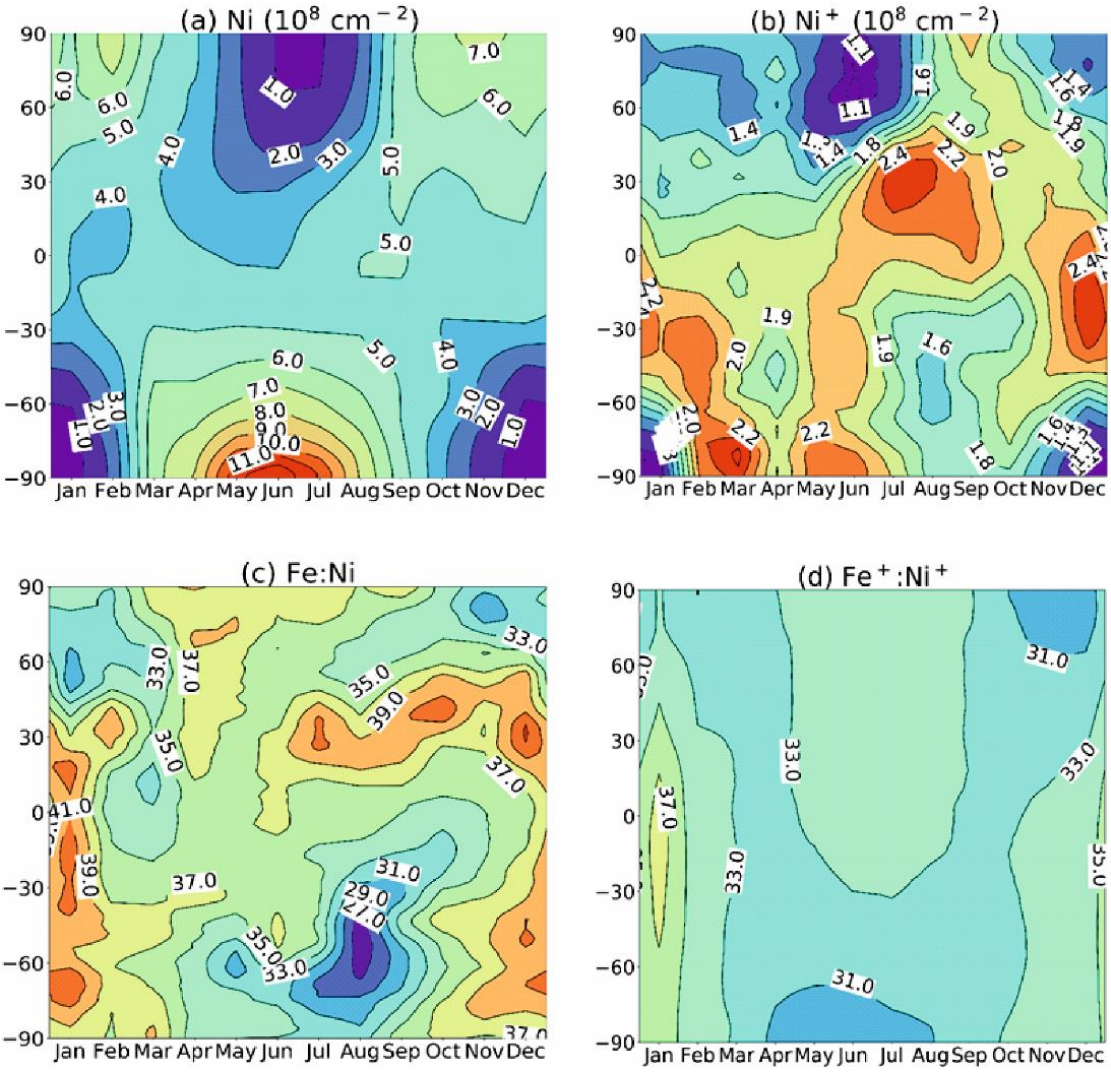

Figure 5.11: Monthly averaged column abundances as a function of season and month, simulated by WACCM-Ni and WACCM-Fe: (a) Ni, (b) Ni^+, (c) Fe:Ni ratio and (d) Fe^+:Ni^+ ratio. Note that (c) and (d) are plotted with the same contour colour scale.

Figure 5.11c denotes the seasonal variation of the Fe:Ni column abundance ratio with altitude, simulated from WACCM. There is no notable trend, other than a decrease in late winter/early spring at the latitude of 60^{o}S. It was suspected that the rate of photolysis of reservoir species NiOH and FeOH were different, causing this decrease at 60oS. Previous work on the

mesospheric Fe layer has determined FeOH to be a major Fe reservoir on the bottom-side of the Fe layer [Feng et al., 2013]. The hydroxide also photolyses quite rapidly with J(FeOH) = (6 ± 3) × 10−3 s−1 [Viehl et al., 2016]. The quantum chemistry used in that study was also applied here to retrieve J(NiOH). Using B3LYP/6-311+g(2d,p) theory [Frisch et al., 2016] and the TD-DFT method for excited states (Section 1) [Bauernschmitt and Ahlrichs, 1996], a value of J(NiOH) = 0.02 s-1 was determined in the MLT, a factor of 3 larger than J(FeOH) [Viehl et al., 2016]. Further investigation of the model output showed that the Ni:NiOH was higher in the August period at 60^{o} S than Fe:FeOH, which supports the loss of NiOH to Ni by photolysis. The global average modelled Fe:Ni ratio from Figure 5.11c is 36 ± 3, which agrees with the observed ratio of 38 ± 11 from the measurements in Kühlungsborn (see Section 5.2). The Fe^{+}:Ni^{+} ratio in Figure 5.11d does illustrate a seasonal variation with a wintertime minimum, although the overall variation is quite small. The mean value of the Fe^{+}:Ni^{+} ratio is 33 ± 1, which is at the upper level of uncertainty of the observed Fe^{+}:Ni^{+} ratio of 20^{+13}_{-8} from rocket-borne mass spectrometry [*Carrillo-Sánchez et al.*, 2020].

5.3.4 Comparison between the Ni and Fe layer profiles

Figure 5.12 below illustrates the neutral metal profiles of night-time Ni and Fe at mid-latitudes (54^{o}N), averaged from January to March 2018. Figure 5.12a denotes the lidar observations of the Ni layer at Kühlungsborn (54^{o}N, 12^{o}E) (Section 5.2) and the Fe layer at Urbana-Champaign (40^{o}N, 88^{o}E). Figure 5.12b shows the night-time layers from the WACCM-Ni and WACCM-Fe output for the same locations and monthly average. The observed and

modelled layers both peak at ~86 km. The lidar study earlier in this Chapter (Section 5.2) and the measurements made by *Collins et al.* [2015] in Alaska, both showed a distinct extension of the bottom-side of the Ni layer by 1 - 2 km lower than the Fe layer between 78 and 85 km (Figure 5.12a). This layer difference has been replicated successfully by WACCM (Figure 5.12b). When initially comparing the kinetics of both these metals, this result is unexpected since the oxidation of Ni by O_3 (R5.1) is ~2 times faster than the rate for the Fe analogue, and the reduction of NiO back to Ni by atomic O (R5.4) is ~3 times slower than the Fe equivalent, suggestive of preferred Ni removal over Fe. However, work by *Rollason and Plane* [2000] measured the rate coefficient for the reaction $FeO + O_3 \rightarrow Fe + 2O_2$ which was one order of magnitude slower than the analogous reaction of NiO (R5.3b). But the largest difference is seen when comparing both metal oxide reactions with CO. The reaction FeO + CO measured by *Smirnov* [2008] is quite slow, k(FeO + CO, 294 K) = 1.5×10^{-13} cm^{-3}. Whereas for NiO (R5.5), $k_{5.5}$(NiO + CO, 294 K) is ~210 times faster (Section 5.3). Since the atomic O density decreases very rapidly below 85 km at night [*Plane*, 2003], R5.4 shows little influence in Ni recovery but there is still a significant amount of O_3 and CO (from CO_2 photolysis). As a result, the NiO + CO reaction becomes more important below 84 km than R5.4 for recycling NiO to Ni, with $NiO + O_3$ playing a secondary role [*Mangan et al.*, 2019]. These two reactions are the main contributors to the broader lower-side of the Ni layer.

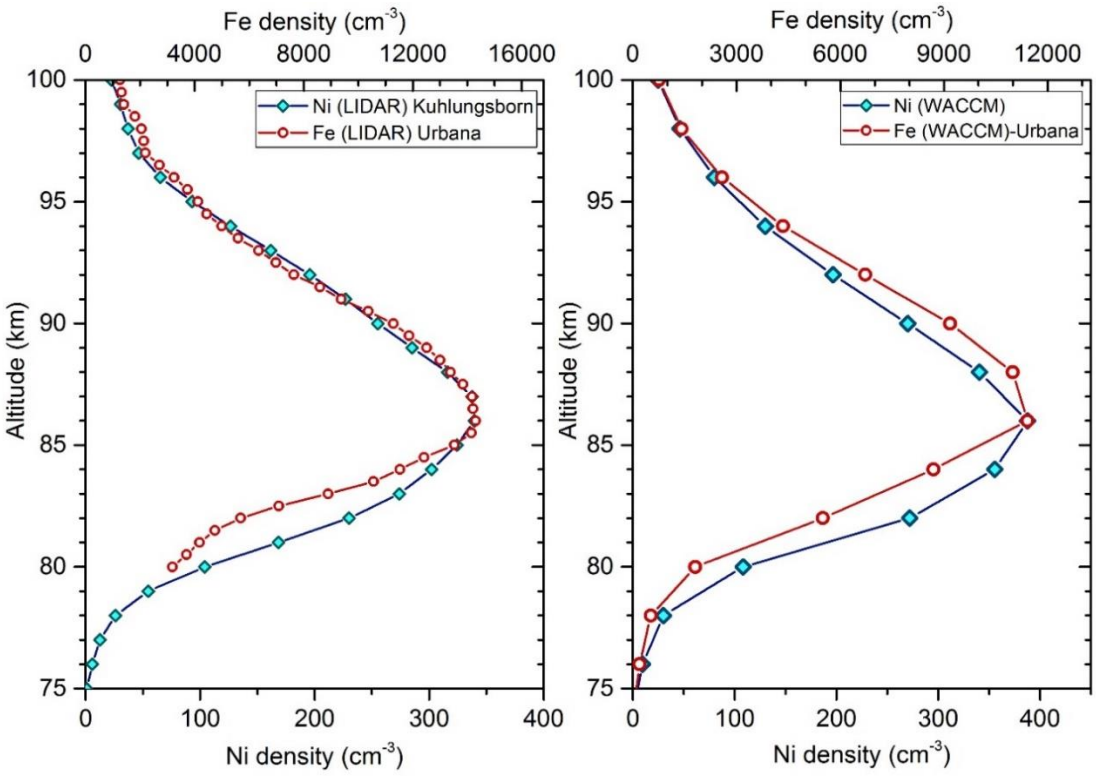

Figure 5.12: Night-time Ni and Fe layer profiles at mid-latitudes, averaged from January and March: (a) lidar observations from Kühlungsborn and Urbana; (b) WACCM output at the same lidar latitudes. The layer peak densities are scaled separately to effectively overlap the densities for Ni density (lower ordinate) and Fe density (upper ordinate).

5.3.5 Nightglow emission from NiO* and FeO*

As discussed in Chapter 1, NiO* chemiluminescence from the night airglow near 87 km was identified by *Evans et al.* [2011] from the GLO-1 [*Broadfoot and Bellaire Jr.*, 1999] and OSIRIS [*Llewellyn et al.*, 2004] spectrographs. The modelled Ni density from WACCM in this study can be used to calculate the emission rate from NiO* for comparison with the observations. Electronically excited NiO* is produced solely from the reaction between Ni and O_3 (R5.1), which is exothermic enough (ΔH^o = -297 kJ mol^{-1} as shown by *Mangan et al.*

[2019]) to produce chemiluminescence at wavelengths longer than 402 nm. This threshold is consistent with the OSIRIS nightglow measurement of an onset at 440 nm [*Evans et al.*, 2011]. An upper limit can be applied to the nightglow emission rate from NiO* by using k_1[Ni][O_3], which would assume that a photon is produced from each individual reaction that takes place between Ni atoms and the O_3 molecule i.e. a quantum yield (QY) of 1. The calculated NiO* emission profile for mid-latitudes between January and March is illustrated in Figure 5.13 below. The FeO* emission profile is also shown which was calculated from the WACCM-Fe output. According to Figure 5.13, the integrated emission intensities from the NiO* and FeO* layers are 54 and 559 R (10^{10} photons sec^{-1} (m^2 column)$^{-1}$), respectively. If both analogues have a similar QY, this would yield NiO*/FeO* = 0.10. The work from *Evans et al.* [2011] showed that the NiO*/FeO* ratio analysed from OSIRIS limb spectra was in the range of 0.05 to 0.3. Since the model estimate falls within this bracket, it would suggest that the QYs are similar. The most recent value for QY(FeO*) estimated by *Unterguggenberger et al.* [2017] is (13 $\pm$ 3)%, which would mean the QY(NiO*) is in the range of 6 - 40%.

The FeO* layer peaks at 84 km in Figure 5.13 and is in excellent agreement with OSIRIS observations [*Evans et al.*, 2011]. WACCM-Ni also predicts that the NiO* layer should peak at the same altitude of 84 km. The satellite limb observations indicate that the peak may be slightly higher (86 - 89 km) [*Evans et al.*, 2011], but the NiO* emission signal is noisy because it is weak and overlain by FeO*, Na D, OH Meinel, O_2 Herzberg and NO_2 emissions, therefore making it difficult to pinpoint.

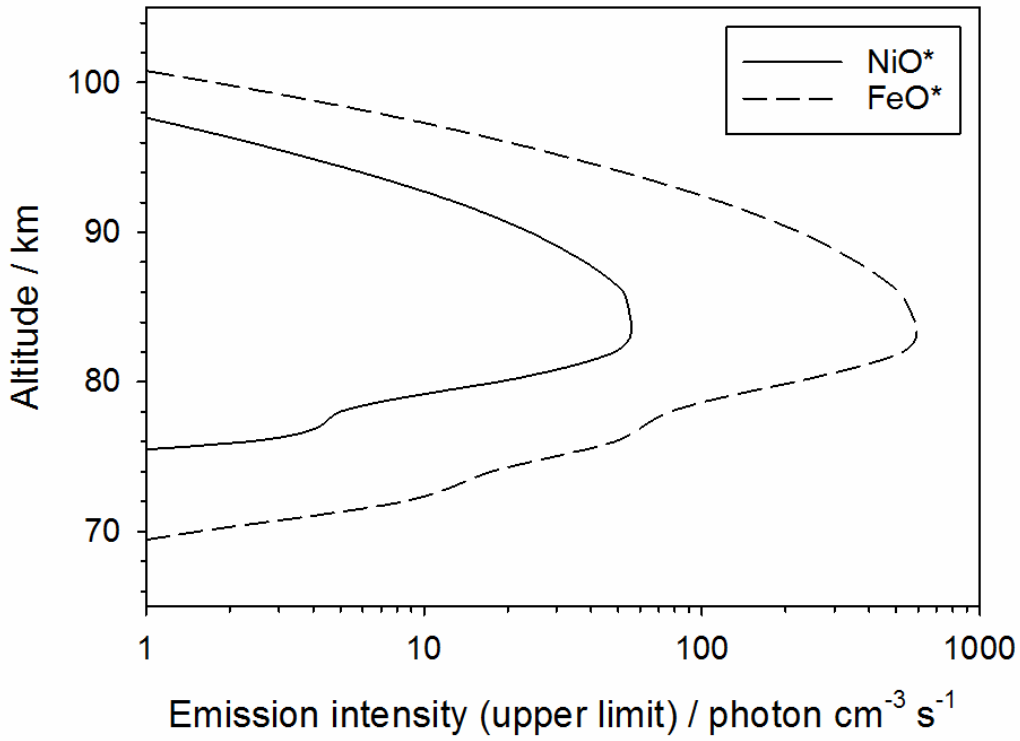

Figure 5.13. Plot of the vertical profiles for NiO* and FeO* chemiluminescence emission rates as a function of altitude. A 100% quantum efficiency was assumed for both the reactions of Ni and Fe with O_3.

5.4 Conclusion

The Ni layer has been successfully observed at a second monitoring location, Kühlungsborn, Germany (54°N), over six nights from January to March 2018. The peak densities reported from the observations were between 280 – 450 cm^{-3}, with column abundances ranging from 3.1×10^8 to 4.9×10^8 cm^{-2}. These densities are in stark contrast to the only previous measurements made in Chatanika, Alaska in 2012 which reported a peak density of 16,000 cm^{-3} and a column abundance of 2.7×10^{10} cm^{-2}, a factor of 50-70 difference. When

compared to the CI Fe:Ni ratio of 18:1 and the ablation ratio of ~16:1, the observed Fe:Ni ratio at Kühlungsborn was ~2.4 times larger at 38 ± 11, which is similar to the observed Fe^+:Ni^+ ratio in Mars' ionosphere. A possible explanation for this could be attributed to Ni being converted to long-term sinks in the MLT more efficiently than Fe or, more likely, the fact that Ni is sub-chondritic in cometary dust. The first model of meteoric Ni in the MLT was then developed, incorporating 43 reactions of Ni and Ni^+ species and a Ni MIF produced from a 2-phase chemical ablation model. A WACCM-Ni simulation with specified dynamics output from the year 2012 was then presented. There was good agreement between the modelled layer and observations at Kühlungsborn once the Ni meteoric input function is reduced by a factor of 2.1 when compared with Fe. The simulated Fe:Ni column abundance ratio in the MLT also showed close correlation, with a value of 36 ± 3, close to the observed ratio of 38 ± 11. However, the modelled Ni^+ peak density shows slight overestimation but falls within the upper limit of the geometric mean recorded by a small number of rocket-borne measurements. The Ni layer observed at the mid-latitudes location was broader on the bottom-side compared to Fe, similar to what was seen in Alaska. This was explained by faster Ni recycling reactions of NiO with CO and O_3. Finally, the quantum yield for photon production from the reaction between Ni and O_3 (contributor to the nightglow) is quite large and similar to that for the analogous Fe reaction.

6 Observations of Al species in the upper atmosphere

Following the successful measurement of the AlO absorption cross section, and the expectation that AlO will dominate over Al because of the fast reaction between Al + O_2 to form AlO (Chapter 3), lidar observations of AlO were attempted. Reactions of most metal atoms with O_2 lead to a MO_2 superoxide species [*Plane et al.*, 2015], but AlO is one of the exceptions because of the very strong Al-O bond. The Flow Tube Calibration Cell (FTCC) for the lidar system (described in Chapter 2) was constructed and transported to the Leibniz Institute of Atmospheric Physics in Germany. The system was tested to estimate the minimum requirements for an AlO signal to be observed. This included the maximum pressure the cell could operate with signal as well as the minimum pulse laser energies and pumping requirements needed. Theoretical calculations reported in this chapter (CBS-QB3 level of theory [*Frisch et al.*, 2016]) were done by Prof. John Plane.

6.1 Lidar soundings of AlO at 484 nm

For each night of lidar operation, a wavelength scan of the dye laser was made at the beginning and end of the observations, to ensure that the dye laser had

not deviated from the selected wavelength. ~5 mJ of dye laser pulse energy was split off using a beam splitter and directed using an optic fibre (2 mJ per pulse after the fibre) into the FTCC for several wavelength scans (see Chapter 2). This was to ensure that the wavelength was set to the highest intensity for fluorescent emission from the AlO(B(0)-X(0)) band. The maximum signal intensity was found to be at λ = 484.3646 nm, under conditions of 2.8 mbar (2.1 Torr), 2000 sccm N_2, 4 sccm O_2 and 5.1 ms reaction time from ablation of the metal Al rod to detection by Laser Induced Fluorescence at 484 nm in the FTCC (see Chapter 2 for FTCC setup).

The resonance dye lidar operated for a total of 21.25 hours over six nights of observations. The three nights of preliminary measurements in 2016 did not employ an AlO calibration cell. If periods with high noise due to sunset and sunrise, and breaks in operation due to dye solution changes, are removed from the data set, this leaves 18.6 hours of operation. The recording times are indicated below in universal time (UT):

<u>2016:</u>

2nd - 3rd Jan **2016** 19:11 – 00:51 UT (5:40 hours)

5th - 6th Jan **2016** 21:23 – 01:00 UT (3:37 hours)

6th - 7th Jan **2016** 16:50 – 17:38 UT (0:48 hours)

<u>2017:</u>

19th - 20th April **2017** – 20:50 – 00:30 UT (03:40 hours – 2:00 hours of useable data)

25th - 26th April **2017** – 20:30 – 01:40 UT (5:10 hours – 4:30 hours of useable data)

26th - 27th April **2017** – 21:15 – 23:40 UT (2:30 hours – 2:15 hours of useable data)

Cloud interference on the 19th - 20th April forced stoppage of the lidar two hours earlier than expected. Measurements were terminated early on the 26th - 27th April as the cuvette for the dye mixture was damaged by the beam and subsequently caused leakage of the Coumarin 102 in methanol dye solution. A Rayleigh-Mie-Raman (RMR) lidar [*Gerding et al.*, 2016] was operated in conjunction with the resonance lidar system. This consisted of green laser light at 532 nm from a Nd:YAG laser. For this study, the RMR lidar was used as a reference instrument for the AlO resonance dye lidar as it could provide an off-resonance measurement of the atmospheric background as well as providing real-time feedback to any cloud interference in the area (the recording software for the dye laser was much older than the more recently installed RMR lidar).

6.1.1 Backscatter observations at 484 nm

Figure 6.1 presents the lidar backscatter with background removed in logarithm form (x-axis) against altitude (y-axis). The background of the backscatter signal was calculated by taking a range of the measured signal at an altitude above the Rayleigh scatter and averaging them. The altitude increment averaged for all the background backscatter signal was between 120-150 km. Note that the lidar data from 2016 and 2017 in Figure 6.1 are plotted separately. This is due to different recording software being used, with the 2016 data logged in 195 m altitude bins (centre altitude = 98 m), and the April 2017 dataset in 200 m altitude bins (centre altitude = 100 m).

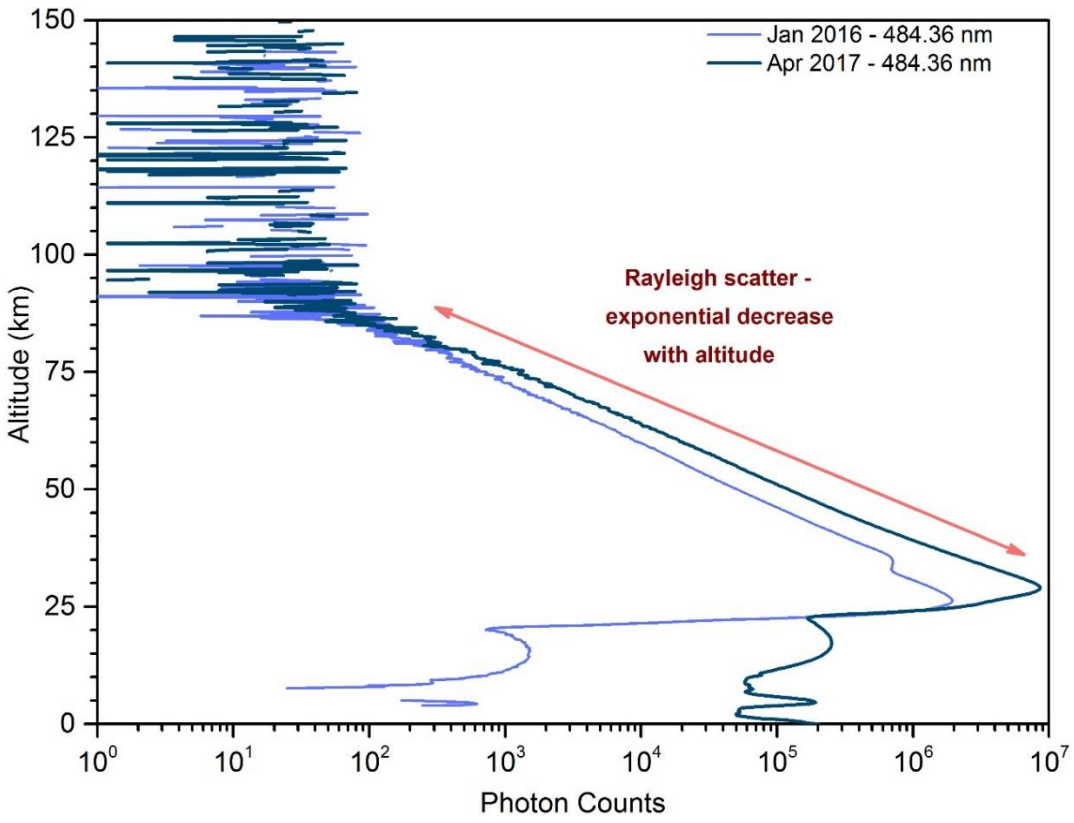

Figure 6.1: The lidar backscatter profile at 484.3646 nm for both the January 2016 and April 2017 periods, where the altitude (km) is plotted against backscattered photon counts (log scale). The signal below 30 km was reduced by using a chopper and the Rayleigh scatter from 30 km decreases exponentially with atmospheric density until ~90 km. No observable resonance signal for AlO was observed.

A rotating chopper was deployed to remove the high levels of Rayleigh scatter below 30 km as this can overload and saturate the sensitive photon-counting photomultiplier tube (PMT). The rotating chopper is synchronized with the laser trigger so that back-scattered photons which are collected by the lidar telescope for up to 200 μs after the laser fires are blocked from the PMT. [*Alpers et al.*, 2004; *Gerding et al.*, 2000]. As shown in Figure 6.1, above 30

km the observed backscatter signal decreases roughly exponentially with height, in accord with the decreasing atmospheric density and the fall off in collection efficiency with the square of the altitude. The proposed AlO layer should peak at an altitude around 90 km, by analogy with the modelled SiO layer [*Plane et al.*, 2016].

6.1.2 Statistical analysis of backscatter at 484 nm

With the Rayleigh scatter reaching an altitude of 88 km before it disappears into the noise (Figure 6.1), it was difficult to identify whether a small resonant signal from an AlO layer was present. After subtraction of the background scatter (see above), the net signal above 88 km consists of a mix of negative and positive values. To resolve this issue, Poisson statistics were applied to investigate the possibility of a small signal [*Gerrard et al.*, 2001], as the total number of photons arriving during a time interval is Poisson distributed [*Liu et al.*, 2006]. The backscatter photon counts over the three measurement periods were treated as the mean. From there, the standard deviation (σ) was calculated by taking the square root of the backscatter signal before removal of the atmospheric background. This was then compared with the backscatter after removal of the background, to see if any signal was present at the 2σ and 3σ (doubled and tripled standard deviation) levels above the Rayleigh scatter. If a peak occurred at the 3σ level above the Rayleigh scatter, then this would indicate a possible resonant AlO layer. Figure 6.2 below illustrates the statistical treatment to the backscatter signal at 484 nm. The scatter is linearly plotted here and the focus is on the noise between 75 - 150 km.

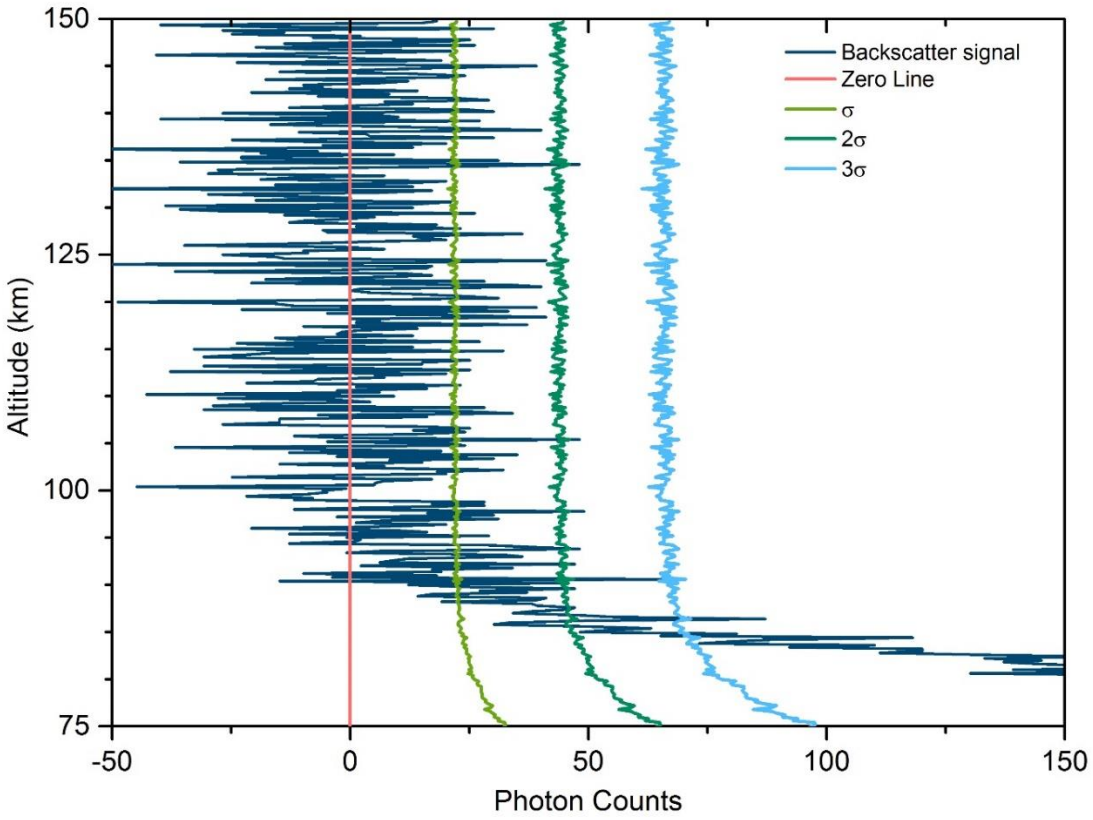

Figure 6.2: Statistical analysis of the backscatter at 484.3646 nm. The altitude (km) is plotted against the observed backscatter (photon counts). The zero line is shown to help identify any specific deviation of the signal. A linear rather than logarithmic scale is used, as it is easier to compare the statistical treatment of the resonant backscatter. Note that the Rayleigh scatter begins close to the altitude where an expected resonance signal might be. An AlO resonance signal is not present statistically at the 3σ level.

As shown in Figure 6.2 no layer profile is larger than σ. The backscatter noise occasionally exceeds 2σ, and 1 point reaches 3σ at ~90 km, but there is no evidence for a layer.

6.1.3 Metal dye backscatter vs Rayleigh-Mie-Raman backscatter signal

The RMR lidar operated in conjunction with the dye lidar during observations. Since the RMR emitted a different wavelength (532 nm of the Nd:YAG) to that for AlO, it could also act as an off-resonance measurement for the backscatter signal at 484.36 nm. Since no off-resonance measurements were taken with the dye lidar at the time, this proved to be the best reference. Therefore, the task was to identify any difference at the end of the Rayleigh scatter that could be attributed to an added resonance signal. Figure 6.3 illustrates the backscatter plots of both the dye lidar and the RMR lidar.

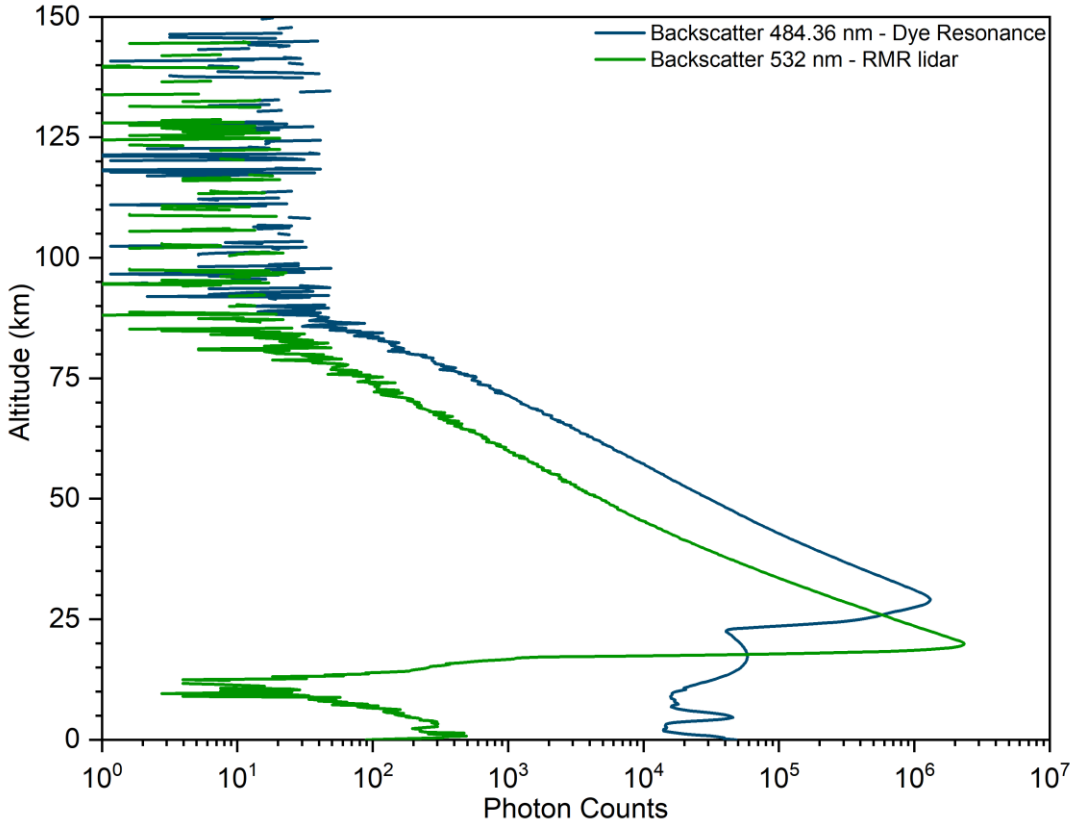

Figure 6.3: Comparison of the backscatter signal between the metal resonance lidar and the RMR lidar, showing altitude against photon counts on a log scale. The RMR backscatter counts were less than the resonance lidar signal as this RMR backscatter was recorded by the lowest Rayleigh channel

(5% of the detected light). The Rayleigh scatter of both profiles decay in a similar way.

In Figure 6.3 the backscatter signal from the RMR was substantially less than the dye laser, even though the laser power of the Nd:YAG was of the order of ~650 mJ compared to the dye laser in the resonance lidar of 25 mJ. The principle of the 'power-aperture' product entails that the received signal, independent of the optical processes involved, is proportional to the power *P* of the lidar transmitter i.e. the laser power, multiplied by the area *A* of the receiving telescope [*She*, 2005]. Following this principle, the RMR-lidar should have a much larger backscatter. The reason why it is smaller here is that the Rayleigh channel used only receives 5% of the incoming light. The other detectors had a larger Rayleigh scatter than the dye lidar as they received most of the incoming light. Comparing to the metal resonance backscatter shows that both Rayleigh signals decay monotonically into the noise.

6.1.4 Calculating the upper limit to the AlO concentration

Since there was no discernible AlO signal in the measured lidar profiles, a detection limit for AlO was determined. This estimate in the future will be crucial as an upper limit for future model runs predicting Al in the upper atmosphere.

Before the upper limit of the lidar signal could be calculated, the resonance signal needed further investigation. After removing the background signal, the signal was then extrapolated from 80 km to 90 km (the purple line in Figure

6.4). Figure 6.4 also compares the extrapolated line against the observed residual backscatter (light blue line), to see if any trace layer remained.

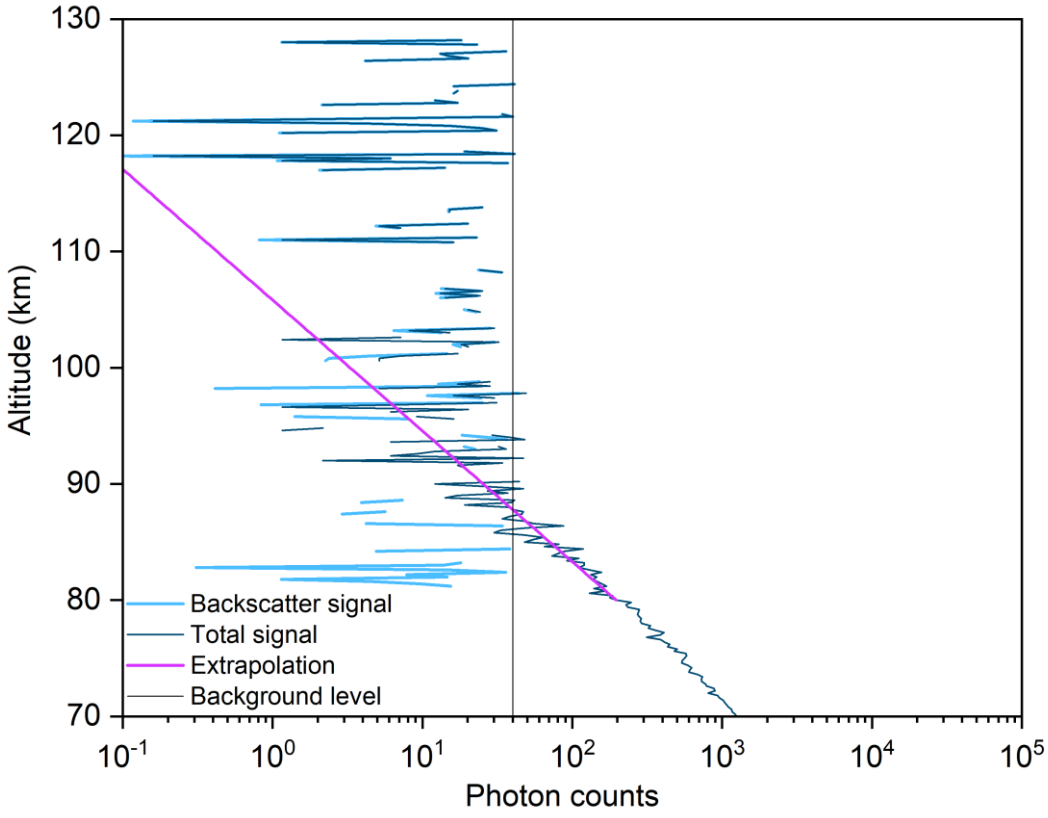

Figure 6.4: Resonance backscatter with background removed (dark blue line) and the extrapolated Rayleigh signal (purple line), showing altitude (km) against the recorded photon counts. The signal was extrapolated from the average counts of the 80-90 km altitude range. The remaining background scatter after subtraction of the extrapolated Rayleigh line (light blue) did not show any distinguishing resonance signal.

To retrieve an upper limit for AlO, it was assumed to exist in a roughly Gaussian-shaped layer extending from 80 to 100 km with a peak at 90 km, analogous to the other metal layers [*Plane*, 2003; *Plane et al.*, 2015]. With no

trace signal of an AlO layer present, a Gaussian profile was fitted to the residual to determine an upper limit to the AlO concentration. The upper limit of the backscatter would then represent the peak concentration at 90 km. Adapting the work of *Tilgner and von Zahn* [1988], an upper limit, n_z(AlO), was calculated as follows:

$$n_z(AlO) = n_{zr}(air)\frac{\sigma_{Ray}(air)}{\sigma_{res}(AlO)}\frac{z^2(AlO)}{z_r^2}\frac{C(AlO)}{C(air)}\frac{1}{Tr^2(z_r,z)} \qquad \text{(E6.1)}$$

[*Tilgner and von Zahn*, 1988]

where n_{zr}(air) is the air density at the reference altitude, σ_{Ray} and σ_{res} are the Rayleigh and resonant AlO cross sections at 484.36 nm, z the altitude taken for the AlO maximum, z_r the reference altitude of 30 km, C(AlO) and C(air) representing the subsequent AlO and air counts, and Tr (z_r, z) is the transmission of the atmosphere between z_r and z at the laser pulse wavelength. The fit gave an upper limit for AlO at the peak of 57 molecule cm^{-3}. Once the maximum concentration of the postulated layer was established, equation (II) was applied to convert the lidar counts into AlO concentration as a function of altitude:

$$n_z(AlO) = \frac{n_{z0}(AlO)}{0.5(C_{01}+C_{02})}C_k(z)\frac{z^2(AlO)}{z_0^2(AlO)} \qquad \text{(E6.2)}$$

[*Tilgner and von Zahn*, 1988]

where n_{zo}(AlO) represented the upper limit of AlO at 90 km, C_{01} and C_{02} the neighbouring values, and C_k(z) the lidar counts. Following this, the total column abundance of the layer can be calculated using equation (III), which entails the integral over the depth of the atmosphere within the limits of the proposed altitude range:

$$[x]_i \Delta z \qquad \text{(E6.3)}$$

where $[x]_i$ represents the summed number densities in cm^{-3} taken at the 200 m intervals and Δz accounted for the density in-between the altitude intervals. This yielded a column density value of 4.1×10^7 molecule cm^{-2}. Figure 6.5 below shows the AlO number density against altitude:

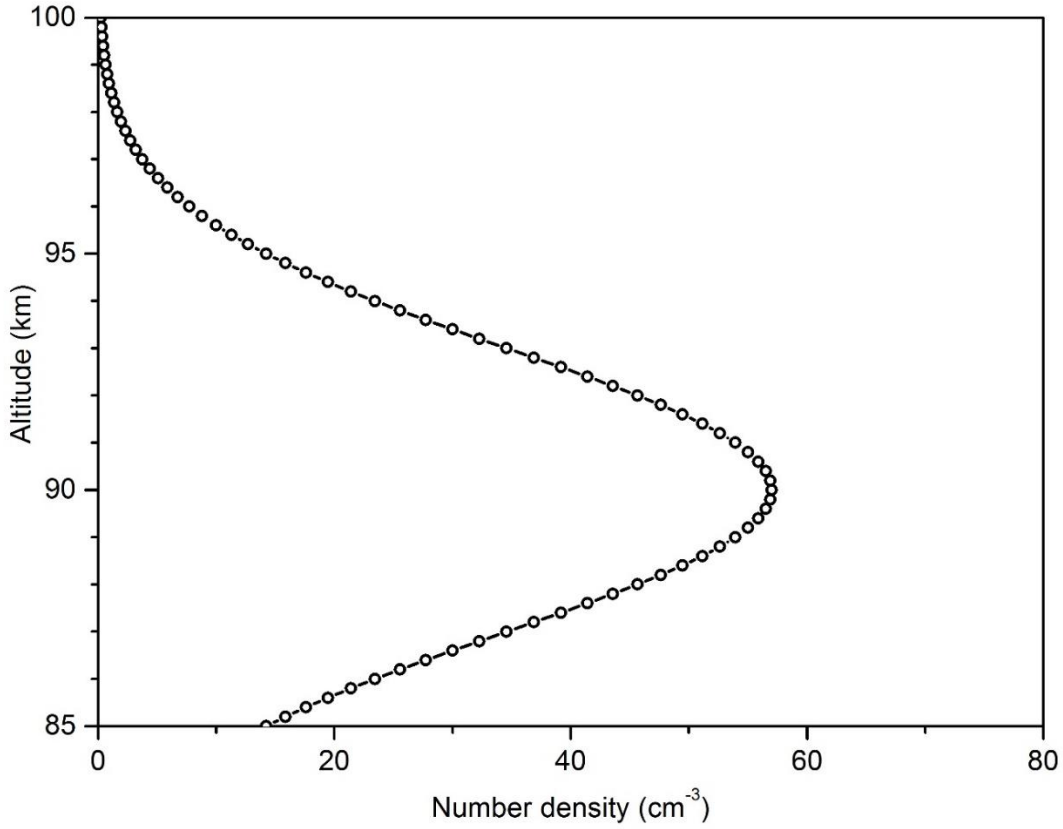

Figure 6.5: Vertical profile of the upper limit to the AlO number density. A fitted Gaussian was applied to create the layer profile, with the peak of the layer at 90 km. The upper limit at the peak is 57 molecule cm^{-3} and the column density is $\leq 4.1 \times 10^7$ molecule cm^{-2}.

6.1.5 Estimating the AlO concentration from rocket releases of tri-methyl-aluminium

To compare with the estimated upper limit of AlO in the MLT from the lidar observations, luminous trails created from tri-methyl-aluminium (TMA) releases were examined. Al has been injected into the MLT using TMA grenades from sounding rockets [*Gole and Kolb*, 1981; *Johnson and Lloyd*, 1963]. Chemiluminescence was observed from these trails and it was suggested that the reaction between AlO and atomic oxygen leads to the chemiluminescence [*Gole and Kolb*, 1981]. Earlier work by *Johnson and Lloyd* [1963], and quite recently by *Roberts and Larsen* [2014], also suggest that the observed luminescence is due to AlO chemiluminescence. Estimates of the trail lifetimes have been made, ranging from 5 - 15 minutes [*Larsen and Odom*, 1997] and 5 - 30 minutes [*Roberts and Larsen*, 2014].

These AlO lifetimes can be used to estimate the AlO concentration in the ambient atmosphere. To do this, the rate of injection of Al from meteoric ablation rate is required. *Carrillo-Sánchez et al.* [2016] and *Carrillo-Sánchez et al.* [2020] estimate a value of 2×10^{-3} atom cm^{-3} s^{-1} at ~90 km. The AlO at steady-state is then the injection rate multiplied by the lifetime from the TMA. Conversely, the upper limit of AlO determined from the lidar measurements (see above – Section 6.1.4) divided by the injection rate gives an upper limit to the atmospheric lifetime.

Figure 6.6 compares the AlO lifetimes derived from the TMA releases and the lidar upper limit. Four launches were taken for this comparison, with the JOULE 2 launch as the longest-lasting AlO trail [*Roberts and Larsen*, 2014].

An AlO lifetime of 30 minutes corresponds to a steady-state AlO concentration of 4 cm^{-3}. The deployed resonance lidar would require a detection limit of ~1 cm^{-3} to observe this, a factor of 60 times lower than what was achieved so far. This upper limit however will provide a useful reference for the modelled output of AlO from WACCM-Al once it is developed.

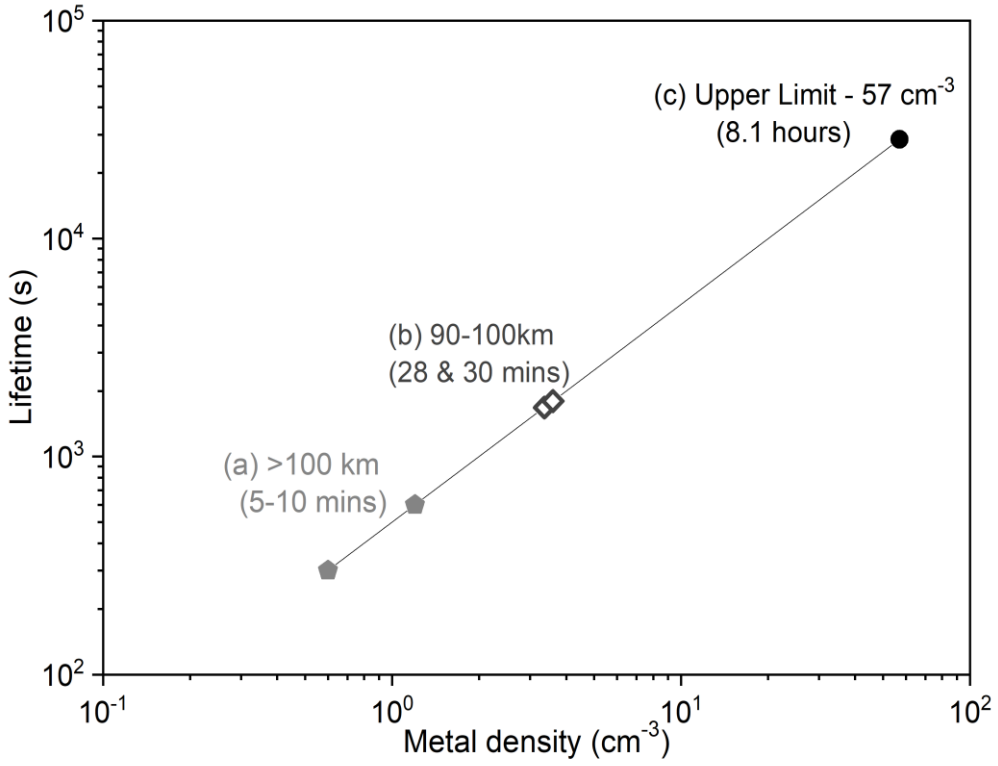

Figure 6.6: Comparison between the AlO trails (a) & (b) [*Roberts and Larsen*, 2014] and resonance signal upper limit (c), where the lifetime (s) was plotted against concentration (cm^{-3}). The maximum observation time for an AlO trail was about 30 minutes. The measured upper limit of 57 cm^{-3} from the resonance lidar would require the AlO trace to have a lifetime of ~8 hours in the MLT. This comparison indicates that the lidar detection limit would need to decrease by a factor of 60 for AlO to be measurable.

6.2 Ion measurements

This section the ion species required investigation. Al has 22 known isotopes ranging from ^{22}Al to ^{43}Al but ^{27}Al is the only naturally occurring isotope [*Kohman*, 1997; *Wang et al.*, 2017]. $^{27}Al^+$ measurements in the MLT were taken from rocket-borne mass spectrometric measurements at m/z 27 (see Table 2.2 in Chapter 2).

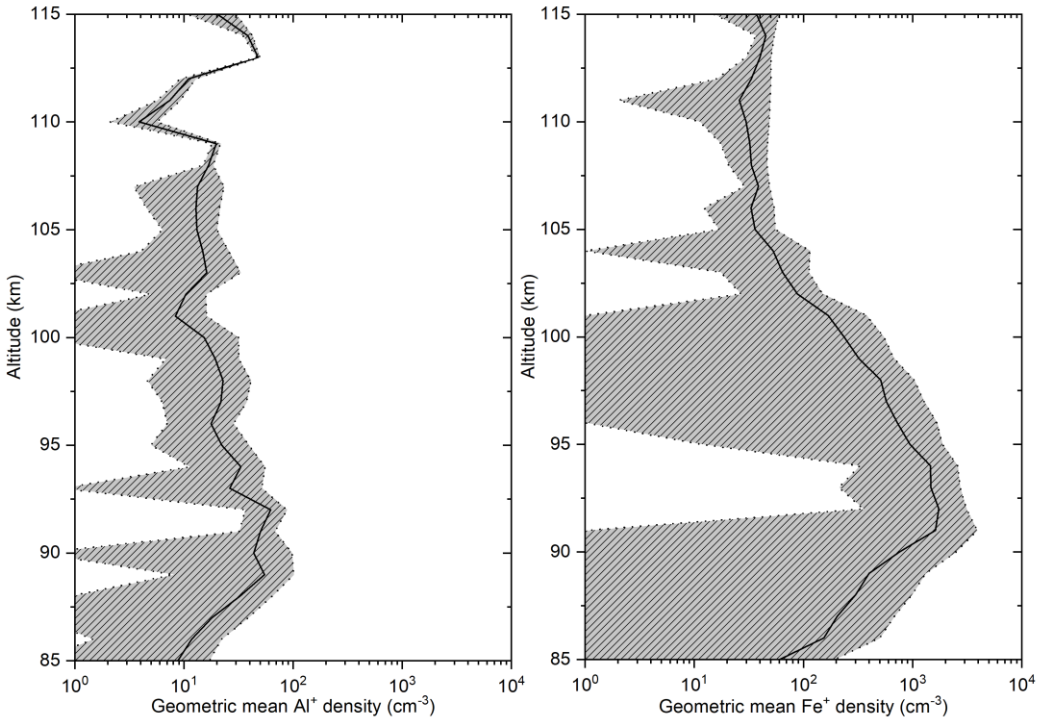

Figure 6.7: Al^+ and Fe^+ density profiles on a log scale (measured by mass spectrometry from 8 rocket flights excluding the 'Ue06' flight). The solid black line represents the geometric mean calculated from the flight rockets for each species, with the shaded dashed regions indicating the 1σ upper and lower limits.

The Al^+ profile was similar in shape to the observed Ni^+ density discussed in Chapter 5. The main difference is that the Ni^+ ions peaks between 91 – 95 km

compared to Al^+, which peaks between 88 – 92 km (54 cm^{-3} at 88 km with an upper limit of ~100 cm^{-3}, and 62 cm^{-3} at 92 km with an upper limit of 87 cm^{-3}, respectively). This difference can also be seen in Figure 6.7 when comparing to Fe^+, which peaks at a similar height to Ni^+. The log scale profile was almost vertical with increasing altitude which suggested that the mixing ratio of Al^+ increased with altitude, at least in the range from 85 – 115 km. In contrast, Fe^+ decreases with height (constant mixing ratio). Each rocket flight only represents a 'snapshot' profile, therefore the recorded counts varied from flight to flight, leading to relatively large 1σ values. This leads to large fluctuations in the plotted $\bar{x} - \sigma$ and $\bar{x} + \sigma$ as shown in Figure 6.7. Figure 6.8 below shows the Fe^+:Al^+ ratio in the same altitude range, and is compared to both the CI ratio measured by [*Lodders and Fegley*, 2011] and the Chemical Ablation MODel-ZoDiacal Cloud Model (CABMOD-ZoDy) ablation ratio calculated by *Carrillo-Sánchez et al.* [2020].

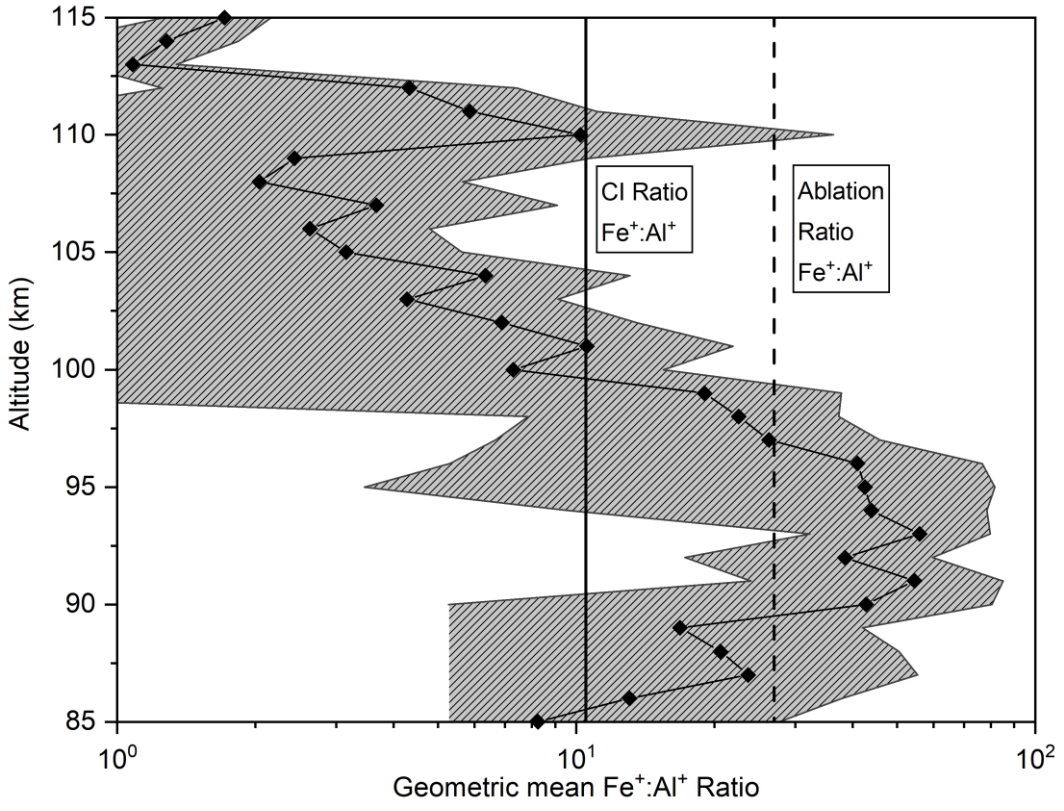

Figure 6.8: Ratio of the geometric means for Fe^+:Al^+ ion density, against altitude (km). Ratio shown in log scale. The chondritic (CI) ratio and modelled ablation ratio are represented as the black solid line and dashed line respectively. The average Fe^+:Al^+ ratio from 85 – 115 km for the rocket flights is 24 ± 10, which is similar to the modelled ablation ratio of 27 [*Carrillo-Sánchez et al.*, 2020].

The average Fe^+:Al^+ ratio between 85 and 105 km is 24 ± 10, which is similar to the ablation ratio of 27 (dashed line of Figure 6.8). If compared to the atmosphere of Mars, the Fe^+:Al^+ metal ion ratio measured by the Neutral Gas Ion Mass Spectrometer on the MAVEN satellite at 185 km, yielded a similar value of 25 ± 4 [*Benna et al.*, 2015].

6.3 Discussion

The analysis above shows that AlO does not have a sufficiently long lifetime in the MLT for it to build up to concentrations that are detectable by the current resonance lidar. The potential reaction pathways which remove AlO are now discussed. First, a recycling reaction to Al was considered. Al was not included in the lidar measurements as the kinetics study of Al + O_2 in chapter 3 justified the abundance of AlO over Al. However, if a potential back reaction of AlO with atomic O were to occur, the AlO would be recycled in the MLT. As well as this, the Al resonance cross section at 394.4 nm ($^2S_{1/2} \leftarrow {}^2P^o_{1/2}$) was calculated to be 1.7×10^{-12} cm^2, a factor 253 times larger than the experimentally measured cross-section of AlO (see chapter 3). The energetics

of this back-reaction was determined using CBS-QB3 theory electronic theory [*Frisch et al.*, 2016]:

$$AlO + O \rightarrow Al + O_2 \qquad (\Delta H° = -14 \pm 9 \text{ kJ mol}^{-1}) \qquad \text{(R6.1)}$$

Comparing the energetics with the exothermic formation of AlO at -14 ± 9 kJ mol^{-1}, if the estimated upper limit of AlO was of the order of 4 cm^{-3}, then the Al concentration would be considerably less, at 1.3 $\times$ 10^{-5} cm^{-3}. Even assuming thermoneutrality of the back reaction to retrieve Al (i.e. $\Delta H° = 0$), the detection limit would still be 6 $\times$ 10^{-3} cm^{-3}. Therefore, there was still no justification for attempting observations of Al in the upper atmosphere. The alternative was removal of AlO by further reaction routes, until it reached a stable reservoir species. These potential pathways were predicted using CBS-QB3 theory:

$$AlO + O_3 \rightarrow AlO_2 + O_2 \qquad (\Delta H = -291 \text{ kJ mol}^{-1}) \qquad \text{(R6.2)}$$

$$AlO_2 + O \rightarrow AlO + O_2 \qquad (\Delta H = -107 \text{ kJ mol}^{-1}) \qquad \text{(R6.3)}$$

R6.2 and R6.3 are exothermic, with the forward reaction more energetically favourable. However, this pair of reactions just recycles AlO but trace concentrations of H_2O could break the two-step cycle through:

$$AlO + H_2O \rightarrow Al(OH)_2 \qquad (\Delta H = -314 \text{ kJ mol}^{-1}) \qquad \text{(R6.4)}$$

From here, there are two potential reaction pathways for $Al(OH)_2$, as shown in R6.5 – 6.6:

$$Al(OH)_2 + H \rightarrow AlOH + H_2O \qquad (\Delta H = -168 \text{ kJ mol}^{-1}) \qquad \text{(R6.5)}$$

$$Al(OH)_2 + O \rightarrow OAl(OH) + OH \qquad \text{(R6.6)}$$

The OAl(OH) may potentially be a stable species for Al in the MLT, as Al would be in its stable +3 oxidation state.

6.4 Conclusion

In conclusion, observations of AlO were attempted at the Leibniz Institute of Atmospheric Physics during January 2016 and April 2017. A portable flow tube calibration setup was developed to calibrate the wavelength (accurately to 4 decimal places) of the dye laser for the resonance lidar during the April observational period. After ~ 20 hours of measurements, it was established that there was no discernible AlO resonant signal at the current limit of detection. An upper limit of the AlO density (57 cm^{-3}) was compared with AlO lifetimes determined from TMA releases. It was found that the lidar detection limit would need to decrease by a factor of 60 (i.e., to around 1 cm^{-3}), for the AlO layer to be detectable. Al^+ ion measurements from the rocket flights (discussed in Chapters 2 and 5) reveal the Al^+ layer peaks at ~ 60 cm^{-3}, with an upper limit of 100 cm^{-3}. The average Fe^+/Al^+ ratio on Earth from 85 – 105 km was similar to the MAVEN observations of the Martian atmosphere at 185 km.

7 Conclusions and future work

Chapter 1 provided the background on cosmic dust and metal layers in Earth's atmosphere as well as the motivation to study two further metals, Ni and Al, and their interactions in the upper atmosphere. These experimental and modelling methods deployed to answer these questions were described in Chapter 2, with the results detailed in Chapter 3 – 6. This chapter provides the overall conclusions from the result chapters of this thesis along with suggestions of future work. Research relating to Ni is detailed in Section 7.1 with Al discussed in Section 7.2

7.1 Ni

For the kinetics of Ni, the rate coefficients for 15 reactions were successfully measured (3 neutral and 12 ion molecule). Notable reactions include $k(NiO^+ + O) = 1.7 \pm 1.2 \times 10^{-10}$ cm^{-3} molecule^{-1} s^{-1} which was 5.3 times faster the FeO^+ equivalent where $k(FeO^+ + O) = (3.2 \pm 1.5) \times 10^{-11}$ cm^3 molecule^{-1} s^{-1} [*Woodcock et al.*, 2006] and $k(NiO + CO, 294\ K) = (3.0 \pm 0.5) \times 10^{-11}$ cm^{-3} molecule^{-1} s^{-1} which is ~210 times the rate of the analogues $k(FeO + CO, 294\ K) = 1.5 \times 10^{-13}$ cm^{-3} [*Smirnov*, 2008].

To verify the surprisingly large Ni densities (16,000 cm^{-3}) measured by *Collins et al.* [2015], further lidar soundings of Ni were carried out during January to March 2018 period Kühlungsborn, Germany (54^{o}N, 12^{o}E) using the same spectroscopic transition at λ_{air} = 336.96 nm as well as the stronger transition Ni(a^3D_3 - $^3F_4$) at λ_{air} = 341.48 nm, discovered in Leeds [*Mangan et al.*, 2019]. The Ni densities measured were much lower, with peak densities in the 280 – 450 cm^{-3} range and column abundances ranging from (3.1 – 4.9) × 10^8 cm^{-2}. This yielded a Fe:Ni ratio of 38 ± 11, which was a factor of 2.4 ± 0.7 times

larger than the CI ratio, and up to a factor of 32 larger than ratio observed by [*Collins et al.*, 2015]. Both lidar measurements however reported a broader lower-side of the layer compared to Fe, indicative of Ni recycling. 43 reactions of Ni were then imported in the Whole Atmospheric Community Climate Model (WACCM) with the addition of Ni meteoric input function that was reduced by a factor of 2.1 compared to Fe to accommodate for the lack of Ni in the bulk silicate phase [*Bones et al.*, 2019; *Carrillo-Sánchez et al.*, 2020]. There was decent agreement between the simulated Ni output from WACCM-Ni with the limited number of lidar measurements made in Kühlungsborn and the Ni^+ output when compared to the mass spectrometry rocket soundings [*Kopp*, 1997], with just a slight overestimation for the ion species. The modelled Fe:Ni column abundance ratio of 36 ± 3 showed close correlation to the observed ratio of 38 ± 11 (Chapter 5). The bottom side of the Ni layer was finally explained through the faster recycling of Ni from NiO with CO and O_3.

For future work, further observations of Ni are clearly the first step for the metal species. With two separate observations reporting vastly different column abundances, a third party in a separate monitoring location is required to verify the density. If the next lidar soundings show close correlation to the measurements at Kühlungsborn (Chapter 5) then the following task would entail investigating kinetically why the observed Fe:Ni ratio is a factor of 2 larger than the chondritic ratio, specifically the conversion of Ni to long-term atmospheric sinks compared to Fe. It may also be likely that Ni is depleted in cometary dust since the Fe^+/Ni^+ ratio on Mars agrees with the neutral ratio on Earth [*Carrillo-Sánchez et al.*, 2020]. Reactions of atomic H with the higher oxides and hydroxides of Ni would also require measurement and importing into WACCM-Ni later.

7.2 Al

In total, the rate coefficients for 12 reactions of Al- and Al^+-containing species were successfully measured (2 neutral and 10 ion molecule). The rate of $k(Al^+ + O_3, 293\ K) = (1.4 \pm 0.1) \times 10^{-9}\ cm^3\ molecule^{-1}\ s^{-1}$ was faster than all the previous meteoric metal analogues measured (Fe, Ca, Mg, Ni etc). The absorption cross section of AlO was determined to be $\sigma(\lambda_{air} = 484.23\ nm) = (6.7 \pm 1.6) \times 10^{-15}\ cm^2\ molecule^{-1}$. With a bandwidth peak of the cross section at 0.003 nm (only 80 times smaller than the cross section of the Fe line used lidar observations) and showing little temperature dependence when going from 298 K to the mesospheric temperatures of 200 K, the results showed promise for potential detection of AlO in the mesosphere-lower thermosphere (MLT). The measured rate coefficient $k(Al + O_2) = (1.68 \pm 0.24) \times 10^{-10}\ cm^3\ molecule^{-1}\ s^{-1}$ was in close agreement with the two previous measurements by pulse-laser-photolysis laser-induced-fluorescence technique [*Garland and Nelson*, 1992; *Le Picard et al.*, 1997], further supporting the loss of Al to AlO in the MLT due to the very strong Al-O bond (503 kJ mol^{-1}) which contrasts with the other meteoric metals which form MO_2 (where M = Fe, Ni, Na, Ca etc). Only titanium (Ti) is the exception, where $k(Ti(a^3F) + O_2 \rightarrow TiO + O, 300\ K) = (1.5 – 1.6) \times 10^{-12}\ cm^{-3}\ molecule^{-1}\ s^{-1}$ [*Clemmer et al.*, 1993; *Ritter and Weisshaar*, 1990]. However, after 21.25 hours of lidar observations at the lidar sounding site at Kühlungsborn, Germany, there was no discernible resonant signal of AlO detected. Instead, an upper limit of 57 cm^{-3} was retrieved. Investigating AlO chemiluminescence from tri-methyl-aluminium

(TMA) releases in the 1960s and 70s showed that the detection limit required to observe AlO density would be ~4 cm^{-3}.

Therefore, future work should primarily focus on improving the AlO detection limit determined in Chapter 6, by improving the power-aperture product (*PA*). This is a relative measure of the performance of the lidar system and as a result, affects the temporal and spatial resolution possible. The received signal is proportional to the power *P* of the lidar transmitter i.e. dye laser; and to the area *A* of the telescope that receives the signal [*She*, 2005].

For the AlO observations discussed in Chapter 2 and 6, the pumping source (XeCl excimer laser) was previously able to produce pulse energies of ~600 mJ at 308 nm [*Gerding et al.*, 2000] but for the measurements made here, 400 – 500 mJ was achieved. Conversion to 484 nm, using the Lambda Physik FL-series dye laser, produced laser pulse energies ranging from 15 – 25 mJ (3-7% conversion). From there, the backscattered light was then collected using a 78 cm diameter telescope (most conventional telescopes are developed from glass substrates with metallic coatings and can range from 0.25 – 1 m in size) and after 21.25 hours of integration time at 484 nm an upper limit of 57 cm^{-3} was achieved.

The Purple Crow Lidar (PCL) at the University of Western Ontario hosts a 2.65-m diameter liquid-mercury mirror as their receiver [*Argall et al.*, 2000; *Sica et al.*, 1995], which is ~3.4 times larger than the mirror used in the AlO measurements. Applying this change to the PA product, the aperture (where A is in units of m^2) will increase from 0.64 to 7. If the other parameters were kept constant (PMT quantum efficiency, interference filter transmission and

wavelength, etc) then by principle of the *PA* product, the detection limit would drop to 5 cm^{-3}.

The transmitter system could be further improved to reduce the detection limit. The laser system used in Kühlungsborn was originally a twin dye laser setup stationed nearby at Juliusruh (55ºN, 13ºE) [*Alpers et al.*, 1996] before moving to the Leibniz Institute of Atmospheric Physics, Kühlungsborn (55ºN, 12ºE) [*Gerding et al.*, 2000], with the dye laser built in the 1980s. Although this is a robust system and produced a reasonable conversion in the present study, newer dye lasers have been developed over the last 40 years that offer higher % conversions with their respective dyes. The modern-day Cobra-Stretch and Precision-Scan pulsed dye laser systems from SIRAH offer ~30% conversion in the 400 – 920 nm range [*SIRAH*, 2020]. That would provide a 4 – 10-fold increase in conversion, which would in principle decrease the detection limit further from 5 cm^{-3} down to the 0.5 – 1.3 cm^{-3} range. This is in the estimate range of 1 – 4 cm^{-3} determined from the TMA grenade observations (see Chapter 6).

However, bringing the detection limit down to a level this low would require further modification. In Chapter 6, the Rayleigh scatter was already an issue up to 88 km, with the suspected layer residing potentially at 90 km based on the modelled SiO layer [*Plane et al.*, 2016]. With a larger receiver, the Rayleigh and resonance signals would both increase but better signal-to-noise would make it easier to separate them [*Chazette et al.*, 2016].

A new version of WACCM containing Al chemistry is currently under development. This will combine the chemistry from Chapter 3 and further kinetic work on reactions of neutral Al-containing species. The new model will

provide insight into the expected AlO density. The kinetics of AlO + H_2O requires investigation to determine if the hydroxide reservoir is the main repository for the metal. If the hydroxide undergoes a similar rate of photolysis by analogy with other metal hydroxides such as FeOH and NaOH, then it is likely that more Al is recycled during daylight hours, which would once again react with O_2 to form AlO. This would not benefit lidar observations, however, since resonant metal lidars have much lower signal-to-noise at night without background interference from sunlight.

Finally, the next most abundant meteoric metal that hasn't been studied in detail, Ti, could be investigated kinetically and modelled with WACCM but the fraction of Ti in interplanetary dust is so small, that the Ni:Ti and Al:Ti ablation ratios are 56 and 16 respectively [*Carrillo-Sánchez et al.*, 2020].

References

Abo, M. (2005), Resonance Scattering Lidar., *Lidar. Springer Series in Optical Sciences*, *102*, doi:10.1007/0-387-25101-4_11.

Ainslie, N. G., J. D. Mackenzie, and D. Turnbull (1961), Melting Kinetics of Quartz and Cristobalite, *The Journal of Physical Chemistry*, *65*(10), 1718-1724, doi:10.1021/j100827a012.

Alpers, M., R. Eixmann, C. Fricke-Begemann, M. Gerding, and J. Höffner (2004), Temperature lidar measurements from 1 to 105 km altitude using resonance, Rayleigh, and Rotational Raman scattering, *Atmos. Chem. Phys.*, *4*(3), 793-800, doi:10.5194/acp-4-793-2004.

Alpers, M., J. Höfffner, and U. von Zahn (1996), Upper atmosphere Ca and Ca+ at mid-latitudes: First simultaneous and common-volume lidar observations, *Geophysical Research Letters*, *23*(5), 567-570, doi:10.1029/96GL00372.

Alpers, M., J. Höffner, and U. Von Zahn (1990), Iron atom densities in the polar mesosphere from lidar observations, *Geophysical Research Letters*, *17*(13), 2345-2348, doi:doi:10.1029/GL017i013p02345.

Argall, P. S., O. N. Vassiliev, R. J. Sica, and M. M. Mwangi (2000), Lidar measurements taken with a large-aperture liquid mirror. 2. Sodium resonance-fluorescence system, *Appl. Opt.*, *39*(15), 2393-2400, doi:10.1364/AO.39.002393.

Armentrout, P. B., L. F. Halle, and J. L. Beauchamp (1982), Reaction of Cr^+, Mn^+, Fe^+, Co^+, and Ni^+ with O_2 and N_2O. Examination of the translational energy

dependence of the cross sections of endothermic reactions, *J. Chem. Phys.*, *76*, 2449-2457.

Arndt, P., J. Bohsung, M. M., and E. K. Jessberger (1996), The elemental abundances in interplanetary dust particles, *Meteoritics & Planetary Science*, *31*(6), 817-833, doi:10.1111/j.1945-5100.1996.tb02116.x.

Ashbrook., J. (1945), A simple test for nickel in Meteorites, *Popular Astronomy*, *53*, 41.

Asplund, M., N. Grevesse, A. J. Sauval, and P. Scott (2009), The Chemical Composition of the Sun, in *Ann. Rev. Astron. Astrophys.*, edited by R. Blandford, J. Kormendy and E. van Dishoeck, pp. 481-522, Annual Reviews, Palo Alto, doi:10.1146/annurev.astro.46.060407.145222.

Aylett, T., J. S. A. Brooke, A. D. James, M. Nachbar, D. Duft, T. Leisner, and J. M. C. Plane (2019), Optical properties of meteoric smoke analogues, *Atmos. Chem. Phys.*, *19*(19), 12767-12777, doi:10.5194/acp-19-12767-2019.

Baggaley, W. J. (1980), Meteors and Atmospheres, *Symposium - International Astronomical Union*, *90*, 85-100, doi:10.1017/S0074180900066535.

Barnett, J. J., J. T. Houghton, and J. A. Pyle (1975), The temperature dependence of the ozone concentration near the stratopause, *101*(428), 245-257, doi:10.1002/qj.49710142808.

Bauernschmitt, R., and R. Ahlrichs (1996), Treatment of electronic excitations within the adiabatic approximation of time dependent density functional theory, *Chemical Physics Letters*, *256*(4), 454-464, doi:10.1016/0009-2614(96)00440-X.

Bauschlicher, C. W., S. R. Langhoff, and L. A. Barnes (1989), Bonding in zerovalent Ni compounds: NiN_2 and $Ni(N_2)_4$ compared with NiCO and $Ni(CO)_4$, *Chem. Phys.*, *129*(3), 431-437, doi:10.1016/0301-0104(89)85012-8.

Belyung, D. P., and A. Fontijn (1995), The AlO + O_2 Reaction System over a Wide Temperature Range, *The Journal of Physical Chemistry*, *99*(32), 12225-12230, doi:10.1021/j100032a027.

Benna, M., P. R. Mahaffy, J. M. Grebowsky, J. M. C. Plane, R. V. Yelle, and B. M. Jakosky (2015), Metallic ions in the upper atmosphere of Mars from the passage of comet C/2013 A1 (Siding Spring), *Geophysical Research Letters*, *42*(12), 4670 - 4675, doi:10.1002/2015gl064159.

Bills, R. E., and C. S. Gardner (1990), Lidar observations of mesospheric Fe and sporadic Fe layers at Urbana, Illinois, *17*(2), 143-146, doi:10.1029/GL017i002p00143.

Bones, D. L., J. D. Carrillo-Sánchez, A. N. Kulak, and J. M. C. Plane (2019), Ablation of Ni from micrometeoroids in the upper atmosphere: Experimental and computer simulations and implications for Fe ablation, *Planetary and Space Science*, *179*, 104725, doi:10.1016/j.pss.2019.104725.

Bones, D. L., J. C. G. Martin, C. J. Empson, J. D. C. Sanchez, A. D. James, T. P. Conroy, and J. M. C. Plane (2016a), A novel instrument to measure differential ablation of meteorite samples and proxies: The Meteoric Ablation Simulator (MASI), *Review of Scientific Instruments*, *87*(9), 12, doi:10.1063/1.4962751.

Bones, D. L., J. M. C. Plane, and W. Feng (2016b), Dissociative Recombination of FeO^+ with Electrons: Implications for Plasma Layers in the Ionosphere, *The*

Journal of Physical Chemistry A, *120*(9), 1369-1376, doi:10.1021/acs.jpca.5b04947.

Borin, P., G. Cremonese, F. Marzari, and A. J. A. Lucchetti (2017), Asteroidal and cometary dust flux in the inner solar system, *605*, A94, doi:10.1051/0004-6361/201730617.

Bowman, M. R., A. J. Gibson, and M. C. W. Sandford (1969), Atmospheric Sodium measured by a Tuned Laser Radar, *Nature*, *221*(5179), 456-457, doi:10.1038/221456a0.

Božović, A., S. Feil, G. K. Koyanagi, A. A. Viggiano, X. Zhang, M. Schlangen, H. Schwarz, and D. K. Bohme (2010), Conversion of Methane to Methanol: Nickel, Palladium, and Platinum (d9) Cations as Catalysts for the Oxidation of Methane by Ozone at Room Temperature, *16*(38), 11605-11610, doi:10.1002/chem.201000627.

Brackmann, U. (1994), *Lambdachrome laser dyes*, *Lambda Physik GmbH*.

Brasseur, G. P., and S. Solomon (2005), *Aeronomy of the Middle Atmosphere*, The Netherlands.

Broadfoot, A. L., and P. J. Bellaire Jr. (1999), Bridging the gap between ground-based and space-based observations of the night airglow, *Journal of Geophysical Research: Space Physics*, *104*(A8), 17127-17138, doi:10.1029/1999ja900135.

Broadley, S. L., and J. M. C. Plane (2010), A kinetic study of reactions of calcium-containing molecules with O and H atoms: implications for calcium chemistry in the upper atmosphere, *Physical Chemistry Chemical Physics*, *12*(31), 9094-9106, doi:10.1039/C004451B.

Broadley, S. L., T. Vondrak, and J. M. C. Plane (2007), A kinetic study of the reactions of Ca^+ ions with O_3, O_2, N_2, CO_2 and H_2O, *Physical Chemistry Chemical Physics*, *9*(31), 4357-4369, doi:10.1039/B704920J.

Broadley, S. L., T. Vondrak, T. G. Wright, and J. M. C. Plane (2008), A kinetic study of Ca-containing ions reacting with O, O_2, CO_2 and H_2O: implications for calcium ion chemistry in the upper atmosphere, *Physical Chemistry Chemical Physics*, *10*(34), 5287-5298, doi:10.1039/B805356A.

Brown, C. E., S. A. Mitchell, and P. A. Hackett (1991), Dioxygen complexes of 3d transition-metal atoms: formation reactions in the gas phase, *J. Phys. Chem.*, *95*, 1062-1066, doi:10.1021/j100156a009.

Brown, R. L. (1978), Tubular Flow Reactors With First-Order Kinetics *Journal of Research of the Notional Bureau of Standards 83*.

Brown, T. L. (1973), The Chemistry of Metallic Elements in the Ionosphere and Mesosphere, *Chem. Rev.*, *73*(6), 645-667, doi:10.1021/cr60286a003.

Bryans, P., H. Kreckel, E. Roueff, V. Wakelam, and D. W. Savin (2009), Molecular Cloud Chemistry and the Importance of Dielectronic Recombination, *Astrophysical Journal*, *694*(1), 286-293, doi:10.1088/0004-637x/694/1/286.

Bryant, D. A., T. L. Cline, U. D. Desai, and F. B. McDonald (1962), Explorer 12 observations of solar cosmic rays and energetic storm particles after the solar flare of September 28, 1961, *67*(13), 4983-5000, doi:10.1029/JZ067i013p04983.

Carrillo-Sánchez, J. D., J. C. Gómez-Martín, D. L. Bones, D. Nesvorný, P. Pokorný, M. Benna, G. J. Flynn, and J. M. C. Plane (2020), Cosmic dust fluxes in

the atmospheres of Earth, Mars, and Venus, *Icarus*, *335*, 113395, doi:10.1016/j.icarus.2019.113395.

Carrillo-Sánchez, J. D., D. Nesvorný, P. Pokorný, D. Janches, and J. M. C. Plane (2016), Sources of cosmic dust in the Earth's atmosphere, *Geophysical Research Letters*, *43*(23), 11,979-911,986, doi:10.1002/2016GL071697.

Carrillo-Sánchez, J. D., J. M. C. Plane, W. Feng, D. Nesvorný, and D. Janches (2015), On the size and velocity distribution of cosmic dust particles entering the atmosphere, *Geophysical Research Letters*, *42*(15), 6518-6525, doi:10.1002/2015GL065149.

Ceplecha, Z., J. Borovička, W. G. Elford, D. O. ReVelle, R. L. Hawkes, V. Porubčan, and M. Šimek (1998), Meteor Phenomena and Bodies, *Space Science Reviews*, *84*(3), 327-471, doi:10.1023/a:1005069928850.

Chandra, S., C. H. Jackman, E. L. Fleming, and J. M. Russell III (1997), The Seasonal and Long Term Changes in Mesospheric Water Vapor, *24*(6), 639-642, doi:10.1029/97gl00546.

Chazette, P., J. Totems, L. Hespel, and J.-S. Bailly (2016), 5 - Principle and Physics of the LiDAR Measurement, in *Optical Remote Sensing of Land Surface*, edited by N. Baghdadi and M. Zribi, pp. 201-247, Elsevier, doi:10.1016/B978-1-78548-102-4.50005-3.

Cheng, P., G. K. Koyanagi, and D. K. Bohme (2007), Heavy water reactions with atomic transition-metal and main-group cations: Gas phase room-temperature kinetics and periodicities in reactivity, *J. Phys. Chem. A*, *111*(35), 8561-8573, doi:10.1021/jp072661p.

Chu, X., and G. C. Papen (2005), Resonance fluorescence lidar for measurements of the middle and upper atmosphere, *Laser Remote Sensing*.

Chu, X., Z. Yu, C. S. Gardner, C. Chen, and W. Fong (2011), Lidar observations of neutral Fe layers and fast gravity waves in the thermosphere (110–155 km) at McMurdo (77.8°S, 166.7°E), Antarctica, *Geophysical Research Letters*, *38*(23), doi:10.1029/2011GL050016.

Clemmer, D. E., K. Honma, and I. Koyano (1993), Kinetics of excited-state titanium(a^5F) depletion by nitric oxide, oxygen, nitrous oxide, and nitrogen, *The Journal of Physical Chemistry*, *97*(44), 11480-11488, doi:10.1021/j100146a022.

Clemmer, D. E., M. E. Weber, and P. B. Armentrout (1992), Reactions of $Al^+(^1S)$ with NO_2, N_2O, and CO_2: thermochemistry of AlO and AlO^+, *The Journal of Physical Chemistry*, *96*(26), 10888-10893, doi:10.1021/j100205a052.

Clough, S. A., Y. Beers, G. P. Klein, and L. S. Rothman (1973), Dipole moment of water from Stark measurements of H_2O, HDO, and D_2O, *The Journal of Chemical Physics*, *59*(5), 2254-2259, doi:10.1063/1.1680328.

Cohen, N., and K. R. Westberg (1983), Chemical Kinetic Data Sheets for High-Temperature Chemical Reactions, *12*(3), 531-590, doi:10.1063/1.555692.

Collins, R. L., J. Li, and C. M. Martus (2015), First lidar observation of the mesospheric nickel layer, *Geophysical Research Letters*, *42*(2), 665-671, doi:10.1002/2014gl062716.

Continuum (1996), *Minilite (Nd:YAG) User Manual*, 26 pp.

Crank, J. (1986), *The Mathematics of Diffusion*, Oxford.

Crismani, M. M. J., et al. (2017), Detection of a persistent meteoric metal layer in the Martian atmosphere, *Nature Geoscience*, *10*(6), 401-404, doi:10.1038/ngeo2958.

Cziczo, D. J., D. S. Thomson, and D. M. Murphy (2001), Ablation, Flux, and Atmospheric Implications of Meteors Inferred from Stratospheric Aerosol, *Science*, *291*(5509), 1772, doi:10.1126/science.1057737.

Dawkins, E. C. M., J. M. C. Plane, M. P. Chipperfield, W. Feng, J. Gumbel, J. Hedin, J. Höffner, and J. S. Friedman (2014), First global observations of the mesospheric potassium layer, *Geophysical Research Letters*, *41*(15), 5653-5661, doi:10.1002/2014GL060801.

De Avillez Pereira, R., D. L. Baulch, M. J. Pilling, S. H. Robertson, and G. Zeng (1997), Temperature and Pressure Dependence of the Multichannel Rate Coefficients for the CH_3 + OH System, *J. Phys. Chem.*, *101*, 9681.

Dhomse, S. S., R. W. Saunders, W. Tian, M. P. Chipperfield, and J. M. C. Plane (2013), Plutonium-238 observations as a test of modeled transport and surface deposition of meteoric smoke particles, *40*(16), 4454-4458, doi:10.1002/grl.50840.

Duff, J. W., H. Dothe, and R. D. Sharma (2003), On the rate coefficient of the $N(^2D)+O_2 \rightarrow NO+O$ reaction in the terrestrial thermosphere, *30*(5), doi:10.1029/2002gl016720.

Evans, W. F. J., R. L. Gattinger, A. L. Broadfoot, and E. J. Llewellyn (2011), The observation of chemiluminescent NiO* emissions in the laboratory and in the night

airglow, *Atmos. Chem. Phys.*, *11*(18), 9595-9603, doi:10.5194/acp-11-9595-2011.

Fan, Z. Y., J. M. C. Plane, J. Gumbel, J. Stegman, and E. J. Llewellyn (2007), Satellite measurements of the global mesospheric sodium layer, *Atmospheric Chemistry and Physics*, *7*(15), 4107-4115.

Fegley Jr, B., and A. G. W. Cameron (1987), A vaporization model for iron/silicate fractionation in the Mercury protoplanet, *Earth and Planetary Science Letters*, *82*(3–4), 207-222, doi:10.1016/0012-821X(87)90196-8.

Feng, W., D. R. Marsh, M. P. Chipperfield, D. Janches, J. Höffner, F. Yi, and J. M. C. Plane (2013), A global atmospheric model of meteoric iron, *Journal of Geophysical Research: Atmospheres*, *118*(16), 9456-9474, doi:10.1002/jgrd.50708.

Fentzke, J. T., and D. Janches (2008), A semi-empirical model of the contribution from sporadic meteoroid sources on the meteor input function in the MLT observed at Arecibo, *Journal of Geophysical Research: Space Physics*, *113*(A3), doi:10.1029/2007ja012531.

Fontijn, A., and W. Felder (1977), HTFFR kinetics studies of Al + CO_2→AlO + CO from 300 to 1900 K, a non-Arrhenius reaction, *67*(4), 1561-1569, doi:10.1063/1.434986.

Fontijn, A., W. Felder, and J. J. Houghton (1977), Hiffr kinetics studies. Temperature dependence of Al/O_2 and AlO/O_2 kinetics from 300 to 1700/1400 K, *Symposium (International) on Combustion*, *16*(1), 871-879, doi:10.1016/S0082-0784(77)80380-9.

Forget, F., F. Hourdin, R. Fournier, C. Hourdin, O. Talagrand, M. Collins, S. R. Lewis, P. L. Read, and J.-P. Huot (1999), Improved general circulation models of the Martian atmosphere from the surface to above 80 km, *J. Geophys. Res.*, *104*, 24155-24176, doi:10.1029/1999JE001025.

Fricke, K. H., and U. von Zahn (1985), Mesopause temperatures derived from probing the hyperfine structure of the D_2 resonance line of sodium by lidar, *Journal of Atmospheric and Terrestrial Physics*, *47*(5), 499-512, doi:10.1016/0021-9169(85)90116-3.

Frisch, M. J., et al. (2016), Gaussian 09, *Revision A.02*.

Fritts, D. C., and M. J. Alexander (2003), Gravity wave dynamics and effects in the middle atmosphere, *Reviews of Geophysics*, *41*(1), doi:10.1029/2001RG000106.

Fussen, D., et al. (2010), A global climatology of the mesospheric sodium layer from GOMOS data during the 2002-2008 period, *Atmospheric Chemistry and Physics*, *10*(19), 9225-9236, doi:10.5194/acp-10-9225-2010.

Gabrielli, P., et al. (2004), Meteoric smoke fallout over the Holocene epoch revealed by iridium and platinum in Greenland ice, *Nature*, *432*(7020), 1011-1014, doi:10.1038/nature03137.

Garcia, R. R., D. Marsh, D. E. Kinnison, B. Boville, and F. Sassi (2007), Simulations of secular trends in the middle atmosphere, 1950-2003, *J. Geophys. Res.*, *112*, D09301.

Gardner, C. S., A. Z. Liu, and Y. Guo (2017), Vertical and horizontal transport of mesospheric Na: Implications for the mass influx of cosmic dust, *Journal of*

Atmospheric and Solar-Terrestrial Physics, *162*, 192-202, doi:10.1016/j.jastp.2016.07.013.

Gardner, C. S., J. M. C. Plane, W. Pan, T. Vondrak, B. J. Murray, and X. Chu (2005), Seasonal variations of the Na and Fe layers at the South Pole and their implications for the chemistry and general circulation of the polar mesosphere, *110*(D10), doi:10.1029/2004jd005670.

Garland, N. L. (1992), Kinetic Studies of Boron and Aluminum Species, in *Gas Phase Metal Reactions*, edited by A. Fontijn, pp. 73-91, Elsevier, Amsterdam, doi:10.1016/B978-0-444-89070-2.50008-6.

Garland, N. L., and H. H. Nelson (1992), Temperature dependence of the kinetics of the reaction Al + O_2 → AlO + O, *Chemical Physics Letters*, *191*(3), 269-272, doi:10.1016/0009-2614(92)85299-P.

Gelinas, L. J., K. A. Lynch, M. C. Kelley, R. L. Collins, M. Widholm, E. MacDonald, J. Ulwick, and P. Mace (2005), Mesospheric charged dust layer: Implications for neutral chemistry, *Journal of Geophysical Research: Space Physics*, *110*(A1), doi:10.1029/2004JA010503.

Gerding, M., M. Alpers, U. von Zahn, R. J. Rollason, and J. M. C. Plane (2000), Atmospheric Ca and Ca^+ layers: Midlatitude observations and modeling, *Journal of Geophysical Research: Space Physics*, *105*(A12), 27131-27146, doi:10.1029/2000JA900088.

Gerding, M., S. Daly, and J. M. C. Plane (2019), Lidar Soundings of the Mesospheric Nickel Layer Using Ni(^{3}F) and Ni(^{3}D) Transitions, *Geophysical Research Letters*, *46*(1), 408-415, doi:10.1029/2018GL080701.

Gerding, M., J. Höffner, P. Hoffmann, M. Kopp, and F. J. Lübken (2013a), Noctilucent cloud variability and mean parameters from 15 years of lidar observations at a mid-latitude site (54°N, 12°E), *Journal of Geophysical Research: Atmospheres*, *118*(2), 317-328, doi:10.1029/2012JD018319.

Gerding, M., J. Höffner, J. Lautenbach, M. Rauthe, and F. J. Lübken (2008), Seasonal variation of nocturnal temperatures between 1 and 105 km altitude at 54° N observed by lidar, *Atmos. Chem. Phys.*, *8*(24), 7465-7482, doi:10.5194/acp-8-7465-2008.

Gerding, M., M. Kopp, P. Hoffmann, J. Höffner, and F. J. Lübken (2013b), Diurnal variations of midlatitude NLC parameters observed by daylight-capable lidar and their relation to ambient parameters, *Geophysical Research Letters*, *40*(24), 6390-6394, doi:10.1002/2013GL057955.

Gerding, M., M. Kopp, J. Höffner, K. Baumgarten, and F. J. Lübken (2016), Mesospheric temperature soundings with the new, daylight-capable IAP RMR lidar, *Atmos. Meas. Tech.*, *9*(8), 3707-3715, doi:10.5194/amt-9-3707-2016.

Gerrard, A. J., T. J. Kane, J. P. Thayer, C. S. Ruf, and R. L. Collins (2001), Consideration of non-Poisson distributions for lidar applications, *Appl. Opt.*, *40*(9), 1488-1492, doi:10.1364/AO.40.001488.

Gettelman, A., et al. (2019), The Whole Atmosphere Community Climate Model Version 6 (WACCM6), *124*(23), 12380-12403, doi:10.1029/2019jd030943.

Gole, J. L., and C. E. Kolb (1981), On the upper atmospheric chemiluminescent emission observed upon release of aluminum vapor and its compounds, *Journal*

of Geophysical Research: Space Physics, *86*(A11), 9125-9136, doi:10.1029/JA086iA11p09125.

Golomb, D., O. Harang, and F. P. DelGreco (1967), Upper atmosphere densities and temperatures at 105–165 kilometers from diffusion and spectral intensity of AlO trails, *72*(9), 2365-2370, doi:10.1029/JZ072i009p02365.

Gómez Martín, J. C., M. A. Blitz, and J. M. C. Plane (2009), Kinetic studies of atmospherically relevant silicon chemistry Part I: Silicon atom reactions, *Physical Chemistry Chemical Physics*, *11*(4), 671-678, doi:10.1039/B812946K.

Gómez Martín, J. C., D. L. Bones, J. D. Carrillo-Sánchez, A. D. James, J. M. Trigo-Rodríguez, B. Fegley Jr, and J. M. C. Plane (2017), Novel Experimental Simulations of the Atmospheric Injection of Meteoric Metals, *The Astrophysical Journal*, *836*(2), 212, doi:10.3847/1538-4357/aa5c8f.

Gómez Martín, J. C., S. A. Garraway, and J. M. C. Plane (2016), Reaction Kinetics of Meteoric Sodium Reservoirs in the Upper Atmosphere, *The Journal of Physical Chemistry A*, *120*(9), 1330-1346, doi:10.1021/acs.jpca.5b00622.

Gómez Martín, J. C., and J. M. C. Plane (2011), Kinetic studies of atmospherically relevant silicon chemistry. Part III: Reactions of Si^+ and SiO^+ with O_3, and Si^+ with O_2, *Physical Chemistry Chemical Physics*, *13*(9), 3764-3774, doi:10.1039/C0CP01380C.

Gómez Martín, J. C., and J. M. C. Plane (2017), Reaction Kinetics of CaOH with H and O_2 and O_2CaOH with O: Implications for the Atmospheric Chemistry of Meteoric Calcium, *ACS Earth and Space Chemistry*, *1*(7), 431-441, doi:10.1021/acsearthspacechem.7b00072.

Grebowsky, J. M., and A. C. Aikin (2002), In Situ Measurements of Meteoric Ions, *Cambridge University Press*.

Grebowsky, J. M., M. Benna, J. M. C. Plane, G. A. Collinson, P. R. Mahaffy, and B. M. Jakosky (2017), Unique, non-Earthlike, meteoritic ion behavior in upper atmosphere of Mars, *Geophysical Research Letters*, *44*(7), 3066-3072, doi:10.1002/2017GL072635.

Heath, D. F., C. L. Mateer, and A. J. Krueger (1973), The Nimbus-4 Backscatter Ultraviolet (BUV) atmospheric ozone experiment — tow years' operation, *Pure and Applied Geophysics*, *106*(1), 1238-1253, doi:10.1007/bf00881076.

Heays, A. N., A. D. Bosman, and E. F. van Dishoeck (2017), Photodissociation and photoionisation of atoms and molecules of astrophysical interest, *602*, A105, doi:10.1051/0004-6361/201628742.

Helmer, M., J. M. C. Plane, J. Qian, and C. S. Gardner (1998), A model of meteoric iron in the upper atmosphere, *Journal of Geophysical Research: Atmospheres*, *103*(D9), 10913-10925, doi:10.1029/97jd03075.

Herrmann, U., P. Eberhardt, M. A. Hidalgo, E. Kopp, and L. G. Smith (1978), Metal ions and isotopes in sporatic E-layers during the Perseid meteor shower, *Space Research*, 249-252.

Hiroshi, K. (1989), Warm Stratopause in the Antarctic Winter, *46*(3), 435-438, doi:10.1175/1520-0469(1989)046<0435:Wsitaw>2.0.Co;2.

Hughes, D. W. (1997), Meteors and cosmic dust, *Endeavour*, *21*(1), 31-35, doi:10.1016/s0160-9327(96)10030-2.

Hunten, D. M. (1967), Spectroscopic studies of the twilight airglow, *Space Science Reviews*, *6*(4), 493-573, doi:10.1007/bf00173704.

Hurrell, J. W., et al. (2013), The Community Earth System Model: A Framework for Collaborative Research, *Bulletin of the American Meteorological Society*, *94*(9), 1339-1360, doi:10.1175/bams-d-12-00121.1.

Jakosky, B. M., et al. (2015), The Mars Atmosphere and Volatile Evolution (MAVEN) Mission, *Space Science Reviews*, *195*(1), 3-48, doi:10.1007/s11214-015-0139-x.

James, A. D., J. S. A. Brooke, T. P. Mangan, T. F. Whale, J. M. C. Plane, and B. J. Murray (2018), Nucleation of nitric acid hydrates in polar stratospheric clouds by meteoric material, *Atmos. Chem. Phys.*, *18*(7), 4519-4531, doi:10.5194/acp-18-4519-2018.

Jessberger, E. K., T. Stephan, D. Rost, P. Arndt, M. Maetz, F. J. Stadermann, D. E. Brownlee, J. P. Bradley, and G. Kurat (2001), Properties of Interplanetary Dust: Information from Collected Samples, in *Interplanetary Dust*, edited by E. Grün, B. Å. S. Gustafson, S. Dermott and H. Fechtig, pp. 253-294, Springer Berlin Heidelberg, Berlin, Heidelberg, doi:10.1007/978-3-642-56428-4_6.

Johnson, E. R. (1965), Twilight resonance radiation of AlO in the upper atmosphere, *70*(5), 1275-1277, doi:10.1029/JZ070i005p01275.

Johnson, E. R., and K. H. Lloyd (1963), Determination of Diffusion Coefficients from Observations on Grenade Glow Clouds, *Australian Journal of Physics*, *16*(4), 490-499, doi:10.1071/PH630490.

Kane, T. J., and C. S. Gardner (1993), Structure and seasonal variability of the nighttime mesospheric Fe layer at midlatitudes, *98*(D9), 16875-16886, doi:10.1029/93jd01225.

Karazi, S. M., I. U. Ahad, and K. Y. Benyounis (2017), Laser Micromachining for Transparent Materials, in *Reference Module in Materials Science and Materials Engineering*, edited, Elsevier, doi:10.1016/B978-0-12-803581-8.04149-7.

Kinnison, D. E., et al. (2007), Sensitivity of chemical tracers to meteorological parameters in the MOZART-3 chemical transport model, *Journal of Geophysical Research: Atmospheres*, *112*(D20), doi:10.1029/2006JD007879.

Kohman, T. P. (1997), Aluminum-26: A nuclide for all seasons, *Journal of Radioanalytical and Nuclear Chemistry*, *219*(2), 165 - 176, doi:10.1007/BF02038496.

Kopp, E. (1997), On the abundance of metal ions in the lower ionosphere, *Journal of Geophysical Research: Space Physics*, *102*(A5), 9667-9674, doi:doi:10.1029/97JA00384.

Kopp, E., L. André, and L. G. Smith (1985a), Positive ion composition and derived particle heating in the lower auroral ionosphere, *Journal of Atmospheric and Terrestrial Physics*, *47*(1), 301-308, doi:10.1016/0021-9169(85)90140-0.

Kopp, E., P. Eberhardt, U. Herrmann, and L. G. Björn (1985b), Positive ion composition of the high-latitude summer D region with noctilucent clouds, *Journal of Geophysical Research: Atmospheres*, *90*(D7), 13041-13053, doi:10.1029/JD090iD07p13041.

Kopp, E., and U. Herrmann (1984), Ion composition in the lower ionosphere, *Annales Geophysicae (European Geophysical Society)*, *2*(1), 83-94.

Kopp, M., M. Gerding, J. Hoffner, M. Zecha, and F. J. Lubken (2011), Lidar Soundings of Noctilucent Clouds and Temperatures during Day and Night in the Summer Mid-Latitude Middle Atmosphere, in *20th Esa Symposium on European Rocket and Balloon Programmes and Related Research*, edited by L. Ouwehand, pp. 409-412, Esa Publications Division C/O Estec.

Koyanagi, G. K., D. Caraiman, V. Blagojevic, and D. K. Bohme (2002), Gas-phase reactions of transition-metal ions with molecular oxygen: Room-temperature kinetics and periodicities in reactivity, *J. Phys. Chem. A*, *106*(18), 4581-4590, doi:10.1021/jp014145j.

Kramida, A., Y. Ralchenko, J. Reader, and N. A. Team (2018), NIST atomic spectra database (ver. 5.5.6), edited, National Institute of Standards and Technology, Gaithersburg, MD.

Krankowsky, D., F. Arnold, H. Wieder, and J. Kissel (1972), The elemental and isotopic abundance of metallic ions in the lower E-region as measured by a cryogenically pumped quadrupole mass spectrometer, *International Journal of Mass Spectrometry and Ion Physics*, *8*(4), 379-390, doi:10.1016/0020-7381(72)83024-9.

Kraus, D., R. J. Saykally, and V. E. Bondybey (2002), Cavity-Ringdown Spectroscopy Studies of the $B^2\Sigma^+ \leftarrow X^2\Sigma^+$ System of AlO, *ChemPhysChem*, *3*(4), 364-366, doi:10.1002/1439-7641(20020415)3:4<364::AID-CPHC364>3.0.CO;2-G.

Kumar, S., and W. B. Hanson (1980), The morphology of metallic ions in the upper atmosphere, *85*(A12), 6783-6801, doi:10.1029/JA085iA12p06783.

L'Vov, B. V., D. A. Katskov, L. P. Kruglikova, and L. K. Polzik (1976), Absolute analysis by flame atomic absorption spectroscopy: Present status and some problems, *Spectrochimica Acta Part B: Atomic Spectroscopy*, *31*(2), 49-80, doi:10.1016/0584-8547(76)80005-5.

Laimer, J., G. Misslinger, C. G. Schwärzler, and H. Störi (1996), Determination of atomic hydrogen densities in gases by a deuterium based Lyman-alpha absorption method, *Journal of Applied Physics*, *80*(4), 2060-2068, doi:10.1063/1.363099.

Laimer, J., R. Posch, G. Misslinger, C. G. Schwarzler, and H. Stori (1995), Determination of absolute hydrogen atom densities by Lyman- alpha absorption, *Measurement Science and Technology*, *6*(9), 1413.

Langenberg, S., C. Carstens, D. Hupperich, S. Schweighoefer, and U. Schurath (2019), Technical note: Determination of binary gas phase diffusion coefficients of unstable and adsorbing atmospheric trace gases at low temperature – Arrested Flow and Twin Tube method *Atmos. Chem. Phys.*, *in press*.

Langowski, M., M. Sinnhuber, A. C. Aikin, C. von Savigny, and J. P. Burrows (2014), Retrieval algorithm for densities of mesospheric and lower thermospheric metal atom and ion species from satellite-borne limb emission signals, *Atmos. Meas. Tech.*, *7*(1), 29-48, doi:10.5194/amt-7-29-2014.

Langowski, M. P., C. von Savigny, J. P. Burrows, W. Feng, J. M. C. Plane, D. R. Marsh, D. Janches, M. Sinnhuber, A. C. Aikin, and P. Liebing (2015), Global

investigation of the Mg atom and ion layers using SCIAMACHY/Envisat observations between 70 and 150 km altitude and WACCM-Mg model results, *Atmos. Chem. Phys.*, *15*(1), 273-295, doi:10.5194/acp-15-273-2015.

Larsen, M. F., and C. D. Odom (1997), Observations of altitudinal and latitudinal E-region neutral wind gradients near sunset at the magnetic equator, *Geophysical Research Letters*, *24*(13), 1711-1714, doi:10.1029/97GL01469.

Le Picard, S. D., A. Canosa, D. Travers, D. Chastaing, B. R. Rowe, and T. Stoecklin (1997), Experimental and Theoretical Kinetics for the Reaction of Al with O2 at Temperatures between 23 and 295 K, *The Journal of Physical Chemistry A*, *101*(51), 9988-9992, doi:10.1021/jp972122s.

Leuchtner, R. E., A. C. Harms, and A. W. Castleman Jr. (1991), Aluminum cluster reactions, *The Journal of Chemical Physics*, *94*(2), 1093-1101, doi:10.1063/1.460716.

Lide, D. R. (2006), *Handbook of Physics and Chemistry*, *CRC Press*.

Liu, H.-L., et al. (2010), Thermosphere extension of the Whole Atmosphere Community Climate Model, *115*(A12), doi:10.1029/2010ja015586.

Liu, Z., W. Hunt, M. Vaughan, C. Hostetler, M. McGill, K. Powell, D. Winker, and Y. Hu (2006), Estimating random errors due to shot noise in backscatter lidar observations, *Appl. Opt.*, *45*(18), 4437-4447, doi:10.1364/AO.45.004437.

Llewellyn, E. J., et al. (2004), The OSIRIS instrument on the Odin spacecraft, *Canadian Journal of Physics*, *82*(6), 411-422, doi:10.1139/p04-005.

Lodders, K., and B. J. Fegley (2011), *Chemistry of the Solar System*, Cambridge, UK.

Love, S. G., and D. E. Brownlee (1993), A Direct Measurment of the Terrestrial Mass Rate of Cosmic Dust, *Science*, *262*(5133), 550-553, doi:10.1126/science.262.5133.550.

Mangan, T. P., N. McAdam, S. M. Daly, and J. M. C. Plane (2019), Kinetic Study of Ni and NiO Reactions Pertinent to the Earth's Upper Atmosphere, *The Journal of Physical Chemistry A*, *123*(2), 601-610, doi:10.1021/acs.jpca.8b11382.

Marsh, D. R., R. R. Garcia, D. E. Kinnison, B. A. Boville, F. Sassi, S. C. Solomon, and K. Matthes (2007), Modeling the whole atmosphere response to solar cycle changes in radiative and geomagnetic forcing, *Journal of Geophysical Research: Atmospheres*, *112*(D23), doi:10.1029/2006JD008306.

Marsh, D. R., D. Janches, W. Feng, and J. M. C. Plane (2013a), A global model of meteoric sodium, *Journal of Geophysical Research: Atmospheres*, *118*(19), 11,442-411,452, doi:10.1002/jgrd.50870.

Marsh, D. R., M. J. Mills, D. E. Kinnison, J.-F. Lamarque, N. Calvo, and L. M. Polvani (2013b), Climate Change from 1850 to 2005 Simulated in CESM1(WACCM), *Journal of Climate*, *26*(19), 7372-7391, doi:10.1175/jcli-d-12-00558.1.

McBride, N., S. F. Green, and J. A. M. McDonnell (1999), Meteoroids and small sized debris in Low Earth Orbit and at 1 au: Results of recent modelling, in *Space Debris*, edited by W. Flury and H. Klinkrad, pp. 73-82, Pergamon Press Ltd, Oxford, doi:10.1016/s0273-1177(98)00232-4.

McClintock, W. E., N. M. Schneider, G. M. Holsclaw, J. T. Clarke, A. C. Hoskins, I. Stewart, F. Montmessin, R. V. Yelle, and J. Deighan (2015), The Imaging Ultraviolet Spectrograph (IUVS) for the MAVEN Mission, *Space Science Reviews*, *195*(1), 75-124, doi:10.1007/s11214-014-0098-7.

McDonald, D. C., B. C. Sweeny, S. G. Ard, J. J. Melko, J. E. Ruliffson, M. C. White, A. A. Viggiano, and N. S. Shuman (2018), Temperature and Isotope Dependent Kinetics of Nickel-Catalyzed Oxidation of Methane by Ozone, *The Journal of Physical Chemistry A*, *122*(33), 6655-6662, doi:10.1021/acs.jpca.8b02513.

Meister, J., P. Eberhardt, U. Herrmann, E. Kopp, M. A. Hidalgo, and C. F. Sechrist, Jr. (1977), D-region ion composition during the winter anomaly campaign on January 8, 1977, *COSPAR, 20th Plenary Meeting*, *20*.

Melko, J. J., S. G. Ard, T. Lê, G. S. Miller, O. Martinez, N. S. Shuman, and A. A. Viggiano (2017), Determining Rate Constants and Mechanisms for Sequential Reactions of Fe^+ with Ozone at 500 K, *The Journal of Physical Chemistry A*, *121*(1), 24-30, doi:10.1021/acs.jpca.6b08971.

Mills, M. J., et al. (2017), Radiative and Chemical Response to Interactive Stratospheric Sulfate Aerosols in Fully Coupled CESM1(WACCM), *122*(23), 13,061-013,078, doi:10.1002/2017jd027006.

Mlynczak, M. G., et al. (2013), Radiative and energetic constraints on the global annual mean atomic oxygen concentration in the mesopause region, *Journal of Geophysical Research: Atmospheres*, *118*(11), 5796-5802, doi:10.1002/jgrd.50400.

Molod, A., L. Takacs, M. Suarez, and J. Bacmeister (2015), Development of the GEOS-5 atmospheric general circulation model: evolution from MERRA to MERRA2, *Geosci. Model Dev.*, *8*(5), 1339-1356, doi:10.5194/gmd-8-1339-2015.

Monro, P. E. (1970), The diurnal variations of the concentrations of NO+, O2+, NO and N in the ionospheric E-region, *Journal of Atmospheric and Terrestrial Physics*, *32*(3), 373-382, doi:10.1016/0021-9169(70)90009-7.

Murray, B. J., and J. M. C. Plane (2003), Atomic oxygen depletion in the vicinity of noctilucent clouds, *Advances in Space Research*, *31*(9), 2075-2084, doi:10.1016/S0273-1177(03)00231-X.

NCAR (2020), GEOV - IDL viewer, edited.

Nee, J. B., and P. C. Lee (1997), Detection of O(^{1}D) Produced in the Photodissociation of O_2 in the Schumann−Runge Continuum, *The Journal of Physical Chemistry A*, *101*(36), 6653-6657, doi:10.1021/jp970439m.

Nesvorný, D., D. Janches, D. Vokrouhlický, P. Pokorný, W. F. Bottke, and P. Jenniskens (2011), Dynamical Model for the Zodiacal Cloud and Sporadic Meteors, *The Astrophysical Journal*, *743*(2), 129.

Nesvorný, D., P. Jenniskens, H. F. Levison, W. F. Bottke, D. Vokrouhlický, and M. Gounelle (2010), Cometary Origin of the Zodiacal Cloud and Carbonaceous Micrometeorites. Implications for Hot Debris Disks, *The Astrophysical Journal*, *713*(2), 816.

Parnis, J. M., S. A. Mitchell, T. S. Kanigan, and P. A. Hackett (1989), Gas-phase reactions of aluminum monoxide with small molecules, *The Journal of Physical Chemistry*, *93*(24), 8045-8052, doi:10.1021/j100361a017.

Pavlov, A. V. (2012), Ion Chemistry of the Ionosphere at E- and F-Region Altitudes: A Review, *Surveys in Geophysics*, *33*(5), 1133-1172, doi:10.1007/s10712-012-9189-8.

Picone, J. M., A. E. Hedin, D. P. Drob, and A. C. Aikin (2002), NRLMSISE-00 empirical model of the atmosphere: Statistical comparisons and scientific issues, *Journal of Geophysical Research: Space Physics*, *107*(A12), SIA 15-11-SIA 15-16, doi:10.1029/2002JA009430.

Plane, J. M. C. (2003), Atmospheric chemistry of meteoric metals, *Chemical Reviews*, *103*(12), 4963-4984, doi:10.1021/cr0205309.

Plane, J. M. C. (2004), A time-resolved model of the mesospheric Na layer: constraints on the meteor input function, *Atmos. Chem. Phys.*, *4*(3), 627-638, doi:10.5194/acp-4-627-2004.

Plane, J. M. C. (2012), Cosmic dust in the earth's atmosphere, *Chemical Society Reviews*, *41*(19), 6507-6518, doi:10.1039/c2cs35132c.

Plane, J. M. C., J. D. Carrillo-Sanchez, T. P. Mangan, M. M. J. Crismani, N. M. Schneider, and A. Määttänen (2018a), Meteoric Metal Chemistry in the Martian Atmosphere, *123*(3), 695-707, doi:10.1002/2017je005510.

Plane, J. M. C., W. Feng, E. Dawkins, M. P. Chipperfield, J. Höffner, D. Janches, and D. R. Marsh (2014), Resolving the strange behavior of extraterrestrial potassium in the upper atmosphere, *Geophysical Research Letters*, *41*(13), 4753-4760, doi:10.1002/2014GL060334.

Plane, J. M. C., W. Feng, and E. C. M. Dawkins (2015), The Mesosphere and Metals: Chemistry and Changes, *Chemical Reviews*, *115*(10), 4497-4541, doi:10.1021/cr500501m.

Plane, J. M. C., W. Feng, J. C. Gómez Martín, M. Gerding, and S. Raizada (2018b), A new model of meteoric calcium in the mesosphere and lower thermosphere, *Atmos. Chem. Phys.*, *18*(20), 14799-14811, doi:10.5194/acp-18-14799-2018.

Plane, J. M. C., J. C. Gomez-Martin, W. H. Feng, and D. Janches (2016), Silicon chemistry in the mesosphere and lower thermosphere, *Journal of Geophysical Research-Atmospheres*, *121*(7), 3718-3728, doi:10.1002/2015jd024691.

Plane, J. M. C., and C. L. Whalley (2012), A New Model for Magnesium Chemistry in the Upper Atmosphere, *Journal of Physical Chemistry A*, *116*(24), 6240-6252, doi:10.1021/jp211526h.

Portnyagin, Y. (2006), A review of mesospheric and lower thermosphere models, *Advances in Space Research*, *38*(11), 2452-2460, doi:10.1016/j.asr.2006.04.030.

Rees, M. H. (1989), *Physics and Chemistry of the Upper Atmosphere*, Cambridge University Press, Cambridge.

Ritter, D., and J. C. Weisshaar (1990), Kinetics of neutral transition-metal atoms in the gas phase: oxidation of scandium(a^2D), titanium(a^3F), and vanadium(a^4F) by nitric oxide, oxygen, and nitrous oxide, *The Journal of Physical Chemistry*, *94*(12), 4907-4913, doi:10.1021/j100375a028.

Roberts, B. C., and M. F. Larsen (2014), Structure function analysis of chemical tracer trails in the mesosphere-lower thermosphere region, *Journal of*

Geophysical Research: Atmospheres, *119*(11), 6368-6375, doi:10.1002/2013JD020796.

Rollason, R. J., and J. M. C. Plane (2000), The reactions of FeO with O_3, H_2 , H_2O, O_2 and CO_2, *Physical Chemistry Chemical Physics*, *2*(10), 2335-2343, doi:10.1039/B000877J.

Rosinski, J., and R. H. Snow (1961), Secondary Particulate Matter from Meteors Vapors, *Journal of Meteorology*, *18*(6), 736-745, doi:10.1175/1520-0469(1961)018<0736:spmfmv>2.0.co;2.

Saifi, M. A. (2001), Optical Amplifiers, in *Encyclopedia of Materials: Science and Technology*, edited by K. H. J. Buschow, R. W. Cahn, M. C. Flemings, B. Ilschner, E. J. Kramer, S. Mahajan and P. Veyssière, pp. 6416-6423, Elsevier, Oxford, doi:10.1016/B0-08-043152-6/01135-9.

Sakellaris, C. N., and A. Mavridis (2013), First principles exploration of NiO and its ions NiO^+ and NiO^-, *J. Chem. Phys.*, *138*(5), art. no.: 054308, doi:10.1063/1.4789416.

Saunders, R. W., and J. M. C. Plane (2006), A laboratory study of meteor smoke analogues: Composition, optical properties and growth kinetics, *Journal of Atmospheric and Solar-Terrestrial Physics*, *68*(18), 2182-2202, doi:10.1016/j.jastp.2006.09.006.

Schaefer, L., and B. Fegley (2004), Application of an equilibrium vaporization model to the ablation of chondritic and achondritic meteoroids, *Earth, Moon, and Planets*, *95*(1), 413-423, doi:10.1007/s11038-005-9030-1.

Schlemmer, S., A. Luca, and D. Gerlich (2003), Reactions of trapped ions with metal atoms: O_2^+ + Ni and NiN_2^+ + Ni, *Int. J. Mass Spectr.*, *223*(1-3), 291-299, doi:10.1016/s1387-3806(02)00865-5.

Schmunk, R. B. (2020), Panoply netCDF, HDF and GRIB Data Viewer, edited, NASA Goddard Institute for Space Studies.

Schroeder, D. J., and J. E. Mack (1961), Isotope Shift in the Arc Spectrum of Nickel, *Physical Review*, *121*(6), 1726-1731.

Self, D. E., and J. M. C. Plane (2003), A kinetic study of the reactions of iron oxides and hydroxides relevant to the chemistry of iron in the upper mesosphere, *Physical Chemistry Chemical Physics*, *5*(7), 1407-1418, doi:10.1039/B211900E.

Sghaier, O., R. Linguerri, M. M. A. Mogren, J. S. Francisco, and M. Hochlaf (2016), Spectroscopic Constants of the $X^1\Sigma^+$ and $1^3\Pi$ States of AlO+, *The Astrophysical Journal*, *826*(2), 163, doi:10.3847/0004-637x/826/2/163.

She, C.-Y. (2005), On atmospheric lidar performance comparison: from power–aperture product to power–aperture–mixing ratio–scattering cross-section product, *Journal of Modern Optics*, *52*(18), 2723-2729, doi:10.1080/09500340500352618.

Sica, R. J., S. Sargoytchev, P. S. Argall, E. F. Borra, L. Girard, C. T. Sparrow, and S. Flatt (1995), Lidar measurements taken with a large-aperture liquid mirror. 1. Rayleigh-scatter system, *Appl. Opt.*, *34*(30), 6925-6936, doi:10.1364/AO.34.006925.

SIRAH (2020), Cobra-Stretch Dye Laser Datasheet.

Slipher, V. M. (1929), Emission in the spectrum of the light of the night sky, *Publ. Astron. Soc. Pac*, *41*, 262–263.

Smirnov, V. N. (2008), Rate constant of the gas-phase reaction between Fe atoms and CO_2, *Kinetics and Catalysis*, *49*(5), 607-609, doi:10.1134/S0023158408050017.

Smith, A. K., N. M. Pedatella, D. R. Marsh, and T. Matsuo (2017), On the Dynamical Control of the Mesosphere–Lower Thermosphere by the Lower and Middle Atmosphere, *Journal of the Atmospheric Sciences*, *74*(3), 933-947, doi:10.1175/JAS-D-16-0226.1.

Solomon, S., E. E. Ferguson, D. W. Fahey, and P. J. Crutzen (1982), On the chemistry of H_2O H_2 and meteoritic ions in the mesosphere and lower thermosphere, *Planetary and Space Science*, *30*(11), 1117-1126, doi:10.1016/0032-0633(82)90122-2.

Sonnerup, B. U. Ö., and L. J. Cahill Jr. (1968), Explorer 12 observations of the magnetopause current layer, *73*(5), 1757-1770, doi:10.1029/JA073i005p01757.

Spietz, P., U. Gross, E. Smalins, J. Orphal, and J. P. Burrows (2001), Estimation of the emission temperature of an electrodeless discharge lamp and determination of the oscillator strength for the I($^2P_{3/2}$) 183.038 nm resonance transition, *Spectrochimica Acta Part B: Atomic Spectroscopy*, *56*(12), 2465-2478, doi:10.1016/S0584-8547(01)00330-5.

Su, T., and W. J. Chesnavich (1982), Paramterization of the ion-polar molecule collision rate constant by trajectory calculations, *J. Chem. Phys.*, *76*, 5183-5185.

Teitelbaum, H., and J. E. Blamont (1977), Variations of the turbopause altitude during the night, *Planetary and Space Science*, *25*(8), 723-734, doi:10.1016/0032-0633(77)90124-6.

Tilgner, C., and U. von Zahn (1988), Average properties of the sodium density distribution as observed at 69°N latitude in winter, *Journal of Geophysical Research: Atmospheres*, *93*(D7), 8439-8454, doi:10.1029/JD093iD07p08439.

Troe, J. (1985), Statistical adiabatic channel model of ion-neutral dipole capture rate constants, *Chemical Physics Letters*, *122*(5), 425-430, doi:10.1016/0009-2614(85)87240-7.

Unterguggenberger, S., S. Noll, W. Feng, J. M. C. Plane, W. Kausch, S. Kimeswenger, A. Jones, and S. Moehler (2017), Measuring FeO variation using astronomical spectroscopic observations, *Atmos. Chem. Phys.*, *17*(6), 4177-4187, doi:10.5194/acp-17-4177-2017.

Vardhan, D., R. Liyanage, and P. B. Armentrout (2003), Guided ion beam studies of the reactions of Ni_n^+ (n=2-18) with O_2: Nickel cluster oxide and dioxide bond energies, *J. Chem. Phys.*, *119*(8), 4166-4178, doi:10.1063/1.1592502.

Viehl, T. P., J. M. C. Plane, W. Feng, and J. Höffner (2016), The photolysis of FeOH and its effect on the bottomside of the mesospheric Fe layer, *43*(3), 1373-1381, doi:10.1002/2015gl067241.

Vondrak, T., J. M. C. Plane, S. Broadley, and D. Janches (2008), A chemical model of meteoric ablation, *Atmos. Chem. Phys.*, *8*(23), 7015-7031, doi:10.5194/acp-8-7015-2008.

Vondrak, T., K. R. I. Woodcock, and J. M. C. Plane (2006), A kinetic study of the reactions of Fe^+ with N_2O, N_2, O_2, CO_2 and H_2O, and the ligand-switching reactions $Fe^+.X + Y \rightarrow Fe^+.Y + X$ ($X = N_2$, O_2, CO_2; $Y = O_2$, H_2O), *Physical Chemistry Chemical Physics*, *8*(4), 503-512, doi:10.1039/B508922K.

Wagenaar, H. C., I. Novotný, and L. De Galan (1974), The influence of hollow-cathode lamp line profiles upon analytical curves in atomic absorption spectroscopy, *Spectrochimica Acta Part B: Atomic Spectroscopy*, *29*(11), 301-317, doi:10.1016/0584-8547(74)80035-2.

Wandinger, U. (2005), Introduction to Lidar, in *Lidar: Range-Resolved Optical Remote Sensing of the Atmosphere*, edited by C. Weitkamp, pp. 1-18, Springer New York, New York, NY, doi:10.1007/0-387-25101-4_1.

Wang, M., G. Audi, F. G. Kondev, W. J. Huang, S. Naimi, and X. Xu (2017), The AME2016 atomic mass evaluation (II). Tables, graphs and references, *Chinese Physics C*, *41*(3), doi:10.1088/1674-1137/41/3/030003.

Weber, M. E., J. L. Elkind, and P. B. Armentrout (1986), Kinetic energy dependence of $Al^+ + O_2 \rightarrow AlO^+ + O$, *84*(3), 1521-1529, doi:10.1063/1.450497.

Western, C. M. (2016), PGOPHER version 9.1, edited, University of Bristol Research Data.

Western, C. M. (2017), PGOPHER: A program for simulating rotational, vibrational and electronic spectra, *Journal of Quantitative Spectroscopy and Radiative Transfer*, *186*, 221-242, doi:10.1016/j.jqsrt.2016.04.010.

Whalley, C. L., J. C. Gómez Martín, T. G. Wright, and J. M. C. Plane (2011), A kinetic study of Mg^+ and Mg-containing ions reacting with O_3, O_2, N_2, CO_2, N_2O

and H_2O: implications for magnesium ion chemistry in the upper atmosphere, *Physical Chemistry Chemical Physics*, *13*(13), 6352-6364, doi:10.1039/C0CP02637A.

Whalley, C. L., and J. M. C. Plane (2010), Meteoric ion layers in the Martian atmosphere, *Faraday Discussions*, *147*(0), 349-368, doi:10.1039/C003726E.

Willmore, A. P. (1965), *The Ionospheric Measurements from Ariel I.*, Springer, Dordrecht, doi:10.1007/978-94-010-3590-3_40.

Woodcock, K. R. S., T. Vondrak, S. R. Meech, and J. M. C. Plane (2006), A kinetic study of the reactions $FeO^+ + O$, $Fe^+.N_2 + O$, $Fe^+.O_2 + O$ and $FeO^+ + CO$: implications for sporadic E layers in the upper atmosphere, *Physical Chemistry Chemical Physics*, *8*(15), 1812-1821, doi:10.1039/B518155K.